Universitat Politècnica de València

Departamento de Ingeniería Eléctronica

UNIVERSITAT
POLITÈCNICA
DE VALÈNCIA

Doctoral Dissertation

Substrate Integrated Coaxial Filters with Fixed and Tunable Responses

Stefano Sirci

Advisors

Dr. Jorge D. Martínez Pérez (Universitat Politècnica de València)

Dr. Vicente E. Boria Esbert (Universitat Politècnica de València)

Thesis submitted to the Departamento de Ingeniería Eléctronica,
in partial fulfillment of the requirements for:
Título de Doctor por la Universitat Politècnica de València
Date: February 2017, Valencia

. . . alle mie amiche ed ai miei amici, di ogni età e nazionalità,
per avermi sopportato, ascoltato, fatto ridere, sgridato e incoraggiato, sempre. . .

. . . alla mia famiglia, per il loro incessante appoggio ed amore. . .

. . . a mis directores, a quienes les debo mucho,
por haberme animado, guiado, enseñado,
abierto a sus enormes conocimientos a lo largo de esta tesis,
confiando en mí más que yo mismo. . .

. . . e, soprattutto, ad Eleonora, perchè è tutto per me e
se sono arrivato fin qui, è grazie a lei.

Year after year, Running over the same old ground.
And how we found the same old fears. Wish you were here.
How I wish, how I wish you were here.
(Pink Floyd. "Wish You Were Here." *Wish You Were Here.* 1975)

Resumen

Las comunicaciones inalámbricas y móviles juegan un papel importante en nuestras vidas, y esto sólo puede ir a más debido a su enorme importancia y al uso de los modernos teléfonos inteligentes (del inglés, *smartphones*), tabletas y toda clase de dispositivos inalámbricos. Con todo esto en mente, el espectro electromagnético para comunicaciones inalámbricas y móviles se está saturando cada día más, lo que conlleva un constante aumento de los requisitos para los filtros de radio-frecuencia usados en las cabeceras de dichos sistemas.

Este progreso ha llevado a un creciente interés en desarrollar componentes de microondas de bajo coste, alto rendimiento, pequeño tamaño, que permitan implementar soluciones altamente integradas para sistemas de alta frecuencia (i.e. microondas y ondas milimétrica) y sus aplicaciones, incluyendo entre ellas la emergente conexión 5G y las futuras plataformas inalámbricas. En este contexto, los resonadores de elevado factor de calidad constituyen generalmente los bloques básicos para el diseño de muchos circuitos pasivos (entre ellos filtros) y activos de alto rendimiento. Su diseño se ha convertido por tanto en un reto aún mayor en la última década. Como resultado de ello, la tecnología de guía de ondas integradas en substrato (*Substrate Integrated Waveguide*, Substrate Integrated Waveguide (SIW)) ha atraído la atención de la comunidad científica e industrial, al revelarse como una buena aproximación para el desarrollo de dispositivos planares de microondas con excelentes prestaciones eléctricas, y en particular para la implementación de filtros de microondas y onda milimétrica de bajas pérdidas y elevada integración con circuitos en tecnología planar. Además, su flexibilidad se caracteriza también por su adecuación a diferentes procesos de fabricación y producción en masa, en tecnologías tales como los circuitos impresos (*Printed Circuit Board*, Printed Circuit Board (PCB)) o la tecnología de materiales cerámicos multi-capa co-sinterizados a baja temperatura (*Low Temperature Co-fired Ceramics*, Low Temperature Co-fired Ceramics (LTCC)) entre otras. Su enorme similitud con las ya largamente estudiadas guías de onda es, probablemente, una de las principales razones por las cuales el desarrollo de dicho circuitos está creciendo rápidamente entre la comunidad de investigadores. Cabe mencionar como, además de las anteriores ventajas, otras características de la tecnología SIW que podrían ser de gran interés en una amplia gama de aplicaciones inalámbricas y móviles son la miniaturización, la posibilidad de implementar respuestas avanzadas de filtrado y, recientemente, las capacidades de sintonía en frecuencia de los componentes de microondas. Estas características clave se han introducido recientemente en el diseño de filtros microondas para los sistemas inalámbricos de próxima generación, convirtiéndose en objeto prioritario de estudio por parte de la comunidad científica.

De este modo, el trabajo desarrollado a lo largo de esta Tesis Doctoral se ha orientado hacia el planteamiento, análisis y desarrollo de una topología de resonador innovadora y original. Dicha topología se basa en una extensión de las cavidades coaxiales en guía de onda metálica a una implementación integrada en substrato inspirada en la tecnología

SIW.

Esta Tesis Doctoral recapitula los últimos avances que se han producido sobre este tema, empezando desde la descripción de los principios fundamentales de funcionamiento de las estructuras, hasta la demostración de varias aplicaciones concretas útiles para el diseño de filtros de microondas muy compactos, con respuestas filtrantes avanzadas y reconfigurables. Los resultados que se van a mostrar a continuación son prometedores, y demuestran la validez de la topología propuesta. El conocimiento general obtenido de los diferentes prototipos fabricados y caracterizados experimentalmente puede considerarse una buena base para seguir desarrollando esta tecnología, lo que puede ayudar a mejorar su rendimiento electromagnético, así como a contribuir a un uso más extendido de estos dispositivos en el mercado.

Resum

Les comunicacions sense fils i mòbils juguen un paper important en les nostres vides, i això només pot anar a més a causa de la gran importància i l'ús dels moderns telèfons intel·ligents (de l'anglès, smartphones), tablets i tota classe de dispositius sense fil. Tenint en compte tot açò, l'espectre electromagnètic per a comunicacions sense fils i mòbils s'està saturant cada dia més, el que comporta un constant augment dels requisits per als filtres de radiofreqüència usats en les capçaleres d'aquests sistemes.

Aquest progrés ha portat a un creixent interès en desenvolupar components de microones de baix cost, alt rendiment, volum reduït, que permeten implementar solucions altament integrades per a sistemes d'alta freqüència (ie. microones i ones mil·limètriques) i les seves aplicacions, incloent l'emergent connexió 5G i les futures plataformes sense fils. En aquest context, els ressonadors d'elevat factor de qualitat constitueixen generalment els blocs bàsics per al disseny de molts circuits passius (entre ells filtres) i actius d'alt rendiment. El seu disseny s'ha convertit per tant en un repte encara més gran en l'última dècada. Com a resultat d'això, la tecnologia de guia d'ones integrades en substrat (*Substrate Integrated Waveguide*, SIW) ha atret l'atenció de la comunitat científica i industrial, al revelar-se com una bona aproximació per al desenvolupament de dispositius planars de microones amb excel·lents prestacions elèctriques , i en particular per a la implementació de filtres de microones i ones mil·limètriques de baixes pèrdues i elevada integració amb circuits en tecnologia planar. A més, la seua flexibilitat es caracteritza també per la seua adequació a diferents processos de fabricació i producció en massa, en tecnologies com ara els circuits impresos (*Printed Circuit Board*, PCB) o la tecnologia de materials ceràmics multicapa co-sinteritzats a baixa temperatura (*Low Temperature Co-Fired Ceramics*, LTCC) entre d'altres. La seua enorme similitud amb les ja llargament estudiades guies d'ona és, probablement, una de les principals raons per les quals el desenvolupament d'aquests circuits està creixent ràpidament entre la comunitat d'investigadors. Cal destacar com, a més de les anteriors avantatges, altres característiques de la tecnologia SIW que podrien ser de gran interès en una àmplia gamma d'aplicacions sense fils i mòbils són la miniaturització, la possibilitat d'implementar respostes avançades de filtrat i, recentment, les capacitats de sintonia en freqüència dels components de microones. Aquestes característiques clau s'han introduït recentment en el disseny de filtres microones per als sistemes sense fils de pròxima generació, convertint-se en objecte prioritari d'estudi per part de la comunitat científica.

D'aquesta manera, el treball desenvolupat al llarg d'aquesta tesi doctoral s'ha orientat cap al plantejament, anàlisi i desenvolupament d'una topologia de ressonador innovadora i original. Aquesta topologia es basa en una extensió de les cavitats coaxials en guia d'ona metàl·lica a una implementació integrada a substrat inspirada en la tecnologia SIW.

Aquesta tesi doctoral recapitula els últims avanços que s'han produït sobre aquest tema, començant des de la descripció dels principis fonamentals de funcionament de les estructures, fins a la demostració de diverses aplicacions concretes útils per al disseny de

filtres i microones molt compactes, amb respostes de filtrat avançades i reconfigurables. Els resultats que es mostraran a continuació són prometedors, i demostren la validesa de la topologia proposada. El coneixement general obtingut dels diferents prototips fabricats i caracteritzats experimentalment es pot considerar com una bona base per seguir desenvolupant aquesta tecnologia, el que pot ajudar a millorar el seu rendiment electromagnètic, així com a contribuir a un ús més estès d'aquests dispositius en el mercat.

Abstract

Wireless and mobile communications are already playing an important role in our lives, and this will can only grow more and more due to the predominant importance and use of modern smartphones, tablets and any kind of connected devices. With this is mind, the spectrum for wireless and mobile communications is becoming incredibly overcrowded, leading to increasing requirements for RF front-end filters.

This progress has encouraged an impressive need for developing low-cost, high performance, mass-producible, small footprint, and highly integrated front-end solutions for microwave and millimeter-wave systems and applications including emerging 5G and future wireless platforms. In this context, high quality factor resonators are usually typical basic building blocks of many high performance passive and active circuits, and its design has become even more challenging in the last decade. As a result, Substrate Integrated Waveguide (SIW) technology has attracted scientific community and industry attention as a very good candidate for developing such desired high-Q planar microwave devices.

Recently, SIW is demonstrating to be a successful approach for implementing microwave and millimeter-wave filters with high Q-factor, easy integration with other planar circuits, and for mass-production manufacturing processes in many technologies (i.e. Printed Circuit Board (PCB) and Low Temperature Co-fired Ceramics (LTCC) technologies among them). Its enormous similarity with waveguides is probably one of the main reasons why the development of SIW-based components and circuits is rapidly growing among the research community. Other potential features that, combined with the former advantages, could be of huge interest in a wide range of wireless and mobile applications are a lively set of research subjects, such as compactness, advanced filtering responses, and recently frequency-agility capabilities. These key features have been recently introduced in the design of microwave filters for the next-generation wireless systems.

Taking into account the above-mentioned background, the work carried out during the course of this PhD Thesis has been directed towards a further study of SIW technology to propose, analyze and develop an innovative and original resonator topology. The proposed topology is based on the extension of the classical coaxial waveguide resonator to SIW technology, and must take advantage of the characteristics of SIW devices to allow the design of improved and innovative microwave resonator filters for advanced wireless systems.

This PhD Thesis includes the latest improvements made on this topic, from the working principles of the basic coaxial SIW block, until different applications for the design of compact quasi-elliptic and reconfigurable microwave filters. The results are promising and prove the validity of the proposed topology for the design of high-Q microwave filters, as well as its potential application to implement complex designs. The general knowledge gained from these cases of study can be considered a good base for further developing this technology, which can help to improve its EM performance, and also contribute to a more general use in the market.

Contents

1 Introduction **1**
- 1.1 Motivation and Interest of the Topic . . . 1
- 1.2 State of the Art . . . 2
  - 1.2.1 Advanced Filtering Responses in SIW . . . 3
  - 1.2.2 Tunable Microwave Filters . . . 8
- 1.3 Objectives . . . 18
- 1.4 Document Organization . . . 19

2 Coaxial SIW Filters **21**
- 2.1 Basic Theory of Coaxial SIW Resonators . . . 21
  - 2.1.1 Synthesis of Coaxial SIW Resonators . . . 22
  - 2.1.2 Unloaded Quality Factor and Losses . . . 26
- 2.2 Sensitivity Analysis . . . 32
  - 2.2.1 Tolerances of Laminate Dielectric Constant . . . 32
  - 2.2.2 Effects of Temperature . . . 33
  - 2.2.3 Manufacturing Tolerances . . . 34
- 2.3 Inter-resonator Coupling . . . 36
  - 2.3.1 Magnetic Couplings . . . 37
  - 2.3.2 Electric Couplings . . . 38
- 2.4 External Coupling . . . 41
  - 2.4.1 Magnetic Couplings . . . 42
  - 2.4.2 Electric Couplings . . . 43
- 2.5 Synthesis of Coaxial SIW Filters . . . 45
- 2.6 Filter Design . . . 47
  - 2.6.1 Example: X-band Filter in PCB technology . . . 47
  - 2.6.2 Example: X-band Filter in LTCC technology . . . 48

3 Advanced Filtering Responses **53**
- 3.1 Trisection Coaxial SIW Filter . . . 53
  - 3.1.1 Filter Design . . . 54
  - 3.1.2 Experimental Results . . . 55
- 3.2 Coaxial SIW Diplexer . . . 57
  - 3.2.1 Electric Cross-Coupling . . . 58
  - 3.2.2 Channel Filter Design . . . 59
  - 3.2.3 Experimental Results . . . 62
- 3.3 Four-pole Quasi-Elliptic Coaxial SIW Filter . . . 64
  - 3.3.1 Vertical Transition . . . 65
  - 3.3.2 Filter Design . . . 67

3.3.3 Experimental Results . . . 69
3.3.4 Multiphysics Study for the Power Handling Capability Evaluation . 72
3.4 Six-pole Quasi-Elliptic Coaxial SIW Filters for Frequency Conversion . . . 80
3.4.1 Filters Specifications . . . 80
3.4.2 Filters Synthesis . . . 82
3.4.3 Filters Design . . . 87
3.4.4 Simulated Results of the Filters . . . 89
3.4.5 Mixed Cross-Coupling . . . 91

4 Analog and Digitally Tunable Filters 93
4.1 Background . . . 93
4.2 Continuously Tunable Filter . . . 94
4.2.1 Analog Tuning in Coaxial SIW Technology . . . 94
4.2.2 Tuning Element . . . 95
4.2.3 Resonator Design . . . 96
4.2.4 Filter Design . . . 99
4.2.5 Experimental Results . . . 100
4.3 SMD Packaged Varactor-Loaded Tunable Filter . . . 103
4.3.1 Tuning Element . . . 105
4.3.2 Filter Design . . . 105
4.3.3 Experimental Results . . . 106
4.3.4 Power Handling Measurements . . . 107
4.4 Discretely Tunable Filters Using Switched Capacitors in RF MEMS Technology . . . 108
4.4.1 Tuning Element . . . 109
4.4.2 Experimental Results . . . 110
4.4.3 Power Handling Measurements . . . 112
4.5 Discretely Tunable Filters Using PIN Diodes . . . 112
4.5.1 Tuning Element . . . 114
4.5.2 Filter Design . . . 115
4.5.3 Experimental Results . . . 119
4.6 Discretely Tunable Filters Using RF MEMS Resistive Switches . . . 122
4.6.1 RF MEMS Resistive Switch . . . 123
4.6.2 Filter Design . . . 124
4.6.3 Experimental Results . . . 126
4.7 Comparison of Reconfigurable Filter Performance . . . 130

5 Conclusions and Future Work 133
5.1 Conclusions and Future Research Areas . . . 133

A List of Publications 137
A.1 International Journal Publications . . . 137
A.2 International Conference Publications . . . 137
A.3 International Workshops . . . 138
A.4 National Conference Publications . . . 138
A.5 Patents . . . 139

Acronyms 141

Chapter 1

Introduction

1.1 Motivation and Interest of the Topic

Since wireless communication systems are imposing tighter requirements in terms of electrical specifications as well as drastic cost reductions, the area of microwave filters, especially for wireless, mobile and space applications, has experienced significant improvements in theoretical, technological, and performance subjects. In fact, the proliferation of multiband wireless systems is demanding for advanced front ends that can achieve maximum hardware co-sharing for various wireless standards. Different solutions can be applied to improve front ends performance. For instance, the technique of using cross-couplings has demonstrated to be useful for obtaining advanced filtering responses that allow to reduce the number of resonating elements in microwave filters. Therefore, a reduction of insertion losses, footprint size, and design manufacturing costs of a microwave filter can be also obtained.

Nevertheless, in order to design a multi-standard Radio Frequency (RF) front-end that would cover all the different frequency bands (i.e. wireless standards from 2G, 3G, Worldwide Interoperability for Microwave Access (WiMAX), Long Term Evolution (LTE), up to the future 5G) and to fully realize modern multi-functional communication systems, the transceiver would require the introduction of customized RF devices that include tunable filters. As it is well known, reconfigurable filter technology is applicable in any sector of telecommunications that requires the ability to modify the frequency response of microwave filtering devices (i.e. mobile and space communications, test equipment, radar, etc.), as can be the case of commercial or military applications. In most of these applications, the availability of a cost-effective technology that allows for the mass-production of components and systems can be a key factor for its successful use.

The move to reconfigurable filters, with the involved relative reduction of microwave components, could further reduce manufacturing, assembly, integrating and testing costs. In the design of such devices, so far it has been difficult to find an acceptable compromise among high Unloaded Quality Factor (Q_u), small size and wide tuning range. Additionally, tunable microwave filters must meet several specifications such as fast tuning speed, linearity, low manufacturing cost, reliability and low power consumption, which will be very important in most applications, to justify their use in real telecommunication applications, especially in those related to space.

In this context, SIW technology has been recently developed providing a low-profile, low-cost, and low-weight scheme while maintaining high performance. Basically, SIW is a synthesized non-planar waveguide transformed into planar form with linear arrays of

metalized via holes, which can then be integrated into any planar dielectric substrate [1,2], as it is shown in Fig. 1.1.

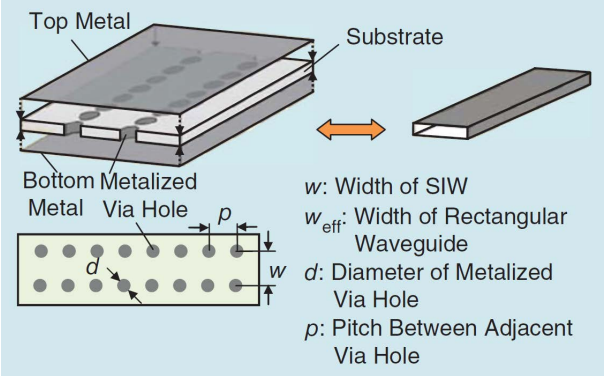

Figure 1.1: A classical representation of an SIW and its equivalent rectangular waveguide (from [2]).

As it has been very well summarized in [3, 4] and also more recently in [5], SIW technology has been applied to many microwave components, such as cavity filters, antennas, directional couplers, oscillators, power amplifiers, and so on, since its first demonstration in [1] almost 20 years ago. Advanced design techniques and innovative structure features in SIW technology have been recently reported in a large number of publications, including some analysis about power handling capabilities of such structures.

The fusion of planar and non-planar structures presents an optimal compromise in terms of Electromagnetic (EM) performance, cost, size, manufacturability, and many other aspects. Among them, the integrability capability is one of most important advantage that SIW technology inherit from its planar nature. Additionally, it is able to fill the technological gap between planar (i.e. microstrip or stripline that offers Q_u in the range of $50-200$) and non-planar solutions (i.e. dielectric resonator or metallic waveguide that present Q_u from 200 to 10000). Actually, SIW offers Q-factors that are between 150 and 1000. This means that an SIW can be considered one of the best approaches for distilling the benefits of both 3D waveguide and planar microwave structures in one solution.

The work behind this PhD Thesis has been directed towards a further study of SIW technology in order to conceive an innovative resonator topology. Basically, this original topology has been created by extending the classical coaxial waveguide resonator to SIW technology. This PhD Thesis includes the latest improvements made on this topic, showing the significant contributions in two areas: the proposed topology is first applied to the design of advanced filtering responses in the microwave band, and then to the design of reconfigurable microwave filters.

1.2 State of the Art

In this section, we are going to present the state of the art of two main topics related to the work that has been performed in this Thesis. First of all, an overview of the design of quasi-elliptic filters in the literature is presented, especially focused on those solutions based on SIW technology. Then, a wide variety of filter tuning techniques available in the literature are described, showing the advantages and disadvantages of each technique.

1.2.1 Advanced Filtering Responses in SIW

Over the last decades, the topic of microwave filters has experienced enormous advances in many subjects, especially for mobile and space communications systems. One of the significant improvements in filter design theory has been utilizing cross-coupling between non-adjacent resonators. As it has been demonstrated some decades ago in [6] by using waveguide technology, and in [7] using microstrip bandpass filters, cross-coupled filter topology introduces a number of alternative paths between the input and output ports in which the flow of the EM signal passes through. Depending on the signal phase, the multi-path effect generates Transmission Zero (TZ) to appear in the transfer function, which can result in the introduction of TZs at finite frequencies or in flattening the group-delay response, or even both simultaneously [8–10]. Therefore, cross-coupling between non-adjacent resonators are often used to obtain a linear phase response or to generate finite TZs for enhanced selectivity, improving rejection at the frequencies where it is needed.

This approach allows to minimize the number of resonating elements required to satisfy a certain specification in terms of selectivity. Thus, a reduction of Insertion Loss (IL), footprint size, and design manufacturing cost of a microwave filter can be also obtained. Clearly, the number of transmission zeros depends on the characteristics of the coupling network, being the relative signs and magnitudes of the cross-coupling coefficients the ones that fix the positions of finite TZs.

All of this can be obtained at the expense of increasing the topological complexity, since cross-coupling mechanisms between non-adjacent resonators must be implemented. Additionally, the need for the introduction of cross-couplings of different signs is sometimes hard work to perform, and it strongly depends on the filter technology.

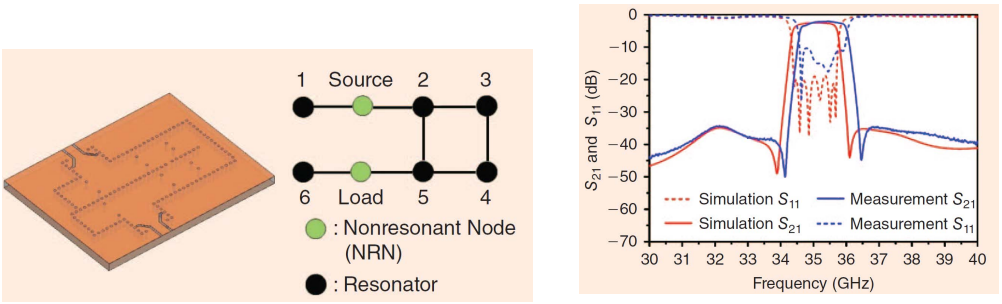

(a) (b)

Figure 1.2: (a) The geometric configuration and structural topology. (b) The frequency responses of a sixth-order self-equalized pseudo-elliptic SIW filter.

The SIW technology has been successfully employed in several works for the design of quasi-elliptic filters in the last decade. The SIWs are very suitable for the implementation of multiple paths and phase relations in above-mentioned filter topologies due to its inherent flexibility, thus allowing easy control for TZs.

Two main approaches have been followed for generating TZs in SIW filters. The first method is based on the extracted-pole filter topology, where a TZ in the passband is produced by a bandstop resonator, typically implemented in SIW technology, but it can be also implemented in microstrip or any other planar technology.

For instance, in [11], TZs have been created on both the imaginary axis and the real axis in a Ka-band self-equalized pseudo-elliptic SIW filter using only magnetic couplings,

as shown in Fig. 1.2. These couplings are realized by a section of SIW evanescent mode that couples adjacent SIW resonators.

On the one hand, two bandstop SIW cavity resonators have been coupled to the source and load of the SIW filter, and are responsible for the generation of two symmetrical TZs adjacent to the filter passband. On the other hand, a linear phase response has been implemented by using a magnetic cross coupling between SIW cavity resonators 2 and 5, following the approach described in 2005 by [12].

The second method for generating TZs makes use of the canonical cross-coupling approach with physical coupling structures to produce multiple paths for the signal flow, as well as using non-physical couplings implemented by higher-order modes. As it has been demonstrated in [10], when different paths are provided in a multi-resonator structure, it is the signal phase-shift between each path that generates the TZ. When two paths are out of phase (i.e. 180° apart) at a certain frequency value, the destructive interference causes a TZ. The frequency location of the TZ depends on the phase-shift contributions of the individual components (i.e. resonators, inter-resonator couplings and cross-couplings) that compose the structure.

In the following Sections, it is worth mentioning that the nomenclature *magnetic* and *electric* couplings will be used for identifying coupling mechanisms that are out of phase between them, without any importance attached to its positive o negative phase shift (even though the negative sign is usually employed in the literature for referring to couplings of electric nature).

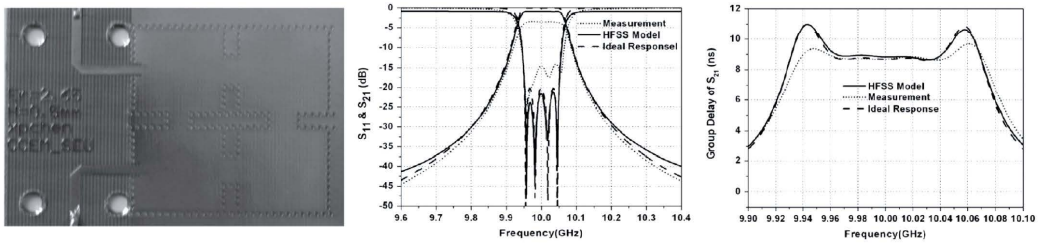

Figure 1.3: (*Left*) Photo of the SIW four-pole linear phase filter. (*Center*) Ideal, simulated, and measured frequency responses. (*Right*) Ideal, simulated, and measured group time delay.

Applications of this method based on physical coupling structures have been demonstrated in SIW in several works. Even if magnetic and electric couplings are generally required for providing multiple paths, magnetic coupling using irises between adjacent resonators has been the preeminent scheme for the first implementations of advanced filtering responses in SIW. This was mainly due to the fact that, on single-layer topology, it is a quite challenging task to simultaneously design magnetic and electric coupling networks for the generation of TZs on the imaginary axis.

Back in 2005, the use of all inductive couplings was demonstrated for implementing linear-phase band-pass SIW filters [12]. In this work, the band-pass filter is composed of four side-by-side horizontally oriented cavities, where inductive irises are used for the three direct coupling, and also for one cross coupling between the first and fourth cavities. As Fig. 1.3 displays, the filter presents a compact size, and its measured responses have good agreements with EM simulations.

The first implementations of TZs demonstrated in SIW made use of non-physical couplings [13]. Using this approach, if a magnetic post-wall iris is properly located in

adjacent coupled resonators, higher-order resonant modes can be used to obtain the 180° phase change, which is equivalent to the generation of electric coupling in other signal paths with conventional TE_{101} resonant modes. In this context, a first work of X. Chen et al. [13] was presented in 2005, in which a single-layer substrate integrated waveguide fourth-order elliptic filter with higher-order mode was described and demonstrated.

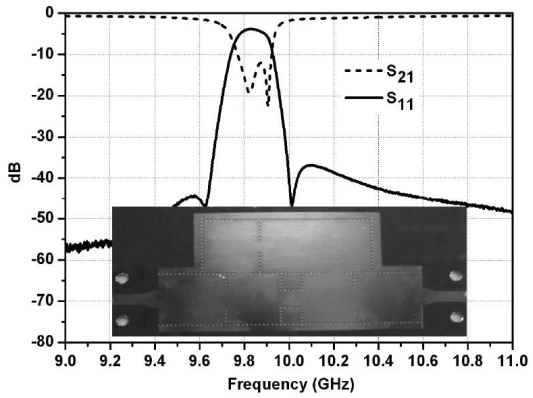

Figure 1.4: Photo of the elliptic fourth-order SIW filter and its measured frequency responses

Specifically, to generate an electric cross-coupling between resonators 1 and 4, a TE_{102} resonance is excited in the third resonator by placing the coupling post-wall iris between resonators 3 and 4 in the second half of resonator 3, as it is shown in Fig. 1.4. This has generated two TZs on the imaginary axis of the complex plane, which can be observed in the frequency response at 9.6 GHz and 10 GHz, having the filter a centre frequency of 9.8 GHz.

Following this approach, more and more advanced filtering responses have been implemented and demonstrated in SIW [14–16]. For example, in [14], a Ka-band fourth-order SIW filter with one TZ located on the left- or right-hand side of the passband was presented. The authors used the TE_{102} mode resonance excited in one SIW cavity for the phase change of the cross-coupling. In [15], non-physical cross-coupling of higher order modes are used for generating multiple TZs distant from the passband, thus improving the stopband attenuation of Ka-band SIW filters. These TZs are generated in two different fourth-order SIW filters by using oversized TE_{101}/TE_{301} and oversized TE_{101}/TE_{201} SIW cavities, respectively.

In [16], an inverter coupled resonator section consisting of one bandpass SIW resonator and one or two bandstop SIW resonators is demonstrated for the first time. This solution allows the design of complex filtering structures, as the case of dual- and triple-passband Chebyshev filters, and dual-passband quasi-elliptic SIW filter. It is worth mentioning that the SIW filters were implemented on a single-layer substrate using only post-wall iris for magnetic coupling in both works.

The main drawback of such approaches is the increasing number of resonators that are necessary for introducing TZs. Some of the former structures are limited in terms of flexibility (i.e. coupling level or resonator positioning) or they require a larger area that affects compactness and EM performance of the proposed elliptic SIW filters. Therefore, the implementation of physical cross-couplings of different signs in SIW is attracting attention in the last years.

The creation of an electric coupling mechanism in SIW technology has been the most difficult task, and it has been investigated by several authors since 2008. In [17] and [18],

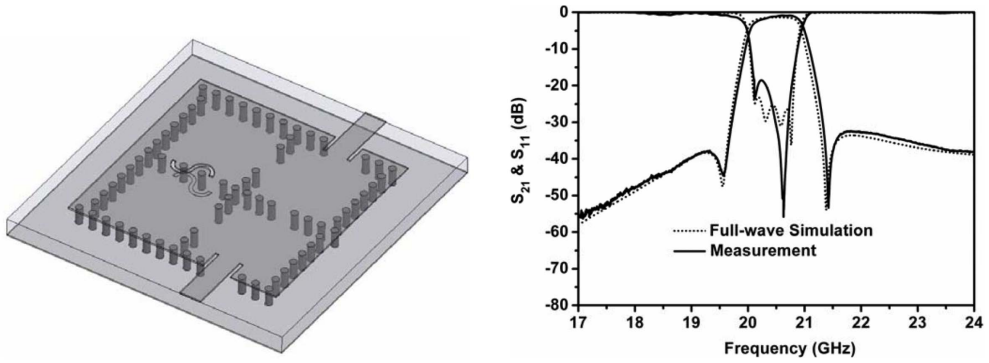

(a) (b)

Figure 1.5: (a) The geometric configuration of the quasi-elliptic SIW filter and (b) a comparison between measured and simulated frequency responses.

the authors present an electric coupling structure between SIW cavity resonators based on a balanced microstrip line with a pair of metallized via holes, as Fig. 1.5 displays in the case of [17]. However, in both structures slots have to be created at top and bottom metal layers limiting the integrability of the device.

In [19], a controllable mixed electric and magnetic coupling has been created using an embedded short-ended strip line that is combined with a conventional post-wall iris. The structure requires a multi-layer PCB fabrication process which increases the complexity. On the other hand, a grounded coplanar line etched only on the top metal layer was proposed in [20] to obtain an electric coupling between standard SIW circular cavities (exciting the TM_{010} modes), even though coupling magnitude is strongly dependent on the substrate height. The authors demonstrated a triplet filter implemented in a high permittivity ceramic substrate. The filter was based on the association of iris-based magnetic couplings with a single electric coupling induced by a grounded coplanar line, thus alleviating problems derived from the common approach in conventional SIW filters that require slots at both sides of the substrate.

It is worth mentioning that these solutions have been successfully applied for designing many quasi-elliptic SIW filters using different type of fabrication processes, as the case of PCB process [17, 19, 20] or the LTCC technology [18].

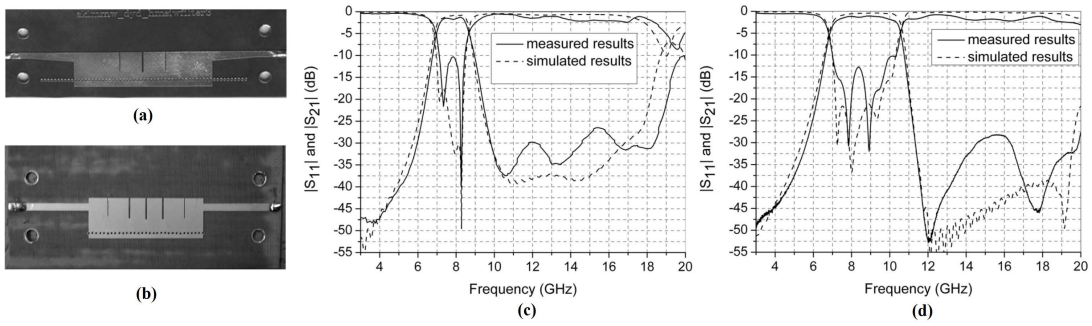

Figure 1.6: Photo of Half-Mode Substrate Integrated Waveguide (HMSIW) filters: (a) 3-pole filter and (b) 5-pole filter. Simulated and measured S-parameters of these filters: (c) 3-pole filter and (d) 5-pole filter.

To conclude this Section, a quick overview of the technical solutions recently provided

for the miniaturization of SIW filters is given. No matter what type of filter technology is considered, minimizing the size of a filter has always received a great attention. Therefore, additional effort of different research groups has been recently focused on the realization of compact SIW microwave filters, which has been approached from different perspectives. As it is well known, SIW filters are still large for applications at low microwave bands, since they are basically based on TE_{101} mode that has a strong frequency dependence.

Thus, several authors have proposed more compact alternatives to conventional SIW cavities by bisecting the resonator at quasi-perfect magnetic walls. Among the most relevant techniques that can be identified in the literature, there are folded [21], half-mode [22, 23] and quarter-mode [24] SIW bandpass filters.

One of the first application of the HMSIW technique has been demonstrated in [23]. The authors have implemented it by cutting the SIW cavity resonator along the center symmetrical plane, which is considered as an equivalent magnetic wall when the SIW is operated with the TE_{101} dominant mode. Note that the Quarter-Mode Substrate Integrated Waveguide (QMSIW) method is a further evolution of the HMSIW approach, since a QMSIW resonator only consists on a quarter of SIW resonator cavity.

Thus, a 3-pole and a 5-pole microwave bandpass filters based on HMSIW technology have been designed and measured, as it is shown in Fig. 1.6. The inter-coupling between HMSIW resonators and external coupling between HMSIW resonators and input/output port are controlled by the transverse slots etched at the top metal layer. The measured results are promising, though the miniaturization is limited to only one psychical size of the devices, and physical cross-coupling are hard to achieve using single-layer implementations.

Recently, it is worth mentioning that the simultaneous use of HMSIW and QMSIW methods for the design of ultra-compact size resonator has been demonstrated in [25], achieving up to 95% of miniaturization compared to conventional full-mode SIW resonators. Even if the filter miniaturization has been obtained maintaining high Q-factor, the increased complexity of the approach (i.e. two different types of resonators have to be used for implementing a trisection filter) reduces its application for the design of complex filtering responses.

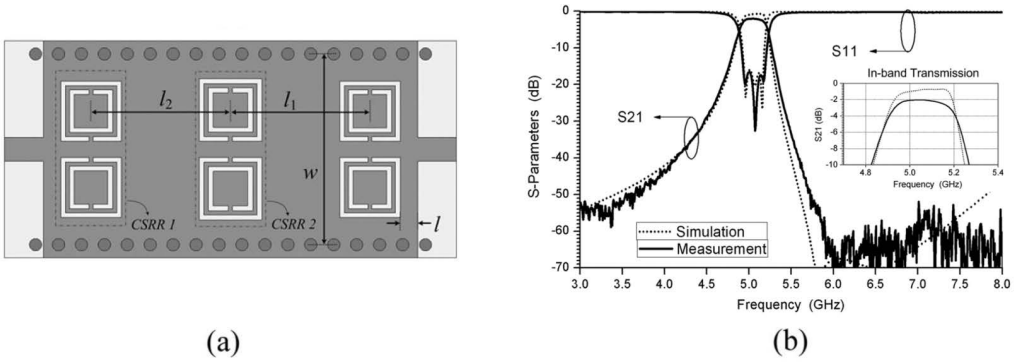

Figure 1.7: (a) Detailed layout of the three-stage filter based on SIW with square Complementary Split-Ring Resonators (CSRRs). (b) Measured and simulated transmission responses of the three-stage filter.

Other approaches have focused on loading the SIW resonator with complementary split-ring resonators [26] or dielectric rods [27]. In this context, the introduction of CSRRs etched on the waveguide surface of an SIW allows for the forward-wave propagation

below the waveguide cutoff, as it has been demonstrated in [26]. This approach is very suitable for miniaturized waveguide filter applications, since the generated passband shows controllable centre frequency and bandwidth that depend on the CSRRs properties. Y. D. Dong et al. in [26] have presented different filter structures, and among them, a 3-pole filter has been designed, fabricated and measured. As it is shown in Fig. 1.7, the filter has a measured centre frequency of 5.05 GHz and a 3-dB Bandwidth (BW) of 330 MHz, with minimum passband IL of 2.03 dB. Note that one TZ is generated in the upper band. This solution presents excellent selectivity with compact size and high planar integration at the expense of a Q degradation with respect to standard SIW approaches. Moreover, the geometrical dimensions of the loading CSRRs structures limits the miniaturization degree.

Most of the former approaches can obtain significant size reduction while keeping integration easiness that is usually of major importance from a practical point of view. Nevertheless, some trade-offs can be highlighted, especially, in terms of Q-factor degradation, manufacturing complexity (i.e. preferably single-layer batch-fabrication processes with solid bottom ground planes instead of multi-layer PCB processes) and design complexity. The latter is a major drawback, since the increased complexity of these approaches can strongly limit their extensibility for the design of complex filtering responses, mainly when high-order or advanced filtering responses are required.

1.2.2 Tunable Microwave Filters

Tunable and reconfigurable RF bandpass filters are expected to be key elements in future reconfigurable and programmable telecommunication systems, both for satellite and terrestrial applications. Only one single device will provide these systems with different filtering functions, such as bandpass filters at different frequencies (i.e. frequency-tunable filters) or bandpass filters having different pass-band widths (i.e. bandwidth-tunable filters).

Size and mass of either satellite or radio-link front-ends in several bands (such as from L/S- to K-band and even above) shall be minimized, and innovative programmable and reconfigurable RF systems will be developed and realized, provided that efficient and reliable solutions for electrically-tunable filters were found. Also conventional switched filter banks may be replaced by reliable and low-cost tunable filters, so leading to both size and mass reduction of the overall component.

Fast tuning speed, high Q_u, wide tuning range, low manufacturing cost and also reliability are very important in most applications. Nevertheless, in the design and realization of frequency-tunable bandpass filters, so far it has been difficult to find an acceptable compromise among these relevant characteristics.

Many existing technologies allow such filters to be designed and implemented with promising results. Therefore, most of them are going to be analyzed in the following. Note that the different solutions will be analyzed according to their EM performance (i.e. from lumped technology to waveguide technology), and then, within a specific technology, according to the tuning elements that has been used. Lastly, since it is strongly related to this Thesis, SIW technology will be presented at the end of this section.

Tunable filters in lumped technology are very compact and have been widely used for several years, and nowadays they are still in use at frequencies from 50 MHz until 2 GHz [28–30]. The simplicity of design, production and low cost are main advantages of using such filters. Tunable lumped element filters can employ different type of tuning ele-

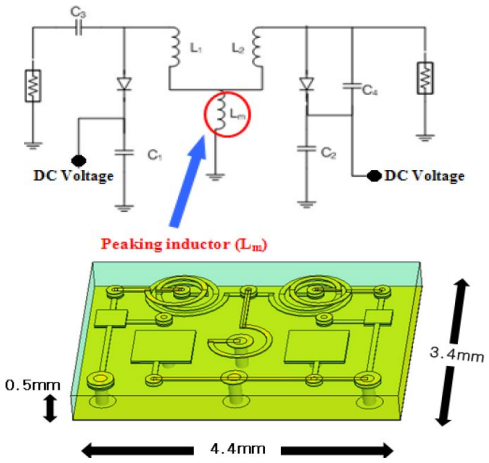

Figure 1.8: Fully embedded tunable filter with inductive coupling circuits [28].

ments, like varactor diodes, Positive-Intrinsic-Negative (PIN) diodes or Radio-Frequency Micro Electro-Mechanical Systems (RF MEMS) switches, to change the resonant frequency or the coupling coefficients of the filter.

Lee and Park [28] demonstrated a highly compact bandpass filter with components embedded into an eight-layered package substrate, as shown in Fig. 1.8. This multi-layered bandpass filter operates in $500 - 900$ MHz range if a bias voltage of varactor diodes is changing from 1 V to 25 V.

Even if this solution provides designers with more compact size and lower manufacturing cost, the limited Q_u of lumped components, which is much below 100, represents its main drawback. The higher the frequency, the lower the resonator Q_u value, thus reducing applications of such solution just for low Ultra High Frequency (UHF) band.

Distributed reconfigurable bandpass filters based on coplanar or microstrip-technology offer highly reconfigurable structure, compact size, low cost solutions and wide tuning range of both frequency and bandwidth. With respect to lumped technology, distributed technology allows to design reconfigurable filters up to S-band showing Q_u values at most of 100. Indeed, the resonator Q_u is still limited by the planar nature of the resonators, which is usually much lower than 200 before assembling any kind of tuning element. In general, the frequency tuning can be close to one octave or even more depending on the capacitance ratio used in the tuning elements (i.e. silicon varactors or RF MEMS switched capacitors) and the resonator length.

Several planar solutions have been realized and tested by different research groups using varactor diodes (among them [31–33] and more recently [34]), ferroelectric components [35], PIN diodes [36, 37] and RF MEMS (i.e. frequency-tunable filters [38–41] and fully tunable filter [42]).

The centre frequency control of a planar microwave filter using a varactor diode has been demonstrated several years ago in [31]. In this work, a combline planar filter is loading by a varactor diode, which allows the loading capacitance to be modified continuously, achieving a wide tuning range. This 2-pole 5%-Fractional Bandwidth (FBW) filter was constructed in suspended substrate stripline and exhibited tuning from 3.2 GHz to 4.9 GHz with a maximum passband insertion loss of 6 dB and a minimum passband return loss of 8 dB. In 2005, M. Sánchez-Renedo et al. [33] have introduced variable coupling reducer in a combline passband filter, achieving a first implementation of tunable-bandwidth planar filter.

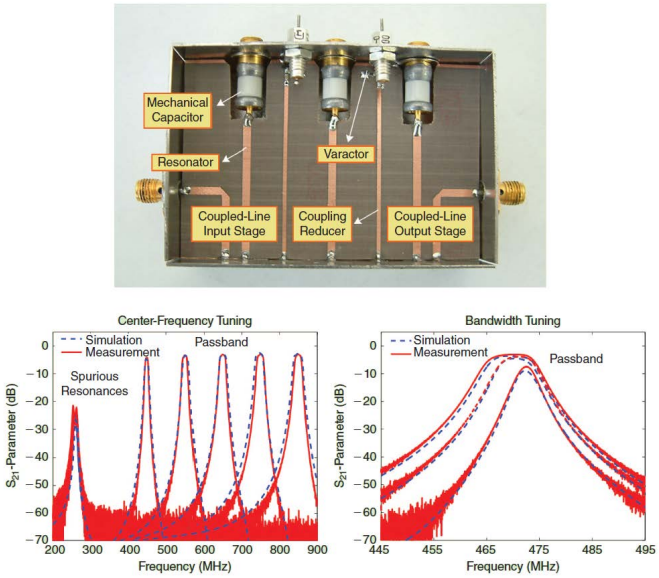

Figure 1.9: Tunable microwave combline-type passband filter with continuous control in center frequency and bandwidth for the UHF band [33].

As it is shown in Fig. 1.9, mechanical capacitors have been used for controlling the filter centre frequency, while the effect of the coupling reduces has been altered by using varactor diode, thus obtaining a continuously control of the filter BW.

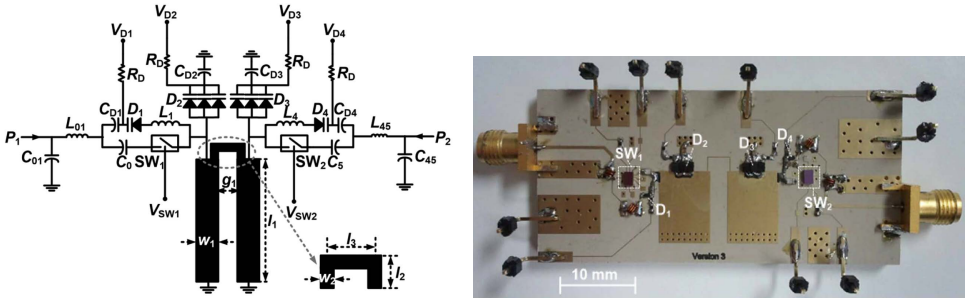

(a) (b)

Figure 1.10: (a) Schematic and (b) photo of the tunable bandpass filter with reconfigurable-pole responses [34].

Recently, in [34] silicon varactor diodes have been used for controlling reconfigurable bandpass filters based on a mix of series resonators and parallel resonators. This solution allows to implement reconfigurable-pole responses, in addition to the control of centre frequency and bandwidth of the filter. Figs. 1.10 and 1.11 depict the schematic of the tunable filters and the measured results. Even if such solutions are very flexible, showing a compact size, the resonator Q_u and power handling are the main drawbacks.

In order to improve these power handling properties while maintaining continuous tuning, Barium Strontium Titanate (BST) varactor has been used as tuning elements in some planar filter. For instance, J. Nath et al. designed, fabricated and measured a third-order combline bandpass filter using thin-film BST Inter-Digital Capacitor (IDC) varactors in [35]. Fig. 1.12-(a) shows the tunable filter, particularly a photo of the first prototype.

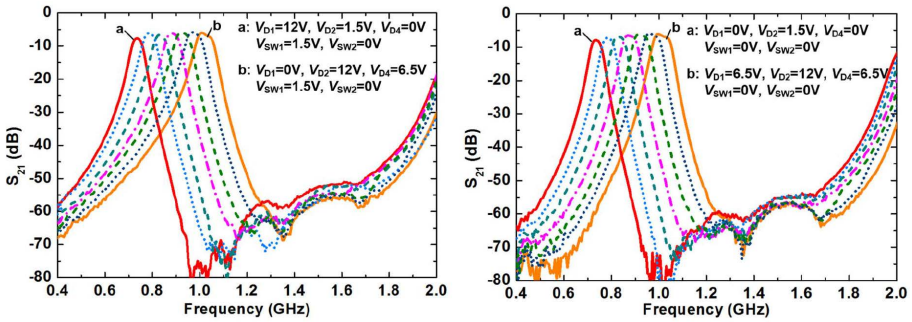

Figure 1.11: Measured results of the 3- and 4-pole state of the tunable bandpass filter with reconfigurable-pole responses [34].

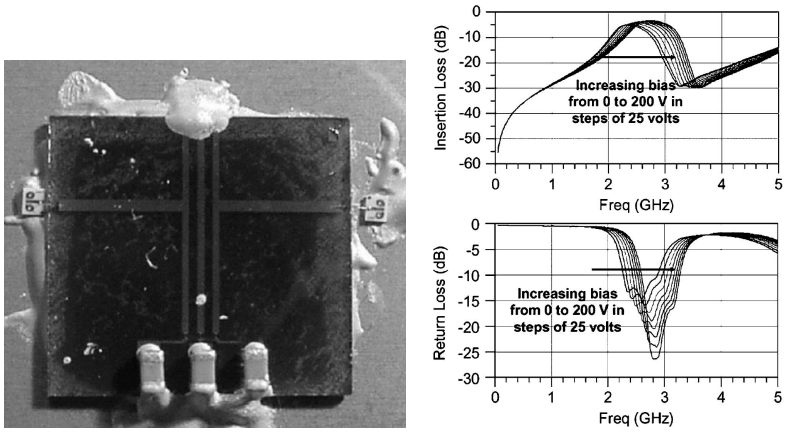

(a) (b)

Figure 1.12: (a) Photo of the BST varactor tunable filter [35] and (b) its measured results.

As Fig. 1.12-(b) shows, the filter centre frequency can be controlled between 2.44 GHz for a bias voltage of 0 V and 2.88 GHz for 200 V, resulting in a tuning range of 16%. Taking into account the filter FBW of 15% and the variation of filter insertion losses (i.e. in the $3.3 - 5.5$ dB interval along all tuning range), the estimated Q_u value of the filter is much lower than 100, and it also requires very high control voltages.

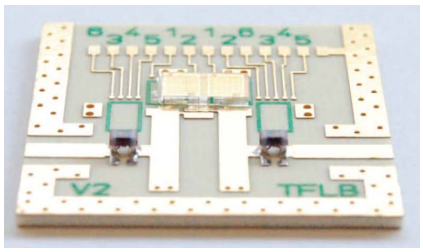

Figure 1.13: Photo of the fabricated 2-bit RF MEMS tunable bandpass filter [41].

RF MEMS have been also employed as tuning element in reconfigurable planar devices. For instance, in [41], a high-power handling tunable filter, based on two-state RF MEMS capacitive device assembled on the top end of combline planar resonators, has been demonstrated in Rogers R4003 (see Fig. 1.13). The RF MEMS tunable filter can be tuned from 900 MHz to 1.5 GHz (see Fig. 1.14), and the measured insertion loss is

less than 3.5 dB. As it can be seen from Fig. 1.14, the measured 1-dB Compression Point (IP1) of the filter is 32.7 dBm and this value is compatible with some wireless data transmission, confirming the progress of the RF MEMS tuning technology in terms of power handling when compared to semiconductor-based tuning elements.

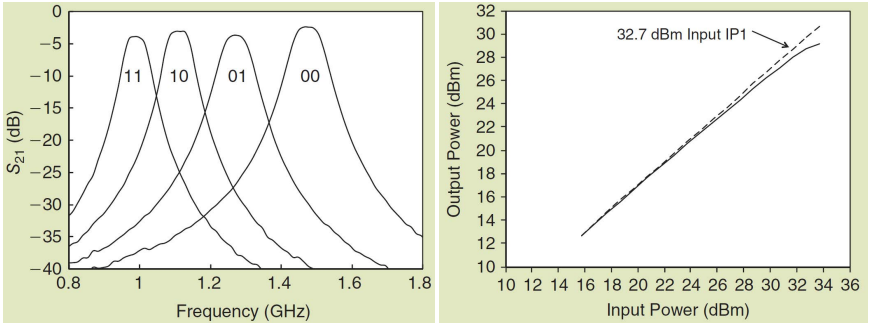

Figure 1.14: Measured S_{21} parameter and linearity of the fabricated 2-bit RF MEMS tunable bandpass filter [41].

Before moving to the waveguide technology, it is worth mentioning that different research groups have recently demonstrated new approaches for designing planar tunable filtering components. In [43–45], tune-all bandpass and bandstop filters have been designed based on intrinsic switching method showing improved frequency agility and reduced complexity.

In [46, 47], authors reported fully reconfigurable bandpass planar filters with ultra-large bandwidth tuning ratio using varactor diodes as tuning elements. These filters are based on two different solutions: spectral controllable signal-interference mechanism in transversal structures and tunable multimode resonators. However, the use of varactor diode limits the power handling of these structures, as well as both approaches do not allow filter miniaturization since its working principle required the introduction of several stubs.

Classical waveguide technology was, and in some cases still is, the mainstream for designing high-performance passive circuits and systems [48–56]. Higher Q_u (> 1000) can be obtained using waveguide resonators exploiting the intrinsic high Q of waveguide structures.

However, these bulky and heavy structures, which are characterized by the large volume of standard cavity resonators at $2 - 10$ GHz, are not suitable for integration and low-cost mass production, limiting their usefulness for tunable wireless systems. Nevertheless, over the years many solutions for implementing tunable filters have been presented in waveguide technology.

Magnetically tunable waveguide filters have wide tuning ranges and high Q_u, but are very bulky and consume a considerable amount of Direct Current (DC) power [48]. Tunable filters based on mechanically tunable cavities (controlled for instance by customized sliding metallic walls driven by electrical stepper motors) can exhibit very high Q-factors ($5000 - 10000$) as shown in [49].

A key parameter in designing such type of filters is the choice of a resonant mode with an appropriate current distribution as explained in [49], where cylindrical cavities using the TE_{011} mode are employed. This solution enables the full control of the filter, but the need of an isolator add some drawbacks: limited power handling, higher insertion loss with respect to a standard waveguide cavity filter and higher complexity.

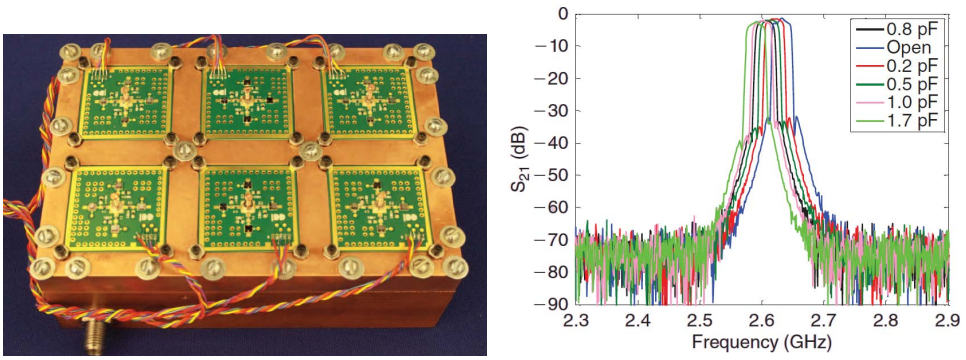

(a) (b)

Figure 1.15: (a) Photo of the fabricated RF MEMS tunable combline waveguide filter, and (b) measured S_{21} parameter of the RF MEMS tunable combline waveguide filter [50].

Recently, electrically controlled tunable waveguide resonators have been presented in [50], as shown in Fig. 1.15. They employ combline resonators tuned by an RF MEMS switched capacitor bank assembled outside the cavity. The reconfigurable filter shows a limited tuning range of 4.5% with a measured resonator Q_u value that varies between 1300 and 375 over the same band (see Fig. 1.15-(b)).

Tunable bandpass filters based on dielectric resonators with embedded RF MEMS have also been demonstrated in [51, 52]. Measured resonator Q_u of $500 - 1500$ have been achieved using specific technology developments as long as embedded MEMS elements, which results in a poor integration and high cost solutions.

E-plane waveguide filters have also been investigated for frequency tunable filters in different research groups. RF MEMS capacitive switches have been employed for the frequency tuning of a 10 GHz substrate-integrated folded E-plane waveguide filter showing a Q_u around 300 [54].

Recently, interesting works using E-plane waveguide filters with MEMS resistive switches as tuning elements are presented in [55, 56]. Pelliccia et al. demonstrated in [55] that RF MEMS switches can be used to virtually narrow the waveguide width so as to modify the resonant frequency of the fundamental mode. This solution enables to obtain Q-factors above 1000 in the case of a K-band filter (as Fig. 1.16 depicts).

However, the tuning range of such structures is narrow (i.e. usually much less than 10%), while complexity of the structure is high. Nevertheless, in order to reduce complexity of such approach, a novel rectangular waveguide resonators loaded with thin E-plane metal strips on a low-loss substrate is demonstrated in [56]. Again, ohmic RF MEMS switches are used to modify the lengths of the different metal strips, so as to digitally change the resonant frequency of the fundamental mode. Power handling of these solutions is still difficult to estimate because power tests have not been performed yet.

Achieving a widely tunable, low power and high-Q resonator with good spurious free range in compact implementations has been demonstrated with the evanescent-mode cavity technology employing different solutions, as it can be seen in [57–62]. Piezoelectric actuator or RF MEMS capacitive/resistive switch could be employed to tune centre frequency and to control coupling coefficients.

An analog frequency-tuning has been obtained in [57] by placing an RF MEMS varactor at the electric field maximum of a ridged cavity, so as to concentrate the electric

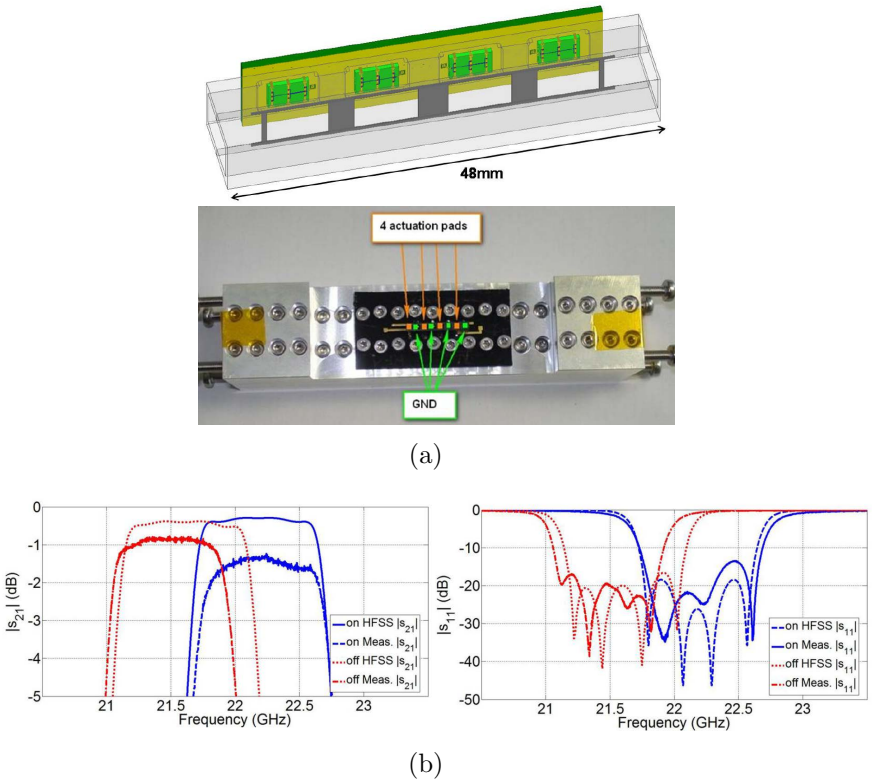

Figure 1.16: (a) Layout and photo of E-plane tunable waveguide filter tuned by RF MEMS, and (b) measured results of the tunable filter proposed in [55].

field inside the RF MEMS device. The measured Q-factor is between 500 and 800 for a tuning range of 500 MHz around 5 GHz.

Similar results have been also achieved in [58], where a high-Q tunable resonator, which consists on a brass surface mountable cavity, can be tuned using RF MEMS varactors (i.e. electrostatic curled cantilever). As Fig. 1.17 shows, a 15% tuning range from 11.9 GHz to 14.2 GHz has been demonstrated, showing a measured Q_u in the range $400-550$ over the operating frequency band. Large volume, high bias voltage and poor mechanical stability are the main drawbacks.

In recent years, 4-bit RF MEMS capacitive switches are used for tuning miniature high-Q evanescent-mode cavities in [59] (as shown in Fig. 1.18). The two-pole filter results in an insertion loss of $4.9-3.2$ dB for a very narrow bandwidth (i.e. $0.45\%-0.7\%$) at $4-5.6$ GHz, corresponding to Q_u values ranging from 300 to 500. Fig. 1.18-(b) shows the measured results of such RF MEMS tunable filter, in terms of S-parameters.

Similar results have been obtained in [61, 62] employing evanescent-mode cavity resonators tuned by RF MEMS membrane fabricated in all-silicon technology. As Fig. 1.19 shows, tunable resonators in the C, X, Ku, and K bands with simultaneous high unloaded quality factors (≥ 500) and tuning ratios ($\geq 1:2$) are presented. As can be seen, these solutions show very good results at the cost of a poor integration, high complex fabrication/assembly. Besides, up to now just the design of very narrow band reconfigurable filters has been accomplished using such approach.

To conclude this section, an overview of reconfigurable structures based on SIW technology is provided, being deeply related to the work performed in this Thesis. Thus, tunable SIW filters have been recently studied and reported showing Q_u easily ranging

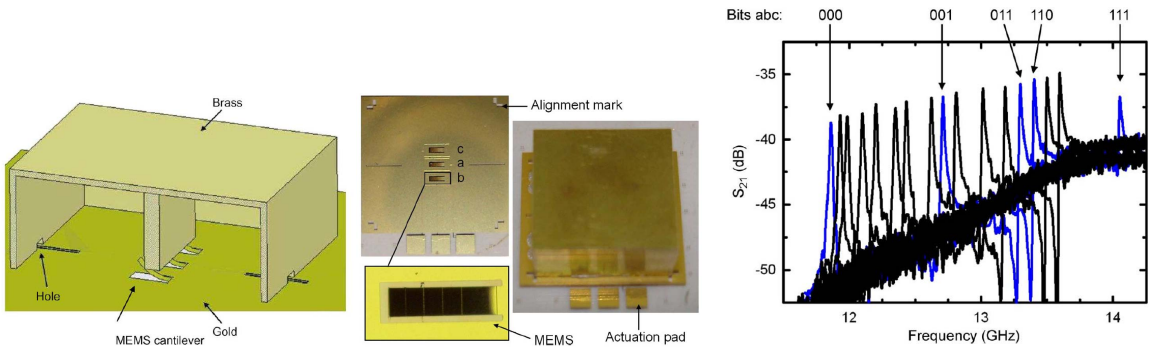

(a) (b)

Figure 1.17: (a) Filter layout including a photo of the prototype and (b) measured S_{21} parameter of the surface mountable RF MEMS tunable cavity resonator [57].

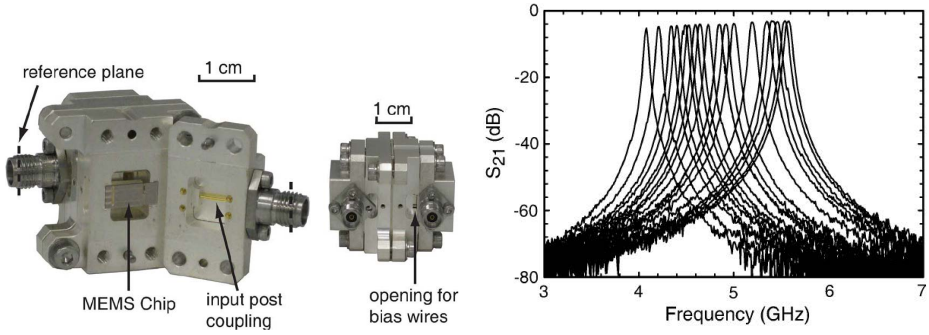

(a) (b)

Figure 1.18: (a): 3D filter layout and photo of the RF MEMS evanescent-mode tunable filter, and its measured results [59].

between $100-200$ and up to ~ 1000, wide tuning range ($\sim 10-30\%$) and compact implementations. Preliminary works on reconfigurable structure in this technology have been published in 2005, but it is only from 2009 that the research activity increases resulting in many publications.

In this context, many types of tuning elements have been used for implementing the reconfigurable filters in SIW, and among them, there are piezoelectric actuators [62], tuning screws [63, 64], varactor diodes [65–67], PIN diodes [68], RF MEMS switches [69] and ferrite slabs [70, 71].

A very interesting work on this topic was developed by Joshi et al. [62] in 2009. They demonstrated fully reconfiguration of substrate-integrated evanescent-mode tunable filters with high tuning range and high Q_u in the range $360-750$. Fig. 1.20 depicts the filter layout and the measured results. The resonant frequency can be controlled by means of external piezoelectric disks, while inter-resonator and external couplings are varied through a low Q-factor varactor, which, however, does not affect the overall performance of the filter.

The well-known hysteresis and creep of piezoelectric actuators present significant system level problems for these tunable resonators and filters. Moreover, the complex assembly and the poor integration of these actuator can be considered additional drawbacks.

An interesting approach to tune an SIW cavity resonator has been demonstrated

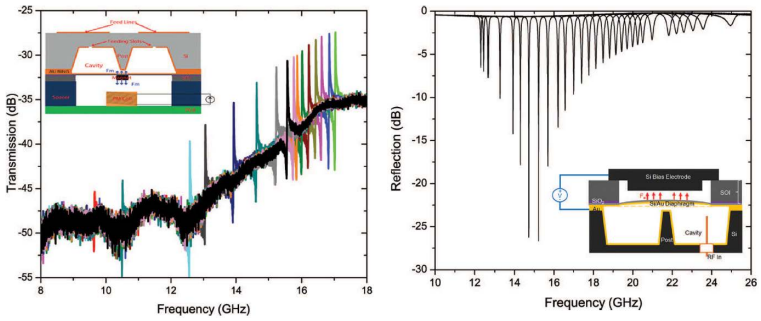

Figure 1.19: 3D filter cross-section and measured results of the RF MEMS evanescent-mode tunable filter in all-silicon technology [61].

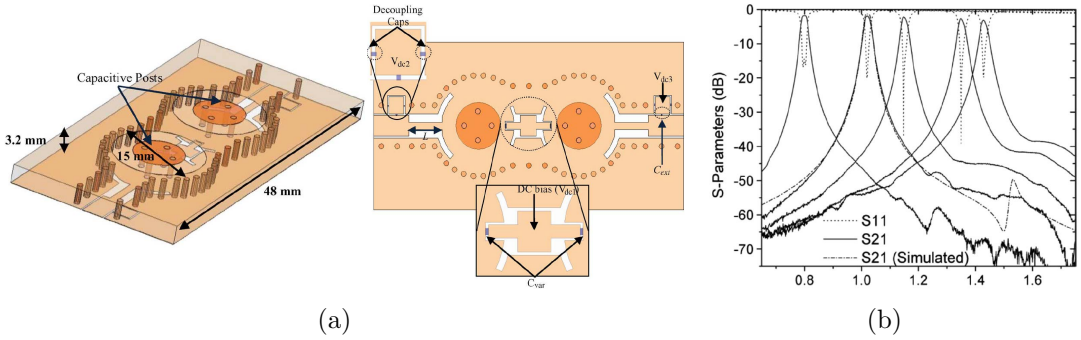

(a) (b)

Figure 1.20: 3D filter layout and measured S_{21} parameter of the substrate-integrated evanescent-mode tunable filters.

in [63]. Mira et al. have created a mechanically tunable structure that is controlled by a screw connected to a flap, as it is shown in Fig. 1.21. This screw has been inserted into a via hole, and both are isolated from the top metal layer using an annular ring slot. By turning the screw, the connection between the flap and the top metal layer is changed, thus performing a frequency tuning. This approach can also be applied as a trimming technique for post-fabrication tuning method. Measured results exhibit a tuning range of 8%, where the resonant frequency varies from 6.85 to 7.42 GHz, with a measured Q_u of 94.

Following this approach, the design of SIW filters with tunable centre frequency and tunable bandwidth have been implemented by the same authors in [64]. Three different filters are designed and implemented, demonstrating 10% tuning of the center frequency, and 100% tuning of the filter bandwidth. Main drawbacks of this solution are related to increased complexity of the fabrication and assembly of the flags. Additionally, mechanical tuning is generally done by hand, so that the process is costly, time consuming, and needs skilled operators. Nevertheless, it could be interesting to perform power tests in order to evaluate the power handling performance of the proposed solutions.

Moving to semiconductor-based tuning elements, Sekar et al. demonstrated in [68] a tunable filter implemented using PIN diodes as switching elements. Each SIW cavity is tuned by perturbing via posts connecting or disconnecting to the cavities top metal layer (see Fig. 1.22). Fig. 1.23 depicts that the two-pole filter disposes of six frequency states resulting in 25% tuning and insertion loss less than 5.4 dB (i.e. Q-factor was estimated to be around 120). A three-layer PCB fabrication process needs to be used for biasing tuning elements, increasing the complexity of the structure and reducing its planar integration.

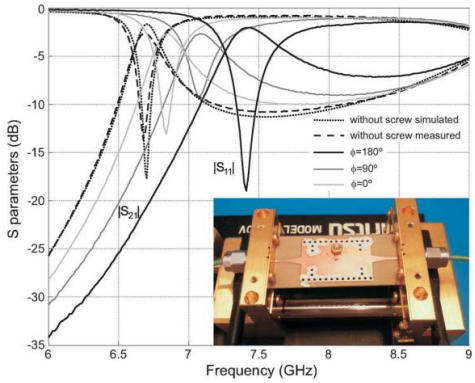

Figure 1.21: Measured results of the mechanically tunable resonator. The inset shows the picture of the prototype [63].

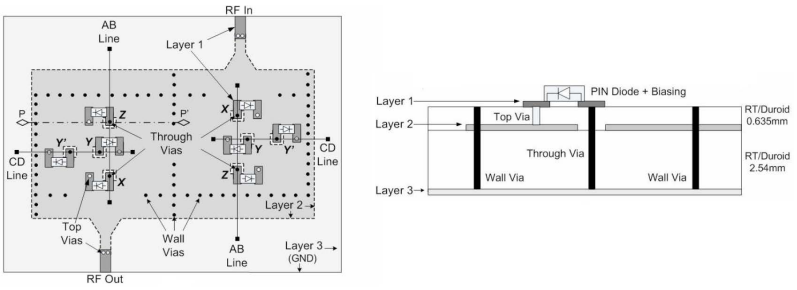

Figure 1.22: 3D filter layout of the tunable SIW filter implemented using PIN diodes [68].

Among the different works that made use of varactor diode, it is remarkable the work developed in [70] in 2012. A two-dimensionally tuned cavity and 2-pole bandpass filter at 12 GHz are demonstrated using a double tuning mechanism. The proposed 2-D tuning mechanism is based on a simultaneous electric and magnetic tuning applied to the SIW resonators, as it is shown Fig. 1.24. The magnetic tuning is based on a planar ferrite slab, which is loaded along one cavity side. This tuning of the SIW cavity is made possible by means of variable external magnetic fields. This solution allows to change virtually the width of the cavity resonator, thus modifying its resonant frequency.

Meanwhile, the electric tuning is based on a lumped capacitor connected between the upper and lower conductor at the central region of the cavity where the electric fields are maximally confined. Thus, a metalized via hole is created at the center of the cavity, at the location where the varactor diode is located. This 2-D tuning not only permits to change the resonant frequency, but also simultaneously optimizing other key parameters such as the return loss or Q_u (see Fig. 1.24-(b)), since a slight control of filter BW can be obtained by applying the magnetic tuning.

To sum up, as it has already been mentioned, SIW technology represents a promising solution for the full integration of active and passive circuits in a planar structure. Taking into account the above mentioned background, SIW is a very good candidate for developing reconfigurable microwave devices with high Q-factor and integration capabilities with all sorts of planar microwave components in the same substrate. The use of this technology allows to design tunable filters in many bands (i.e. from 500 MHz to 30 GHz and even beyond) with: moderate-to-wide frequency tuning range (i.e. up to $\sim 40\%$), Q_u from 100 to 750, low cost fabrication process, high planar integration, compact size, while using many types of tuning elements or tuning mechanisms.

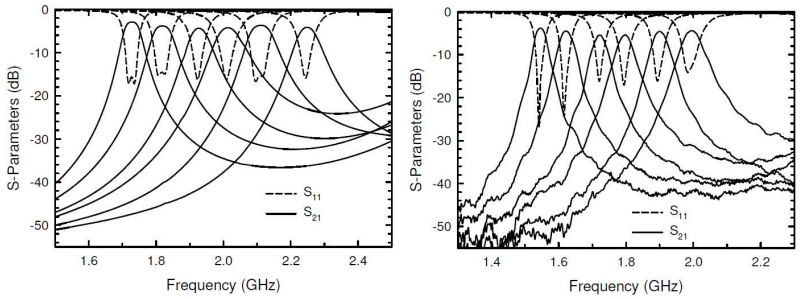

Figure 1.23: Measured results of the tunable SIW filter implemented using PIN diodes proposed in [68].

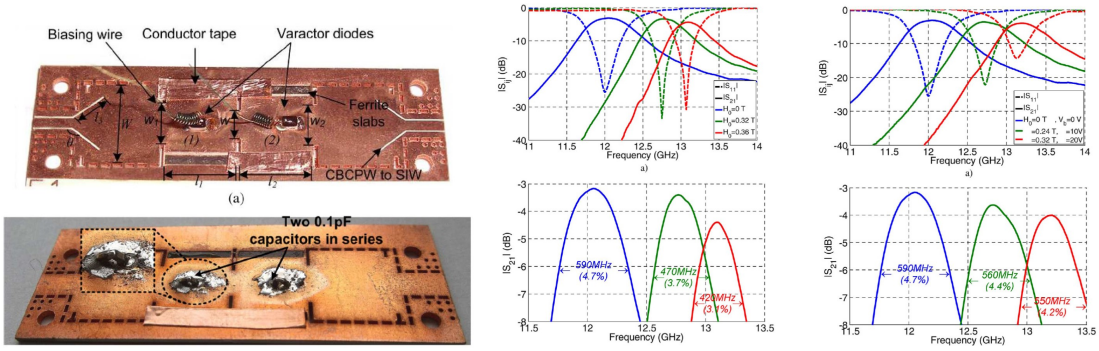

(a) (b)

Figure 1.24: (*a*) 3D filter layout and photo of the 2-pole bandpass SIW filter [70]. (*b*) Measured results of the two-dimensionally tuned SIW 2-pole filter.

1.3 Objectives

SIW technology has already demonstrated to be a successful approach for implementing microwave and mm-wave filters with high Q-factor, easy integration with planar circuits, and mass production manufacturing processes in PCB and LTCC technologies. However, other potential features that, combined with the former advantages, could be of huge interest in a wide range of wireless and mobile applications are a lively set of research subjects, such as compactness, advanced filtering responses, and recently reconfiguration capabilities. These key features have been recently introduced in the design of microwave filters for the next-generation wireless systems.

Taking into account the above-mentioned background, the work carried out during the course of this Thesis has been directed toward a further study of SIW technology to propose and develop an innovative and original topology. The proposed topology, which is named coaxial SIW, is based on the extension of the classical coaxial waveguide resonator to SIW technology, and must take advantage of the characteristics of SIW devices to allow the design of improved and innovative microwave resonator filters for advanced wireless systems. Therefore, the main objectives of the work in this Thesis can be summarized as follows:

- Development and characterization of the novel coaxial SIW resonator, which will be the building block for the design of microwave filters. The working principle and its main EM performance will be object of study in terms of Q-factor, losses and frequency response to efficiently design this component.

- A model for the proposed resonator will be considered, and a systematic procedure for the design of these miniaturized coupled resonator bandpass filters will be presented. A specific set of coupling mechanisms will be studied for this topology in order to allow to generate complex filtering responses.

- The planar integration of these coaxial structures must be as high as the one of standard SIW components, while its performance must be improved. Thus, a low-cost, easy-to-manufacture procedure that can enable the proposed coaxial SIW filters to be assembled using standard Surface Mounting Device (SMD) technology on carrier circuits will be studied. The main aims are to avoid degradation of the filter performance, and to allow the integration of the devices within package as one of the parts of the manufacturing process.

- Introduction of frequency-agility in the proposed SIW topology that will enable to implement reconfigurable microwave filters. The work is focused on creating a frequency tuning mechanism that permits analog-like and digital-like reconfigurations, while maintaining moderate-to-high Q-factor over wide tuning ranges.

- Validation of the proposed solutions by performing frequency measurements and power tests of the fabricated prototypes. A variety of microwave filters featuring advanced responses or tunability will be analyzed, fabricated and tested. Results will be compared with simulations from commercial software tools in order to validate the proposed approach.

1.4 Document Organization

The present PhD Thesis work is divided into five chapters. In this first chapter an overview of the topic developed within the framework of this Thesis has been presented. The state of the art has been divided in two sections. First, an overview of the techniques currently used to design advanced filtering responses in SIW technology is provided. Then, different tunable solutions for realizing reconfigurable components in the microwave range is given. All this gives the reader a good perspective into the strategic importance of SIW technology and its applications in the context of modern passive microwave components. Moving to the structure, the PhD Thesis work is divided as follows:

Chapter 2 The second chapter is devoted to the description and analysis of a novel coaxial topology implemented in SIW technology. Thus, a broad discussion of its structure and a full analysis of its performance is provided. The main goal of this chapter is to characterize the coaxial SIW resonator that will be the key element for the design of symmetric and quasi-elliptic coaxial SIW filters, and later on, for the implementation of the tunable microwaves devices. The novelty of proposed topology is that it allows the design of a low-cost, compact, widely tunable and highly embeddable cavity resonators that can be the basic building block of many microwave devices. Moreover, new external and inter-resonator electric couplings mechanisms formed by a capacitive probe is studied.

Chapter 3 This chapter presents a series of microwave components based on the proposed topology developed in Chapter 2 that are analyzed and studied in order to validate its flexibility. Thus, some advanced filtering responses in coaxial SIW

technology are presented using rectangular or circular combline resonators. These components uses the external and inter-resonator coupling mechanisms proposed in this Thesis. A broad description of the design, fabrication and measurements of these filters will be shown.

Chapter 4 In this chapter, continuously and discretely tunable filters based on coaxial SIW resonators are successfully designed, fabricated and measured, providing a broad description of the designed devices. Since tuning elements are key factors when designing such reconfigurable components in terms of EM performance, in this chapter varactor diodes, PIN diodes, RF MEMS switched capacitors and RF MEMS resistive switches are considered and employed for providing frequency-agility of coaxial SIW resonators. Additionally, power handling tests have been performed on reconfigurable filters that are described in this Thesis, and the results of these power tests will be shown.

Chapter 5 This chapter summarizes the main conclusions of this work. Likewise, it describes potential research and development lines associated with the work performed in the framework of this Thesis, and especially related to future improvements of the proposed coaxial topology in SIW technology.

Chapter 2

Coaxial SIW Filters

A microwave resonator is the basic building block of any microwave filter. In order to design such filters with stringent performance, it is evident the need for a high performance single resonator. In this chapter we present, analyze and study a novel structure for implementing moderate-to-high Q-factor cavity resonators based on coaxial SIW technology. In this context, developing an equivalent circuit model can be considered the first step in designing such a resonator, and it helps to clarify the resonator performance. Thus, an equivalent model of the proposed resonator is provided, and a systematic procedure for the design of miniaturized SIW bandpass filters is presented.

2.1 Basic Theory of Coaxial SIW Resonators

As it is well known, coaxial or combline filters have been extensively used in waveguide and planar technologies, especially for the design of high order filters. In its simplest form, a combline resonator in waveguide technology consists of a conductive cavity (either rectangular or circular) with a cylindrical conductive rod placed within it symmetrically [72–74]. The latter is short circuited at one end located at the bottom of the metallic cavity, while the other end is spaced some distance from the top cover of the cavity. The inner conductive rod can be rectangular, or can have other cross section in shape (depending on the manufacturing process).

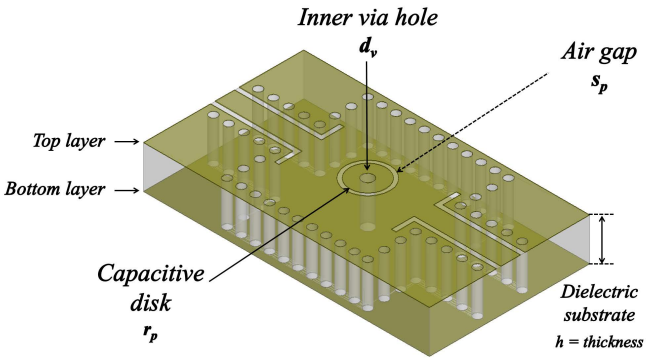

Figure 2.1: 3D view of the coaxial SIW resonator.

The extension of the rectangular waveguide combline resonator to SIW technology is proposed and studied in this Thesis, and was presented for the first time in [75]. The topology of a coaxial resonator is shown in Fig. 2.1 displaying the resonator layout, including its main design parameters.

A coaxial SIW resonator consists on a square or circular SIW cavity where a plated via hole has been inserted at the center. The inductive section of the combline resonator has been obtained by the plated via hole, which is connected to ground at one of its ends. At the other side, a metallic disk having a size much bigger than the post diameter d_v is connected. Between this disk and the top metal plane a small air gap s_p is inserted, so generating a high capacitance towards ground (termed loading capacitance C_l), which represents the capacitive section of the coaxial resonator. In particular, the fringing fields across the air gap generate the integrated loading capacitance, which can be clearly seen by observing the electric field distribution around the air gap as it is shown Fig. 2.2.

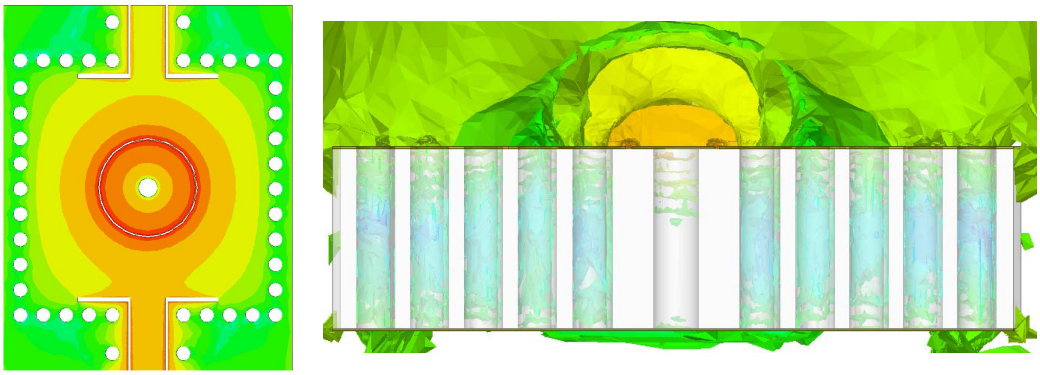

(a) (b)

Figure 2.2: 3D Electric field distribution for a coaxial SIW cavity: (a) on the top metal layer and (b) in the air surrounding the structure.

Thus, the loading capacitance of a typical combline configuration has been easily created at the top metal layer of the substrate. The proposed solution allows us to set C_l in a very easy way by changing the patch size or the width of the air gap. Moreover, the patch can present any shape or form, so the design can be focused on compactness or on the integration of tunable elements, or in other aspects. For example, the capacitive patch can be square with a semi-side length or circular with radius (both variables named r_p), as it is shown in Fig. 2.1. Similarly, the inductive properties of the coaxial topology can be easily set by changing the diameter d_v of the inner metalized hole and/or the SIW cavity side (l_{siw} if it is square).

However, an important advantage of such configuration is the straightforward accessibility to the capacitance section of the coaxial resonator. As it will be shown in the following sections, its external location enables the designers to implement the control of the loading capacitance in very practical ways. This characteristic can be used to design frequency tunable microwave components, to applying post-manufacturing tuning capabilities, and it also enables implementing out-of-phase couplings between resonators.

2.1.1 Synthesis of Coaxial SIW Resonators

As it is clear by observing the structure layout, the inner via is short-circuited at the bottom metal layer and open-ended at the top. So, the proposed resonator can be seen as a circular-square coaxial line of length h and characteristic admittance Y_0 embedded into the dielectric substrate [76]. The external square conductor is composed by the via hole walls that form the SIW cavity, while the coaxial inner circular conductor is the central plated via hole.

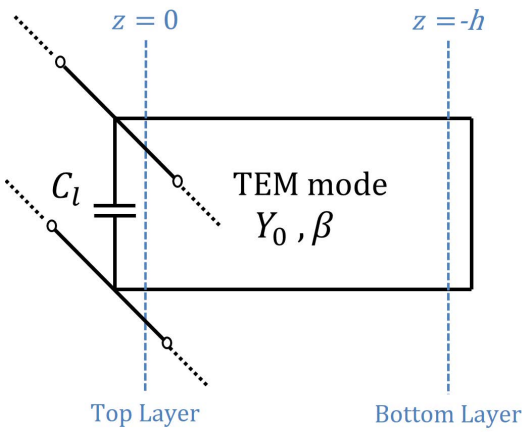

Figure 2.3: Equivalent circuit of the SIW coaxial resonator.

Such resonator can be modeled as a TEM-mode combline resonator short-circuited at one end and terminated with a capacitor on the other side. A scheme of the resonator equivalent circuit is depicted in Fig. 2.3. The TEM resonant frequency is given by the condition $B(\omega) = 0$, taking into account that the susceptance of the coaxial SIW resonator can be expressed as

$$B(\omega) = \omega C_l - \frac{1}{Z_0} \cot \beta h \tag{2.1}$$

where β is the propagation constant of the TEM-mode, and Z_0 is the characteristic impedance of the coaxial resonator. It should be remarked that the length of the coaxial transmission line h corresponds to the thickness of the dielectric substrate. Thus, the substrate characteristics are now key design parameters that increase the design flexibility of these structures.

As it has been demonstrated in [77], for a circular inner conductor of diameter d_v and a square contour of side l_{siw}, the coaxial characteristic admittance Y_0 can be well approximated by

$$Y_0 = \left[\frac{60}{\sqrt{\epsilon_r}} \ln \left(1.079 \frac{l_{siw}}{d_v} \right) \right]^{-1} \quad \text{for } l_{siw} \gg d_v \tag{2.2}$$

where ϵ_r is the permittivity of the dielectric substrate.

In the case of C_l that has been created at the top side, it could be approximated by using the elementary expression for the capacitance of parallel-plate capacitors, which is given by $C = \epsilon_r A / s_p$ with A the plate area and s_p the plate spacing gap (see Fig. 2.4). Nevertheless, this formula underestimates the true capacitance because it ignores the fringing fields that extend into space beyond the electrodes.

Therefore, as it has been explained in [78], and taking into account that the following equation is only valid for a circular loading patch neglecting the metal layer conductor thickness, it is possible to estimate the value of the capacitance established between the top metal layer and the circular patch of radius r_p from

$$C_l = \frac{2\pi r_p (1 + \epsilon_r)}{\ln \left(1 + \frac{s_p}{r_p} \right)} \int_0^\infty [J_0(\gamma r_p) - J_0(\gamma (r_p + s_p))] \frac{J_1(\gamma r_p)}{\gamma} d\gamma \tag{2.3}$$

where J_n is the n-th order Bessel function of the first kind. It is worth mentioning that this value exemplifies a good approximation of the real value of C_l, but an optimization

of the structure by means of 3D EM simulations is usually needed to finely tune this parameter. Indeed, the total value of C_l will depend on the final thickness of the top metal layer of the structure. Therefore, its value will rely on the fabrication process selected for implementing such SIW components.

The synthesis procedure of a coaxial resonator starts by choosing the resonator slope parameter b at the desired center angular frequency ω_0. The susceptance slope parameter b for resonators having zero susceptance at ω_0 is defined by [8]

$$b = \frac{\omega_0}{2} \frac{dB(\omega)}{d\omega}\bigg|_{\omega=\omega_0} \tag{2.4}$$

Taking into account (2.1), the slope parameter for the proposed coaxial resonator can be particularized as

$$b = \frac{1}{2}\left[\omega_0 C_l + \frac{\theta_0}{Z_0 \sin^2\theta_0}\right] \tag{2.5}$$

Then, the corresponding characteristic impedance Z_0, and the ratio between the outer cavity side l_{siw} and the via diameter d_v may be expressed as

$$Z_0 = \left(\frac{\cot\theta_0 + \theta_0 \csc^2\theta_0}{2b}\right) \tag{2.6}$$

$$\frac{l_{siw}}{d_v} = 0.9268 \cdot e^{\frac{Z_0\sqrt{\epsilon_r}}{60}} \tag{2.7}$$

$$\omega_0 C_l = \frac{\cot\theta_0}{Z_0} \tag{2.8}$$

where θ_0 is the resonator electrical length at the desired centre frequency f_0 that in our case is $\theta_0 = \beta_0 h$. The loading capacitance value is fixed by changing the size of the capacitive patch r_p and/or the width of the annular gap s_p for a particular resonant frequency. Iterations and adjustments of these dimensions should be performed until the desired resonant frequency values match the extracted values from full-wave simulation, thus providing the desired resonator configuration.

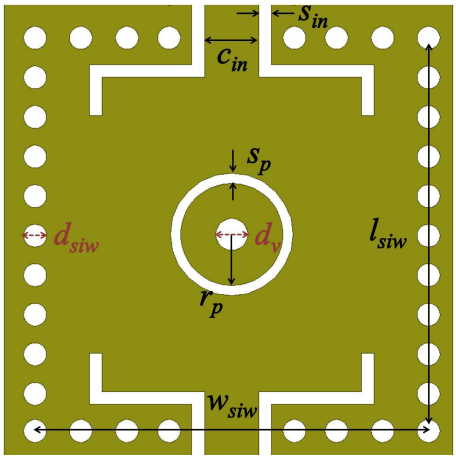

Figure 2.4: Layout of the coaxial SIW resonator implemented in 2.54 mm-thick Rogers TMM10i.

The slope parameter has to be conveniently chosen as a trade-off between Q-factor, compactness and physical feasibility of synthesized values of C_l and Z_0. In order to increase component compactness, it is very important to set the inner via hole diameter to the minimum diameter permitted by the fabrication technology, as well as to keep s_p as small as possible. This allows us to reduce radiation from apertures, thus helping to preserve a reasonable value for the resonator Q-factor, as it will be explained in the next Section 2.1.2.

In order to validate the aforementioned statements and to study the performance of the coaxial SIW topology, let us consider a single cavity resonator having center frequency 4 GHz and using the 2.54 mm-thick Rogers Thermoset Microwave Material 10i (TMM10i) dielectric substrate [79], with permittivity $\epsilon_r = 9.8 \pm 0.245$ and loss tangent $\tan\delta = 2{\cdot}10^{-3}$. The thickness of the copper base layers is $t = 17$ μm.

The resonator electrical length corresponds to 38.2°, i.e. $0.1\,\lambda_g$, where λ_g is the guided wavelength at 4 GHz. The coaxial resonator has been designed to present $b = 37$ mS that gives a loading capacitance of $C_l = 1.25$ pF while $Z_0 = 40.8\ \Omega$. By using both values and choosing a diameter of $d_v = 0.8$ mm for the inner via hole, the SIW resonator cavity size is $w_{siw} \times l_{siw} = 6.3 \times 6.3$ mm^2 (i.e. $0.26 \times 0.26\,\lambda_g^2$ and $0.08 \times 0.08\,\lambda_0^2$), whilst the circular patch radius r_p is 2 mm with an air gap of $s_p = 0.125$ mm between the patch and the ground plane. Both last geometrical parameters have been optimized by means of 3D EM simulations in order to set the resonance frequency at the corresponding value. The 3D layout of this coaxial resonator is shown in Fig. 2.1, and Fig. 2.4 depicts a top view of the resonator showing its main parameters that are reported in Table 2.1.

Table 2.1: Dimensions of the coaxial SIW resonator. (Units: mm)

d_{siw}	0.5	d_v	0.8
l_{siw}	6.3	w_{siw}	6.3
s_p	0.125	r_p	2
c_{in}	0.5	s_{in}	0.15
h	2.54	t	0.017

Full-wave simulations performed with ANSYS HFSS 2014 [80] of the coaxial SIW resonators at C-band are depicted in Fig. 2.5. For this particular configuration, resonator wide-band response highlights a spurious free band of more than one octave. As it can be seen, the resonator frequency responses above the TEM resonance show a higher order spurious band around 11.3 GHz, which is due to the excitation of the TE_{101} mode of the SIW cavity.

Frequency response of the proposed resonator is also compared to the one of a conventional TE_{101} SIW cavity resonator. This conventional resonator is implemented in the same dielectric material, presenting the same physical dimensions of the SIW cavity. Fig. 2.6 shows that the resonant frequency of the fundamental mode of the coaxial structure (i.e. TEM mode) has been strongly reduced with respect to the one of the fundamental mode (i.e. TE_{101} mode) of the conventional implementation, especially for this particular resonator configuration. In fact, the resonant frequency of the fundamental mode reduces from 11.3 GHz to 4 GHz.

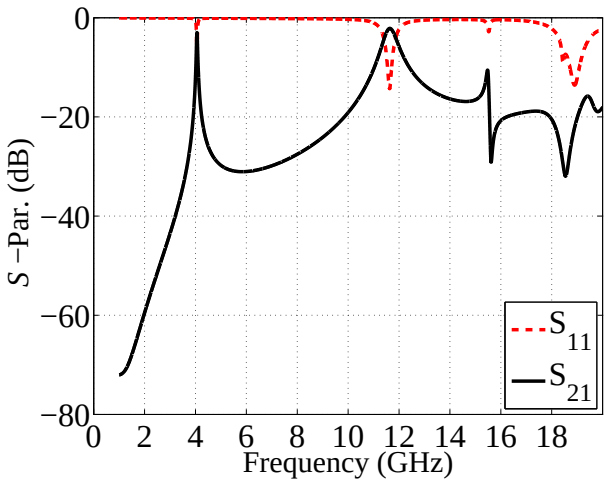

Figure 2.5: Simulated S_{21} and S_{11} parameters for an under-coupled combline SIW resonator implemented in 2.54 mm-thick Rogers TMM10i.

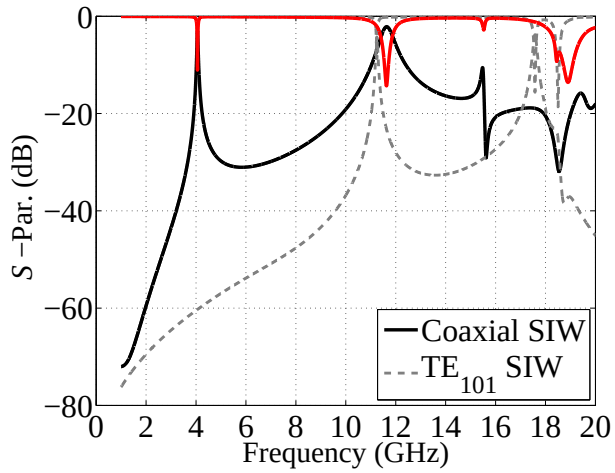

Figure 2.6: Simulated S-parameters for an under-coupled coaxial SIW resonator at C-band implemented in Rogers TMM10i, and its comparison with a conventional TE_{101} SIW cavity resonator.

2.1.2 Unloaded Quality Factor and Losses

An SIW structure is inherently a dielectric-filled synthesized rectangular waveguide with periodic metalized via holes or slot arrays. In this context, the selection of the substrate plays a very important role for the physical and electrical performance of any microwave SIW filter, even more than for other technologies, as the case of microstrip or Coplanar Waveguide (CPW) filter. For instance, the intrinsic sources of losses in SIW structures are due to the metal layers (conductor loss) and to the dielectric substrate (dielectric loss). It is worth pointing out that the characteristics of the dielectric substrate are directly related to the performance of an SIW device, as the case of a bandpass filter, in terms of size, insertion loss, and also power handling capability.

Moreover, the EM performance of conventional TE_{101}-mode SIW structures depends also on the diameter of the metalized holes of the lateral sidewalls, their longitudinal spacing (i.e. the via hole pitch p_v) and the equivalent width W_{eff} of the waveguide. In particular, if the longitudinal spacing becomes large, the EM field is not confined anymore inside the waveguide and the SIW tends to radiate throughout the surrounding dielectric.

This radiation effect is considered as a power leakage in the case of structures designed to be transmission lines, and it can be considered the third source of losses in SIW structures.

Since the SIW structure geometry can be optimized for radiation loss minimization, the radiation leakage is considered negligible if it does not exceed the other types of loss effects. The effect of the radiation leakage between via holes is minimized by closely spacing the metal holes. This condition defines a set of constraints for the geometrical parameters of the structure: in particular, dimensions of via hole diameter and separation must be properly chosen. As shown in [81], the leakage is negligible if the ratio between p_v and the via hole diameter d_{siw} is

$$\frac{p_v}{d_{\text{siw}}} < 2.5 \tag{2.9}$$

A more restrictive and general condition for negligible leakage losses is

$$\frac{p_v}{d_{\text{siw}}} \leq 2 \tag{2.10}$$

To avoid any bandgap in the operating bandwidth of TE_{101} mode and other related guided-wave modes if involved, the following condition must be also respected

$$\frac{p_v}{\lambda_g} < 0.25 \tag{2.11}$$

where λ_g is guided-wave wavelength. Finally, a desirable condition for avoiding degradation of the substrate mechanical rigidity is that the number of via holes should not exceed 20 per wavelength, as stated in

$$\frac{p_v}{\lambda_g} > 0.05 \tag{2.12}$$

The aforementioned statements are completely valid for the proposed coaxial SIW topology, even though in these structures there are other parameters that strongly affect the EM performance. As previously explained, the fundamental mode of a coaxial SIW resonator is the TEM-mode, meanwhile in a standard SIW cavity that mode is the TE_{101}-mode. Therefore, the electric-magnetic field distribution of each resonator mode is completely different between each other, as it can be observed in Fig. 2.7 that shows the EM field distribution for both SIW resonator modes. Fig. 2.7-(a) displays the electric and magnetic fields within the substrate for the coaxial case, while Fig. 2.7-(b) depicts the EM fields for the TE_{101}-mode case.

As can been seen, the EM field of the TEM-mode is mainly concentrated around the integrated loading capacitance, with a high current that flows along the inner via hole. Hence, for the proposed coaxial SIW the most important design parameters that control EM performance are the inner via diameter d_v, the gap spacing s_p and the perimeter p_p of the capacitive patch.

In order to study the effects of these parameters on the resonant frequency f_0 and the unloaded Q-factor Q_u, an analysis of the EM performance of the coaxial SIW resonator of Fig. 2.4 has been done. The baseline configuration of the coaxial resonator that has been employed in the following simulations is shown in the previous Table 2.1.

Fig. 2.8 depicts the simulated Q_u and f_0 changing the thickness of the substrate laminate. Clearly, the resonant frequency of the structure strongly depends on the length of the coaxial line. Since this parameter can be changed by using laminates of different thickness, a coarse tuning of f_0 can be achieved by choosing narrower or thicker substrates.

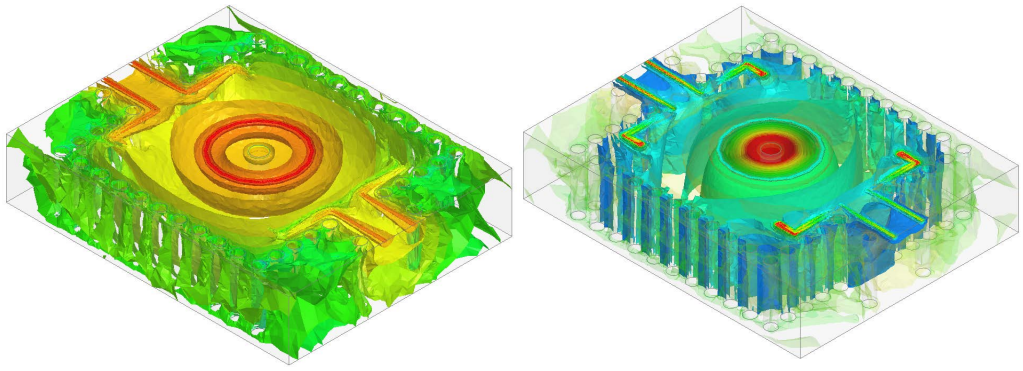

(a)

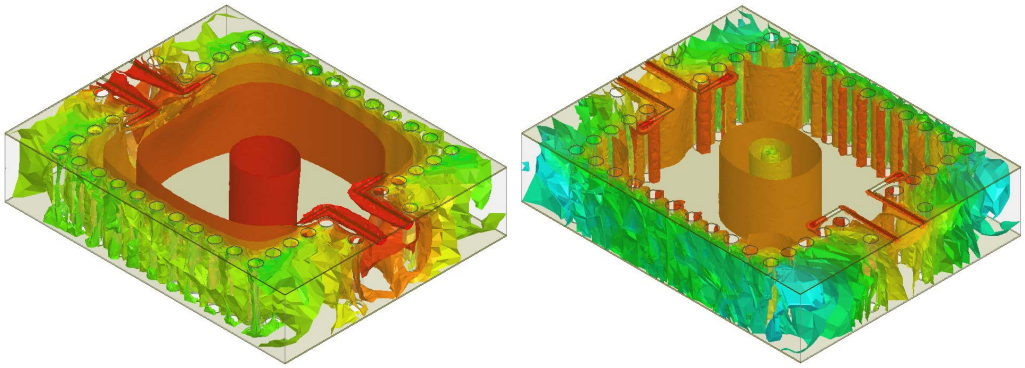

(b)

Figure 2.7: (*a*)-(*left*) Electric field distribution and (*a*)-(*right*) magnetic field distribution within the dielectric substrate for the combline SIW resonator. (*b*)-(*left*) Electric field distribution and (*b*)-(*right*) magnetic field distribution within the dielectric substrate for the TE_{101} SIW cavity resonator.

For instance, if h is changed from 0.5 mm to 4 mm, the reduction of f_0 is about 60%, while the Q_u can be increased up to 40%, being 295 the maximum value for $h = 2.5$ mm. These results set out another demonstration that the fundamental mode of the proposed topology is the TEM mode that is resonating along the vertical direction of the resonator. Additionally, increasing h allows to strongly improve the spurious-free band-stop performance of the coaxial resonator, since the first spurious mode of the SIW cavity (i.e. the TE_{101} mode in the case of square cavities) does not depend on this parameter.

Fig. 2.9 depicts the simulated Q_u and f_0 varying the inner via diameter. As it is shown, the smaller the d_v, the smaller the Q_u as well as the lower is f_0 of the coaxial resonator. Changing d_v from 1.1 mm to 0.5 mm, the reduction of f_0 is about 22% meanwhile the Q_u reduces its value up to 15%.

The loading capacitance depends on the size of the capacitive disk. Therefore, bigger patches mean higher C_l, and so causes f_0 to decrease. The disk perimeter effect on Q_u and f_0 is shown in Fig. 2.10. In this case, increasing p_p between 10.5 mm and 14.5 mm corresponds to lowering the f_0 from 4.35 GHz to 3.75 GHz, which is 16%. Concerning Q_u, its reduction is limited to 6.5%, from $\simeq 315$ to $\simeq 300$.

However, Fig. 2.11 shows that the best way to control the resonant frequency of the coaxial SIW resonator, without affecting its EM performance in terms of Q_u, is controlling the size of the annular gap. For instance, it is possible to set the f_0 in the $3.6 - 4.4$ GHz range, which corresponds to 18% of tuning range, while maintaining a constant estimated

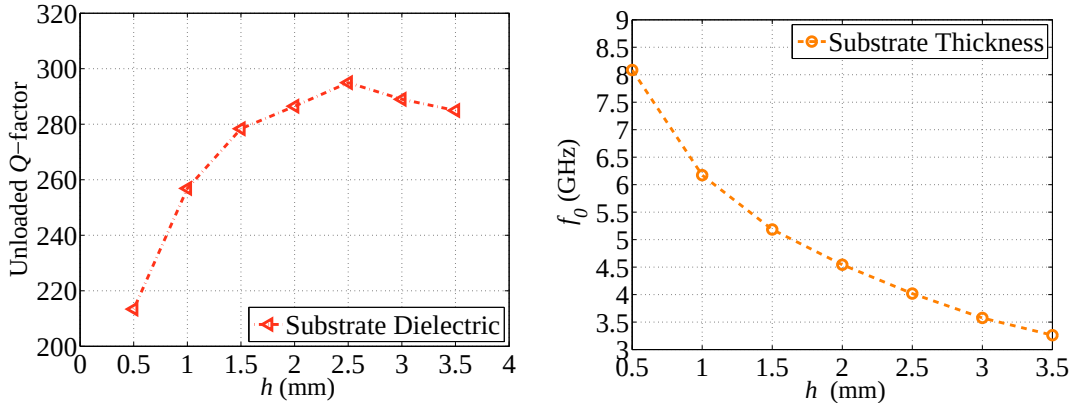

Figure 2.8: (a) Q_u and (b) f_0 versus the thickness h of substrate laminate.

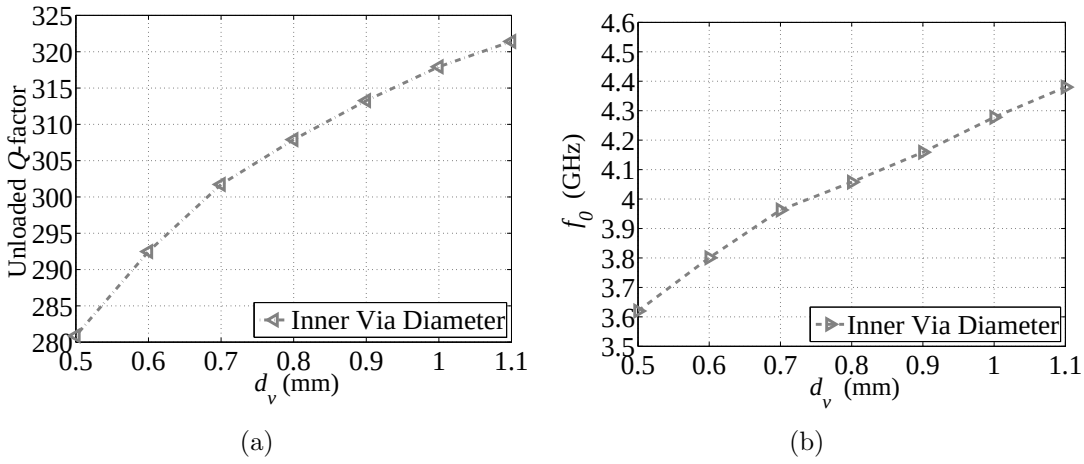

Figure 2.9: (a) Q_u and (b) f_0 versus the diameter d_v of inner via hole.

Q_u value of 305 by changing s_p.

In order to summarize the analysis, Fig. 2.12 highlights the Q_u variation versus f_0 for the different design parameters of the coaxial SIW resonator implemented in TMM10i. For improving Q_u is important to reduce the size of the capacitive patch, and, especially, a wider diameter of the inner via hole is needed. Again, by setting the annular gap, the resonant frequency of the coaxial resonator can be fine adjusted at the desired value. It is worth mentioning that the spacing s_p has a dominant effect on f_0, so this constraint plays a major role in the choice of the fabrication technology.

Clearly, in the case of SIW coaxial structures, the radiation problem could be also related to the isolating gap that surrounds the capacitive patch on the top metal layer. In order to demonstrate that such structures do not tend to radiate at resonance frequency, the radiation pattern for the previously presented coaxial SIW resonator has been studied, considering in this case a strongly coupled resonator.

To analyze the radiated fields associated with the SIW coaxial structure, we have defined a boundary radiation surface over which the fields will be calculated. The values of the fields over this surface are used to compute the fields in the space surrounding the device. In this context, near-field strength decrease more rapidly with distance from the radiator, resulting in relative lack of near-field effects within a few wavelengths of the

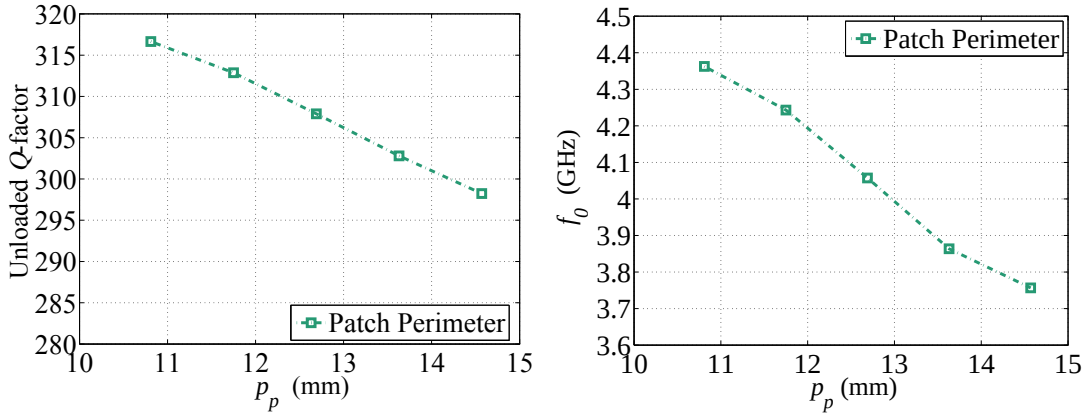

(a) (b)

Figure 2.10: (a) Q_u and (b) f_0 versus the perimeter p_p of the integrated capacitive disk.

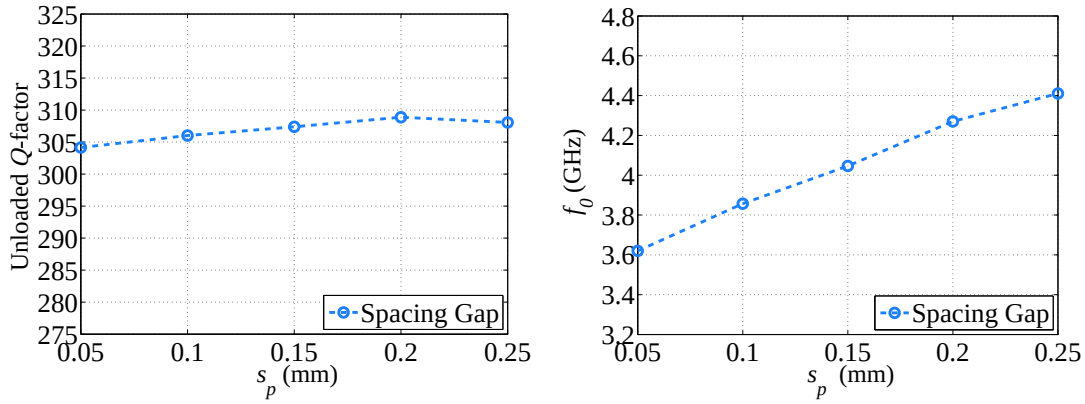

(a) (b)

Figure 2.11: (a) Q_u and (b) f_0 versus the spacing s_p of the integrated capacitive disk.

radiator. In order to study these radiated fields, the far-field region has been considered. Concerning the 3D EM simulations, some parameters have been calculated and depicted in next Fig. 2.13. In particular:

1. P_{IN} is the time-averaged accepted power entering the structure through one input port.

2. P_R is the amount of time-averaged radiated power exiting the structure through the defined radiation boundary.

3. P_L is the amount of time-averaged total power loss of the SIW coaxial structure.

As it has already been explained, the total power loss P_L consists of three different elements: conductor, dielectric and radiation losses. For the doubly loaded coaxial SIW resonators, this parameter has been calculated from 3D EM simulations as:

$$P_L = 1 - |S_{11}|^2 - |S_{21}|^2 \tag{2.13}$$

Thus:

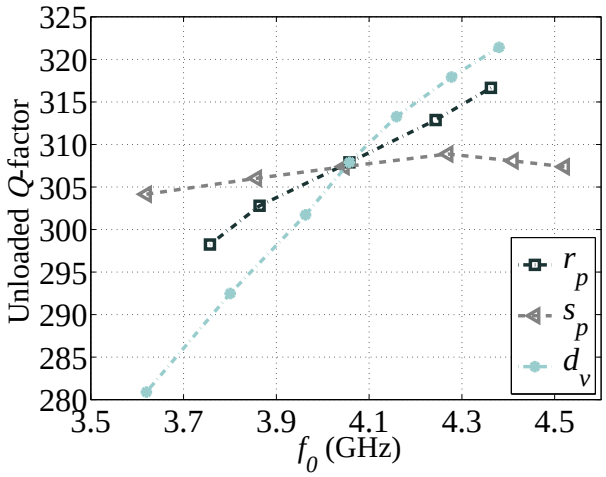

Figure 2.12: Q_u versus f_0 for an SIW coaxial resonator, changing d_v, s_p and p_p. This graph allows us to understand which parameter degrades the EM performances while controlling the resonant frequency.

1. $\frac{P_L}{P_{IN}}$ is the relation between total power losses and input power.
2. $\frac{P_R}{P_{IN}}$ is the relation between radiated power and input power.
3. $\frac{P_R}{P_L}$ is the relation between radiated power and total power losses of the device.

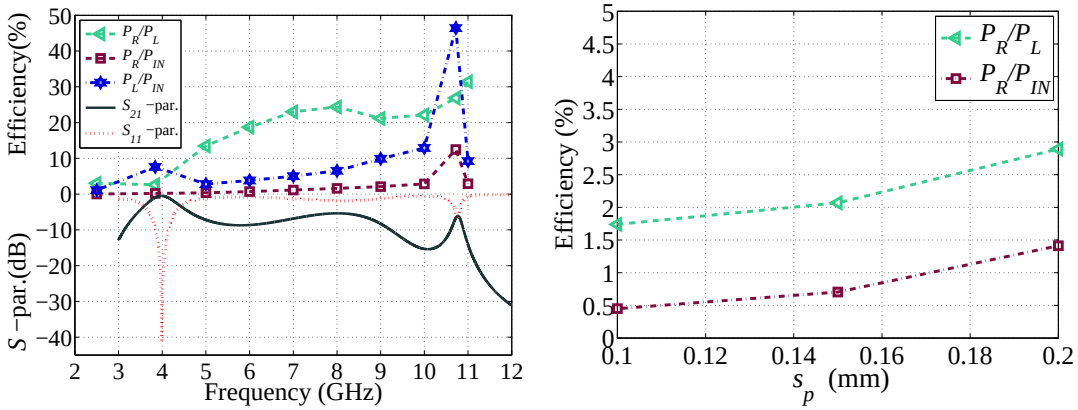

(a) (b)

Figure 2.13: (a) A summary of the radiation efficiency for a strongly coupled SIW coaxial resonator. P_R is the radiated power, P_L is the total loss power and P_{IN} is the input power at the coaxial SIW resonator. (b) P_R versus P_L $(green)$ and versus P_{IN} (red) at $f_0 = 4$ GHz for increasing air gap width s_p, which has been created at the top metal layer.

where it is considered that $P_{IN} = 1$ W. All parameters will be expressed in percentage, in order to simplify understanding of the obtained results. The last parameter of the previous list is the key index, because it helps us to understand which part of the total loss of the device depends on radiated power. Fig. 2.13 displays that the power loss due to radiation issues at 4 GHz is practically negligible. In fact, P_R is much less than 3% of P_L and less than 1% of P_{IN} at the structure. Radiated power only exceeds 1% of

P_{IN} above 10 GHz. Moreover, the radiated power slightly depends on the width of the capacitive patch spacing, as shown in Fig. 2.13-(b). Nevertheless, the radiation issue tends to increase in correspondence to the first spurious mode of the SIW structure. In this case, P_L increases up to 50% of the input power and, especially, P_R reaches 10% of P_{IN} and it corresponds to 30% of the total power losses.

2.2 Sensitivity Analysis

This section is devoted to perform a sensitivity analysis of the proposed SIW coaxial resonator. The goal is the study of how the uncertainty in the frequency response of this resonator can be apportioned to different sources of uncertainty in its physical characteristics. Thus, a deep study of the effect of temperature, dielectric constant variation and manufacturing tolerances on the performance of the resonator presented in Section 2.1.1 is provided.

In order to investigate these effects in PCB substrate materials for microwave applications, 3D EM simulations of under-coupled coaxial SIW resonator have been made and preliminary results are reported in the following. As it has already been mentioned, a 2.54 mm-thick Rogers TMM10i dielectric substrate has been selected and its physical properties have been taken among other sources from data sheets and internet [79]. The main dimensions of this resonator are shown in Table 2.1.

2.2.1 Tolerances of Laminate Dielectric Constant

An important parameter to take into account when designing an SIW component, it is the percentage deviation of the ϵ_r that characterizes the selected dielectric laminate. This percentage deviation from the rated value can be obtained from the data sheets of the material that is given by the manufacturer. Due to the inherent properties of the SIW, any variation of ϵ_r can affect the EM performance, generating undesirable frequency shifts.

Table 2.2: Properties of Rogers TMM10i

Property	**Rogers TMM10i**
Dielectric Constant ϵ_r	9.8
Variation of ϵ_r	$\pm$0.245
Percentage Variation of ϵ_r	$\pm$2.5%

The main properties of the Rogers TMM10i are shown in Table 2.2. Thus, preliminary simulated results for the under-coupled coaxial resonator show that the frequency deviation could reach a maximum value of $\pm$1.3%. This deviation corresponds to a total frequency shift of 89 MHz around 4 GHz.

In order to compare these results, a similar study has been performed using a standard TE_{101} square SIW resonator, resonating at 4 GHz, which has been implemented in the same laminate. From simulated results, it has been estimated that the frequency shift would be around $\pm$1.2%, being very similar to the previous results of the coaxial approach.

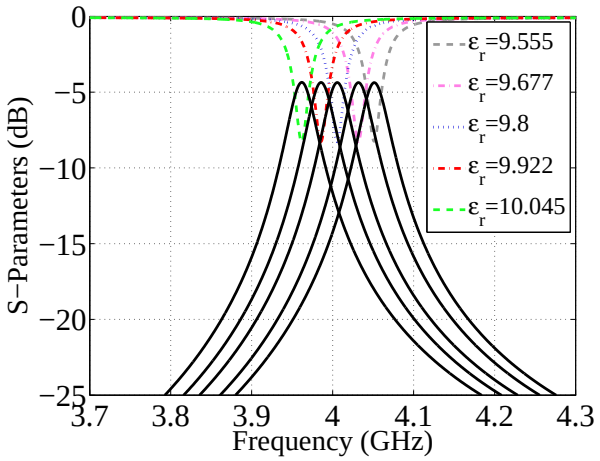

Figure 2.14: S-parameter responses versus dielectric constant variation for under-coupled coaxial SIW resonator, considering TMM10i material. Frequency shift is around ±1.3%.

2.2.2 Effects of Temperature

Again, the effect of the temperature on the EM performance of a microwave coaxial SIW resonator is mainly related to the properties of the dielectric substrate that forms it. Variations of temperature modify the dielectric constant of the laminate, while its Coefficient of Thermal Expansion (CTE) affects the physical size of the laminate, thus the size of the SIW itself, altering the resonant frequency. In this context, Rogers TMM laminates have a very low thermal coefficient of dielectric constant, typically less than 50 ppm/°C. Moreover, the material isotropic coefficients of thermal expansion, very closely matched to copper, allow for production of high reliability plated via holes, and low etch shrinkage values. In this context, Table 2.3 highlights its main properties.

Table 2.3: Thermal properties of Rogers TMM10i

Property	**Rogers TMM10i**	**Units**	**Condition**
Dielectric Constant ϵ_r	9.8		
Thermal Coefficient of ϵ_r	-43	ppm/K	−55 to +125
CTE X-Y Direction	19	ppm/K	0 to +140
CTE Z Direction	20	ppm/K	0 to +140

EM simulations have been performed taking into account a variation of the temperature in the range of −15°C to +65°C with a step of 40°C. The simulated frequency responses are shown in Fig. 2.15. The estimated frequency shift is very limited for this material, being less than ±0.035% around 4 GHz. Thus, the shift is just few MHz for the proposed C-band coaxial resonator. As a result, it appears that Rogers TMM10i substrate with a permittivity thermal coefficient of −43 ppm/K from −55°C to +125°C, a thermal expansion coefficient of 19 ppm/K in the X- and Y-direction, 20 ppm/K in the Z-direction, may be a suitable candidate for implementing SIW coaxial resonators.

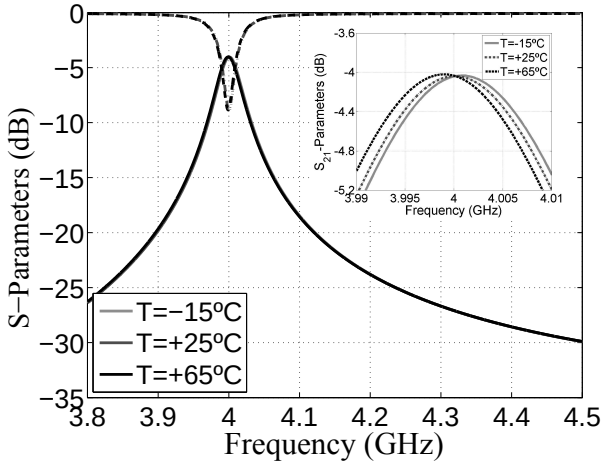

Figure 2.15: S-parameter responses versus thermal variation for under-coupled coaxial SIW resonator, considering TMM10i material. Frequency shift is around 0.035%.

2.2.3 Manufacturing Tolerances

As it is well known, manufacturing tolerances associated with fabrication processes cause deviations with respect to the ideal EM responses of microwave structures, without restriction to the different technologies that are used for their implementation. Since many fabrication processes can be successfully applied to the manufacturing of the SIWs, a PCB fabrication process is considered because it is one of the most widely used.

Thus, common fabrication tolerances of a standard double-layer PCB process are taken into account, and are used for introducing deviations in geometrical dimensions of the coaxial structure. These values are shown in Table 2.4.

Table 2.4: General tolerances for double-layer PCB circuit board process (Source: Lab Circuits SA [82]).

PCB Fabrication Process	**Special**	**Units**
Spacing width (thickness copper foil)	±15% (35μm)	
	±10% (17μm)	
Plated via hole diameter	+0.1	mm
	0	mm
Total copper foil thickness tolerance	±5%	
Finished plated via hole copper thickness	35	μm

Among several possible error sources for coaxial SIW structures, the inner via hole diameter d_v, the width of s_p, the thickness of the dielectric material h as well as the final copper foil thickness are the main ones. The latter is increased during the through-hole electro-plating process that is necessary for implementing metalized via holes. Note that the growth of copper foils thickness influences the total value of the integrated loading capacitance of the resonator, thus must be taken into account for the analysis and design of these structures.

Looking at Table 2.4, the tolerance related to the plated via hole diameter can be considered a worst case for the coaxial SIW topology. When using standard PCB fabrication, it is sometimes important that the final diameter of a plated hole matches the required value. Therefore, when the drilling of the laminate is performed, a bigger drilling tool is usually used so that the hole diameter can be reduced during the through-hole plating, when a copper foil is growing inside the hole.

On the other hand, in the SIW coaxial topology, it is very important that the diameter of the inner via hole matches the value that has been used in the simulation stage (i.e. d_v). In this context, the thickness of the metal layer inside the hole does not play any role in the working principle of the structure. Thus, while performing the drilling phase in a PCB manufacturing, the diameter of the drilling tool must correspond to d_v, without restriction to the final diameter of the plated hole. As it has been demonstrated, the size of the hole created in the dielectric material does control the resonant frequency of the structure. Therefore, the uncertainty related to this tolerance can be easily cancel out by choosing values of d_v that corresponds to available penetrating tools, which provide very precise cuts nowadays. In the following simulations, a tolerance of $\pm 5\%$ has been accounted for d_v that reflects the precision of the tool.

To determine the robustness of the proposed topology, the response of the coaxial resonator is obtained from dimensions chosen randomly (with the application of an appropriate error distribution function). Such deviations will generate frequency shifts of the resonant frequency, towards lower or higher frequencies.

A suitable approach for performing this tolerance analysis, in order to determine the sensitivity of the frequency response with respect to random variations of its physical dimensions, is a statistical analysis in a full-wave simulator, as the case of ANSYS HFSS 2014.

In order to summarize the tolerance effect of PCB fabrication process, Fig. 2.16 shows 25 statistical outcomes of both transmission response using an uniform distribution function for mentioned tolerances.

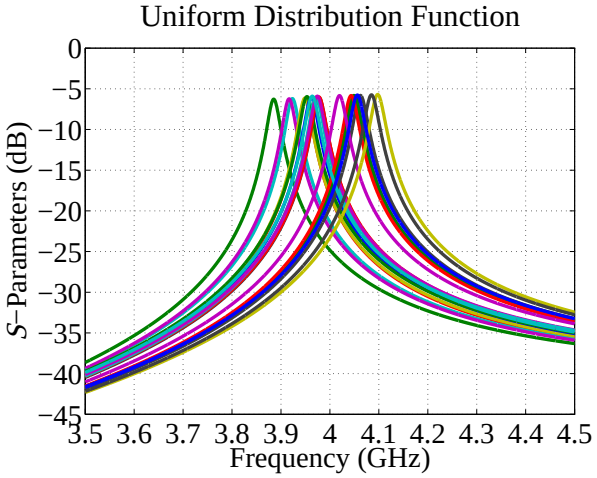

Figure 2.16: Tolerance analysis considering deviation in s_p, d_v, final copper foil thickness and laminate thickness using an uniform distribution function. Total relative frequency shift could be around $\pm 2.75\%$, between 3.88 GHz and 4.1 GHz.

The results show that the relative frequency shift could reach within $\pm 2.75\%$ around the nominal resonant frequency. Analyzing separately the single deviation, the change

in the diameter of inner via hole d_v and in the spacing gaps s_p play an important role. Considering the above mentioned deviation over a standard value, the relative frequency shifts are in the range of $\pm 1\%$ and $\pm 1.1\%$, respectively.

Clearly, standard SIW components are less sensitive to manufacturing tolerances, as it has been demonstrated in [83]. The relative frequency shift caused by the metalized via hole radius tolerance is approximately within 0.5%, which is almost the same as that caused by the substrate permittivity tolerance in the case of a Rogers RT/Duroid 6002 material (i.e with a permittivity of $2.94 \pm 1.36\%$). Since the fundamental mode of these structures is strongly related to the size of the resonator cavity, this allows us to obtain very robust designs. For instance, manufacturing tolerances related to copper foil thickness or spacing width do not have any effect in such structures.

To sum up, it is clear that the coaxial SIW topology is more sensitive than a standard SIW approach due to the cumulative effect of the uncertainty introduced by the materials and the manufacturing processes. Therefore, the introduction of the coaxial topology in the SIW technology allows to increase design flexibility and compactness at the expense of an higher sensitivity.

2.3 Inter-resonator Coupling

In this section, the inter-resonator coupling mechanisms that can be used for coupling coaxial SIW resonators are presented and studied. Two different coupling structures will be analyzed. The first one is a conventional coupling system based on post-wall irises widely used in SIW applications, which is usually classified as magnetic coupling. Secondly, a novel electric coupling mechanism especially suited for coaxial SIW resonator is presented and deeply studied. This solution enables us to increase the internal coupling for strongly loaded coaxial SIW resonators with respect to the conventional post-wall iris magnetic coupling.

In order to study the performance of the proposed inter-resonator coupling topologies, let us consider a different coaxial SIW resonator having centre frequency 5.5 GHz and using the 1.524 mm-thick Rogers R4003C dielectric substrate [84], with permittivity $\epsilon_r = 3.55 \pm 0.05$ and loss tangent $\tan\delta = 2.1 \cdot 10^{-3}$. The thickness of the copper base layers is $t = 17$ μm. The resonator electrical length corresponds to 18.9°, i.e. $0.052\,\lambda_g$, where λ_g is the guided wavelength at 5.5 GHz. The coaxial SIW resonator has been designed to present $b = 29.4$ mS that gives a loading capacitance of $C_l = 0.825$ pF while $Z_0 = 103.5\ \Omega$. By using both values and choosing a diameter of $d_{via} = 0.6$ mm for the inner via hole, the SIW resonator cavity size is $w_{siw} \times l_{siw} = 14.6 \times 14.6$ mm^2 (i.e. $0.5 \times 0.5\,\lambda_g^2$ and $0.27 \times 0.27\,\lambda_0^2$) whilst the square patch side r_p is 4.2×4.2 mm^2 with an air gap of $s_p = 0.24$ mm between the patch and the ground plane. This specific coaxial configuration will be used for demonstrating high selectivity applications in the following chapters.

In order to study the inter-resonator coupling, coupled coaxial SIW resonators are considered and simulated in ANSYS HFSS 2014. Both resonators are weakly-coupled at the input/output ports. The formula for extracting the coupling coefficients in terms of the characteristic frequencies of synchronously tuned coupled resonators is, according to [8],

$$k_{i,i+1} = \pm \frac{f_{p2}^2 - f_{p1}^2}{f_{p2}^2 + f_{p1}^2} \tag{2.14}$$

where, f_{p2} and f_{p1} are the two split resonance frequencies extracted from full-wave simu-

lations.

2.3.1 Magnetic Couplings

The post-wall iris coupling used in SIW presents a structure very similar to the one used in classical metallic waveguide technology. Thus, some via holes have been removed from the via hole wall that separates adjacent SIW cavity resonators. The post-wall iris can be seen as a form of discontinuity, which works by exciting evanescent higher order modes. The vertical edges composed by via holes are parallel to the E field and excite TE modes. The stored energy in TE modes is predominantly related to the magnetic field, and consequently the lumped equivalent circuit of this structure is an inductor.

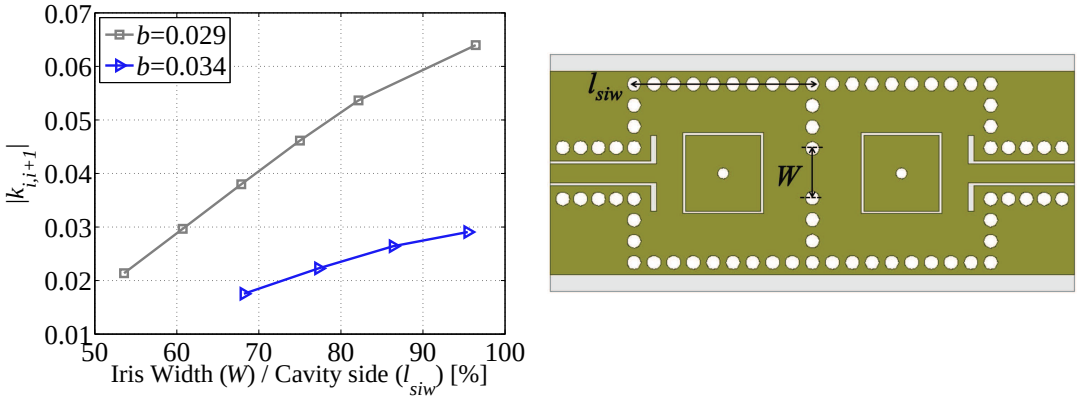

(a) (b)

Figure 2.17: (*a*) Coupling coefficient $k_{i,i+1}$ variation versus the relation between the post-wall iris width W and the SIW cavity side l_{siw}. (*b*) Inter-resonator coupling system based on post-wall iris, showing design parameters.

The main parameters of the coupling system are shown in Fig. 2.17, and those are the width W of the coupling post-wall iris, and the diameter d_{via} of via holes that form the post-wall iris. Let us consider a fixed value for d_{via} because $k_{i,i+1}$ slightly depends on this parameter, and let us study the effect of W.

In Fig. 2.17, the coupling provided by a post-wall iris is depicted as function of W, for two different values of slope parameter. As it can be observed, $k_{i,i+1}$ raises for increasing value of W. Nevertheless, the post-wall iris coupling is not well suited for the miniaturization of coaxial SIW structures.

In fact, by increasing the slope parameter of such structures, the magnetic coupling between coaxial SIW resonators is strongly reduced. For example, let us consider a variation of b from 0.029 S to 0.034 S, which corresponds to diminish the SIW cavity side from 14.6 mm to 11.5 mm, while C_l of the capacitive disks increases from 0.825 pF to 0.95 pF. Both coaxial SIW resonators resonate in all cases at the same frequency, which is 5.5 GHz. As can be observed in Fig. 2.17, the maximum $k_{i,i+1}$ achievable diminishes from $\simeq 0.065$ to $\simeq 0.03$, which means that only very narrow bandpass filters can be designed employing such solution when a higher miniaturization is required.

In order to enhance the magnetic coupling in these structures, CPW probes can be introduced at the top metal layer in a similar manner to the CPW-to-SIW transition widely used for the external coupling of SIW filters [85]. Thus, current probes have been etched on the top metal layer at the centre of the post-wall iris, which is opened between

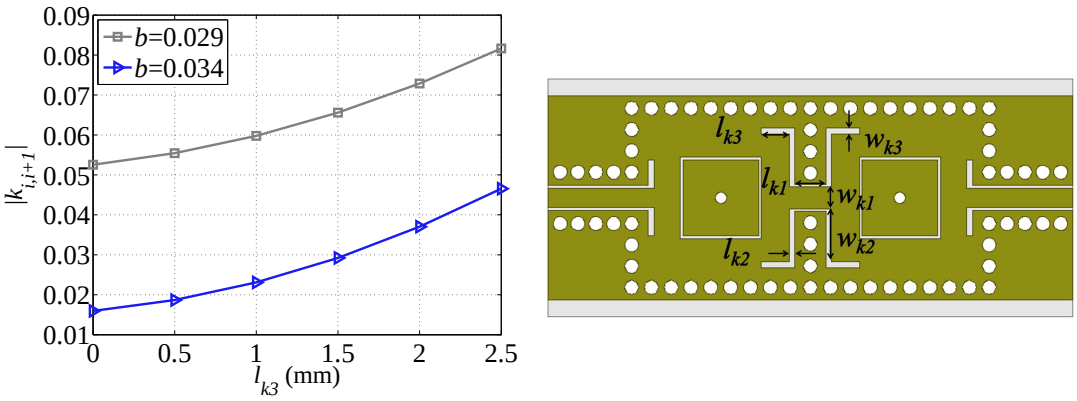

(a) (b)

Figure 2.18: (a) Coupling coefficient $k_{i,i+1}$ variation versus the length of l_{k3}. (b) Inter-resonator coupling system based on post-wall iris and current CPW probes, showing design parameters.

adjacent resonators, as it is shown of Fig. 2.18-(b). The coupling mechanism features current probes in both cavities, being w_{k2} and l_{k3} the main parameters that are used for controlling the coupling magnitude. In Fig. 2.18-(a), the coupling is graphically presented as function of l_{k3}, again for two different values of slope parameter. In the case of the resonator that presents $b = 0.029$ S, a fixed value is considered for w_{k2}, which is 5.5 mm. Other parameters have been also fixed, being: $l_{k1} = 1.1$ mm, $l_{k2} = 0.3$ mm, $w_{k1} = 0.8$ mm, $w_{k3} = 0.3$ mm and $s_k = 0.3$ mm. The latter is the spacing of the CPW line of length l_{k1} located at the centre of post-wall iris. Note that this dimension has not been specified in Fig. 2.18-(b). When studying the case of the coaxial resonator having $b = 0.034$ S, the value of w_{k2} has been set to 3 mm.

Comparing these results to the ones of the previous simple post-wall iris, it is clear that higher coupling values can be obtained. Nevertheless, the proposed mechanism suffers significant magnitude reduction in the case of miniaturized coaxial resonators, thus for increasing b. In addition, the need of large current probes for obtaining higher coupling could be a problem when folded filter configurations or cross couplings of different sign must be implemented.

2.3.2 Electric Couplings

The electric coupling structure has been firstly proposed in [86]. This electric coupling scheme can be used to obtain a further reduction of the filter size and increased bandwidth compared to conventional magnetic irises. The proposed solution to realize an electrical coupling between coaxial SIW resonators is based on a capacitive probe implemented by a high impedance CPW line. The two ends of such a line penetrate into the head of the resonator capacitive patches, i.e. in the region with the highest intensity of electric field. A gap s between the capacitive patch of the resonator and the probe is ensured. Part of the field is then collected by the probe and transferred to the adjacent resonator, so realizing an electric coupling.

In absence of the probe described above, the main source of coupling would be due to the magnetic field inside the SIW cavities. For the considered structure, the sign of the magnetic coupling is opposite to the electrical one. Therefore, in order to boost the effect

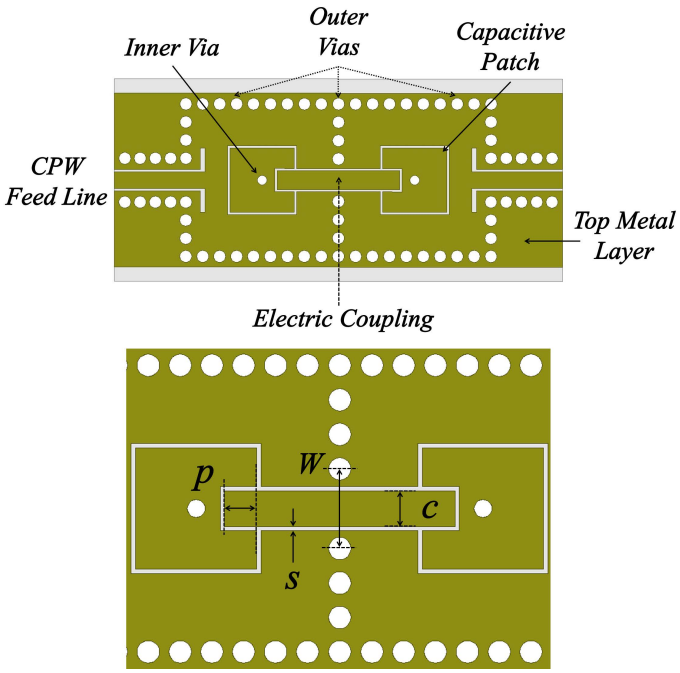

Figure 2.19: Topology of the proposed electric coupling for coaxial SIW resonators.

of the probe and get higher values of coupling, the magnetic coupling must be minimized. Such condition can be achieved with a wall of via holes placed across the resonators, because these holes strongly confines the magnetic field coupling. The probe can still be realized if the width c of the CPW line is sufficiently smaller than the gap W between the central via-holes realizing the wall, as shown in Fig. 2.19.

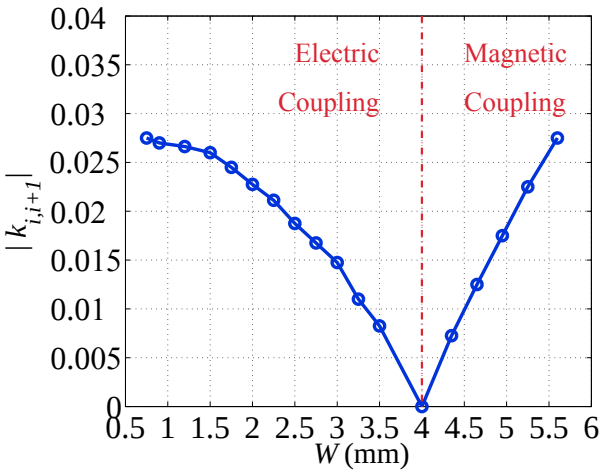

Figure 2.20: Coupling coefficient $k_{i,i+1}$ variation versus iris width W for $p = 1$ mm, $c = 0.25$ mm and $s = 0.15$ mm. As the iris width increases, the total coupling decreases until it changes from electric to magnetic coupling and then increases again.

It is worth to mention that the proposed coupling system is only located at the top metal layer, which represents a clear advantage compared to other implementations of electric coupling mechanisms in SIW structures. In [17] and [18], a negative coupling structure between SIW cavity resonators is proposed using a balanced microstrip line

with a pair of plated via holes. However, in both structures, slots need to be etched at the top and bottom layers of the substrate, limiting the integration and packaging possibilities of the devices. In [19], a controllable mixed coupling is created using an embedded short-ended strip-line combined with a wall iris, at the expense of a multi-layer fabrication process that increases the complexity of the structure.

Fig. 2.20 shows the total coupling $k_{i,i+1}$ as function of W (obtained from the contribution of both electric and magnetic couplings), where i is a generic i-th resonator. Such trace was derived with a constant value for the insertion p (i.e. $p = 1$ mm) of the probe inside the head of the resonator. For increasing values of W, the wall becomes more similar to a coupling iris with reference to classical waveguide structures. The curve shows that as the iris opens up, the total coupling starts to decrease until a certain point after which it starts to rise again.

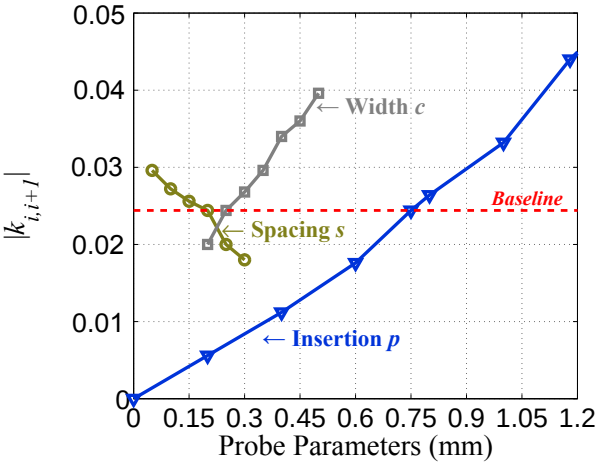

Figure 2.21: Coupling coefficient $k_{i,i+1}$ variation versus CPW probe dimensions: conductor width c, spacing s and insertion p on capacitive disks. Red line is the simulation baseline (i.e. $s = 0.15$ mm, $c = 0.25$ mm and $p = 0.75$ mm). The post-wall iris width is $W = 0.75$ mm.

This effect can be explained by considering that when W is minimum, the iris is completely closed and we are in the condition of minimum magnetic coupling between the two resonators. Therefore, the major contribution to the coupling $k_{i,i+1}$ is given by the probe (i.e. electric coupling). When W starts to increase, the magnetic coupling between the two resonators is not negligible anymore, and it starts to counteract the effect of the electrical coupling, until they reach the same magnitude and the total coupling collapses to zero ($k = 0$). From this point on, if W is increased the magnetic coupling starts to prevail, and the effect of the electric probe is not visible anymore.

This analysis demonstrates that, in order to obtain electrical coupling between the two resonators, it is not sufficient to implement the probe described above, but it is also necessary to minimize the magnetic coupling by means of a narrow post-wall iris.

The insertion of the probe inside the head of the resonators is the main parameter to control the magnitude of the coupling $k_{i,i+1}$. The behavior of $k_{i,i+1}$ as function of p for the structure of Fig. 2.19 is shown in Fig. 2.21, which considers two coupled resonators implemented on a substrate Rogers R4003C as previously described. As expected, $k_{i,i+1}$ becomes stronger as the insertion p within the head of the resonator is increased. Clearly, $k_{i,i+1}$ also depends on c and s, and this behavior is also reported in Fig. 2.21. Nevertheless, these parameters present a mitigated control of the coupling coefficient magnitude if

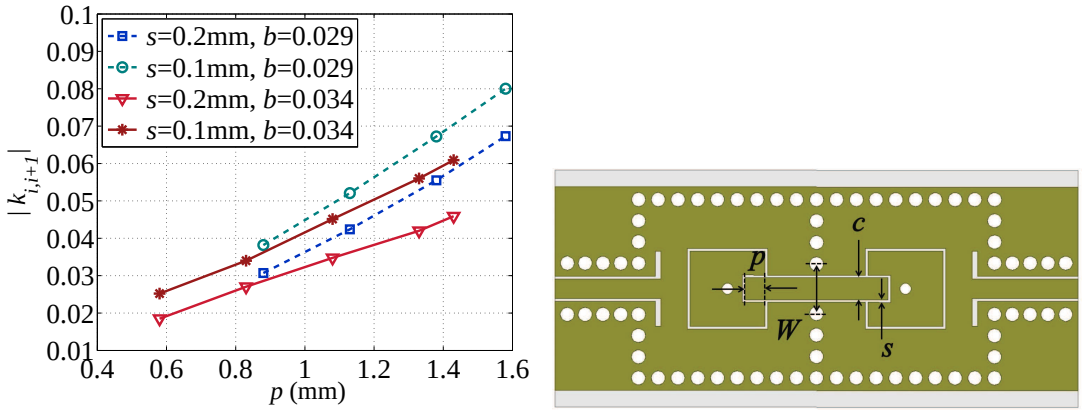

(a) (b)

Figure 2.22: (a) Coupling coefficient $k_{i,i+1}$ variation versus electric coupling probe insertion p. Other parameters are: $W = 2.2$ mm and $c = 1.45$ mm. (b) Inter-resonator coupling system created at the top metal layer of the SIW resonator, showing design parameters.

compared to the probe insertion one. Thus, we can definitely settle these values fixed, and controlling the coupling by means of p.

A main advantage of the proposed electric coupling is to make for increasing direct inter-resonator coupling, especially for strongly loaded coaxial SIW resonators. As a way of comparison, one can look at Figs. 2.17 and 2.22 where the coupling strength capabilities of the magnetic and electric coupling schemes are compared for the same coaxial SIW topology. As previously explained, in Fig. 2.17, the coupling given by a post-wall iris is depicted for two different values of slope parameter that feature coaxial SIW resonators. As it is shown, by increasing the slope parameter of such structures, the magnetic coupling is strongly attenuated. Now, applying the proposed electric coupling for the same pair of coaxial resonators, it is possible to see how higher values are easily implementable in more compact structures. Fig. 2.22 depicts the inter-resonator coupling values that can be obtained using the proposed electric CPW probe, together with a scheme of the coupling with its main design parameters. As it can be observed, the maximum $k_{i,i+1}$ achievable just diminishes a little bit by increasing the resonator b value, which means that a higher design flexibility is obtained.

2.4 External Coupling

As it is well known, resonant circuits are always coupled to other circuitry that are usually the external source and the external load. In order to ensure that SIW components can be measured or integrated with other planar device, SIW-microstrip transition has been widely used to control the coupling between the cavity resonator and these input/output ports [1]. Another coupling mechanism widely used is based on an CPW-to-SIW transition made with current probes etched on the metal layer [85].

Taking into account these standard approaches for SIW, two input/output coupling structures for coaxial resonators are presented in this section. In the first place, a conventional external coupling mechanism for controlling External Quality Factor (Q_e) in standard SIW structures is introduced. Secondly, a novel electrical external coupling especially suited for coaxial resonators is then presented and studied.

In order to show the external coupling behavior, a singly loaded coaxial SIW resonator is considered and simulated in ANSYS HFSS 2014. The simulated resonator structure will be the same of the previous Section 2.1.1.

As shown in [8], Q_e will be extracted from the group delay of S_{11} (expressed as $\tau_{S_{11}}$) at resonance using the following expression

$$Q_e = \frac{\omega_0 \tau_{S_{11}}(\omega_0)}{4} \tag{2.15}$$

2.4.1 Magnetic Couplings

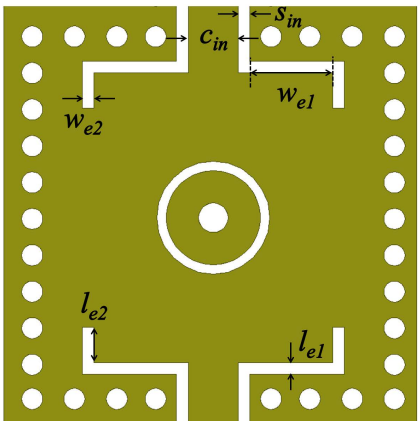

Figure 2.23: Physical layout of the SIW coaxial resonator with magnetic external coupling.

The magnetic external coupling consists on a CPW-to-SIW transition with 90° bend slots, firstly reported in [85]. These current slots are created on the top metal layer, and the external quality factor Q_e decreases with increasing size of ground plane openings that are etched at the end of the input/output CPW lines. Fig. 2.23 shows the external coupling mechanism and its design parameters, being w_{e1} - w_{e2} and l_{e1} - l_{e2} the main geometrical dimensions that control the external coupling value.

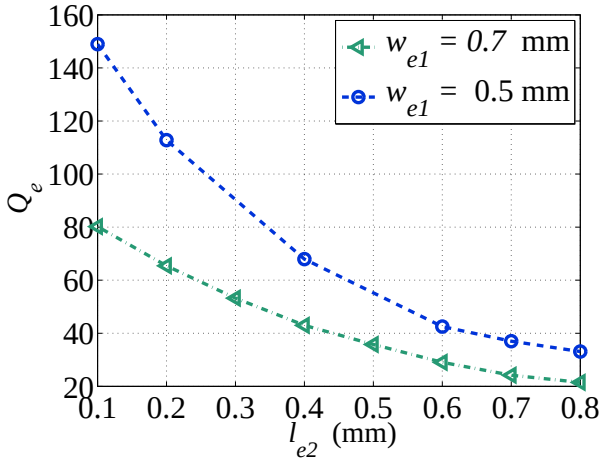

Figure 2.24: Q_e as a function of the length of the current slots l_{e2}. Two different values of the current slot width w_{e1} have been taken into account.

Fig. 2.24 depicts curves of the Q_e values as function of the l_{e2}, while the other sizes of the ground plane openings are $w_{e1} = 0.5 - 0.7$ mm, $w_{e2} = 0.1$ mm and $l_{e1} = 0.1$ mm. It is worth mentioning that this solution can be used even if input/output ports and inter-resonator coupling are rotated through 90°, for example in the case of first/last resonators of a folded coupled resonator bandpass filter.

The characteristic impedance Z_0 of the input/output ports can be set by adjusting other design parameters, such as s_{in} and c_{in}. This means we can independently set Q_e and Z_0 at their optimal values.

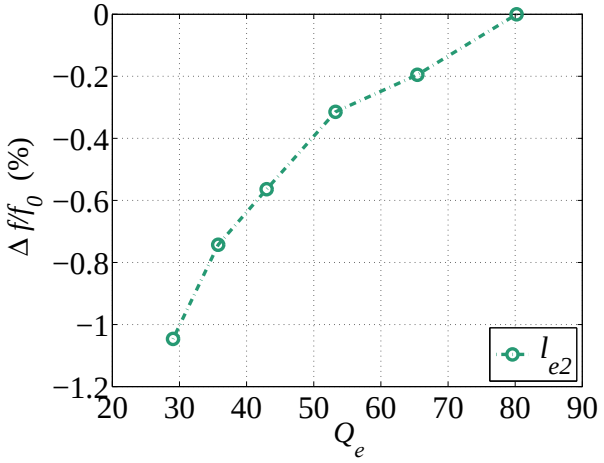

Figure 2.25: Resonant frequency of a coaxial SIW resonator versus Q_e varying l_{e2}. The other parameters l_{e1}, w_{e1} and w_{e2} are 0.1 mm, 0.5 mm and 0.1 mm, respectively.

As it is shown in Fig. 2.25, the resonant frequency of the structure decreases when increasing the intensity of the external coupling, which is an expected effect due to the loading effect introduced by the coupling mechanism. Thus, to obtain a proper value of Q_e at the desired operation frequency, it is necessary to adjust the capacitive patch size or annular gap width in order to set the resonance.

2.4.2 Electric Couplings

The electrical external coupling between the coaxial SIW resonators and the input/output ports is based on CPW capacitive probes that are inserted within the capacitive patch, as it is shown in Fig. 2.26. The CPW probe is inserted in the region with the highest intensity of electric field. A gap s_{in} has been created between the capacitive circular disk and the CPW probe, thus the gap creates a coupling capacitance. Then, the electric field is transferred from the CPW probe to the integrated loading capacitance, exciting the fundamental mode of the coaxial SIW resonator. The Q_e decreases with increasing insertion p_e within the capacitive disk (see Fig. 2.27). Thus, the higher the insertion of the CPW probes is, the lower the Q_e value is.

It is worth mentioning that this coupling mechanism enables us to obtain higher input-output coupling in the case of strongly loaded coaxial SIW resonators with respect to the standard CPW-to-SIW magnetic coupling. Moreover, the proposed coupling scheme maintains the advantage of the single layer implementation, providing accurate control of the coupling level and improved flexibility.

Again, this mechanism is well suited for folded filters, where input-output ports and inter-resonator coupling are rotated through an angle of 90° in the first and last coaxial

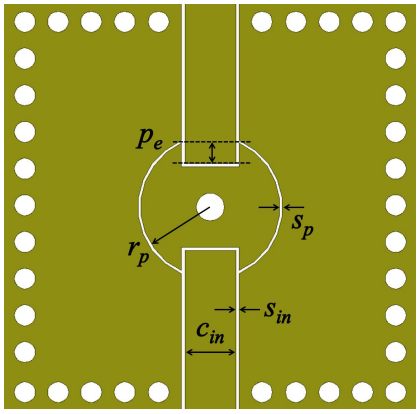

Figure 2.26: Physical layout of the SIW coaxial resonator with electrical external coupling.

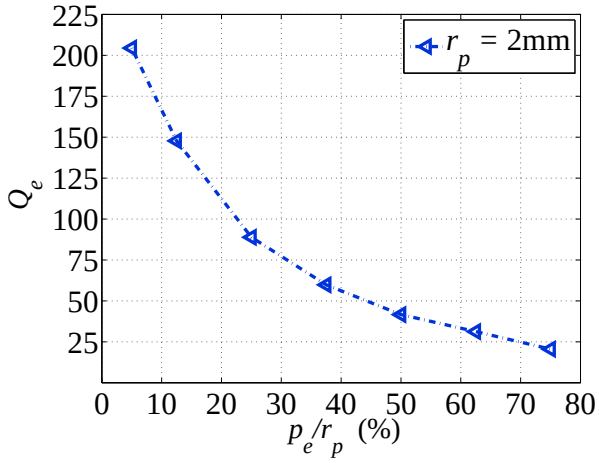

Figure 2.27: Q_e as a function of the insertion of the CPW capacitive probes p_e.

resonators, as it will be shown in the next Section 3.4.

It is worth mentioning that the Q_e value does not have a strong dependence on the width c_{in} of the CPW feed line, thus the CPW impedance can be easily set at an optimal value (i.e. 50 Ω) while maintaining a desired Q_e value. Nevertheless, a simple triangular taper could be introduced on the CPW feed line before inserting the capacitive patch. The taper size should be optimized in order to achieve a desired Q_e value for a fixed probe insertion. This solution would increase the flexibility of the input/output CPW probe design, thus both coupling and CPW impedance specifications could be easily satisfied.

Fig. 2.28 depicts the effect of the capacitive probe insertion on the resonant frequency of the coaxial SIW resonator for increasing coupling. Compared to the previous external coupling, the frequency shift towards lower frequencies increases up to 3.5% for this particular case study. The shift is mainly due to the loading effect of CPW probe that directly penetrates the capacitive disk, modifying its structure and increasing its total C_l. Accordingly to the mentioned capacitive effect, this mechanism can be classified as an electric external coupling. By adjusting the capacitive patch size or annular gap width, Q_e can be easily fixed at the desired operation frequency.

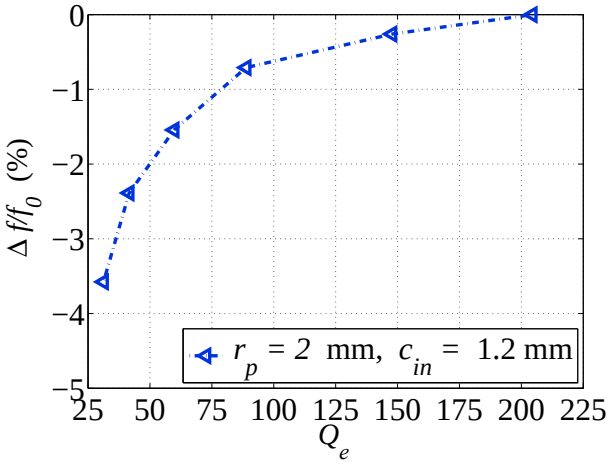

Figure 2.28: Resonant frequency of a coaxial SIW resonator versus Q_e varying the insertion p_e. The other parameters r_p, c_{in} and s_{in} are 2 mm, 0.5 mm and 0.15 mm, respectively.

2.5 Synthesis of Coaxial SIW Filters

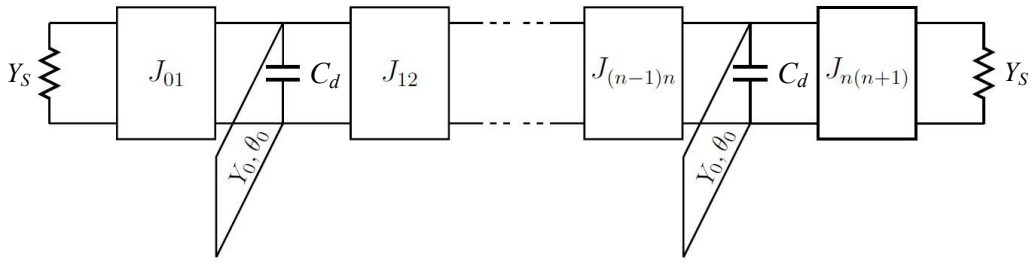

Figure 2.29: Prototype of a coaxial SIW bandpass filter using shunt resonators and frequency-invariant admittance inverters.

The prototype of an all-pole direct-coupled coaxial SIW bandpass filter using shunt resonators and frequency-invariant admittance inverters is shown in Fig. 2.29. Given a filter response with centre frequency $\omega_0 = \sqrt{\omega_L \omega_H}$ and bandwidth $\triangle\omega$, being ω_H and ω_L the upper and lower cutoff frequencies, C_l and Y_0 can be obtained by mapping the resonator susceptance and the admittance inverters of the bandpass filter with those of the low-pass prototype. The former condition can be expressed as

$$B(\omega) = \omega' \left(\frac{b\frac{\triangle\omega}{\omega_0}}{\Omega_C} \right) \tag{2.16}$$

where ω' and $\Omega_C = 1$ rad/s the angular frequency and cut-off frequency of the low-pass prototype, respectively. Now, substituting (2.1) into (2.16) for the corresponding pass-band edge frequencies ($\omega' = \pm 1 \Rightarrow \omega = \{\omega_H, \omega_L\}$), we can obtain

$$C_l = \left(b\frac{\triangle\omega}{\omega_0} \right) \frac{\cot\theta_H + \cot\theta_L}{\omega_H \cot\theta_L - \omega_L \cot\theta_H} \tag{2.17}$$

$$Y_0 = \left(b\frac{\triangle\omega}{\omega_0} \right) \frac{\omega_H + \omega_L}{\omega_H \cot\theta_L - \omega_L \cot\theta_H} \tag{2.18}$$

where $\theta_H = \beta_H h$ and $\theta_L = \beta_L h$, and β_H and β_L are the phase constants at the pass-band edge frequencies.

Finally, the admittance inverters can be computed from the low-pass prototype coefficients $g_0,\ g_1, \cdots,\ g_{n+1}$ using the well-known expressions [8]

$$J_{01} = \sqrt{\frac{Y_S\left(b\frac{\triangle\omega}{\omega_0}\right)}{g_0 g_1}} \tag{2.19}$$

$$J_{n,n+1} = \sqrt{\frac{Y_S\left(b\frac{\triangle\omega}{\omega_0}\right)}{g_n g_{n+1}}} \tag{2.20}$$

$$J_{i,i+1} = \left(b\frac{\triangle\omega}{\omega_0}\right)\sqrt{\frac{1}{g_i g_{i+1}}} \tag{2.21}$$

for $i = 1$ to $(n-1)$, where Y_S is the admittance of the input/output ports.

In order to design a coaxial SIW bandpass filter, the first step is to design the basic cell that is a coaxial SIW cavity resonator. After choosing the level of the slope parameter b, the diameter of the inner via d_v is chosen sufficiently small in order to reduce the cavity size for a given admittance level. However, this will be ultimately limited by the fabrication process and its tolerances. Then, the cavity side l_{siw} of a square SIW cavity can be calculated from the synthesized admittance Y_0 using (2.2). Next, given the required C_l, the capacitive disk radius and its air gap can be obtained numerically from (2.3), and optimized by means of 3D EM simulations taking into account the metal layer thickness. Again, the minimum annular gap will be also limited by the selected fabrication process. It is worth mentioning that the resonator Q_u will depend on these selected values, so the analysis of Section 2.1.2 should be taken into account to set those values in order to obtain the best unloaded Q-factor for a given resonator b.

Once the resonators are designed, the input/output and inter-resonators couplings will be dimensioned. The Q_e and $k_{i,i+1}$ coefficients are obtained from the synthesized $J_{i,i+1}$ values as follows

$$Q_{e,1} = \frac{bY_S}{J_{01}^2} \tag{2.22}$$

$$Q_{e,n} = \frac{bY_S}{J_{n,n+1}^2} \tag{2.23}$$

$$k_{i,i+1} = \frac{J_{i,i+1}}{b} \tag{2.24}$$

Then, using full-wave EM simulations it is possible to estimate Q_e and $k_{i,i+1}$ by setting the proposed coupling mechanisms reported in Sections 2.3 and 2.4. Since the method is based on the coupled-resonator filter design, the next step is to establish the relationship between the coupling coefficients and the physical dimensions of the coupled resonators. Thus, the Q_e and $k_{i,i+1}$ curves for the specific configuration of the coaxial SIW resonators that composes the designed filter can be calculated. Finally, a fine tuning procedure has to be performed using full-wave EM simulations. During this process, Y_0 and especially C_l of the resonators must be slightly modified due to the loading effect of the inverters. Both parameters of the distributed equivalent circuit are finely controlled through the

modification of the SIW cavity sides l_{siw} and disk radius r_p (and/or air gap s_p), respectively. From a practical point of view, it is recommended to perform optimization directly on C_l values, since a fine control of the resonant frequency of the coaxial resonators is easily attained.

2.6 Filter Design

In this section, the design of substrate integrated coaxial filters is applied to two bandpass filters operating at X-band, which have been manufactured using different fabrication processes. The first section shows the design of a 3-pole bandpass filter in single-layer PCB substrate, while the second section illustrates the design of a 2-pole bandpass filter in LTCC technology.

2.6.1 Example: X-band Filter in PCB technology

In order to validate the proposed approach for filter miniaturization, a 3-pole Chebyshev filter has been designed, fabricated in a Rogers RO4003C substrate and measured [76]. The synthesized filter is centered at 9.8 GHz with 5% FBW and 0.05 dB in-band ripple. Thus, a loading capacitance of $C_l = 0.2$ pF and resonator admittance of $Y_0 = 8.22$ mS have been obtained for a susceptance slope parameter $b = 14$ mS. The inverter values are $J_{01} = J_{34} = 0.0036$ and $J_{12} = J_{23} = 0.007$ for an input/output impedance $Z_S = 65\,\Omega$.

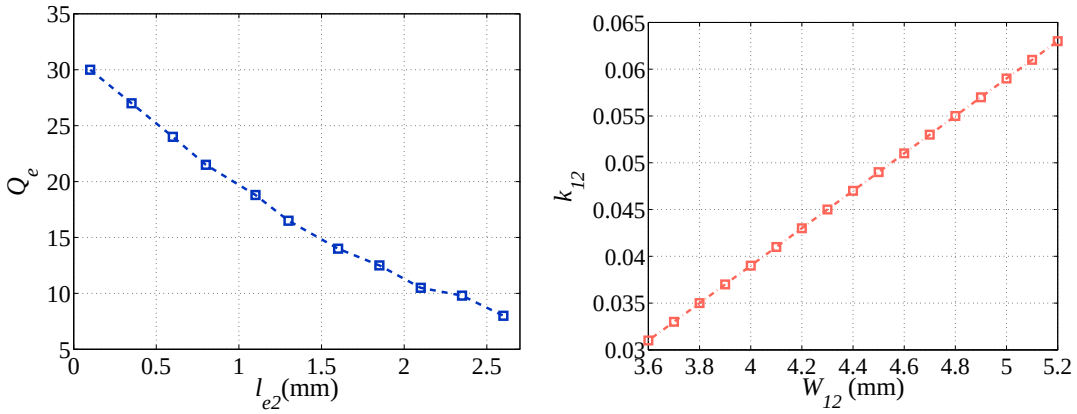

(a) (b)

Figure 2.30: (*a*) Q_e as a function of the slot length l_{e2} of the input/output CPW-to-SIW transition with 90° bend slots.(*b*) k_{12} versus iris width W_{12}.

Then, the external quality factor has been estimated from the group delay of the reflected response of a singly-loaded cavity using full-wave EM simulations, as it has been explained previously. For a given CPW-to-SIW transition with 90° bend slots, the length l_{e2} of the slots is modified in order to increase the coupling. The inter-resonator coupling coefficient has been also obtained from the reflected response of two coupled loaded cavities, and it has been obtained as a function of the iris width W_{12}. The Q_e and k_{12} curves for the designed coaxial SIW filter can be seen in Fig. 2.30.

The filter was fabricated in a 1.524 mm-thick Rogers R4003C substrate ($\epsilon_r = 3.55 \pm 0.05$, $\tan\delta = 2.7 \times 10^{-3}$@10 GHz) using standard single-layer PCB processing technology (see Fig. 2.31). Filter size is 8×17.7 mm^2 (i.e. $0.5 \times 1.1\,\lambda_g^2$ and $0.26 \times 0.58\,\lambda_0^2$), while the

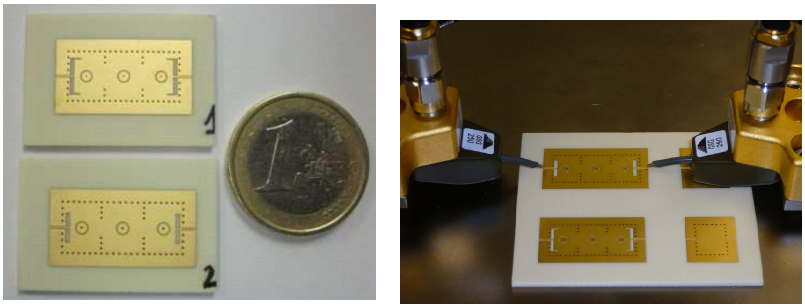

(a) (b)

Figure 2.31: (*a*) Photo of the fabricated 5% FBW 3-pole Chebyshev filter.(*b*) Photography of the fabricated filter during measurements.

equivalent conventional SIW filter would require about 12×36 mm^2 (i.e. $0.4 \times 1.18\,\lambda_0^2$) for square cavities using the TE_{101} dominant mode.

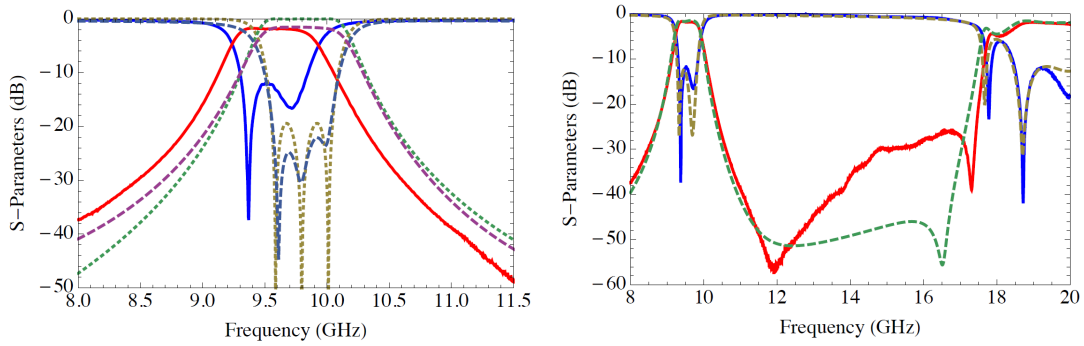

(a) (b)

Figure 2.32: (*a*) Measured (*solid*), simulation (*dashed*) and synthesized (*dotted*) response of the 5% FBW 3-pole Chebyshev filter.(*b*) Measured (*solid*) and simulated (*dashed*) wide-band response of the fabricated 3-pole SIW filter considering the metallization thickness of top and bottom metal layers.

The device was measured using a network analyzer on a probe station with GSG-250 pitch probes, and S-parameters were re-normalized to the port impedance of 65 Ω. The simulated response together with the measured results can be seen in Fig. 2.32(*a*)-(*b*), showing mid-band insertion losses of 1.7 dB with measured 1-dB bandwidth of 5.8%. The filter pass-band has shifted towards lower frequencies, because the thickness of the SIW metallization associated to the parallel-plate capacitance has not been initially included in the 3D EM simulations, thus the fringing fields at the edges of the metal layer were not taken into account. The thickness of the metallization has been measured and incorporated into the EM simulations, showing excellent agreement with the measurements as can be seen in Fig. 2.32(*b*). Wide-band response of the filter shows a spurious-free band of almost one octave with a rejection level better than 30 dB up to 17 GHz.

2.6.2 Example: X-band Filter in LTCC technology

The second coaxial SIW filter shown in this section is a 2-pole Chebyshev filter that has been designed, fabricated and measured in an 8-layer LTCC stack-up [87]. The

LTCC tape used in this design was the Heraeus HL2000 substrate [88] ($\epsilon_r = 7.4 \pm 0.2$, $\tan\delta = 2.6 \times 10^{-3}$@2.5 GHz), and conductive pastes based on silver (Ag) metallization system has been used in the LTCC fabrication process. The un-fired thickness of the layers employed is 0.134 mm, with a fired thickness of 0.091 mm that results in a total thickness of the fired 8-layer substrate of 0.73 mm.

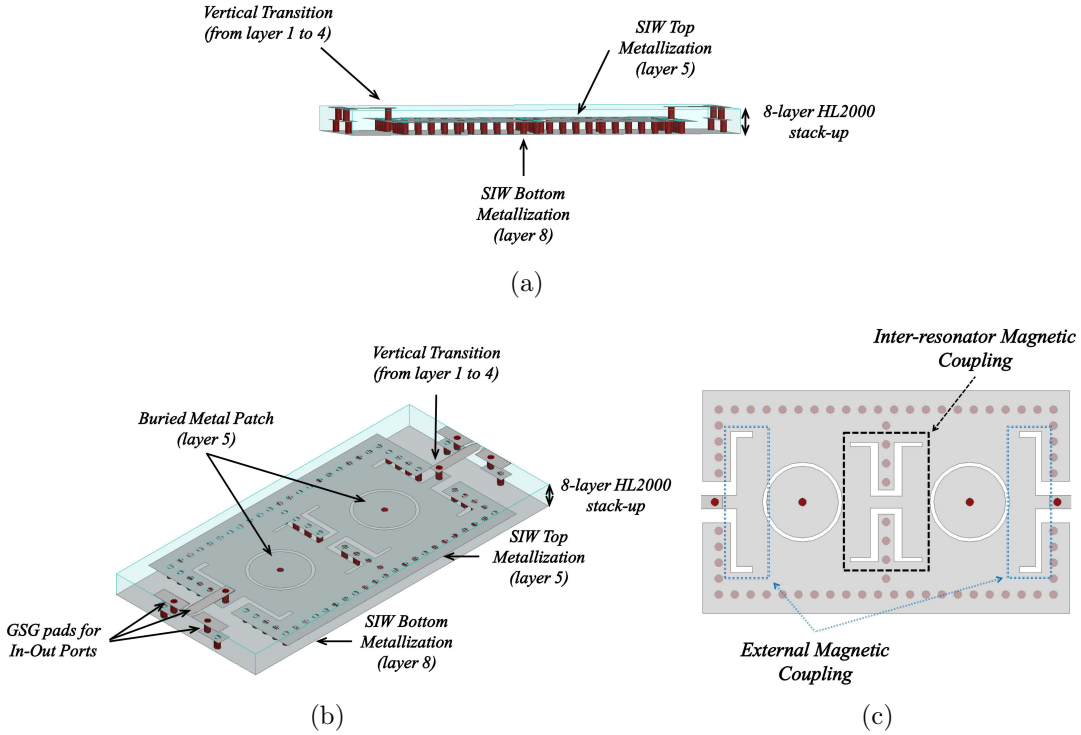

Figure 2.33: (a) Lateral view of the proposed embedded coaxial SIW filter where the scheme of the microstrip-to-coplanar transition can be observed. (b) Structure of the 2-pole coaxial filter in LTCC. The coupling between resonators is obtained through coplanar current probes created on the post-wall iris. (c) Inter-resonator and external coupling mechanisms created at the buried SIW top metallization.

The use of the LTCC technology allows us to create embedded coaxial SIW cavity resonators as it is shown in Fig. 2.33. Thus, the top metal layer of the coaxial SIW structure is moved from an external layer to an internal layer of the LTCC stack-up, and hence the capacitive patch is completely covered by dielectric material. In this specific design, the coaxial resonators are created between layer 5 and 8 (i.e. external bottom layer). Between layer 1 (i.e. external top layer) and 4, a vertical transition consisting on a single plated via is created in order to access the buried cavities. This transition has been designed to match the external microstrip input/output to the buried CPW line. Ground-Signal-Ground (GSG) pads have been inserted at the external top metallization of layer 1 in order to enable the device's measurement using a probe station.

The proposed solution shows the advantages of the LTCC technology in terms of miniaturization and Q-factor compared to other traditional approaches in multi-layer technology. In order to validate the concept, a single resonator has been designed at 11.5 GHz, and its f_0 and Q_u have been studied as a function of C_l. These variations have been obtained modifying the spacing gap s_p of the circular capacitive patch, while its radius has been fixed to $r_p = 0.9$ mm.

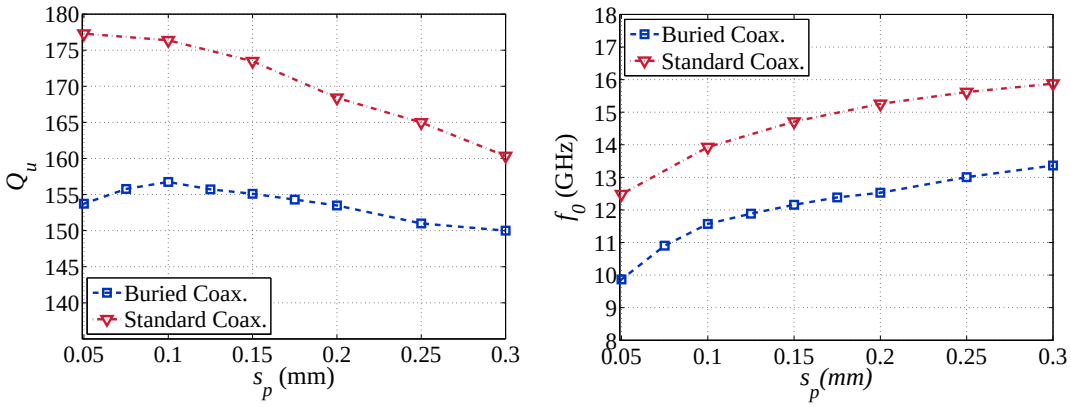

(a) (b)

Figure 2.34: (a) Unloaded Q_u of an embedded SIW resonator as a function of the disk isolating gap s_p.(b) Resonant frequency of an embedded SIW resonator as a function of s_p. The radius of the circular disk has been kept constant at 0.9 mm.

Fig. 2.34 shows the comparison of performance for the proposed embedded coaxial SIW resonator against those of a standard coaxial approach having same size and same substrate, which instead presents the loading capacitance in the external top metal layer, as shown in previous sections. As can be seen, Q_u is approximately constant about 150 in the frequency range $8.5 - 12.5$ GHz.

The embedded solution shows lower f_0 and constant Q_u over frequency with respect to the standard solution. It is clear that C_l increases its value when embedded because fringing fields are induced only inside the dielectric material, and not in the air surrounding the gap as in the case of standard coaxial SIW resonators. Indeed, this is the reason for which a slight degradation of the Q_u of the embedded solution can be observed in Fig. 2.34 with respect to the standard solution. In spite of the Q-factor degradation, this solution presents advantages in terms of reduced radiation effects of the isolating gap, and above all it makes for increased filter miniaturization since more loaded configurations can be easily implemented.

2.6.2.1 Filter Design

The synthesized 2-pole filter is centered at 10.75 GHz with 4.3% 1-dB FBW and return losses higher than 15 dB, and it consists of two square SIW cavities coupled through inductive post-wall irises created on the adjacent cavity walls. For increasing the inter-resonator coupling level, CPW probes have been introduced at the internal top metal layer of the SIW structure, as it is presented in Section 2.3.1. The external coupling is generated by the magnetic topology of Section 2.4.1, which is composed of the CPW-to-SIW transition with 90° bend slots. Regarding the size of the via holes used for the square cavity resonator, the diameter and center-to-center spacing have been chosen as 0.2 and 0.4 mm, respectively.

The resonator slope parameter has been set to $b = 59.7$ mS that gives a $C_l = 0.87$ pF while $Z_0 = 74.9\,\Omega$. As mentioned, the inner via diameter is $d_v = 0.2$ mm, so the SIW resonator cavity size is $w_{siw} \times l_{siw} \times h = 5.6 \times 5.6 \times 0.73$ mm^3 (i.e. $0.54 \times 0.54 \times 0.07\,\lambda_g^3$ and $0.2 \times 0.2 \times 0.026\,\lambda_0^3$). Finally the circular patch radius r_p has been set to 0.9 mm with a spacing gap of $s_p = 0.1$ mm. The total size of the filter including the microstrip-to-CPW

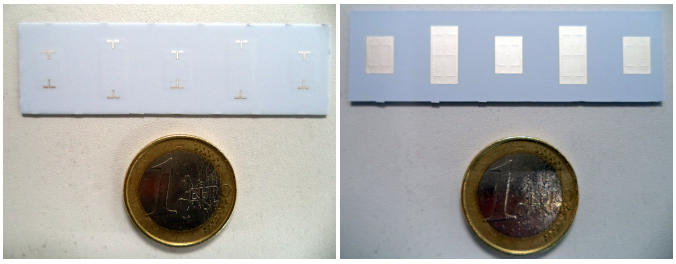

(a)

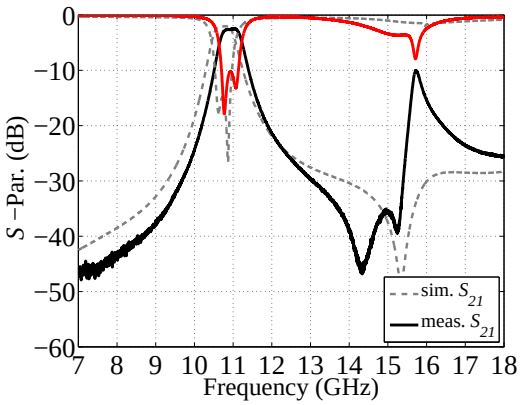

(b)

Figure 2.35: (*a*) Photo of the fabricated 2-pole coaxial SIW filter, where (*Left*) and (*Right*) are top and bottom views, respectively.(*b*) Measured (*solid*) and simulated (*dashed*) wide-band response of the fabricated 2-pole SIW filter.

transition is only 5.6×11.8 mm^2 (i.e. $0.54 \times 1.15\,\lambda_g^2$ and $0.2 \times 0.42\,\lambda_0^2$) showing a very compact size.

The filter has been measured using a network analyzer on a probe station with GSG-250 pitch probes. The simulated and measured results of the SIW filter are shown in Fig. 2.35. A return loss value better than 10 dB is achieved, while the measured in-band insertion loss is 2.5 dB. The measured 1-dB FBW is 4.2%, which is almost the same as the designed value.

It is worth to mention that filter insertion losses have increased from a simulated value of 2 dB to a measured value of 2.5 dB. Seeing that, the degradation of the resonator Q_u could rely upon the properties of the conductive paste materials that have been used for the via filling and screen printing steps. From measured results, Q_u has been estimated to be 120 instead of 150. Finally, the frequency shift of the filter pass-band is around 250 MHz towards higher frequency (i.e from 10.75 GHz to 11 GHz), which corresponds to 1.5%. Basically, this shift can be attributable to different factors that concerning the LTCC process. Among them, the most relevant effects are: the fabrication tolerances of the conductor printing process (which could generate a variation in the spacing gap widths), or the LTCC tape shrinkage variation in Z-axis from green state to fired state that alters the final stack-up thickness.

Chapter 3

Advanced Filtering Responses

Wireless communication systems are imposing increasingly stringent requirements for selectivity and in-band insertion loss of RF and microwave filters [8]. The efficient use of the frequency spectrum demands advanced filtering responses, in order to minimize the inter-channel guard bands and to enable the co-existence of different applications, standards and regulations in close proximity. The technique of using cross-couplings to produce asymmetric frequency responses and to produce TZs has become popular in order to satisfy these demands.

In this chapter, some advanced filtering responses in coaxial SIW technology are presented using rectangular or circular combline resonators, thanks to the use of the different coupling structures proposed in Chapter 2, which can be used for implementing out-of-phase couplings and cross-coupling of non-adjacent resonators. In the following, a broad description of the design, fabrication and measurements of such novel SIW filters will be shown.

3.1 Trisection Coaxial SIW Filter

The first advanced filtering response in coaxial SIW technology that will be studied is a Chebyshev-response tri-section filter centered in the Wireless Local Area Network (WLAN) applications, especially between $5.15 - 5.35$ GHz [89]. The proposed filter implements a cross-coupled tri-section topology, which allows to add a TZ at the upper-side in order to reject strong interferes, as it is requested for WLAN applications.

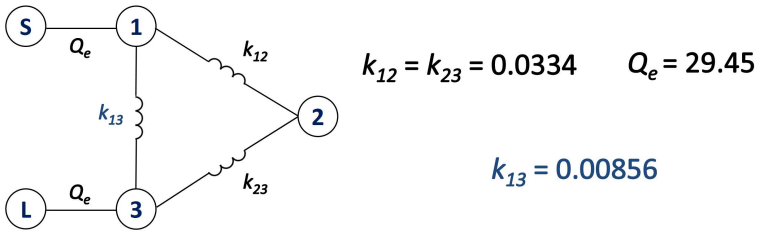

Figure 3.1: Multipath coupling diagram for the cross-coupled trisection filter.

The coupling scheme of the triplet filter topology is given in Fig. 3.1. There is a unique cross-coupling between resonators 1 and 3, termed k_{13}, while the other inter-resonator couplings are k_{12} and k_{23}. This configuration is particularly interesting because it improves the selectivity generating a TZ located above or below the filter passband,

depending of the sign of the cross-coupling. If the sign of k_{13} is the same as the direct ones, a TZ appears at the upper-side of the passband. On the contrary, if the sign is opposite, the TZ appears at the lower-side [10]. As it was previously mentioned in Section 1.2.1, in [20], the authors demonstrated the trisection topology in circular SIW technology, especially for operation at higher frequency bands. In fact, the filter response in [20] presents a TZ located at 14.15 GHz, which is 150 MHz below the bandpass centered at 14.3 GHz. The TZ is generated by a controllable mixed electric and magnetic cross-coupling, which uses an embedded short-ended strip line combined with a conventional post-wall iris.

3.1.1 Filter Design

The proposed trisection filter in coaxial SIW technology has been designed to have a centre frequency of 5.25 GHz with an equi-ripple bandwidth of 200 MHz (i.e. $FBW = 3.8\%$), resulting in a passband between 5.15 and 5.35 GHz. That means the filter is covering the low power Unlicensed National Information Infrastructure (U-NII)-1/2 bands, and the introduction of a transmission zero located above the passband would be of great interest for improving the rejection of the upper 5 GHz WLAN sub-bands.

In fact, in the particular case of 5-GHz WLAN applications, which are becoming more extended in short-range high-speed wireless digital communications, the allocated spectrum is divided into four different sub-bands. The 802.11a standard requires transmitter power control in order to minimize adjacent cells interference and provide the devices with longer battery life. The devices operating at lower power bands from $5.15-5.35$ GHz (i.e. U-NII-1/2) are devoted mostly to in-door applications while nearby frequency bands from $5.47-5.825$ GHz, which are named U-NII-2e and U-NII-3, make for up to 1 W of transmitted power. Thus, in the U-NII-a1/2, there is a need for filtering topology providing high rejection of interferences that could come from the close U-NII-2e/3 bands.

Therefore, the same coupling structure has been used for both the direct and the cross paths, allowing the introduction of a TZ at 5.65 GHz (i.e. 300 MHz above the passband) in order to obtain more than 30 dB of isolation in the corresponding U-NII-2e/3 frequency bands. The specifications in terms of rejection for the upper 5-GHz sub-band is usually higher than 30 dB, while the in-band return loss has to be lower than 15 dB.

Concerning the design procedure, the trisection Chebyshev filter has been synthesized by optimization, using a circuital simulator. Thus, the value of the J_{13} inverter and the resonant frequencies of each resonator can be easily obtained from the targeted asymmetric response, using as initial point the response of a direct-coupled Chebyshev 3-pole filter centered at 5.25 GHz. Although analytical expressions of the coupling matrix for a trisection filter can be obtained, the optimization-based approach enables us to include more general design goals without requiring extensive computation times.

Moving to the filter properties, the characteristic admittance of the circular coaxial SIW resonators is $Y_0 = 8.04$ mS, which results in a cavity diameter $r_{siw,i} = 10$ mm (for $i = 1, 2, 3$) having an inner via hole diameter $d_v = 0.4$ mm. These values give a susceptance slope parameter of $b = 25.47$ mS and a loading capacitance for the resonators $C_l = 0.75$ pF. The admittance inverters can be obtained from the low-pass prototype coefficients of the 3-pole Chebyshev filter with 0.1 dB of in-band ripple using the well-known expressions of [8].

In the proposed filter, these values are $J_{0,1} = J_{3,4} = 4.34 \times 10^{-3}$ S and $J_{1,2} = J_{2,3} = 8.04 \times 10^{-4}$ S. Using the former values as an initial guess, and starting with a weak cross-

coupling level, an optimization procedure of the equivalent circuit has been carried out. From the synthesized values of the resonators and inverters, a first dimensioning of the trisection filter can be performed, and then a fine tuning of each parameter is carried out using the group delay method [90].

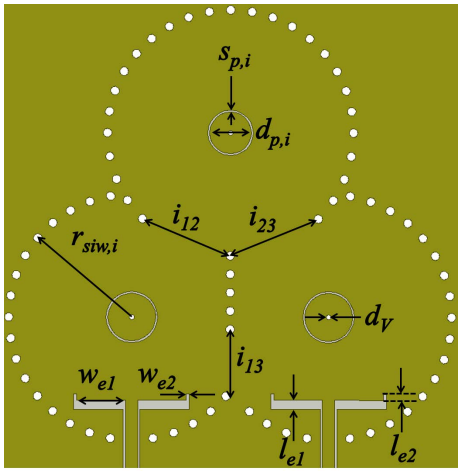

Figure 3.2: Top view of the proposed cross-coupled trisection SIW filter, showing its main dimensions.

For controlling the external quality factor, the width and length of the 90° bend slots of the CPW-to-SIW transition have been modified for obtaining the targeted coupling level. Following the same procedure, the direct inter-resonators couplings between resonators 1 and 2 (and between resonators 2 and 3) have been adjusted by changing the width of the magnetic post-wall irises i_{12} (and i_{23}). Then, the loading capacitance of the resonators are adjusted in order to obtain the required group delay value while keeping the symmetry around the centre frequency.

Starting with a weak coupling level, the magnetic cross-coupling between resonators 1 and 3 is progressively increased by widening the iris i_{13} in order to set the TZ frequency. The resonant frequencies of the resonators are modified at the same time in order to keep the in-band response. Due to the asymmetric response, the resonators are not synchronously tuned, and the optimized values for the loading capacitance of the three resonators are $C_{l,1} = C_{l,3} = 0.7498$ pF and $C_{l,2} = 0.7401$ pF. Moreover, the final values of the inverters are $J_{0,1} = J_{3,4} = 4.376 \times 10^{-3}$, $J_{1,2} = J_{2,3} = 8.828 \times 10^{-4}$, and the inter-resonator coupling is $J_{1,3} = 2.181 \times 10^{-4}$.

3.1.2 Experimental Results

The filter has been fabricated in a 1.524 mm-thick Rogers R4003C substrate ($\epsilon_r = 3.55 \pm 0.05$, $\tan\delta = 2.7 \times 10^{-3}$@10 GHz) with 17/17 μm Cu clad, using standard single-layer PCB processing technology and Electroless Nickel Immersion Gold (ENIG) finishing. The latter is a type of surface plating widely used for printed circuit boards. It consists of an electroless nickel plating covered with a thin layer of immersion gold, which protects the nickel from oxidation. Previous to the gold covering, the nickel is deposited on the palladium-catalyzed copper surface by means of an auto-catalytic process, which is called electroless nickel step.

The trisection filter consists on three circular coaxial SIW cavity resonators coupled by means of post-wall irises, including the one for the cross-coupling. These have been

Table 3.1: Dimensions of the coaxial SIW cross-coupled trisection filter. (Units: mm)

r_{siw1}	10	r_{siw2}	10	r_{siw3}	10
d_{p1}	3.89	d_{p2}	3.4	d_{p3}	3.89
s_{p1}	0.15	s_{p2}	0.15	s_{p3}	0.15
d_{siw}	0.7	d_v	0.4	p_{siw}	1.8
i_{12}	8	i_{23}	8	i_{13}	5.5
w_{e1}	3.95	w_{e2}	0.25	h	1.524
l_{e1}	0.18	l_{e2}	0.5	t	0.017

opened on the adjacent walls between the circular resonators. The use of circular cavities permits us to intersect cavities each other, thus reducing the whole size of the filter. The layout of the proposed filter with its main dimensions is shown in Fig. 3.2, while the final values are reported in Table 3.1. The trisection filter size is 36.7×37.35 mm^2 (i.e. $1.21 \times 1.23\ \lambda_g^2$ and $0.64 \times 0.65\,\lambda_0^2$), while the equivalent conventional SIW filter would require about 42×42.75 mm^2 (i.e. $0.74 \times 0.75\,\lambda_0^2$) for circular cavities based on the TM_{010} fundamental mode. This means that the coaxial SIW trisection filter shows a 24% of area reduction if compared with a conventional SIW implementation.

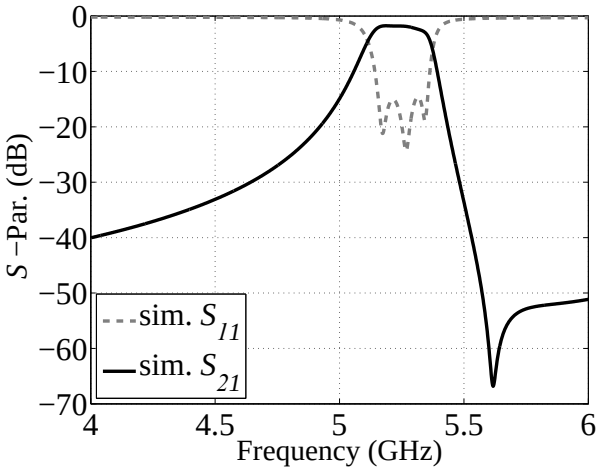

Figure 3.3: Simulated S_{21} and S_{11} parameters of the cross-coupled trisection filter.

Full-wave EM simulations of the optimized trisection filter are shown in Fig. 3.3. The insertion loss is estimated to be around 1.5 dB at the centre of the pass-band, while the in-band return loss is better than 16 dB. The transmission zero is located at 5.61 GHz providing rejection better than 30 dB from 5.48 GHz, so both U-NII-2e/3 bands are completely covered and typical rejection specifications are satisfied.

A picture of the fabricated prototype is shown in Fig. 3.4-(a), while the measured S-parameter responses of the designed trisection filter can be seen in Fig. 3.4-(b). The filter response presents a 3-dB bandwidth of 260 MHz, around 5.3 GHz. Thus, there is a frequency shift of about 70 MHz to higher frequencies of the filter passband, due to the variation of the galvanization process used in the through-hole plating process that affects the total metal layer thickness. Above all, the frequency shift can be mainly related to the variation of isolating gap widths of the capacitive patches, and especially to implementation of wider gaps than required.

It is worth mentioning that the frequency shift worsens the rejection provided by the filter in the U-NII-2e band (i.e. 5.470-5.725 GHz), which is now higher than the required value only as of 5.58 GHz (i.e. $S_{21} < -30$ dB).

Nevertheless, the measured response is quite promising showing insertion losses around 1.8 dB at mid-band, just 0.2 dB more than expected, with return losses better than 17 dB in the filter passband. Note that the use of ENIG finishing is related to the increase of the filter IL due to the deposition of the nickel layer that does not show good conductor properties.

Finally, the TZ can be clearly seen at 5.68 GHz providing rejection higher than 40 dB on the U-NII-3 band (i.e. 5.725-5.825 GHz), and better than 30 dB up to 7.5 GHz.

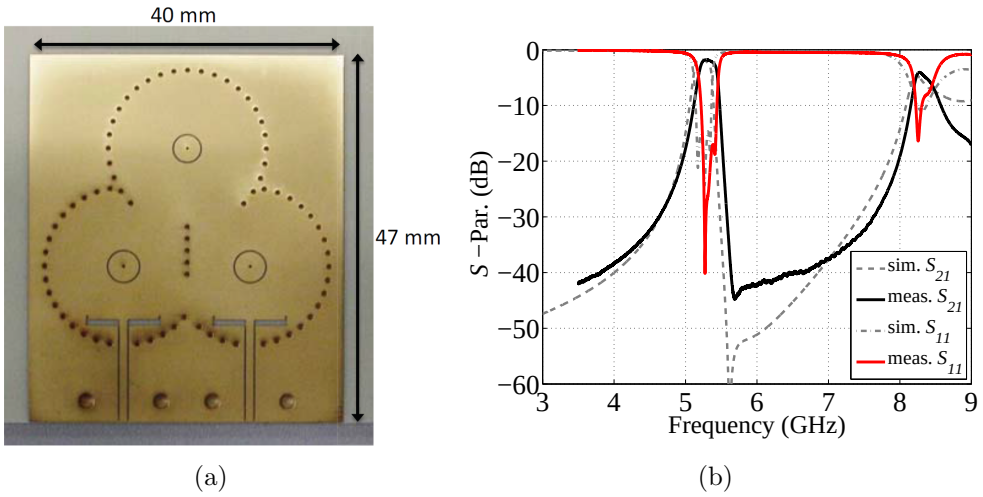

(a) (b)

Figure 3.4: (*a*) Photo of the fabricated cross-coupled trisection filter in coaxial SIW topology. (*b*) Measured (*solid*) and simulated (*dashed*) wide-band frequency response of the fabricated filter.

3.2 Coaxial SIW Diplexer

Following the previous approach for the design of advanced filtering structures, and employing the electric coupling between coaxial SIW resonators that has been introduced in Section 2.3.2, the design of an SIW diplexer is now demonstrated [91]. The diplexer is based on coaxial SIW triplet blocks, which now implement magnetic and electric couplings for the cross-couplings, and hence having TZs placed below and above the passband. Indeed, this solution allows us to change the location of the TZs with respect to the passband depending on the sign of the cross-coupling.

Therefore, magnetic and electric cross-couplings are now implemented in circular triplet sections, in order to achieve high rejection in compact diplexers with narrow inter-channel separation. It has been shown in Section 2.3.2 that electric coupling can be easily introduced in a single side of the structure, thus alleviating problems derived from the common approach in conventional SIW filters that require slots at both sides of the substrate, as demonstrated among others in [17]. So, the proposed approach maintains the advantage of a low cost single-layer PCB process, and it does not need multi-layer processes.

In this specific design, the objective is to develop a highly compact implementation of an SIW diplexer in a low-cost 1.524 mm-thick PCB substrate based on circular coaxial

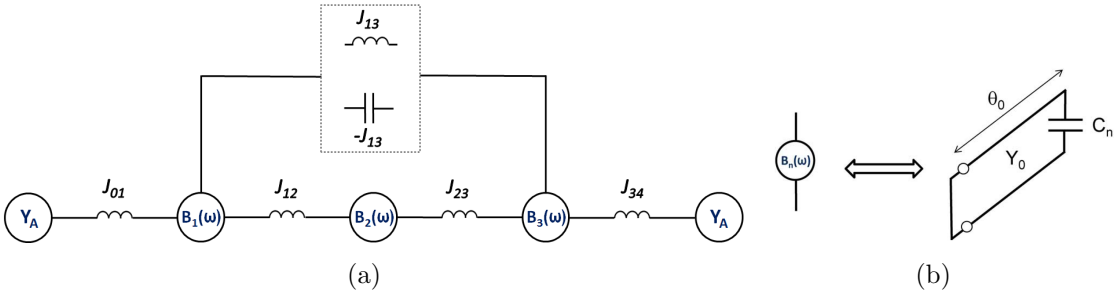

(a) (b)

Figure 3.5: (a) Equivalent circuit of the coaxial substrate integrated waveguide (SIW) triplet, and (b) equivalent circuit of the coaxial SIW resonator.

SIW resonators. The diplexer has been designed to be centered at X-band having channel centre frequencies at 9.5 GHz and 10.5 GHz, respectively, and absolute bandwidths of 400 MHz. That means the lower channel filter presents a FBW= 4.21%, while the upper channel filter FBW is 3.81%. The TZs are located at 10.2 GHz and 9.8 GHz in order to achieve high rejection level at the opposite channel band. Fig. 3.5 shows the equivalent circuit of each triplet.

3.2.1 Electric Cross-Coupling

In order to improve rejection between channels, two TZs will be generated in correspondence with the channel passbands, one for each triplet block. Thus, the lower-band channel introduces a TZ at the upper-side. This can be done using a magnetic cross-coupling between resonators 1 and 3, as it has already been demonstrated in the previous Section 3.1.

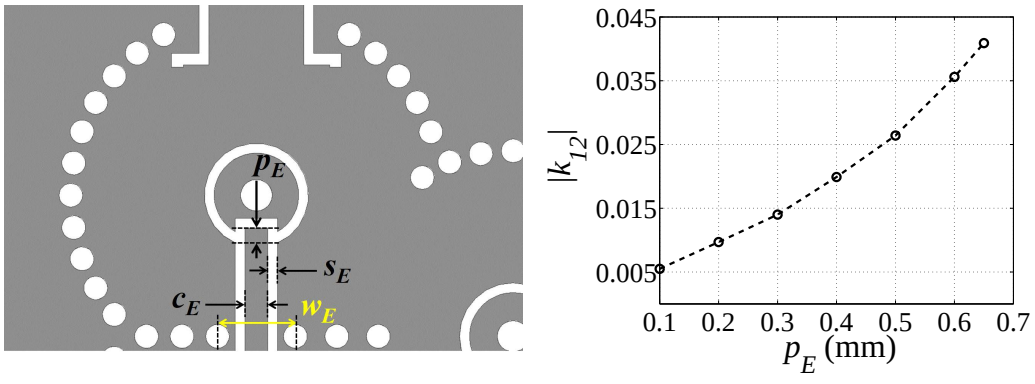

(a) (b)

Figure 3.6: (a) Structure of the electric coupling between coaxial SIW resonators. (b) Coupling coefficient $k_{i,i+1}$ variation versus CPW probe insertion p_E on capacitive disks with $s_E = 0.15$ mm, $c_E = 0.6$ mm. The post-wall iris width is $w_E = 1.4$ mm.

On the contrary, the upper-band filter introduces a TZ at the lower-side by means of an electric electric coupling between resonators 1 and 3. This novel electric cross-coupling is achieved using an open-ended capacitive probe located at the top side of the substrate, entering the loading capacitive disk of each resonator. Note that the probe passes through an iris window created between the shared resonator wall of the non-contiguous resonators, as Fig. 3.6-(a) shows.

Due to the mixed character of this coupling, the electric or magnetic contribution can be controlled by changing the probe dimensions (i.e. penetration p_E, conductor width c_E and isolating spacing s_E) and/or the post-wall iris width w_E. The mixed coupling is dominated by the electrical contribution for a given probe penetration when the iris width is reduced. As previously explained, the insertion of the probe inside the resonator capacitive patch is the main parameter for controlling the magnitude of the inter-resonator coupling. The behavior of $k_{i,i+1}$ as function of p_E for this particular coaxial SIW topology is shown in Fig. 3.6-(b), which considers two coupled interleaved circular resonators implemented on a substrate Rogers R4003C having thickness $h = 1.524$ mm.

3.2.2 Channel Filter Design

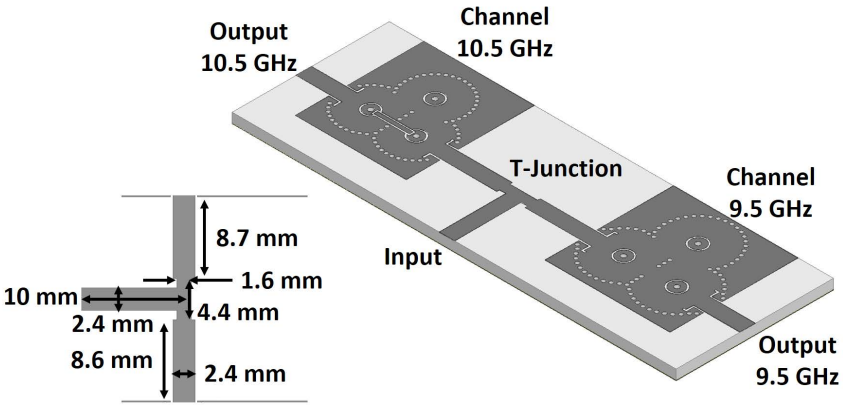

Figure 3.7: Scheme of the proposed diplexer using substrate integrated triplets in coaxial SIW topology.

The diplexer structure is composed of two channel filters connected to a common input port through a microstrip T-junction, as it is shown in Fig. 3.7. The filters are independently designed using again three interleaved circular substrate integrated coaxial resonators. Moving to the filter synthesis, the procedure starts by setting the slope parameter b of the basic cell at the centre frequency of each filter, which is $b = 20$ mS in this design. Then, the impedance of the coaxial resonator and the ratio between the inner via d_v and the outer via wall diameter $(2 \cdot r_{siw})$ are obtained from the expressions of the susceptance slope parameter and of the impedance of a circular-circular coaxial transmission line, respectively. Thus, these values are obtained using the following equations

$$Z_0 = \left(\frac{\cot \theta_0 + \theta_0 \csc^2 \theta_0}{2b} \right) \tag{3.1}$$

$$\frac{2 \cdot r_{siw}}{d_v} = 0.9268 \cdot e^{\frac{Z_0 \sqrt{\epsilon_r}}{60}} \tag{3.2}$$

It is worth to mention that the physical length for all resonators is always the same, because it corresponds to the substrate thickness. However, due to the different channel centre frequencies, the values of the electrical length are $\theta_{0,l} = 32.73°$ and $\theta_{0,u} = 36.18°$ for the low-band and up-band channel filters, respectively. For these values, we obtain

that the values of the coaxial resonator impedances are $Z_{0,l} = 87.75\,\Omega$ and $Z_{0,u} = 79.48\,\Omega$, corresponding to the following relations

$$\left(\frac{2 \cdot r_{siw}}{d_v}\right)_l = 14.60 \tag{3.3}$$

$$\left(\frac{2 \cdot r_{siw}}{d_v}\right)_u = 11.24 \tag{3.4}$$

Finally, using a circuit-level optimization of both filters, the loading capacitance of each coaxial SIW resonator and the inverter values have been estimated. To do that, an initial guess considering under-coupled cross-couplings and synchronous resonators is used, forcing a symmetrical filter topology. The values of the loading capacitances $C_{l,i}$ and inverters $J_{i,i+1}$ for the lower and upper filter are reported in Table 3.2.

Table 3.2: Properties of the channel SIW filters of the diplexer.

$C_{l1,l}$	0.283 pF	$C_{l1,u}$	0.273 pF
$C_{l2,l}$	0.270 pF	$C_{l2,u}$	0.276 pF
$C_{l3,l}$	0.283 pF	$C_{l3,u}$	0.273 pF
$J_{01,l}$	$3.65 \cdot 10^{-3}$ S	$J_{01,u}$	$3.62 \cdot 10^{-3}$ S
$J_{12,l}$	$6.51 \cdot 10^{-4}$ S	$J_{12,u}$	$6.5 \cdot 10^{-4}$ S
$J_{23,l}$	$6.51 \cdot 10^{-4}$ S	$J_{23,u}$	$6.5 \cdot 10^{-4}$ S
$J_{34,l}$	$3.65 \cdot 10^{-3}$ S	$J_{34,u}$	$3.62 \cdot 10^{-3}$ S
$J_{13,l}$	$1.64 \cdot 10^{-4}$ S	$J_{13,u}$	$-1.49 \cdot 10^{-4}$ S

Thus, the channel filter layouts have been obtained from the previously optimized equivalent circuit of each channel. Starting from the basic resonator cell, inner via diameter has been fixed to $d_v = 0.8$ mm and the radius of the SIW circular cavity can be easily derived from 3.1 and 3.2. Then, $C_{l,i}$ values have been adjusted by changing the diameter d_p of the circular loading patch for a particular resonant frequency, while its annular gap $s_{p,i}$ has been fixed at 0.25 mm.

Input and output couplings and magnetic inter-resonator couplings have been implemented following the approach of the previous triplet filter, thus using 90° bend slots of the coplanar waveguide-to-SIW transition and magnetic post-wall irises, respectively. Fig. 3.8 shows variations of Q_e and $k_{i,i+1}$ as function of the bend slot length and the iris width, respectively, for these specific resonator configurations.

The design procedure starts with the values obtained from the equivalent circuit and using the former design curves for Q_e and $k_{i,i+1}$, followed by a final refinement using 3-D full-wave analysis. Concerning the cross-couplings, a weak coupling level has been initially set in both channel filters. Then, the electric and magnetic cross-coupling between resonators 1 and 3 are progressively increased in the two filters to center the respective TZs at the desired frequencies.

In the lower channel filter, the cross-coupling is controlled by changing the magnetic iris width i_{13}. On the contrary, in the higher channel filter, the TZ position has been controlled by increasing the penetration p_E of the capacitive probe. In the meantime, the resonant frequencies of the resonators are modified adjusting the patch diameter $d_{p,i}$ to maintain a proper in-band response.

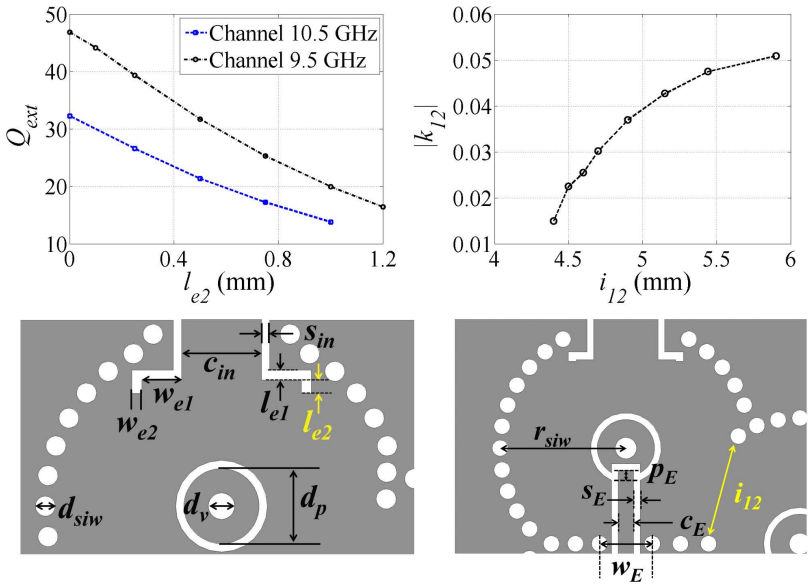

Figure 3.8: Q_e and $k_{i,i+1}$ as a function of (*left*) the coplanar current probe length l_{e2} inside the cavity and of (*right*) the iris width i_{12}, respectively.

Table 3.3: Dimensions of the coaxial trisection filter - 9.5 GHz channel. (Units: mm)

$r_{siw,l1}$	5.25	$r_{siw,l2}$	5.25	$r_{siw,l3}$	5.25
$d_{p1,l}$	2.27	$d_{p2,l}$	2.29	$d_{p3,l}$	2.27
$s_{p1,l}$	0.25	$s_{p2,l}$	0.25	$s_{p3,l}$	0.25
d_{siw}	0.7	d_v	0.4	p_{siw}	1.8
$i_{12,l}$	4.55	$i_{23,l}$	4.55	$i_{13,l}$	2.75
$w_{e1,l}$	1.15	$w_{e2,l}$	0.3	h	1.524
$l_{e1,l}$	0.3	$l_{e2,l}$	0.35	t	0.017

Finally, Fig. 3.9-(a) shows detailed views of the channel coaxial SIW filters highlighting their main dimensions, which are also reported in Tables 3.3 and 3.4. The synthesized and the optimized simulated responses for the channel filters are depicted in Fig. 3.9-(b), showing a very good agreement with the synthesized responses even if the latters do not consider losses.

A simple T-junction has been designed for the common port. Thus, an open-circuit condition has been forced at the junction for the opposite channel filter in order to improve isolation, and minimize channel filter interaction. Therefore, given the input impedance $Z_{in,\{l,u\}}(f)$ of each filter seen from the junction reference plane, a section of transmission line has been added in order to force the following conditions, while keeping the matching condition at the centre frequency of each channel filter

$$Z_{in,l}(f_{0,u}) = \infty \tag{3.5}$$

$$Z_{in,u}(f_{0,l}) = \infty \tag{3.6}$$

Additionally, a small step in width on the microstrip T-junction ports has been added for compensating the direct discontinuity. Lastly, the T-junction dimensions have been

Table 3.4: Dimensions of the coaxial trisection filter - 10.5 GHz channel. (Units: mm)

$r_{siw,u1}$	4.7	$r_{siw,u2}$	4.7	$r_{siw,u3}$	4.7
$d_{p1,u}$	2.16	$d_{p2,u}$	2.2	$d_{p3,u}$	2.16
$s_{p1,u}$	0.25	$s_{p2,u}$	0.25	$s_{p3,u}$	0.25
d_{siw}	0.7	d_v	0.4	p_{siw}	1.8
$i_{12,u}$	4.1	$i_{23,u}$	4.1	w_E	1.97
$w_{e1,u}$	1	$w_{e2,u}$	0.3	h	1.524
$l_{e1,u}$	0.3	$l_{e2,u}$	0.05	t	0.017
s_E	0.25	c_E	0.57	p_E	0.41

optimized at circuital level without any change on the designed channel filters. The dimensions of the T-junction have already been shown in Fig. 3.7.

3.2.3 Experimental Results

The diplexer has been manufactured in 1.524 mm-thick Rogers 4003C with 17 μm/17 μm Cu clad using a standard single-side fabrication process. The 9.5 GHz-channel filter size is 18.7×19.5 mm^2 (i.e. $1.12 \times 1.16\,\lambda_g^2$ and $0.59 \times 0.62\,\lambda_0^2$), while the 10.5 GHz-channel filter size is 16.5×17.2 mm^2 (i.e. $1.08 \times 1.14\,\lambda_g^2$ and $0.58 \times 0.6\,\lambda_0^2$). The whole device dimensions are 58.4×18.7 mm excluding the microstrip feeding lines, which correspond to $3.67 \times 1.17\,\lambda_g^2$ and $1.95 \times 0.62\,\lambda_0^2$ at 10 GHz.

A photo of the fabricated device is shown in Fig. 3.10, together with the simulated and measured results, which have very good agreement. Note that the common input port is stated as port 1, the output of the lower channel as port 2 and the one of the upper channel as 3. As it can be seen, an additional TZ is obtained at the upper-channel filter (i.e. the standard TZ is located at 9.64 GHz and the additional one at 9.34 GHz) due to the cancellation of the electric and magnetic contribution of the mixed coupling between non-adjacent resonators. The TZs are now located at 9.64 GHz and 10.25 GHz providing more than 45 dB of rejection, respectively, for the upper and lower channels.

Table 3.5: Comparison Table Between References and Proposed SIW Diplexer

Ref.	**Size**	**IL(dB)**	**Rejection(dB)**	**Isol.**
[92]	$2.71 \times 3.35 \times 0.009\,\lambda_0^3$	2.6/3.2	55@5.42GHz / 55@5.96GHz	53dB
[93]	$0.27 \times 0.22 \times 0.008\,\lambda_0^3$	1.6/2.3	43@4.66GHz / 28@5.80GHz	32dB
[94]	$1.44 \times 0.98 \times 0.022\,\lambda_0^3$	2.2/2.4	22@7.75GHz / 22@8.25GHz	–
This	$1.95 \times 0.62 \times 0.053\,\lambda_0^3$	1.6/2.1	42@9.50GHz / 37@10.50GHz	35dB

The minimum insertion losses are $IL_{21,l} = 1.65$ dB and $IL_{31,u} = 2.12$ dB, while return loss at the common port is better than 10 dB in both cases. Stopband suppression for both channels is good, being better than 37.5 dB over the entire channel bandwidths. Concerning the isolation, a minimum value of S_{32} between the outputs of the channel filters of -34 dB has been measured, while between 9.6 GHz and 10.5 GHz the isolation is even better than 40 dB.

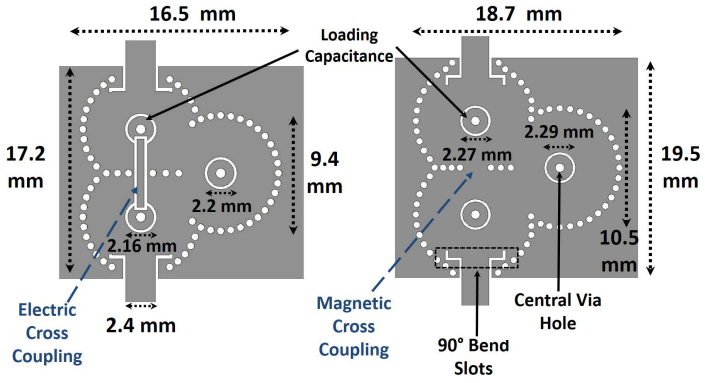

(a)

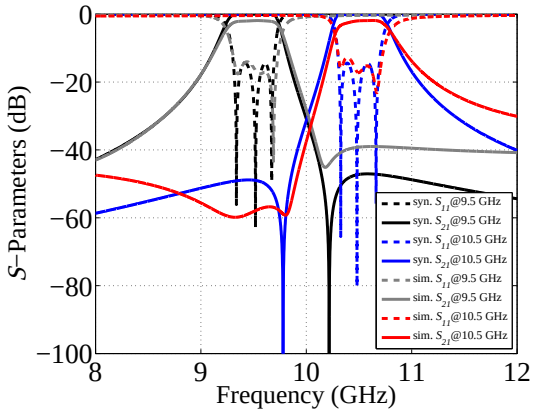

(b)

Figure 3.9: (*a*) Detail of the upper channel filter (*left*) and lower (*right*) channel filter. (*b*) Synthesized (black and blue lines) and simulated (grey and red lines) S_{11} and S_{21} parameters of the diplexer channel filters.

As Table 3.5 shows, the proposed approach for the design of SIW diplexers shows important advantages in terms of size reduction, while keeping good EM performance as well as high rejection levels. Looking at recent SIW diplexers [92–94], the solution proposed in [93] shows the highest miniaturization degree. This work is based on the application of CSRRs etched on the waveguide surface of the SIW, which allows high miniaturization even in the case of low-permittivity dielectric material.

Even in this case, the proposed coaxial topology permits a remarkable miniaturization when compared to standard SIW implementations, as the case of [92, 94]. In this context, a good compromise between high rejection and compact size has been accomplished thanks to the use of cross-coupling. For instance, by introducing TZs located at the opposite channel band, rejection levels that have been obtained are better than in [93, 94] without the need for higher channel filter order. To put it in context, in [92], a very high rejection has been achieved by using 5-pole SIW filters in both channel at the expense of compactness.

To sum up, this work presents good performance in terms of low losses, high rejection and isolation even for almost contiguous channels, while showing reasonable size compared to these other SIW structures.

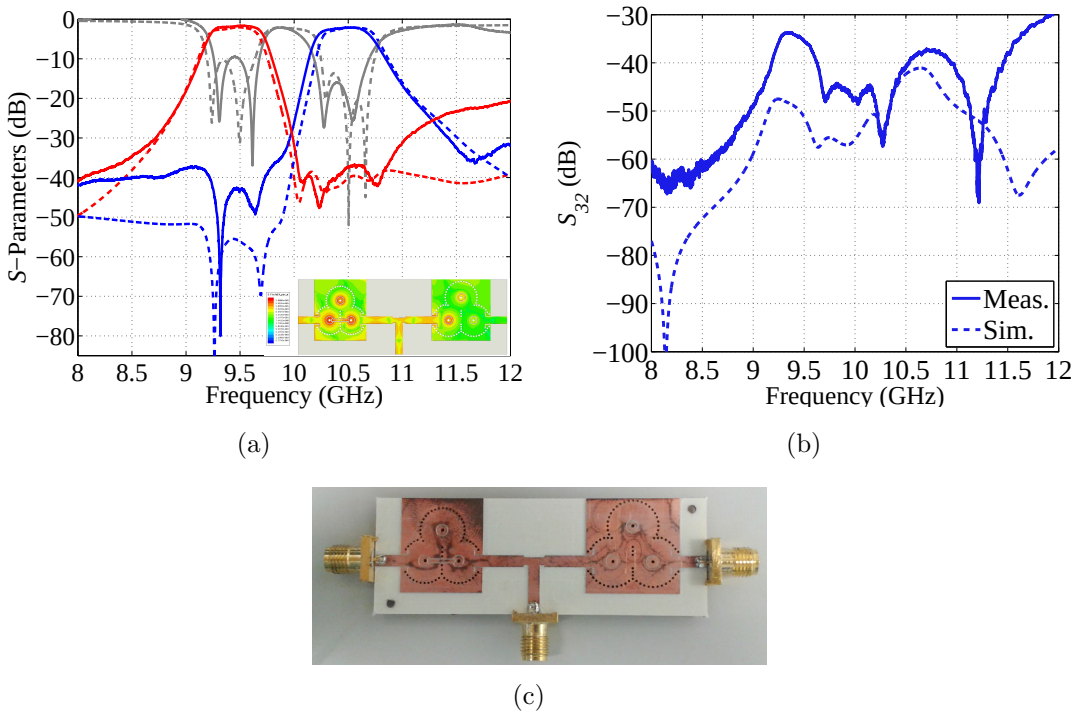

Figure 3.10: (*a*) Measured (*solid*) and simulated (*dashed*) S_{21}(*red*), S_{31}(*blue*) and S_{11}(*grey*) parameters of the diplexer. Electric field distribution at 10.5 GHz is also shown in the subfigure. (*b*) Isolation between lower channel and upper channel. (c) Photo of the fabricated diplexer in coaxial SIW topology.

3.3 Four-pole Quasi-Elliptic Coaxial SIW Filter

In this section, to demonstrate the flexibility of the proposed electric coupling, a 4-pole narrow-band combline SIW filter is designed to have a quasi-elliptic frequency response [86, 95]. The filter scheme is given in Fig. 3.11. This topology is particularly interesting because TZs are generated both above and below the filter passband when the cross-coupling k_{14} between resonators 1 and 4 is out of phase with the other couplings.

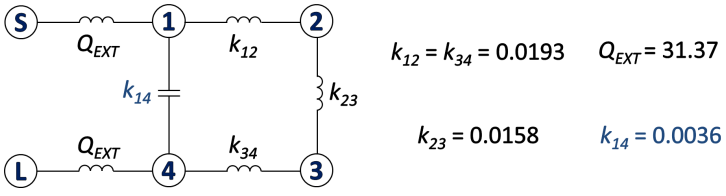

Figure 3.11: Multipath coupling diagram for the cross-coupled filter.

Additionally, a method for enabling SMD assembly of the coaxial SIW filters is developed and analyzed considering a PCB fabrication process. This solution shows promising results, having potential advantages in terms of design flexibility, size reduction, low loss and high planar integration.

3.3.1 Vertical Transition

For the SMD packaging of the coaxial SIW filter, connections must be provided to the filter input and output. The proposed approach provides the input/output ports with accesses by means of plated half-a-hole vias, resulting in a self-packaged solution. The proposed system is illustrated in Fig. 3.12, where a scheme of the filter mounted onto a carrier substrate and side views of the vertical transition structure are shown. The bottom layer will interface between the carrier board and the packaged filter through a vertical pseudo-CPW structure. As it is well known, CPW is a very versatile structure that allows for easy matching of line impedance by setting its design parameters. Specifically, these are width c_{in} and spacing gap s_{in} that surrounds the central conductor.

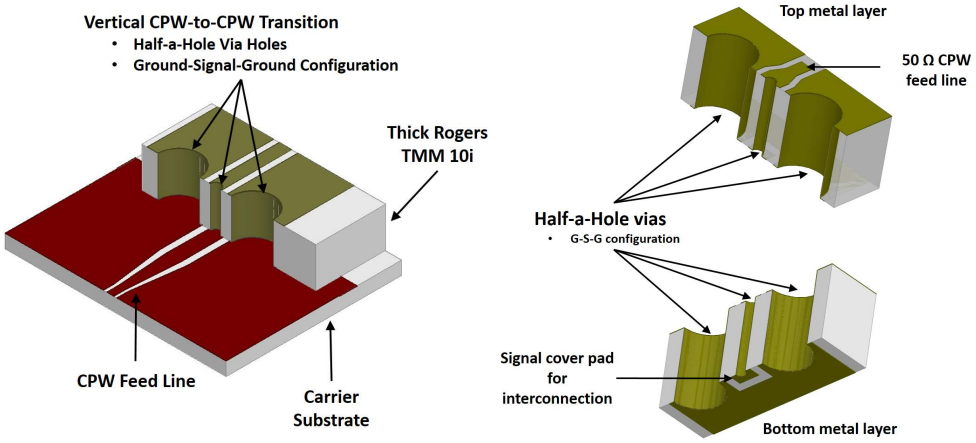

Figure 3.12: (*Left*): Possible configuration of the packaged filter assembled on carrier substrate. (*Right*): Side views of the vertical CPW-CPW transition.

Since the CPW structure has both signal and ground on the same plane, the connection of the device to the host board is simple. In fact, the device can be easily placed and soldered onto the carrier substrate. Moreover, due to the use of CPW probes as feeding lines of the filter, the increased thickness of the substrate does not affect the required filter port impedance.

Concerning the vertical structure, the transition between the coplanar footprint and the filter input/output is performed through a vertical CPW-to-CPW transition consisting on a ground-signal-ground configuration. The vertical interconnection is composed by metallized half-a-hole vias, which are also called castellated via holes. The signal half-a-hole via presents cover pads at both sides of the substrate. The ones located on the bottom layer are used to ensure easy assembly and electrical connection to the host substrate. By the way, to reduce the complexity of the design, only two half-a-hole vias per CPW transition have been used for ground connections, one castellated hole per side. If it were necessary to maintain a good matching between the vertical CPW transition and the CPW line that feeds the filter, a triangular taper of length t_T could be introduced at the top metal layer.

The diameter and spacing of the transition half-a-hole vias are the most important design parameters for controlling the EM performance. Therefore, these have been optimized in order to obtain a good matching within the band of interest. Fig. 3.13 shows the top and bottom views of the transition including the main design parameters.

EM simulations were carried out to optimize the placement and dimensions of the half-a-via holes in terms of matching. It is worth noting that most of the design parameters

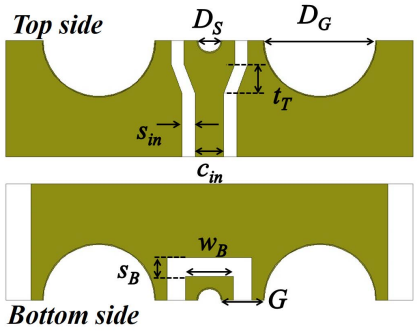

Figure 3.13: Main design parameters of the vertical CPW transition.

have been set considering the limitation of the fabrication process, as the case of hole cover pads, the via pitch or the minimum castellated hole diameter that is limited by the fabrication aspect ratio. Thus, the size of the cover pad for the signal castellated hole is set to be $W_B = D_S + 2 \cdot 0.2$ mm. At the bottom side, the spacing of the cover pad has been fixed to $S_B = 0.3$ mm in order to ease the filter assembly. Both parameters have not been modified during the design of the vertical transition.

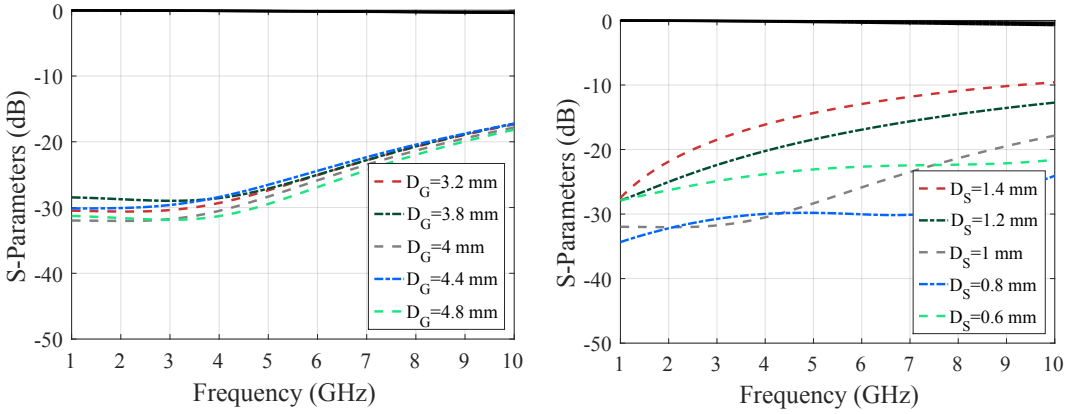

Figure 3.14: (a): S-parameters versus ground castellated hole diameter D_G. The signal via hole diameter D_S is set to 1 mm. (b): S-parameters versus signal castellated hole diameter D_S. In this case, D_G is 4 mm.

Considering a substrate with $\epsilon_r = 4.5 \pm 0.45$ and thickness $h = 3.175$ mm, the simulated configuration is made up of the CPW vertical transition that connects the 50 Ω CPW feed line of the filter (i.e. $c_{in} = 1$ mm, s_{in} =0.2 mm). Fig. 3.14-(a) shows the effect of the ground castellated hole diameter D_G on the S-parameters, and Fig. 3.14-(b) depicts the S-parameters varying the diameter of the signal castellated hole D_S, which is the central hole. In both cases, the distance between walls of ground and signal via holes has been fixed to $G = 0.9$ mm. So, the corresponding via hole pitch will be $\frac{D_S}{2} + \frac{D_G}{2} + 0.9$ mm. The insertion loss is always moderate, and it is recommended to keep the diameter of the signal castellated hole less than 1.2 mm for achieving better return losses.

As Fig. 3.15 displays, simulated results show that the response of the proposed vertical transition is good up to 10 GHz, demonstrating the importance of the vias sizing and their placement to improve return losses. The insertion loss of a single transition is better than

0.2 dB at 6 GHz (see Fig. 3.15-(b)), and the return loss is less than 30 dB in a frequency span of 1 to 7 GHz. Taking into account that the frequency band of the filter is centered at 5.75 GHz, the analysis of the EM simulations points out that the vertical transition configuration that shows the best response presents $D_S = 1$ mm $D_G = 4$ mm and the pitch is 3.4 mm.

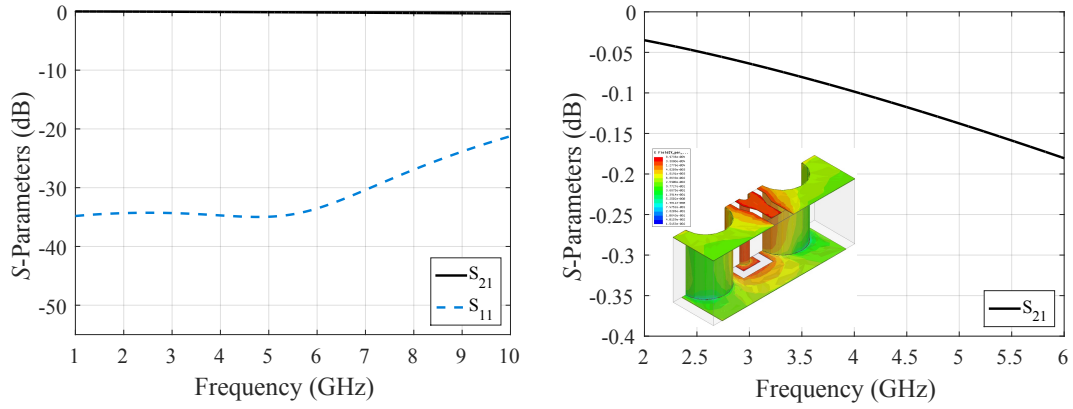

Figure 3.15: (a): S-parameters of the vertical half-a-hole transition for the selected configuration. (b): Zoom of the S_{21} curve versus frequency for the selected configuration of the vertical transition, showing also the EM field at 6 GHz.

3.3.2 Filter Design

Moving to the design of the 4-pole quasi-elliptic coaxial SIW filter, the centre frequency is chosen to be 5.75 GHz, thus at C-band, with an equi-ripple bandwidth of 114 MHz (FBW=2%). The TZs are set at 5.63 and 5.87 GHz, respectively, corresponding to the centre frequencies of adjacent filters in a multiplexer application with contiguous channels.

First, the synthesis of the desired response has been performed providing the following coupling coefficients: $k_{12} = k_{34} = 0.0193$, $k_{23} = 0.0158$, $k_{14} = -0.0036$ and $Q_e = 31.37$. Then, using the same design procedure of the previous filters, which uses the values obtained from the equivalent circuit and design curves for Q_e and $k_{i,i+1}$, the 4-pole filter has been designed. Again, a final refinement using 3-D full-wave simulations was necessary for the optimization of the final response.

Given that the filter is narrow-band, to reduce the in-band insertion loss is important to increase the resonator Q_u. There are many approaches that can be applied to do that with coaxial SIW resonators. As Fig. 2.12 depicts, it is recommended to reduce the loading effect of the capacitive patch on the resonator to increase Q_u. Of course, this has to be done maintaining the same resonant frequency. Therefore, the SIW cavity size has to increase when the loading capacitance C_l is reduced to keep the resonator centered at the desired frequency. Basically, the Q_u of coaxial SIW resonators can be increased if the resonator slope parameter b is reduced.

The main drawback of this approach is the need for bigger cavities, thus at the expense of the structure compactness. Nevertheless, increasing the electrical length of the resonators could be a solution, since it allows us to keep the cavity size constant while the resonant frequencies can be compensated for the variations of C_l. To do that, thicker

dielectric substrates have to be selected in order to design coaxial resonators having longer electrical lengths. In this context, the vertical transition shown in the previous section is a key element in the design of SIW coaxial filters as it allows to attain high design flexibility, low loss and high planar integration, even if thicker substrates are employed.

In this design, to keep the resonator Q_u as close as possible to 400, the slope parameter of the combline SIW resonator is chosen to be just b=16 mS. The dielectric substrate that has been chosen is a Rogers TMM4 substrate ($\epsilon_r = 4.5 \pm 0.45$, $\tan\delta = 2 \cdot 10^{-3}$) [79] having thickness of $h = 3.175$ mm. This means the resonator electrical length (i.e. corresponds to h) is now 46.5° that is $0.13\lambda_g$ at 5.75 GHz. The corresponding loading capacitance is $C_l = 33.5$ fF, while the characteristic coaxial impedance is $Z_0 = 78.35\,\Omega$.

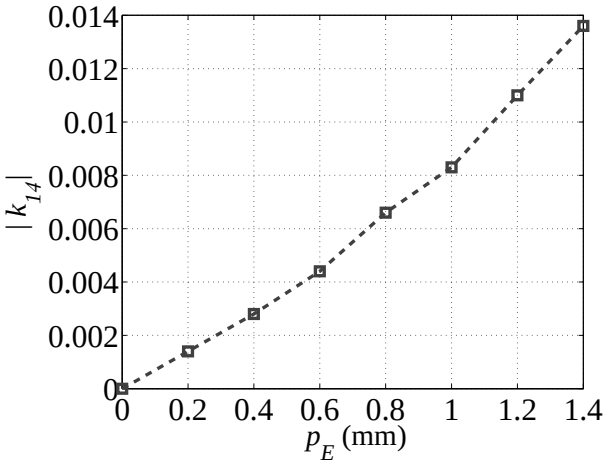

Figure 3.16: Coupling coefficient k_{14} versus insertion p_E of the capacitive probe in the loading capacitive disk. The post-wall iris width w_E is 0.75 mm. The capacitance probe presents a conductor width $c_E = 0.25$ mm and an isolating gap $s_E = 0.15$ mm.

Now, using both previous values and choosing an inner conductor diameter of $d_v = 0.7$ mm, the resonator structure can be optimized with EM full-wave simulations adjusting the size of the loading capacitive disk and the isolating slot. Thus, the resonator size is $w_{siw} \times l_{siw} = 10.6 \times 10.6$ mm^2, i.e. $0.43\lambda_g \times 0.43\lambda_g$, while the capacitive disk diameter is $d_p = 0.915$ mm with a spacing of $s_p = 0.15$ mm. Since the coaxial SIW filter is made up of four resonators having square shape, they will be arranged in a folded topology, in order to reduce its final area. Finally, the filter size is 21.2×21.2 mm^2 ($0.86\lambda_g \times 0.86\lambda_g$), being a very compact-size component. From 3D EM simulations, the estimated Q_u of such configuration of the coaxial SIW resonator should be around 405 at 5.75 GHz.

3.3.2.1 Electric Coupling

To calculate the electric cross-coupling coefficient k_{14} for the proposed coaxial SIW structure, two coupled resonators with input/output ports are studied by using full-wave simulations on the selected substrate. In this design, only the insertion p_E will be used to set the magnitude of the electric cross-coupling, while the other parameters will be kept constant: $c_E = 0.25$ mm, $s_E = 0.15$ mm and $w_E = 0.75$ mm.

Clearly, k_{14} becomes stronger as the insertion p_E within the capacitive disks is increased, as it is shown in Fig. 3.16. Since the proposed scheme is basically a mixed electric and magnetic coupling mechanism, the post-wall iris has been kept as small as possible in order to obtain an electric contribution and permit a fine control of its value.

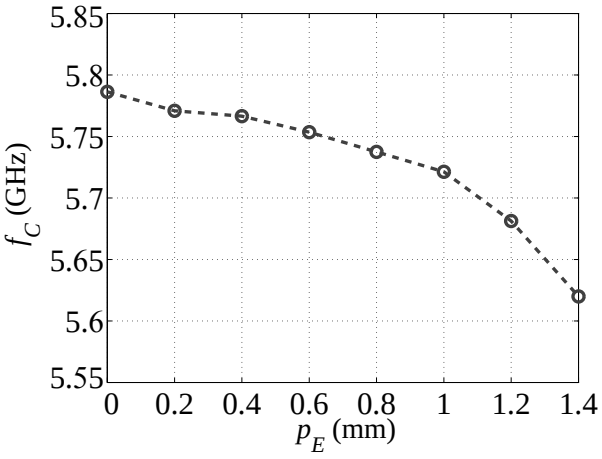

Figure 3.17: Centre frequency of two coupled combline SIW resonators versus capacitive probe insertion p_E.

In fact, the latter would be very useful for setting the position of the TZs at the desired frequency bands.

Fig. 3.17 shows the effect of the electric coupling probe on the central frequency of the two-coupled combline SIW resonators. As can be observed, the centre frequency decreases as the electric coupling probe inserts the capacitive disk. This suggests that the capacitive contribution of the probe increases the total loading capacitance C_l, thus reducing the resonant frequency of both SIW resonators. Even if the variation is less than 3%, the first and fourth combline SIW resonators have to be re-optimized to centre the resonator frequency at the desired value during the filter design procedure. It can be done by adjusting $d_{p,i}$ and/or $s_{p,i}$ since both parameters affect the value of C_l.

Finally, a conventional external coupling system based on a coplanar waveguide-to-SIW transition with 90° bend slots is used to control the external coupling. So, Q_e decreases for increasing size of the ground plane slots, which are etched on the top metal layer.

3.3.3 Experimental Results

Fig. 3.18 shows the geometric configuration of the 4-pole cross-coupled coaxial SIW filter, which highlights the electric cross-coupling and some main dimensions. Moreover, the dimensions are given in Table 3.6, where t is the thickness of the substrate Cu-clad, and i_{in} is the width of the input/output post-wall iris windows, which have been created in correspondence to the 90° bend slots of the CPW-to-SIW transition.

Full-wave EM simulation results of the filter are depicted in Fig. 3.20. The minimum insertion loss is expected to be 2.2 dB, while the two TZs are located at 5.63 and 5.87 GHz providing −35 dB and −27 dB of minimum rejection, respectively.

The designed filter has been fabricated on a 3.175 mm-thick Rogers Thermoset Microwave Material 4 (TMM4) substrate ($\epsilon_r = 4.5 \pm 0.45$, $\tan\delta = 2 \cdot 10^{-3}$) with 17 μm/17 μm Cu clad using a standard single-side PCB process. The diameter and centre-to-centre pitch of the external via holes are 0.6 mm and 1.1 mm, respectively. For testing purpose, the device has been assembled onto a carrier substrate in 1.524 mm-thick Rogers R4003C, which arranges specific pads for conventional SMD assembly.

The total size of the component, including the host substrate, is 51.7×36 mm^2. A

Table 3.6: Layout Dimensions of the Designed Filter (Units: mm)

c_{in}	1.2	s_{in}	0.15	h	3.175	t	0.017
$c_{in,carrier}$	1.2	$s_{in,carrier}$	0.15	$h_{carrier}$	1.524	$t_{carrier}$	0.017
$l_{siw,1}$	10.6	$l_{siw,2}$	10.6	$l_{siw,3}$	10.6	$l_{siw,4}$	10.6
$w_{siw,1}$	10.6	$w_{siw,2}$	10.6	$w_{siw,3}$	10.6	$w_{siw,4}$	10.6
d_{p1}	1.83	d_{p2}	1.88	d_{p3}	1.88	d_{p4}	1.83
s_{p1}	0.2	s_{p2}	0.2	s_{p3}	0.2	s_{p4}	0.2
s_E	0.15	c_E	0.25	p_E	0.32	w_E	1.45
w_{e1}	2.6	w_{e2}	0.3	l_{e1}	0.3	l_{e2}	1.08
i_{12}	4.98	i_{23}	4.62	i_{34}	4.98	i_{in}	2.5
D_G	4	D_S	1	G	0.9	w_B	1.3
s_B	0.6	d_{siw}	0.6	d_v	0.7	p_{siw}	1.06

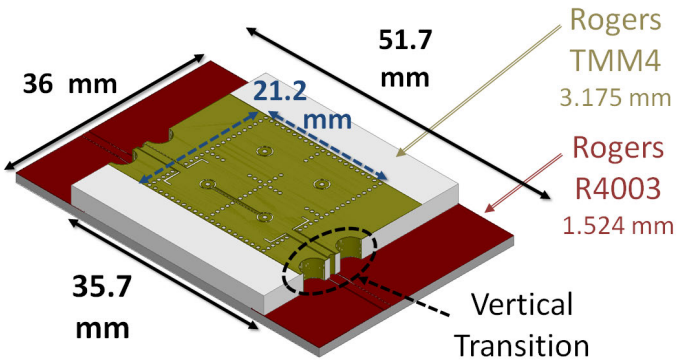

Figure 3.18: Layout of the cross-coupled filter implemented in combline SIW technology. Open-ended CPW line provides the filter with electric coupling.

photograph of the filter prototype assembled on the host substrate is shown in Fig. 3.19, while Fig. 3.20 shows the measured frequency responses of the cross-coupled SIW filter. It is worth mentioning that simulated and measured S-parameters include the vertical transition for connecting input/output ports, and a TRL calibration was performed using a home-made CPW cal-kit in Rogers R4003C.

As can be observed, the agreement between measurements and simulations is very good, since no frequency shift has been detected. The measured return losses are better than 15 dB and the 1-dB bandwidth is 102.5 MHz that corresponds to 1.8%, and it becomes 200 MHz at -20 dB level. The upper stop-band is in very good agreement with simulations up to 12 GHz, being the attenuation always better than 28 dB up to 12 GHz, as shown in Fig. 3.21.

Nevertheless, it is worth mentioning that the minimum IL has increased up to 4.1 dB from an estimated value of 2.2 dB, resulting in an estimated Q-factor of just 180. As it has already been mentioned, the increase of the filter IL is due to the ENIG finishing, and especially, to the thickness of the nickel layer that has been deposited on the copper foil. A scheme of the standard ENIG finishing is shown in Fig. 3.22-(a).

Typically, the ENIG finishing presents 0.05 μm-0.2 μm of gold deposited over 3 μm-6 μm of nickel. The gold layer protects the nickel from oxidation during storage, and also provides the device with low contact resistance, excellent shelf-life and it is gold

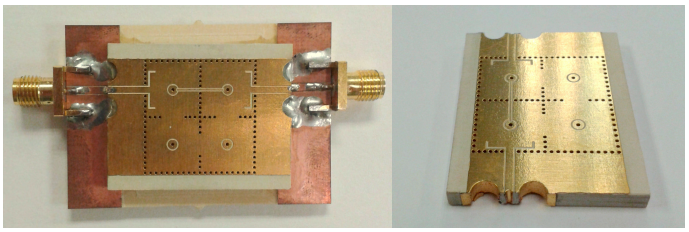

Figure 3.19: Photo of the filter prototype assembled on its substrate carrier.

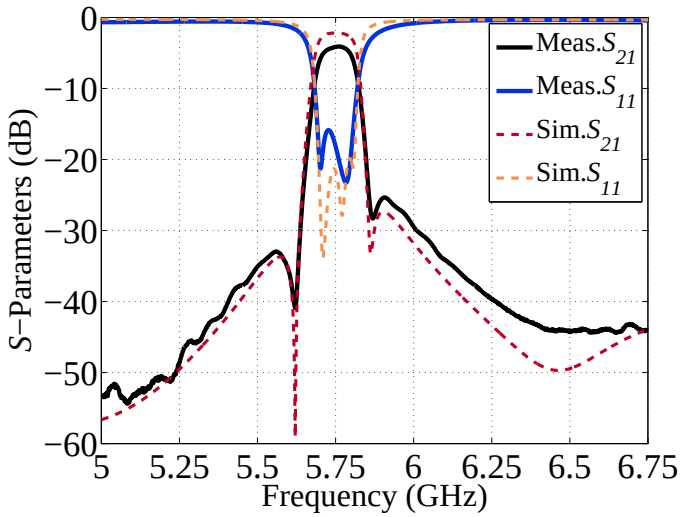

Figure 3.20: Simulated and measured responses of the proposed SIW filter. Solid and dashed lines depict the measured and simulated results, respectively. The measured IL is 4.1 dB at 5.75 GHz.

wirebondable. But the electroless nickel layer has undesirable magnetic properties and shows very low conductivity.

As in the coaxial topology the fringing fields across the air gap generate the loading capacitance, the maximum electric field is located around this gap. If we look at Fig. 3.22-(b), it is possible to see how the current flow exiting the inner via hole reaches the air gap and then it starts to flow all around it. Since the nickel is also deposited on the vertical sides of the air gap, the EM field penetrates into it, resulting that the EM performance of the coaxial topology are strongly related to the nickel layer thickness.

After taking into account the Ni-Au finishing of the PCB process in the HFSS 3D model, which now includes $\simeq 3$ μm of Ni layer deposited on every face of the $\simeq 35$ μm of Cu layer (i.e. 17 μm from the substrate copper foil plus $\simeq 18$ μm from the electroplating process), the simulated IL readjusts very well to the measured one. Thus, to increase the EM performance of this topology, a different PCB finishing has to be taken into account, as it could be the case of immersion Silver and immersion Tin among others.

Table 3.7 shows the comparison between this cross-coupled filter and other similar SIW filters shown in the references. Clearly, the proposed approach permits that two TZs were generated at both sides of passband, while presenting a good spurious rejection and high compactness degree. In addition, this solution permits the SIW filter to be directly integrated with other planar structures, thus guaranteeing high planar integration.

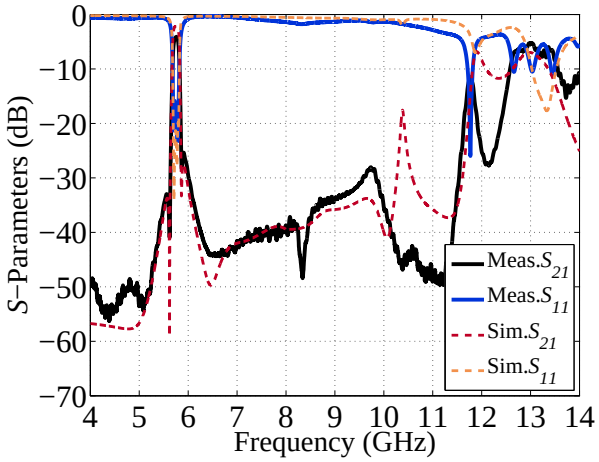

Figure 3.21: Simulated and measured wideband responses of the proposed SIW filter. Solid and dashed lines depict the measured and simulated results, respectively.

Table 3.7: Comparison of Cross-Coupled Filters in SIW Tech. (Note:B=Below,A=Above)

REF.	f_0(GHz)	FBW	IL(dB)	Size(λ_g^2)	TZs
[17]	20.5	4%	0.9	1.42×1.36	1 B, 1 A
[19]	27	7.4%	2.1	1.45×1.14	1 B, 2 A
[96]	2.5	4%	≈ 4	1.6×1.6	1 B, 1 A
[97]	5.1	4.2%	2.05	1.55×0.98	1 B, 1 A
[98]	20	3%	1.7	1.88×1.42	2 B, 2 A
This work	5.75	2%	4.1	0.86×0.86	1 B, 1 A

3.3.4 Multiphysics Study for the Power Handling Capability Evaluation

In this section the Power Handling Capability (PHC) of the coaxial SIW resonator that composes the quasi-elliptic filter is studied in detail. Two different kinds of studies are addressed: *a*) Average Power Handling Capability (APHC), where it is assumed that a Continuous Wave (CW) signal is applied to the circuit and the electro-thermo-mechanical coupling is analyzed in order to determine the maximum temperature and thermal stress of the circuit as a function of the input signal power. And *b*) Peak Power Handling Capability (PPHC), in such a case pulsed signals are applied to the circuit and the corona discharges are examined as a function of the input signal power and pressure.

3.3.4.1 Average Power Handling Capability

For moderated CW signal powers (1-5 W) high temperatures can be achieved in planar circuits due to self-heating, which limits the APHC [99–101]. Planar circuits present three loss mechanisms: conductive, dielectric and radiation losses. They are linearly proportional to the input power, but only the two former loss mechanisms produce heat in the circuit, so that they can be defined as the internal heat sources of the structure. In particular, dielectric loss is treated as a volumetric heat source whereas conductive loss

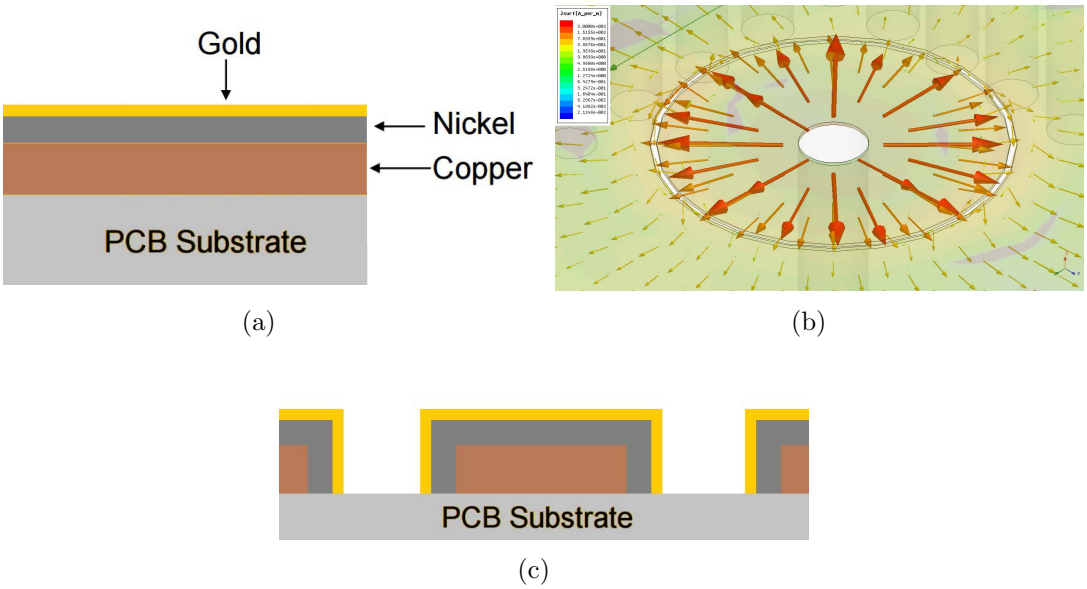

Figure 3.22: (a): Electrolytic Nickel/Gold finishing for PCB laminates.(b): Current vector distribution around the air gap that surrounds the capacitive patch in a coaxial SIW resonator.(c): Electrolytic Nickel/Gold finishing in the case of coaxial SIW structures.

as a surface heat source.

In SIW technology, due to its large aspect ratio w_{siw}/h, and the fact that conductive losses are equal both in top and bottom planes, the whole heat source Q_{int} can be assumed to be homogeneous in a differential region $w_{siw} \cdot h \cdot l_{siw}$, consequently providing a homogeneous temperature in this volumetric region. This assumption is also favoured by the use of via holes conforming the SIW, which propagate the heat between the top and bottom layers. From the Newton's Law of cooling, the generated heat is equal to the total heat delivered to the environment by means of convection and/or thermal radiation. Thus, this energy balance can be written as

$$Q_{int} + Q_{ext} = \sum_{i=1}^{m} h_{conv,i}\, A_i\, (T_{hot} - T_{amb}) + \sum_{j=1}^{n} h_{rad,j}\, A_j\, (T_{hot} - T_{amb}) \tag{3.7}$$

where

$$Q_{int} = \Gamma P_{in} \tag{3.8}$$

being Γ the loss factor of the structure and P_{in} the input signal power. Q_{ext} is any external heat source (such as solar radiation), T_{amb} is the temperature in the surroundings, A_i and A_j are the surface layers exposed to convection and radiation boundary conditions, respectively, and h_{conv} and h_{rad} are the convection and radiation coefficients. The values h_{conv} and h_{rad} depend on the external conditions of each layer, i.e., if there is a heat sink attached, natural or forced convection, emissivity, etc. From (3.7), the maximum temperature T_{hot} can be computed for a given P_{in} and if the environment conditions (h_{conv} and h_{rad}) are known. An expected conclusion from this equation is that, if Q_{int} is kept, the bigger the surface A, the lower the T_{hot} is, and therefore, the higher the APHC.

For the coaxial SIW resonators, the electric-magnetic field distribution which defines the heat source pattern is different to that presented by standard SIW rectangular cavities,

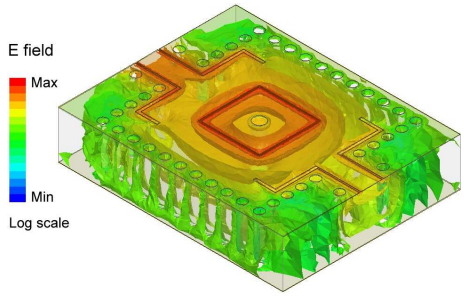

Figure 3.23: 3D Electric Field distribution for an combline SIW cavity.

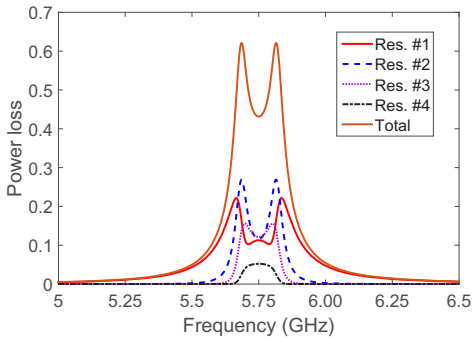

Figure 3.24: Power loss in each resonator per watt from the equivalent lumped element circuit model. $Q_u = 320$.

as seen in Fig. 3.23. However, the large aspect ratio w_{siw}/h as well as the use of the outer via holes and the inner conductor, make the temperature in the coaxial cavity nearly homogeneous, and therefore, (3.7) can be used as a first order approximation.

For the APHC analysis of the filter, firstly, the power loss per resonator is computed from the equivalent lumped element circuit whose behaviour is modeled by the coupling matrix shown in Fig. 3.11. $Q_u = 320$, $f_0 = 5.75$ GHz and FBW= 2% are used for such a computation. As seen from Fig. 3.24, the total highest power loss is found at the inband corners, at 5.68 and 5.82 GHz, with $\Gamma = 0.62$. In particular, resonator 2 presents the highest level of losses, so that it is expected that this resonator limits the APHC. (3.7) can be used in order to calculate the average temperature in the whole circuit. For $P_{in} = 5$ W at 5.82 GHz, assuming natural convection with $h_{conv} = 10$ W/m^2·°C and $T_{amb} = 22$°C, with a whole circuit area of $A_{top} = A_{bottom} = 35.7 \times 28.2$ mm^2 and neglecting thermal radiation, the average temperature in the circuit is found to be 176 °C. ANSYS Multiphysics [102] is used in order to accurately obtain the thermal profile for such an example. Fig. 3.25 shows its thermal profile where the hottest spot is found in resonator 2, as predicted, with a value of 205°C. The simulated average temperature in the circuit is very close to the computed value according to (3.7).

The APHC is limited by that P_{in} which creates such a thermal gradient leading to exceed the glass transition temperature of the substrate T_g or, that P_{in} which generates a thermal stress able to destroy (or deform) the circuit. The minimum of those values limits the APHC. For the electro-thermo-mechanical coupling needed to evaluate the thermal stress, ANSYS Multiphysics is used again. Table 3.8 summarizes the thermo-mechanical parameters required for the study. It should be remarked that the thermal conductivity in the substrate both in SIW and SIW coaxial cavities is not a critical parameter for the reduction of the gradient of temperature as it is in microstrip technology. The yield

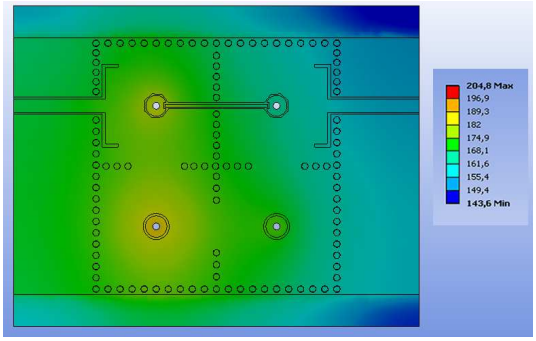

Figure 3.25: Thermal profile of the quasi-elliptic filter. P_{in} = 5 W at 5.82 GHz with natural convection around the circuit with h_{conv} = 10 W/m^2·°C and T_{amb} = 22 °C.

Table 3.8: Thermo-mechanical Properties of TMM4

	Copper	Dielectric
Thermal conductivity (W/m·°C)	400	0.7
CTE (x,y,z) (ppm/°C)	17	16, 16, 21
Young's Modulus (GPa)	117	11.9
Poisson's Ratio	0.33	0.2
Yield Strength (MPa)	220	—
Glass Transition Temperature (°C)	—	425

strength point gives the maximum stress that a material can afford before permanent deformation. It defines the transition between the linear mechanical behaviour (elastic behaviour) of the material and the non-linear one.

Fig. 3.26 shows the maximum equivalent stress (Von-Mises) as a function of P_{in} at the frequency where losses are the highest (5.82 GHz) and for two different load cases (bottom of the circuit is fixed or unfixed). Obviously, when the bottom is fixed the stress produced is higher and the elastic limit is reached for lower power levels. The maximum stress happens in the metal, both in layers and the via holes, whereas the stress provoked in the substrate is much lower. From these figures, it can be concluded that $P_{in} < 2$ W in order to keep the circuit in safety ranges of applied power. It should be noted that for this circuit, due to the high value of T_g, APHC is limited by thermal stress. With respect to the deformation produced in the circuit while the CW signal is applied, in the case of the bottom is fixed, deformation is insignificant (maximum deformation < 8 μm for $P_{in} = 5$ W). In the case when the bottom is unfixed, although the maximum deformation is still low, it can produce a small frequency shift in the transfer function for high P_{in} (maximum deformation < 82 μm for $P_{in} = 5$ W).

3.3.4.2 Peak Power Handling Capability

The coaxial SIW topology presents an important density of electric field through the air, between the loading capacitive disk and the top layer ground. Thus, this resonator can be susceptible to present corona discharges for high power applied signals. The situation is different for standard SIW technology, since the electric field is mainly distributed through the dielectric and the critical areas for air ionization are the slot edges of the coplanar line feeding the SIW cavities [83].

In order to evaluate any possible corona discharge, the maximum voltage (and con-

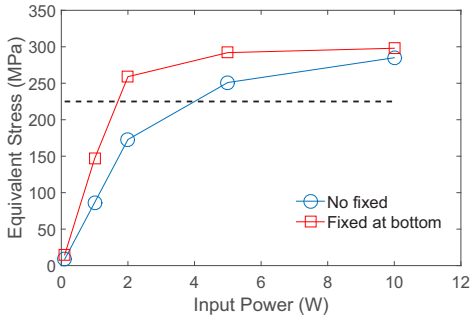

Figure 3.26: Maximum equivalent Von-Mises Stress as a function of P_{in}. At 5.82 GHz and assuming natural convection on the circuit with $T_{amb} = 22$ °C.

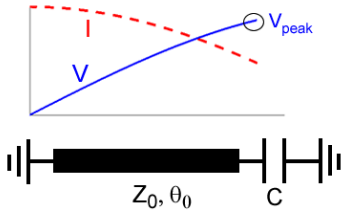

Figure 3.27: Scheme of the coaxial SIW resonator where the current and voltage distributions are shown at resonance frequency.

sequently, the expected maximum electric field) of the coaxial filter should be found as a function of the input signal power. From the equivalent lumped element circuit, the voltage and current in each resonator i of the filter can be computed as

$$v_i = \frac{v_g}{q_e} [A]^{-1}_{i,1} \tag{3.9}$$

$$i_i = \frac{v_g}{q_e R} [A]^{-1}_{i,1} \tag{3.10}$$

where v_g is the generator voltage, q_e the normalized external quality factor, R is the reference impedance and $[A]$ is the normalized impedance/admittance matrix defining the filter network [103]. Once the equivalent voltages/currents are known, the stored energy can be found as

$$W_i = \frac{4P_{in}}{q_e \mathrm{BW}} [A]^{-2}_{i,1} \tag{3.11}$$

where P_{in} is the available power at the input port and BW is the absolute bandwidth of the filter in rad/s. At resonance, the stored energy by every resonator of the equivalent lumped element network should be the same as that associated to the distributed resonators [104, 105]. Fig. 3.27 shows the scheme of a combline resonator where the voltage and current standing waves are also plotted at resonance. From the standing waves the stored energy by the distributed resonator $W_{distr,i}$ can be calculated as [106, 107] by integrating the standing waves (in form of sinusoidal functions) along the resonator. Thus, by making $W_i = W_{distr,i}$ the peak voltage in the coaxial SIW resonator can be found at the capacitive patch as

$$V_{peak,i} = 4\sqrt{\frac{P_{in} Z_{0,i}}{q_e \mathrm{FBW} \chi}} [A]^{-1}_{i,1} \tag{3.12}$$

where

$$\chi = \theta_0 + \frac{\sin 2\theta_0}{2} \tag{3.13}$$

It should be noted that for the case θ_0 is small, the combline SIW resonator behaves as a lumped element resonator, and therefore, the values found with (3.12) are the same as those obtained with (3.9).

The air ionization is a phenomenon linked to the electric field strength rather than to the voltage [105, 108]. So, the electric field strength must be estimated in the capacitive patch of the resonators forming the filter. Although the electric field distribution along the air gap is not evident, as a fast approximation the maximum electric field in each resonator can be computed as

$$|E_{peak,i}| = \frac{V_{peak,i}}{s_i} \tag{3.14}$$

where s_i is the annular gap of the resonator i. For high pressure regime (pressures >100 mbar), the air ionization breakdown threshold (peak value) can be determined by following the rule [109]

$$|E_{break}| = 42.7\sqrt{p^2 + 2f^2} \ \text{(V/cm)} \tag{3.15}$$

where p is the pressure in torr and f is the operation frequency in GHz. At this point, from (3.14) and (3.15) the PPHC can be analytically computed in filters based on combline resonators for high pressure regime. For low pressure regime, the continuity equation describing the electron density evolution must be solved. This arduous task must be done numerically, in this work the software tool AURORASAT™ SPARK3D® is employed. This tool uses the real electromagnetic field distribution of the device under test in order to solve the continuity equation, and provides the power breakdown threshold of the device from some input parameters such as pressure, kind of gas (air or nitrogen) or temperature. As a validation example, the PPHC is computed for the quasi-elliptic filter by using the equations derived in the previous lines and by using SPARK3D. The input parameters are $f = 5.82$ GHz (where the voltage is maximum, which happens at the capacitive patch of resonator 2; this frequency coincides with the frequency of maximum losses) and $p = 500$ mbar. From the derived equations, PPHC is analytically calculated as 7.3 W whereas from SPARK3D is 11.2 W. If the maximum electric field strength of the structure is simply taken from an electromagnetic tool (such as HFSS or CST; note that a normalization could be needed depending on the software used), and by applying the rule (3.15), the obtained PPHC is 0.9 W, which is a value considerably lower than those previously obtained. From these results, it can be concluded that taking the maximum electric field from the EM simulation results, which is indeed a strategy commonly used for waveguides or coaxial resonators, gives a very conservative limit for PPHC in combline SIW resonators. This is due to the fact that the maximum electric field values are very concentrated around the capacitive patch edges, in a region involving just some microns, which is not enough to alter the electron density. Additionally, some field singularities could appear in the resolution of the field around such corner edges. Another conclusion is that the approximation made in (3.14) gives a reasonable value of electric field strength in order to determine the PPHC.

Fig. 3.28 shows the Paschen curves of the filter for each resonator, obtained from SPARK3D at the frequency where losses and voltage magnification are maximum. Resonator 2 is limiting the PPHC, as expected. The critical pressure is around 5-10 mbar, where PPHC is just 0.6 W. So, it is presumed that in a low pressure regime corona limits PHC rather than the thermo-mechanical effects. An interesting effect has been also

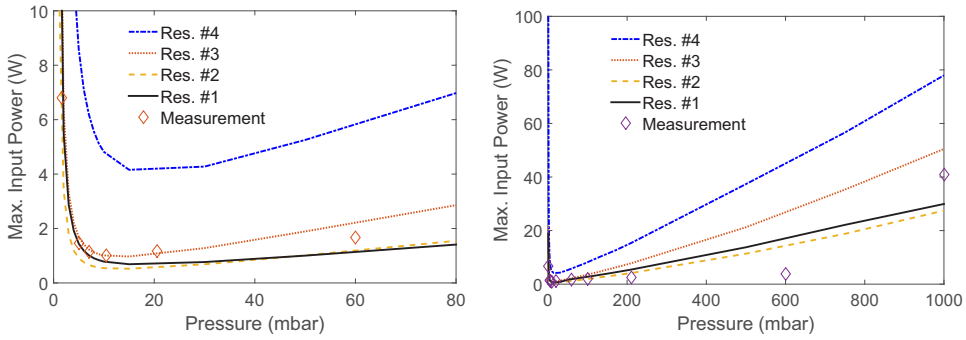

Figure 3.28: Simulated Paschen Curves for the resonators involved in the filter under test. (a) Critical pressure region. (b) The whole pressure range. In this simulation, $f = 5.82$ GHz and $T_{amb} = 22$ °C.

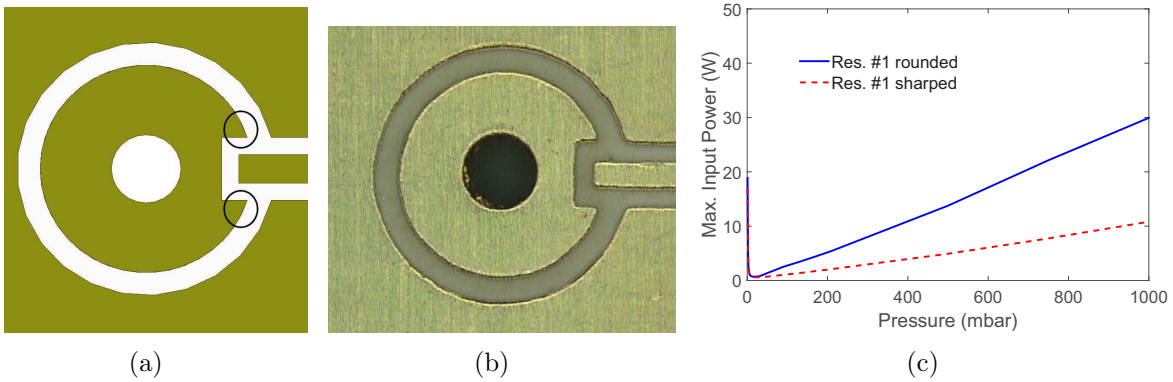

Figure 3.29: Zoom in of the resonator #1. (a) Layout. (b) Fabricated. (c) Simulated Paschen Curves comparison between the sharp and rounded corner cases.

detected in this filtering structure: due to the sharp shape of the first (and fourth) resonator corners (see Fig. 3.29), it is found that there is a high concentration of electric field density around those corners, providing higher values of electric field strength than those of resonator 2. Thus, resonator #1 may limit the PPHC of the filter even though the voltage in this resonator is lower than that in resonator 2 at the frequency of analysis. However, after fabrication, those corners are rounded, as seen in Fig. 3.29(b), leading to a reduction of the electric field density around them. Fig. 3.29(c) shows the simulated Paschen Curves for the first resonator when the corners are sharped and rounded. As deduced from this figure, rounding the corners can considerably increase PPHC in this filter topology. In Fig. 3.28 the Paschen Curve of resonator #1 corresponds to the rounded corner case. Obviously, for both cases the filter response remains constant.

3.3.4.3 APHC and PPHC Measurements

In order to validate the calculated and simulated results, high power measurements have been performed at the European High-Power RF Space Laboratory (Valencia, Spain). Fig. 3.30 shows a schematic diagram of the employed test-bed. Several methods have been used for the corona discharge detection: third harmonic detection, nulling of the forward/reverse power at the operation frequency, electron probe and by visual inspec-

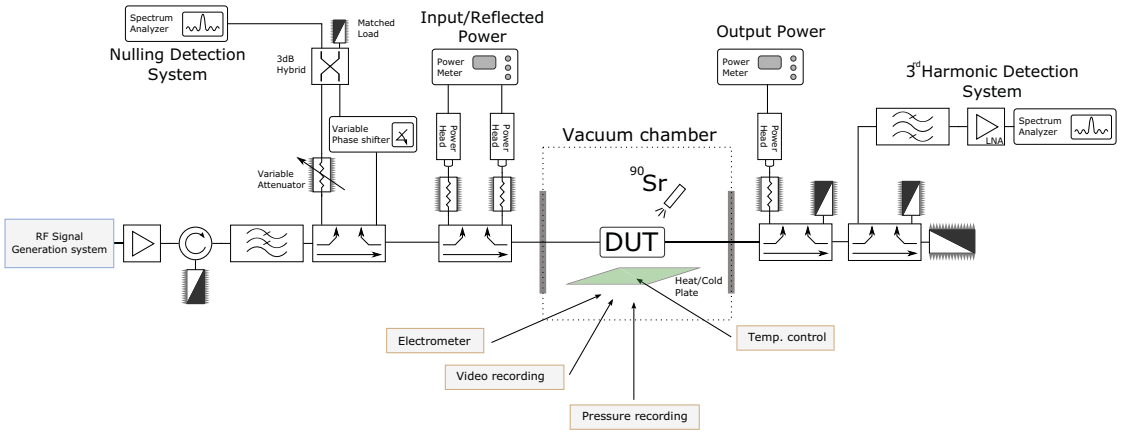

Figure 3.30: Scheme of the testbed configuration used for corona breakdown detection.

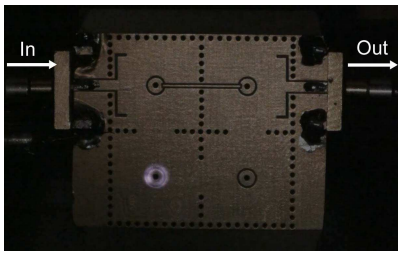

Figure 3.31: Capture of a corona discharge at the second resonator of the filter under test.

tion by recording the circuit with a video camera. The applied signal to the filter has been a pulsed signal with a carrier frequency of 5.75 GHz (frequency where the voltage magnification and losses are maximum in the measured filter), a pulse width of 20 μs and a duty cycle of 1%. These pulsed signal characteristics avoid any self-heating effect in the device, whereas the pulse width is wide enough to assume that the pulse breakdown threshold converges to the CW one. The PPHC has been evaluated for different pressures in order to obtain the Paschen Curves of the device.

In Fig. 3.28 the measured data can be also observed. For all scenarios corona breakdown has firstly appeared in resonator 2, as expected. There is a reasonable good agreement (especially at lower pressures) with the simulated results what validates the theoretical prediction and the study done. The maximum difference between the measured and simulated breakdown field levels has been of 45%, which has been found for a pressure of 600 mbar. Fig. 3.31 shows the capture from the video camera at the moment of a corona discharge has occurred. As seen, the spark is uniformly originated along the annular slot.

With respect to the APHC measurement, a CW signal at the same frequency has been applied to the circuit at ambient pressure ($p = 1000$ mbar) and temperature. The temperature has been measured by means of thermocouples attached to the resonators in regions where their impact is low. The circuit was suspended so that natural convection can be assumed on all faces. The thermal steady-state was reached after around 5 minutes the signal is switched on. The measured temperatures for the different CW applied signal power samples have been close to the analytically calculated and simulated values, with differences lower than 20%.

Up to 5 W there were no evidences of any rupture point in the circuit, however $P_{in} > 5$ W should be avoided since temperatures higher than 150 °C were measured.

Furthermore, for $P_{in} > 5$ W a frequency shift can be noticed in the measured response as well as a considerable increase of losses. After switching on/off the applied signal, the circuit could recover its original electromagnetic performance, although probably with a slight permanent material deformation. The CW applied power was increased up to obtain the complete failure of the device. The circuit was finally destroyed by a continuous corona discharge which occurred for $P_{in} = 14$ W. This value is lower than the one measured at ambient pressure for the pulsed signal case and shown in Fig. 3.28. This can be due to the following reasons: the air temperature was much higher because of self-heating, which reduces the corona breakdown threshold for high pressure regime and, because corona breakdown thresholds are normally lower for the CW case than for the pulsed signal case, unless a very wide pulsed signal width is used.

3.4 Six-pole Quasi-Elliptic Coaxial SIW Filters for Frequency Conversion

The purpose of this section is to present a potential application that can benefit from the higher Q-factor, further miniaturization and self-packaging of substrate integrated coaxial filters. A set of realistic specifications have been proposed, studied and implemented in coaxial SIW topology leading to the development of two different bandpass filters. Thus, a preliminary analysis of the adequate filter topologies for meeting these specifications is carried out. Then, full-wave EM analysis of substrate integrated coaxial resonators aimed at different frequency bands (i.e. C- and K-bands) will be completed, in order to identify the main trade-offs between the fundamental design parameters of the structure for its optimization in terms of losses and miniaturization.

3.4.1 Filters Specifications

Apart from the highly selective channel filtering carried out at intermediate frequency (IF), several microwave filters are usually present in schemes with multiple conversion stages, or when cross-conversion between different frequency bands is required. On the one hand, the purpose of these filters is usually double, since before the mixing stage it is necessary to strongly reject the transmission frequency band.

On the other hand, after the mixer, it is required to filter out any harmonics and inter-modulation products generated by the mixing stage. In the latter case, the filters present particularly challenging specifications that must be met:

- Very strong rejection on frequency bands adjacent to the filter passband.
- Flat insertion loss and group delay responses in order to avoid degradation of the RF chain performance.
- Small size and easy integration with compact and hermetically packaged solutions.

It is clearly seen that a structure combining features like moderate Q_u, compact size and advanced filtering responses could be of great interest for implementing filters for frequency conversion applications in space with enhanced performance.

As a matter of fact, the introduction of flexibility at satellite payload level should improve the capacity of the spatial infrastructure to follow the market evolution during

Table 3.9: C-band Filter Specifications

Parameter	**Unit**	**Frequency Band**	**Unit**	S_{21}	S_{11}
Useful C-band BW	MHz	3875-4125	dB	> -3	< -15
Spurious Band 1	MHz	3375-3750	dBc	< -40	
Spurious Band 2	MHz	< 3375	dBc	< -30	
Spurious Band 3	MHz	> 4250	dBc	< -30	

Parameter	**Unit**	**Specification**
Flatness	dB	1
Group Delay Variation	ns-pp	1.5
Size	mm^3	$19 \times 19 \times 2$

a longer life time in orbit. For example, different frequency conversion stages are employed in flexible payload, enabling both flexible spatial and frequency routing at payload level. In this context, such quasi-elliptic filters can help to meet the increasingly stringent requirements for filtering at the frequency conversion stages.

Therefore, the specifications of two different filters are proposed at C- and K-band. The filter requirements are about moderate to low insertion loss in the pass band, while high selectivity to reject signal must be given at frequencies close to the passband. Concerning the group delay, the objective is to have a very flat response in both frequency bands, in order to obtain filters with quasi-linear phase response. As it is well known, flattening the group delay response is highly desirable in many satellite applications, especially when advanced modulation schemes are used.

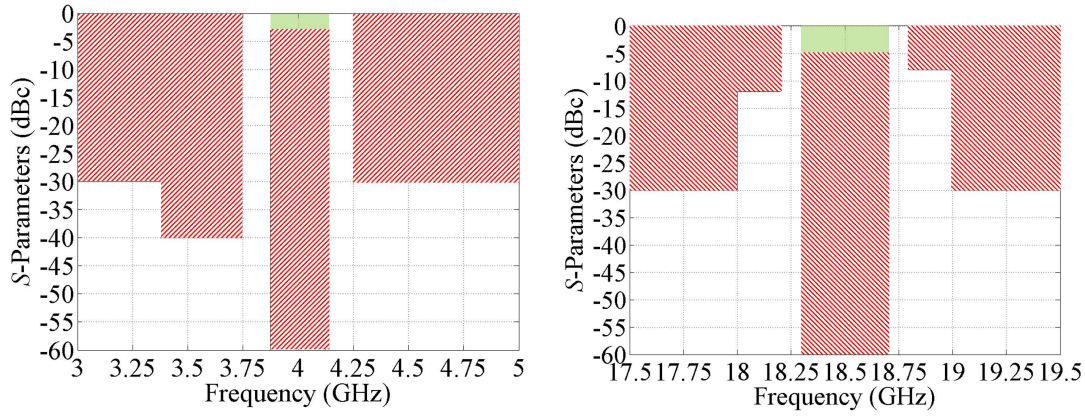

(a) (b)

Figure 3.32: (a): Frequency mask for the C-band Filter. (b): Frequency mask for the K-band Filter.

The technical requirements for the C-band and K-band filters are shown in Table 3.9 and Table 3.10, respectively, while Fig. 3.32 depicts both required filter frequency masks. It is worth mentioning that the C-band filter imposes very relevant miniaturization requirements, limiting the total size of the device up to $19 \times 19 \times 2$ mm^3. This is an extremely compact implementation at this frequency band.

Table 3.10: K-band Filter Specifications

Parameter	**Unit**	**Frequency Band**	**Unit**	S_{21}	S_{11}
Useful K-band BW	MHz	18300-18700	dB	> -5	< -15
Spurious Band 1	MHz	18000-18200	dBc	< -12	
Spurious Band 2	MHz	18800-19000	dBc	< -8	
Spurious Band 3	MHz	< 18000	dBc	< -30	
Spurious Band 4	MHz	> 19000	dBc	< -30	

Parameter	**Unit**	**Specification**
Flatness	dB	1
Group Delay Variation	ns-pp	1

On the contrary, for the K-band case, very important limitations on the group delay ripple are imposed that will imply the use of some kind of equalization technique. Finally, both filters must enable an SMD packaging solution in order to permit SMD assembly on host substrates.

3.4.2 Filters Synthesis

3.4.2.1 C-band Synthesis

In order to overcome problems with the group delay variations and size limitations, the proposed solution for satisfying the C-band specifications is a 6 pole filtering function with two symmetrical TZs placed at both sides of the bandwidth. It is a trade-off solution between rejection level and maximum achievable bandwidth, enabling the filter to comply simultaneously with the attenuation of the first spurious band and the in-band group delay ripple specifications. The filter topology consists on a folded 6-pole scheme, as can be seen in Fig. 3.33, where the folded configuration makes also for additional size reduction. The filter centre frequency is 4 GHz, while the FBW can be increased up to 8.6% (i.e. the required value of 250 MHz corresponds to 6.25%), thus the group delay variation in the bandwidth is reduced below the required 1.5 ns-pp level.

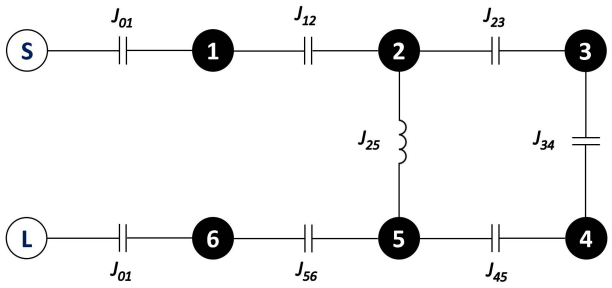

Figure 3.33: Filter topology for C-band specifications: 6-2 filter having magnetic cross-couplings between resonators 2 and 5.

The quasi-elliptic frequency response is obtained introducing an out-of-phase cross-coupling between resonators 2 and 5. Thus, a pair of TZs located above and below the

Table 3.11: C-band Filter Extraction

Filter Parameter	Unit	Value
Q_e		12.228
$k_{12} = k_{56}$		-0.06829
$k_{23} = k_{45}$		-0.04984
k_{34}		-0.05683
k_{25}		0.00958
$f_{0,1} = f_{0,6}$	GHz	3.99868
$f_{0,2} = f_{0,5}$	GHz	3.99332
$f_{0,3} = f_{0,4}$	GHz	3.99429

passband can be controlled changing k_{25} coupling coefficient, thus improving filter selectivity. The flexibility of the coaxial SIW topology allows us to select the best coupling configuration that should guarantee both strong direct couplings and out-of-phase couplings in a very compact implementation. Thus, direct couplings between resonators are obtained by means of electric couplings, implemented by the proposed electric coupling, while the cross-coupling is implemented by means of a standard magnetic post-wall iris providing magnetic coupling. Table 3.11 reports the filter parameters for the C-band case.

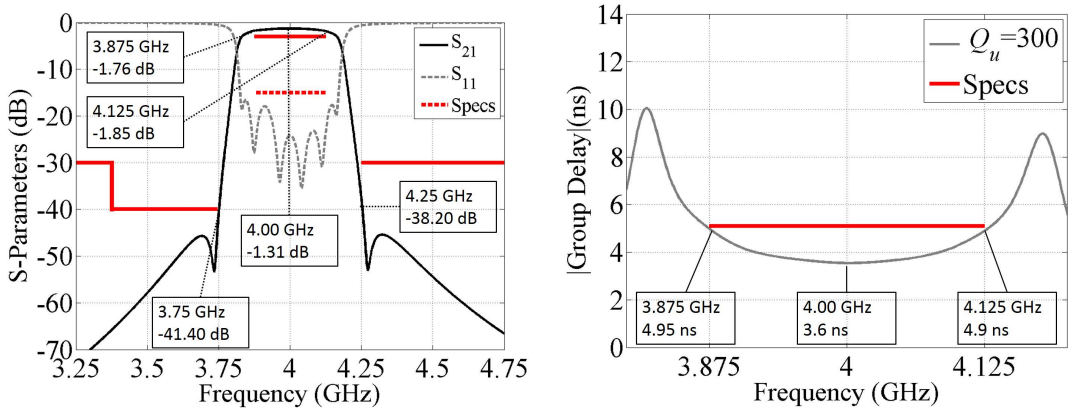

(a) (b)

Figure 3.34: (a): S-parameters responses for C-band filter and (b) the group delay response when the resonators Q_u is 300.

Moving to filter analysis, the proposed folded 6-2 filter topology satisfies group-delay requirement for any resonator Q_u value. Concerning the IL at central frequency and its variation over the bandwidth, an unloaded Q-factor better than 250 is required for the coaxial SIW resonator, so that, IL would be around 2 dB with a variation within 1 dB along the passband. Obtaining a resonator Q_u value about 250-300 could be considered reasonable and absolutely realistic for the proposed technology.

To conclude the analysis of the C-band filter case, S-parameter and group delay responses of the proposed folded filter topology for a resonator Q_u value of 300 are shown in Fig. 3.34. The IL variation over the bandwidth is around 0.5 dB, being 1.85 dB the maximum IL value at 4.125 GHz. The maximum in-band group delay variation is 1.3 ns-pp between the edges of the passband and the filter centre frequency.

In order to reduce the resonator size and to obtain the desired resonator Q_u, a 2.54 mm-thick Rogers TMM10i substrate ($\epsilon_r = 9.8 \pm 0.245$, $\tan\delta = 2 \cdot 10^{-3}$) has been selected for implementing the C-band filter. The resonator slope parameter has been set to $b = 36.5$ mS that gives a $C_l = 1.25$ pF while $Z_0 = 40.8\,\Omega$. This value represents a good compromise between the need of compactness and moderate-to-high Q_u.

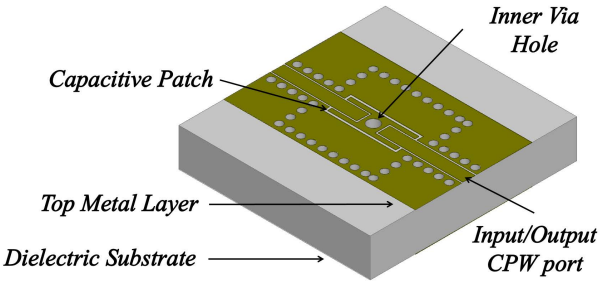

Figure 3.35: 3D view of the coaxial resonator for the C-band case.

As it has been demonstrated in the previous Section 2.1.2, it is important to keep the patch perimeter as small as possible and select a wide inner via diameter in order to maintain a high resonator Q_u while setting C_l. To do that in this design, the air gaps have been initially set at narrow values (i.e. close to 0.135 mm) and the patch sides are then adjusted to center the resonant frequency at 4 GHz, resulting in a capacitive patch perimeter of 12.69 mm. It is worth noting that, due to the use of electric inter-resonator couplings in a folded topology, the capacitive patches show L-shaped rectangular forms that allows us to independently control the frequency and the couplings, as it is displayed in Fig. 3.35.

Finally, the inner via diameter has been set to $d_v = 0.9$ mm, which can be considered a wide value that guarantees a higher Q_u, so the SIW resonator cavity size is $w_{siw} \times l_{siw} \times h = 6.4 \times 6.4 \times 2.54$ mm^3 (i.e. $0.267 \times 0.267 \times 0.106\,\lambda_g^3$ and $0.085 \times 0.085 \times 0.034\,\lambda_0^3$).

3.4.2.2 K-band Synthesis

The group delay requirement seems to be the most problematic target value to be accomplished in the K-band case. In order to avoid increasing too much the filter order, the use of the cross-coupling mechanisms to create TZs both at real and imaginary axes enables us to achieve high selectivity and linear phase. Thus, the proposed solution for satisfying the K-band specifications is again a folded 6-pole filtering function with two symmetrical TZs placed at both sides of the bandwidth, which are produced by the out-of-phase cross-coupling between resonators 2 and 5. These symmetrical TZs will increase filter selectivity, enabling us to improve such parameter while enlarging the filter bandwidth in order to reduce the in-band insertion loss.

In addition, if another out-of-phase cross-coupling between resonators 1 and 6 is considered, a pair of TZs at the real axis is introduced, which helps us flatten the group delay response with a corresponding trade-off on the rejection lobe level. In Fig. 3.36, a sketch of the filter configuration is shown, highlighting the magnetic direct couplings (k_{12}, k_{23}, k_{34}, k_{45} and k_{56}) and the electric cross-couplings (k_{16}, k_{25}).

As it is well known, the resonator unloaded Q is directly related to the filter selectivity: the higher the Q_u, the better the selectivity and the lower the IL of the filter. One of the fundamental problems of filter design is that the IL is inversely related to the

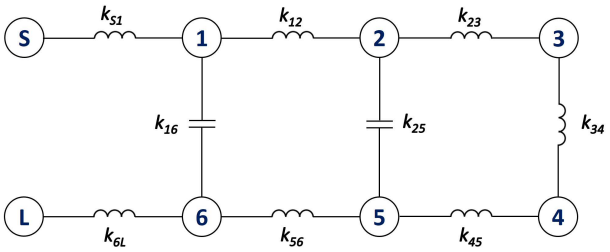

Figure 3.36: Filter topology for K-band specifications: 6-pole filter having 2 magnetic cross-couplings, between resonators 1 and 6, and between resonators 2 and 5.

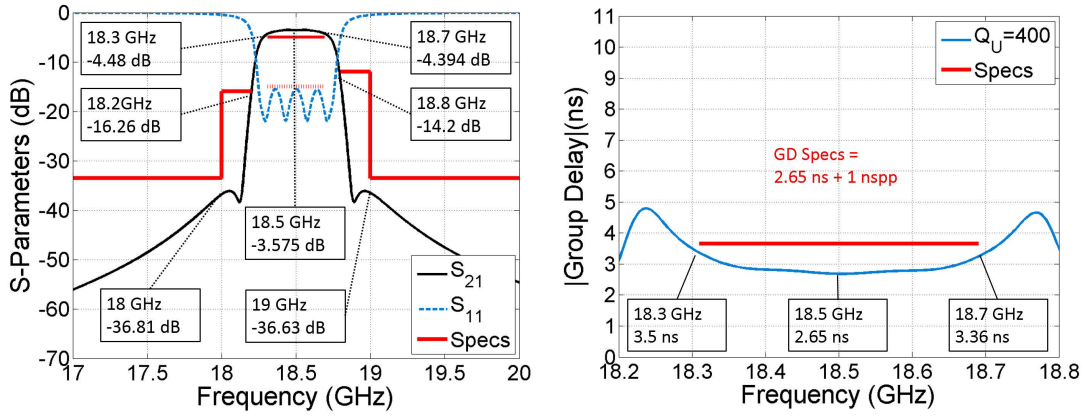

(a) (b)

Figure 3.37: (a): S-parameters responses for K-band filter. (b): Group delay response.

filter bandwidth, so that high Q_u is necessary to achieve a reasonably flat passband with acceptable IL in narrow band filters. According to Table 3.10, the K-band filter can be considered a narrow band design, being FBW around 2%. So, a Q_u close to 450 is required, which is high when compared to the C-band case.

Concerning the K-band filter analysis, circuital simulations have been carried out again considering the resonator model with losses. The filter response in terms of S-parameters and group-delay are shown in Fig. 3.37. The resonator Q_u should be higher than 400 for obtaining IL under 4 dB with less than 1 dB of variation along the passband. Return loss remains constantly below -15 dB independently of the resonator Q-factor. Fig. 3.37 shows that the group delay variation for the proposed filter topology satisfies requirements, while Table 3.12 shows the filter parameters for the K-band case.

Being Q_u the bottleneck requirement for the K-band filter, our approach to fulfill specifications is based on the use of the LTCC technology for implementing the proposed solution. This allows us to obtain coaxial SIW resonators having higher Q_u and reasonable cavity size at 18.5 GHz. The Ferro A6M green tape [110] ($\epsilon_r = 5.9 \pm 0.02$, $\tan\delta = 9 \cdot 10^{-4}$) has been selected as dielectric material, due to its very low loss tangent and low permittivity compared to other commercial green tape.

In order to satisfy specifications, we have started designing the coaxial SIW cavity to resonate at 18.5 GHz by reducing as much as possible the capacitive patch side and by increasing the inner via diameter. Again, this approach enables us to increase the Q_u of the coaxial resonator. Due to fabrication process limitations, the diameter of the inner via d_v has been set to 0.5 mm. In fact, increasing too much d_v could generate via-posting problems, which is an accumulation of conducting paste during the via-filling step that

Table 3.12: K-band Filter Extraction

Filter Parameter	Unit	Value
Q_e		54.21967
$k_{12} = k_{56}$		0.01891
$k_{23} = k_{45}$		0.01496
k_{34}		0.01610
k_{16}		-0.000975
k_{25}		-0.000868
$f_{0,1} = f_{0,6}$	GHz	18.49863
$f_{0,2} = f_{0,5}$	GHz	18.49859
$f_{0,3} = f_{0,4}$	GHz	18.49807

could cause stack-up deformations. Standard LTCC design rules would recommend to stagger via holes vertically (i.e. zig-zag position of the holes between layers) in order to limit the paste accumulation, being this a very simple and effective solution. Nevertheless, in such coaxial SIW topology, the via holes that form the inner conductor are not recommended to be staggered vertically, since the need for cover pads in each layer can affect the EM performance of the topology in terms of Q_u and resonant frequency. Finally, we have chosen a reasonable wide value for the inner via diameter so that it is possible to stack up to five green tape layers guaranteeing a proper via filling.

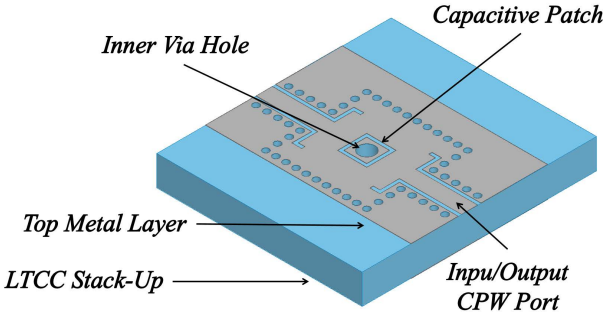

Figure 3.38: 3D view of the coaxial resonator for the K-band case.

Finally, the filter stack-up is composed of 5-layers Ferro A6M substrate, where each layer has a thickness of $h = 0.254$ mm in green state. Therefore, taking into account the tape shrinkage in Z-axis from green state to fired state (i.e. $28 \pm 0.3\%$ of shrinkage), the final thickness of the stack-up will be 0.9144 mm. In order to reduce the capacitive patch perimeter, we fixed this value to the minimum one permitted by the fabrication process. This means that the patch side corresponds to the smallest cover pad that surrounds the inner via hole (i.e 0.15 mm of cover pad per side, thus 0.3 mm bigger than d_v). Thus, to resonate at 18.5 GHz, the patch side r_p and the inner via hole diameter d_v have been set to 0.8 mm and 0.5 mm, respectively, resulting in an isolating gap s_c of 0.125 mm. It means that the resonator slope parameter is $b = 24.6$ mS that gives a $C_l = 0.155$ pF, a $Z_0 = 47.4\,\Omega$ and an electric length of 49°. The 3D view of the proposed resonator is shown in Fig. 3.38. During the filter design steps, the resonant frequency of the structure will be set at the desired values by adjusting just s_c.

3.4.3 Filters Design

The design procedure that has been applied for the two six-pole filters is based on the synchronous frequency tuning of each resonator, the tuning of the couplings between resonators and the external Q-factor of the first and last resonator. Starting from given specifications for both cases, filter approximations using ideal lumped LC resonators and frequency-invariant inverters have been initially obtained, and then substrate integrated coaxial-based filters have been modeled using distributed circuit models. Tables 3.11 and 3.12 list both filter approximations.

After the computation of the physical filter dimensions of the actual hardware, EM full-wave simulations have been necessary to optimize both filter responses. In this context, filter physical dimensions have been synthesized by dividing the filter structure into sections, and then relating each section and a specific physical dimension with proper filter parameters (i.e. Q_e, $k_{i,i+1}$, etc.). Thus, specific parametric curves have been calculated for each parameter that describe the properties of the coaxial SIW resonators, as it has been demonstrated in the previous chapter by now.

In the following, the physical dimensions of the C-band filter that connects each parameter with the specific parametric curve of the coaxial SIW resonators are listed. These physical dimensions have been modified during the filter design to optimize the simulated response. It is worth mentioning that all 3D EM simulations have been performed with ANSYS HFSS 2014.

- Electric external coupling: the insertion p_e of the CPW probe within the capacitive patch controls the external coupling Q_e (see Fig. 2.26).

- Electric inter-resonator coupling: the CPW coupling probe insertion $p_{k(i,i+1)}$ within the capacitive patches controls $|k_{i,i+1}|$ (see Fig. 2.19).

- Magnetic inter-resonator coupling: the cross-coupling is function of the post-wall iris width W_{25} (see Fig. 2.17-(b)).

- To set the resonant frequencies $f_{0,i}$ of the coaxial SIW resonators that form the C-band filter, we set the values of r_p and d_v while the air gap s_p will be the design parameter (see Fig. 2.4). Narrower the spacing, lower the resonant frequencies.

Since the K-band filter has been implemented using magnetic direct couplings and electric cross-couplings, the design physical dimensions are now:

- Magnetic external coupling: the length of the bend slots $w_{e,1}$ of the CPW-to-SIW transition controls the external coupling Q_e (see Fig. 2.23).

- Magnetic inter-resonator coupling: direct couplings $|k_{i,i+1}|$ depend on the post-wall iris width $W_{i,i+1}$ (see Fig. 2.17-(b)).

- Electric inter-resonator coupling: the CPW coupling probe insertion p_k within the capacitive patches controls the cross-couplings between resonators 1-6 and 2-5 (see Fig. 2.19).

- Again, to adjust the resonant frequencies $f_{0,i}$, we set the values of r_p and d_v while the spacing s_p will be the design parameter.

Table 3.13: C-band Filter Design and Optimization

Parameter	Unit	Initial	Final
$p_{e,1}$	mm	1.801	1.7309
$s_{p,1} = s_{p,6}$	mm	0.1367	0.2095
$s_{p,2} = s_{p,5}$	mm	0.1355	0.1484
$s_{p,3} = s_{p,4}$	mm	0.1357	0.1472
$p_{k,12} = p_{k,56}$	mm	1.461	1.4592
$p_{k,23} = p_{k,45}$	mm	1.1453	1.2723
$p_{k,34}$	mm	1.2444	1.3293
$W_{k,25}$	mm	2.8668	1.7215

Other parameters of the coaxial SIW filters have not been modified in the filter design steps. Table 3.13 and 3.14 list the final results of the optimization process compared to the initial filter configurations for the C-band filter and K-band filter, respectively, in terms of dimensions of the design parameters. As can be seen, variables that control the resonant frequencies of the filter elements have suffered wide variations with respect to the starting points. This is mainly due to the lower external coupling level of the resonator that has been used for extracting the resonant frequency curves versus the air gap. As it is well known, the coupling level modifies the resonant frequencies of a coaxial SIW resonator: lower Q_e, lower f_r.

Finally, Fig. 3.39 and Fig. 3.40 depict the final layouts of the coaxial SIW filters for the C-band and K-band case, respectively, which include the vertical transition for SMD assembly onto a host substrate.

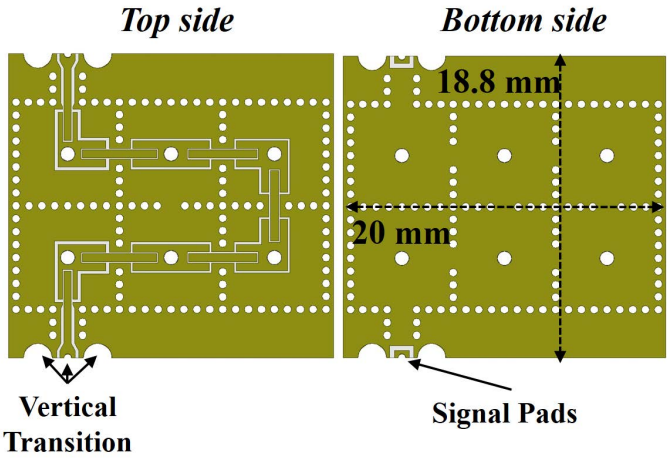

Figure 3.39: Final layout of the self-packaged C-band filter.

The total size of the 6-pole C-band filter including the vertical transition is only 18.8×20 mm^2 (i.e. $0.78 \times 0.84\,\lambda_g^2$ and $0.25 \times 0.266\,\lambda_0^2$), showing a remarkable very compact size. It is worth mentioning that a low-cost single-layer PCB fabrication process can be employed for fabricating such devices in TMM10i material.

Concerning the K-band filter, the total size of the layout including the vertical transition is $10 \times 10 \times 0.9144$ mm^3 (i.e. $1.5 \times 1.5 \times\ 0.14\lambda_g^3$ and $0.617 \times 0.617 \times 0.06\,\lambda_0^3$), taking into account that the SIW resonator cavity size is $w_{siw} \times l_{siw} \times h = 3.3 \times 3.3 \times 0.9144$ mm^3.

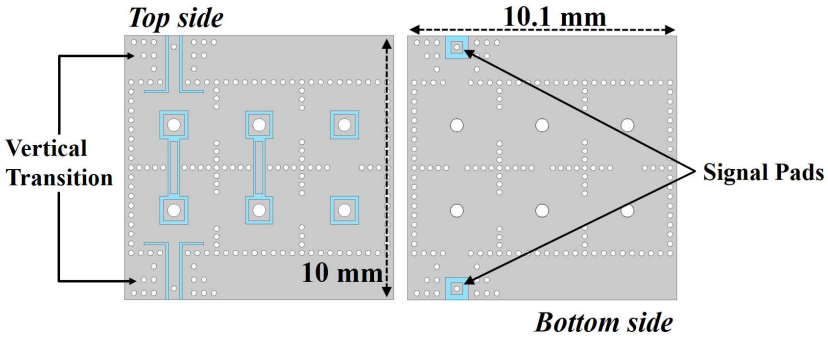

Figure 3.40: Final layout of the self-packaged K-band filter.

Table 3.14: K-band Filter Design and Optimization

Parameter	Unit	Initial	Final
$w_{e,1}$	mm	0.9534	0.87
$s_{p,1} = s_{p,6}$	mm	0.1244	0.1222
$s_{p,2} = s_{p,5}$	mm	0.1244	0.114
$s_{p,3} = s_{p,4}$	mm	0.1244	0.123
$W_{12} = W_{56}$	mm	1.3898	1.3723
$W_{23} = W_{45}$	mm	1.285	1.2844
W_{34}	mm	1.3045	1.2955
$p_{k,16}$	mm	-0.22199	-0.225
$p_{k,25}$	mm	-0.22533	-0.225

3.4.4 Simulated Results of the Filters

Since both 6-pole filters are being fabricating during the drafting of this Thesis, it has not been possible to show measured results of these prototypes. Nevertheless, simulated results will be deeply analyzed in the following sections, so that preliminary conclusions can be extracted.

3.4.4.1 C-band Filter

Concerning the C-band case, Fig. 3.41 shows the initial filter responses and the optimized filter responses in terms of (a) S-parameters and (b) group delay response that are obtained using 3D EM simulations.

As it is clearly shown, the C-band filter does not satisfy specification at the upper band, especially at 4.25 GHz where the rejection is 18.75 dBc instead of 30 dBc. Even though, the rejection satisfies totally requirements below 3.75 GHz, especially at lower frequencies where the filter provides more than 55 dBc of rejection (i.e. below 3.375 GHz). Even if the group delay variation exceeds the specification from 3.875 GHz to 3.89 GHz, where it gets a maximum variation of 0.35 ns from the target value, this specification is satisfied in the 95.6% of bandwidth, which means from 3.89 to 4.125 GHz.

Moving to the in-band performance, both insertion and return losses are fulfilled. The in-band flatness is around 0.54 dB, less than the required value of 1 dB, and 2.1 dB at 4.05 GHz is the minimum IL value in the passband. Moreover, the return losses are always

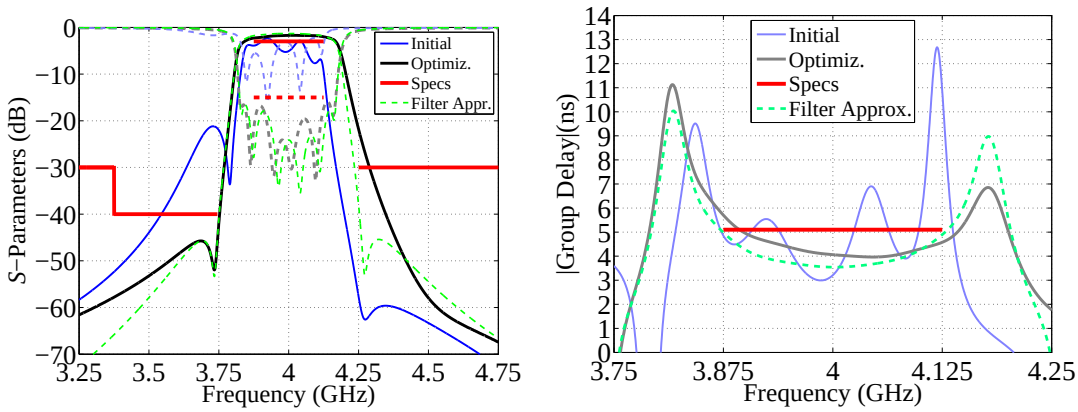

(a) (b)

Figure 3.41: (a): Initial and optimized simulated S-parameters responses for the C-band filter. (b): Initial and optimized simulated group delay response.

better than 18.15 dB, which means that are more than 3 dB better than required.

3.4.4.2 K-band Filter

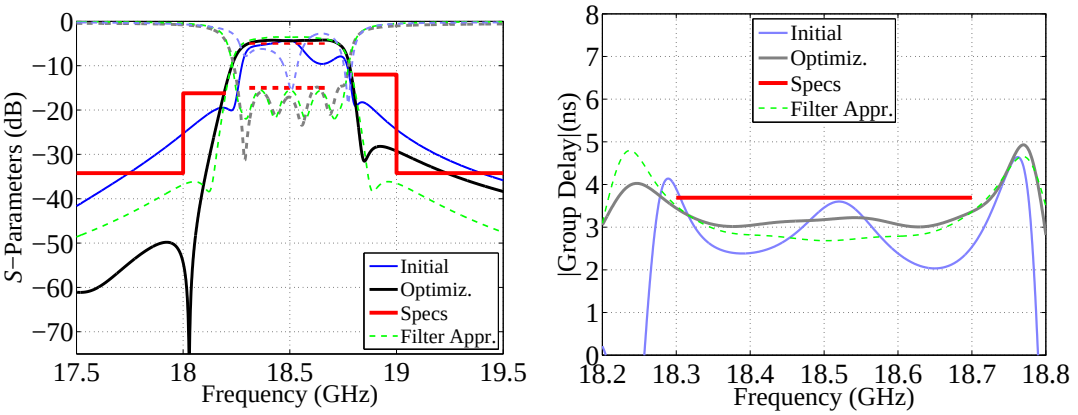

(a) (b)

Figure 3.42: (a): Initial and optimized simulated S-parameters responses for the K-band filter. (b): Initial and optimized simulated group delay response.

Fig. 3.42 highlights initial and optimized responses of the (a) S-parameters and the (b) group delay responses, separately, for the proposed K-band filter. As it is clearly shown, the K-band filter satisfies specification at the lower band, especially at 18 GHz where the rejection is 51.8 dBc, much better than the required 35 dBc. Also at 18.2 GHz the filter response satisfies the specification, providing a rejection level of 12 dBc better than the target value.

As Fig. 3.42-(a) clearly shows, the filter does not comply with the specifications at the upper band. Especially, at 19 GHz the rejection is 5 dBc worst than expected, and the S_{21} response is below the required level only beyond 19.2 GHz. Nevertheless, in the case of the K-band filter, priority has been given to fulfill the requirements in terms of

in-band group delay and rejection at the lower band, providing flexibility when setting the specifications above 19 GHz.

Concerning the in-band performance, the filter fulfills requirements in terms of both insertion and return losses. The minimum IL value is 4.22 dB at 18.62 GHz, and return losses are always below 15 dB, having a minimum value of 15 dB at 18.63 GHz. It is worth to mention that the in-band flatness completely fulfills requirements, showing a variation of 0.6 dB over the passband. Here, the maximum IL value is 5 dB at lower edge of the passband (i.e. 18.3 GHz).

The introduction of the cross-coupling between the first and last resonators of the filter have permitted us to fulfill the group delay requirements, which was the primary goal of the design. Over the entire bandwidth, the maximum variation is just 0.44 ns, which is just half of the targeted value.

3.4.5 Mixed Cross-Coupling

Both simulations of the proposed filters show that the responses are not symmetrical, since the TZs will present different rejection levels at either sides of the passband. This effect is mainly due to the mixed response of the coupling topologies that have been used, which presents both magnetic and electric components at the same time. As it has already been mentioned for the proposed structures, the total coupling magnitude will be obtained as the difference between the magnetic and the electric contributions.

As it can be observed in Fig. 3.42-(a) for the K-band filter, the upper band TZ is closer to the passband than the lower band TZ. This means that the electric cross-coupling between resonator 2 and 5 is providing a higher coupling value above the passband than below the passband. Since in this filter direct couplings have been implemented using magnetic couplings and the cross-couplings using the electric ones, it is clear that the electric contribution in the cross-coupling becomes dominant at higher frequencies with respect to the magnetic one. Thus, the result is a more coupled TZ above the passband than below.

To confirm that, let us take a look to the C-band filter. This has an inverse coupling configuration: electric for the direct couplings and magnetic for the cross-coupling. Looking at the simulated response shown in Fig. 3.41, it can be seen that the upper TZ does not appear while the lower one is centered at the desired frequency. So, again the magnetic contribution of the cross-coupling decreases at higher frequencies with respect to the electric one, thus providing a total cross-coupling values so weak that the TZ is not visible.

To sum up, the magnetic and electric contribution of the mixed cross-coupling are changing over frequency with different slopes. Therefore, it seems that, for a fixed coupling configuration, the magnetic contribution becomes weaker than the electric contribution for increasing frequencies.

Chapter 4

Analog and Digitally Tunable Filters

In this chapter, continuously and discretely tunable filters based on the proposed coaxial SIW technology are successfully designed, fabricated and measured, providing a broad description of the designed devices. Since tuning elements are key factors when designing such reconfigurable components in terms of EM performance, in this work varactor diodes, PIN diodes, RF MEMS switched capacitors and RF MEMS resistive switches are considered and employed for providing frequency-agility of coaxial SIW resonators.

As it will be shown in the following sections, experimental and simulation results are in good agreement, showing the potential advantages of this kind of reconfigurable structures in terms of tuning range, compactness and design flexibility. Moreover, additional advantages are the following ones: analog or digital tuning range easily implantable, simple integration, negligible power consumption and low-cost fabrication process. Additionally, the use of RF MEMS allows us to improve the power capabilities of reconfigurable filters.

4.1 Background

The availability of high-Q tunable resonators is of primary concern in the design of low-loss reconfigurable filters for microwave applications. These devices, among other applications, are of enormous importance in the development of future multi-band multi-standard miniaturized front-ends. While frequency and bandwidth tunability have been extensively demonstrated in planar and waveguide technologies using different tuning elements (e.g. varactor diodes, ferroelectrics, RF MEMS, piezoelectric actuators, motors, etc. . .), an increasing interest has grown on electronically tunable SIW cavity resonators as an enabling technology for the design of very low-loss tunable filters that can be an alternative to filter banks in several applications.

Among the vast availability of tuning elements that enables frequency-agility in microwave devices, there is a growing interest on RF MEMS because they are called to be key elements in the future generations of tunable filters, tunable antennas, reconfigurable matching networks and so on. These components have been developed since the 1970s, but only in the early 1980s, various research groups in the United State of America (USA) have been studying the possibility to create MEMS switches for low-frequency applications. The basic idea was essentially to create miniature devices that use a mechanical movement to achieve a short circuit or an open circuit in a transmission line, so that an RF MEMS switch should operate in a similar way to conventional radio-frequency mechanical relay, but on a silicon chip size scale.

4.2 Continuously Tunable Filter

4.2.1 Analog Tuning in Coaxial SIW Technology

The main advantage of the proposed topology for implementing frequency-agility in SIW components stems from the fact that the resonant frequency can be easily controlled by changing the loading capacitance C_l that is located at the top metal layer. The frequency tuning is achieved by modulating that capacitance using a suitable capacitive tuning element. In order to achieve continuous tuning range, GaAs varactor diodes are used, enabling a fine control of the centre frequency at the cost of a partial degradation of the resonator EM performance in terms of Q_u.

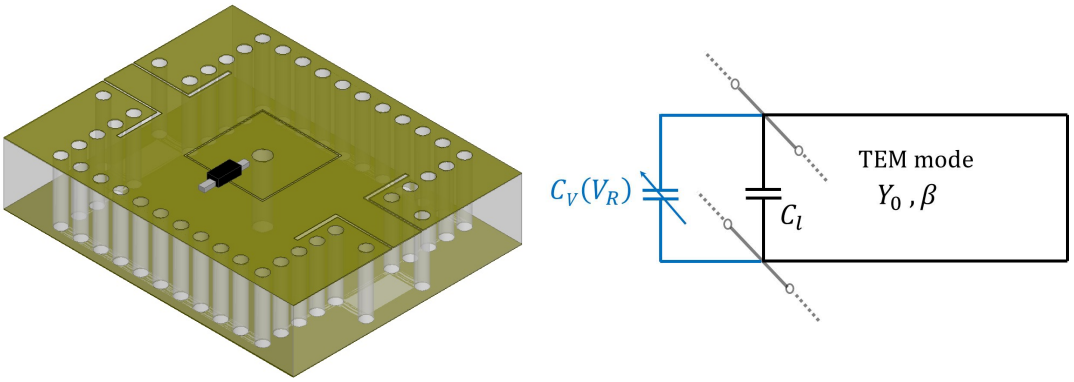

Figure 4.1: (a) First attempt of reconfigurable coaxial SIW resonator and (b) its equivalent circuit.

Let us consider a coaxial SIW square cavity as microwave resonator and a varactor diode as tuning element. The simplest scheme for implementing a tunable coaxial SIW resonator and its equivalent circuit are shown in Fig. 4.1. The tuning element and the loading capacitance would be in a shunt connection, achieving an easy and effective control of the resonator f_R. Anyway, it is clear to observe that the tuning element is short-circuited to ground at both sides due to presence of the inner via hole at the center of the loading patch, thus the varactor diode cannot be biased properly.

To operate in a reverse bias state the varactor diode, the cathode and the anode should be connected at two different patches, then a DC voltage between them can be applied. Thus, Fig. 4.2 shows the modified layout of a reconfigurable coaxial SIW resonator.

It consists on the same SIW cavity where a floating metal patch has been introduced between the capacitive patch and the ground plane of the SIW resonator, being completely isolated from them. The loading capacitance C_l, which would initially include the capacitance between the loading metal patch and the SIW top plate, can be controlled by inserting a varactor diode connecting both the capacitive patch and the floating metal island, as it can be seen in Fig. 4.2-(a). The varactor cathode is connected to the metal island, where the bias voltage can be directly applied by means of simple wire, and then, the anode is connected to the capacitive patch, which is short-circuited to ground by means of the inner via hole.

Looking at the equivalent circuit of Fig. 4.2-(b), the air-gap of the floating island generates a capacitance, named C_S, which is in series connection with the varactor capacitance. Since its value is usually much lower than C_V, C_S would dominate the series

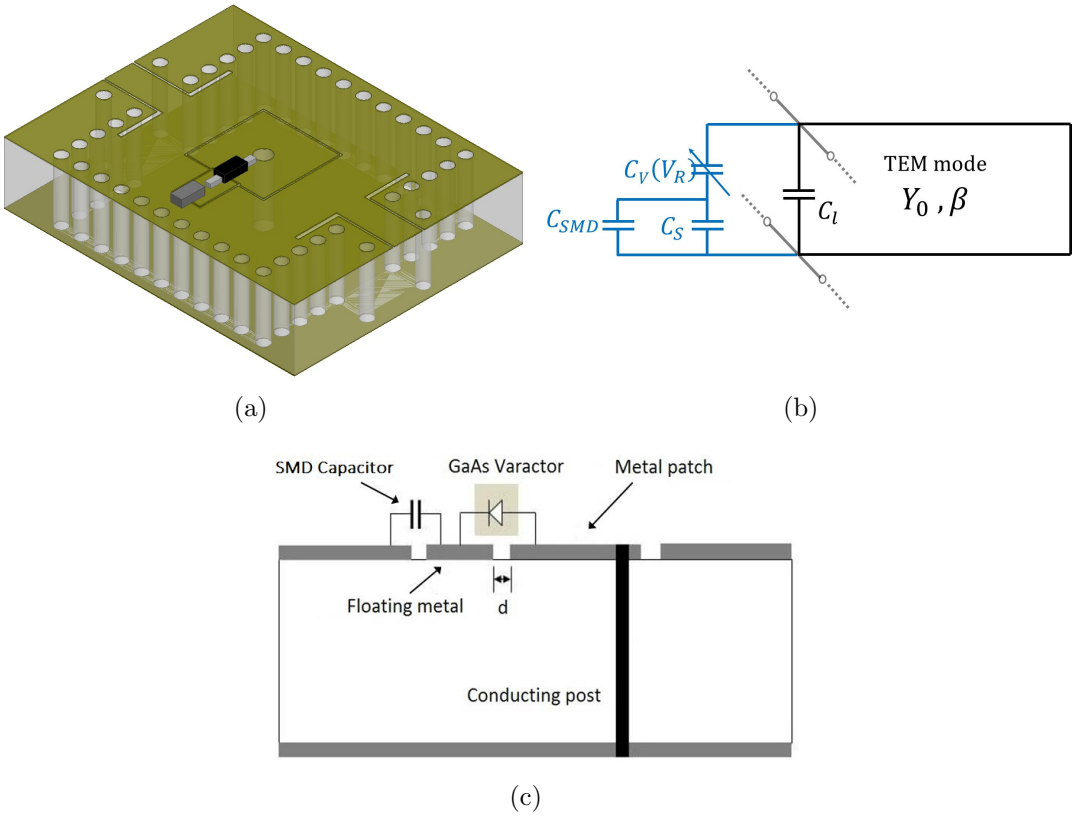

Figure 4.2: (a) Varactor-tuned coaxial SIW resonator, (b) its equivalent circuit and (c) a cross-section of the tunable SIW resonator showing the inner via hole and both floating and capacitive metal patches.

connection, thus reducing the modulation effect of C_V on the resonator C_l.

To solve that problem, a fixed SMD capacitance C_{SMD} is then inserted in series between the floating metal and the patch in order to control the tuning range, since C_{SMD} and C_S turn out to be in a shunt connection. The bigger the C_{SMD} is, the largest the effect of C_V on the resonant frequency of the structure, because C_V would dominate the series connection between itself and the shunt connection of C_{SMD} and C_S.

4.2.2 Tuning Element

A hyper-abrupt junction GaAs varactor has been used as tuning element. Particularly, we have chosen the varactor diode MA46H200 from MACOM$^{\text{TM}}$ [111] that presents a gamma γ that varies between 1.13 and 1.38 in the range $V_R = 2 - 20$ V, while the total capacitance C_V for $V_R = 4$ V is ranging between 0.5 pF and 0.7 pF. Taking into account $\gamma = 1.25$ as recommended in the data-sheet, the varactor capacitance would range from 0.2 pF to 1.2 pF for a reverse bias voltage between 20 and 2 V, which are similar to the ones used in the previous simulations.

Being 3000 the measured quality factor of the component at 50 MHz for $V_R = 4$ V, the extracted series resistance R_S of the varactor is around 1.76 Ω. Therefore, in the frequency band of interest, the varactor Q-factor should vary from 50 at 3 GHz to 75 at 2 GHz, again, if $V_R = 4$ V. Fig. 4.3 shows the performance of the selected MA46H200 from MACOM$^{\text{TM}}$.

Concerning the bias of the varactor diode, we have kept the varactor bias circuit as

Gamma 1.25 Hyperabrupt Tuning Varactors
Breakdown Voltage @ 10 μA = 22 V minimum
Reverse Current @ 16 V = 100 nA maximum
Gamma = 1.13 - 1.38, V_R = 2 to 20 V

Model Number	Total Capacitance (pF)	Nominal Total Capacitance Ratio (C_{T2}/C_{T20})	Typical Q
	f = 1 MHz V_R = 4 Volts	f = 1 MHz V_R = 2/V_R=20	f=50 MHz V_R = 4 Volts
MA46H200	0.5 - 0.7	3.0	3000

(a)

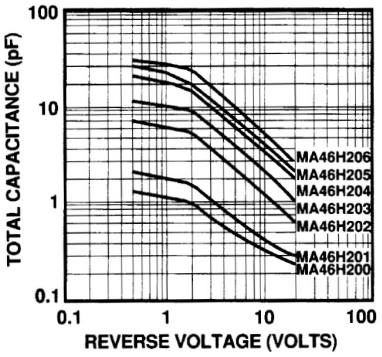

(b)

Figure 4.3: (a) Performance table of MA46H200 from MACOM^{TM}. (b) Typical performance curves C_V vs V_R.

simple as possible, so a thin wire has been connected from the floating metal island to a bias pad for providing the reverse voltage. Finally, DC bias and ground have been isolated from the RF path by means of 1 MΩ resistors.

4.2.3 Resonator Design

The first reconfigurable structure proposed in this chapter is a continuously tunable resonator [112]. It has been designed for working at S-band, concretely between 2 and 3 GHz. In this design, the basic cell is a modified structure for implementing high-Q frequency agile resonators based on the coaxial SIW topology, and its configuration is shown in Fig. 4.4.

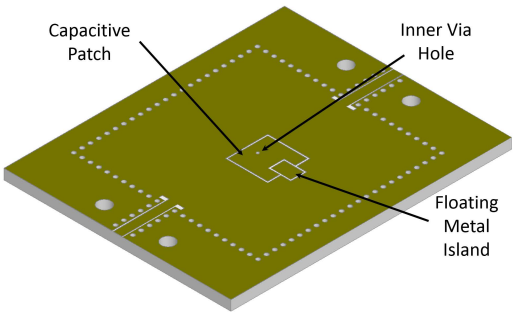

Figure 4.4: (a) View of the tunable SIW resonator showing both floating and capacitive metal patches. The varactor is connected between the island and the capacitive patch.

In order to validate the proposed concept, we have studied the tuning range and unloaded quality factor of a varactor-tuned resonator. Firstly, a device centered around 3.5 GHz has been designed using full-wave 3D simulation of the structure using ANSYS HFSS 2014. Then, in order to combine 3D EM simulations with circuital simulations using the equivalent models of the lumped components, internal ports have been created at the places where the varactor diode and the fixed SMD capacitance will be inserted and assembled. The dimensions of the proposed coaxial SIW resonator can be seen in Table 4.1, where $r_{i,x}$, $r_{i,y}$ and $s_{p,i}$ stands for the floating patch sides and its gap, respectively.

Table 4.1: Dimensions of the varactor-tuned coaxial SIW resonator. (Units: mm)

l_{siw}	27.5	r_p	6	s_p	0.1
$r_{i,x}$	3	$r_{i,y}$	2	$s_{p,i}$	0.1
d_{siw}	0.6	d_v	0.4	p_{siw}	1.25
w_e	1	l_e	0.5	h	1.524

In this design, in order to obtain a value of C_l close to 2 pF, the slope parameter of the SIW coaxial resonator is set to be $b = 39$ mS. We have chosen a dielectric substrate that presents $\epsilon_r = 3.55$, loss tangent $\tan\delta \approx 3 \times 10^{-3}$ and a thickness of $h = 1.524$ mm.

The resonator has been strongly under-coupled in order to enable us the accurate measurement of Q_u from the transmission response of the device, thus the S_{21} parameter has been kept below the level of -20 dB. As it has been demonstrated in [8], the unloaded Q-factor is extracted by

$$Q_u = \frac{Q_L}{1 - S_{21}(f_R)} \tag{4.1}$$

where the loaded quality factor Q_L is obtained from

$$Q_L = \frac{f_R}{\triangle f_{R,-3dB}} \tag{4.2}$$

To study the tuning range of the proposed solution, EM simulations have been carried out considering that the varactor capacitance would change between 0.1 pF and 1.5 pF. Different values of C_{SMD} have been considered to understand its effect on the tuning range. Therefore, such EM simulations can be used for checking out the equivalent circuit of the tunable resonator shown previously.

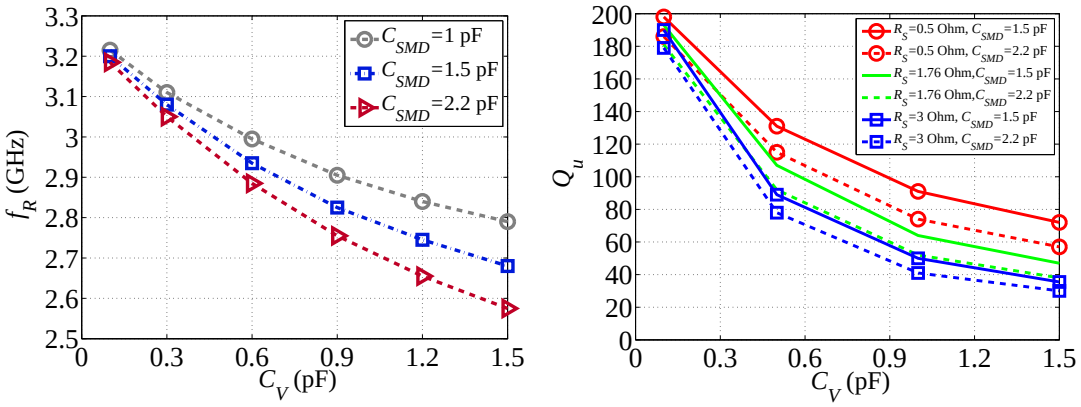

(a) (b)

Figure 4.5: (a) Resonant frequency versus varactor diode capacitance for the tunable SIW resonator. (b) Resonator Q_u versus varactor diode capacitance for the tunable SIW resonator.

As Fig. 4.5-(a) confirms, the resonant frequency decreases for increasing values of C_V. Moreover, the tuning range can be increased if bigger C_{SMD} are used. For instance,

increasing the latter capacitance from 1 pF to 2.2 pF, the tuning range can be increased from 15% to 21.5% considering the predefined varactor capacitive range.

Thus, these results demonstrates that C_{SMD} is in a parallel connection with the capacitance of the floating island. Note that for the proposed varactor capacitance range, to obtain more than 20% of tuning range, C_{SMD} should be higher than 1.5 pF.

Concerning the EM performance of the proposed solution, different values of the varactor R_S have been considered in order to evaluate the degradation of the resonator response in terms of Q_u due to the tuning element. For these simulations, we consider that SMD capacitors show a Q of 100.

The resonator Q_u curves are shown in Fig. 4.5-(b), where it is possible to see that, considering $R_S \approx 1.8\,\Omega$, Q_u value would range between 180 at 3.2 GHz and 40 at 2.6 GHz for $C_{SMD} = 2.2$ pF. Taking into account that the Q_u of coaxial SIW building block is close to 240, it is clear that the the varactor Q is controlling the EM performance of the microwave device while performing the tuning.

Even though slightly, better values can be obtained reducing C_{SMD}, as the case of C_{SMD} =1.5 pF, but this would be valid only in narrower tuning ranges. So, for the proposed SIW coaxial resonator, C_{SMD} should be chosen equal or bigger than 1 pF in order to increase the capacitive effect of the varactor without worsening too much the resonator Q_u. For instance, a C_{SMD} of 2.2 pF has been selected in the following tests, so that the tuning range of the structure can be maximized.

The results shown in Fig. 4.5 demonstrate that the tuning range could be simply increased by designing combline SIW resonators with smaller C_l compared to the varactor capacitance. However, this approach would have the effect of increasing the losses of the reconfigurable microwave device, since the EM field would be mainly concentrated into the tuning variable capacitance, which usually has a lower Q-factor.

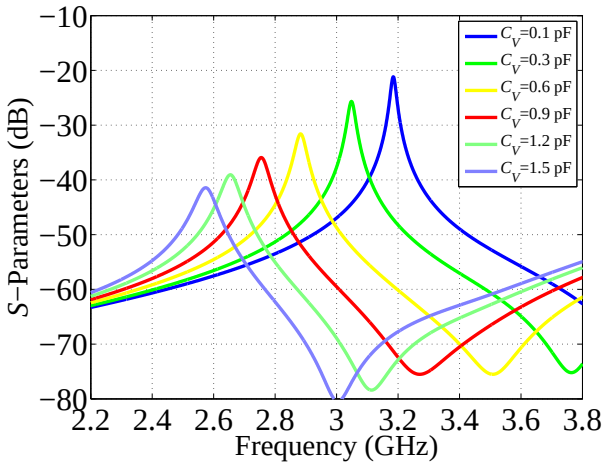

Figure 4.6: Simulation results of the tunable SIW resonator for a varactor capacitance ranging from 0.1 pF to 1.5 pF.

Finally, co-simulations of the varactor-tuned SIW resonator for different values of C_V have been carried out for the selected configuration, and the S_{21}-parameter response are shown in Fig. 4.6. The resonant frequency can be controlled between 3.2 GHz and 2.6 GHz changing C_V between 0.1 pF and 1.5 pF while considering $C_{SMD} = 2.2$ pF. That frequency variation corresponds to a tuning range of 600 MHz (i.e. 21% with respect to 2.9 GHz).

4.2.4 Filter Design

Moving to the varactor-tuned 2-pole SIW filter, this is firstly designed in its fixed state with equi-ripple FBW of 5%, centre frequency of 3.1 GHz while the requested in-band return losses are 20 dB. The filter consists on two square coaxial SIW cavity resonators coupled by means of post-wall iris, while 90° bend slots of the CPW-to-SIW transition control the external coupling.

To implement in a dielectric substrate having $\epsilon_r = 3.55$, loss tangent $\tan\delta \approx 3 \times 10^{-3}$ and thickness of $h = 1.524$ mm, an SIW coaxial resonator that has $b = 39$ mS, the inner hole diameter has been set to 0.4 mm, while the square capacitive patches present $r_p = 6$ mm and $s_c = 0.1$ mm. Thus, we have obtained that $C_l \approx 1.98$ pF, the characteristic coaxial impedance is $Z_0 = 137\,\Omega$, while the resonator electrical length is 10.7° that is $0.03\lambda_g$ at 3.1 GHz, which can be considered a very short electrical length.

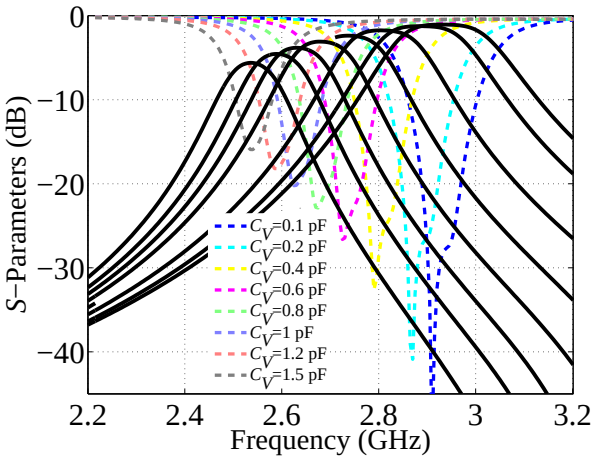

Figure 4.7: Simulated results of the tunable filter for a varactor capacitance ranging from 0.2 pF ($f_c = 2.88$ GHz) to 1.5 pF ($f_c = 2.54$ GHz).

To perform EM simulations of the tunable filter, internal ports have been used for considering the presence of the tuning elements and SMD capacitors, as previously explained. Then, a final optimization of the filter dimensions is performed for the minimum capacitance value of the tuning element.

For obtaining the targeted external quality factor, the width and length of the 90° bend slots of the CPW-to-SIW transition have been adjusted (i.e. see Section 2.4.1). Following the same procedure, the direct inter-resonators couplings between resonators 1 and 2 have been adjusted by changing the width of the magnetic post-wall irises (i.e. see Section 2.3.1).

In addition to the varactor diode MA46H200 from MACOM™, in the tunable filter we have chosen to use SMD capacitances of 1.5 pF, since this value guarantees a good compromise between wide tuning range and reduced Q_u degradation. The simulated response of the designed tunable filter for the whole varactor capacitance range can be seen in Fig. 4.7. The tuning range should be close to 400 MHz around a central frequency of 2.7 GHz, with filter IL that should be better than 7 dB at the lowest tuning frequency.

4.2.5 Experimental Results

4.2.5.1 Tunable Cavity Resonator

A picture of the fabricated varactor-tuned coaxial SIW cavity resonator [112] including the biasing wires is shown in Fig. 4.8. This was designed, fabricated and measured in a 1.524 mm-thick Rogers R4003C substrate ($\epsilon_r = 3.55 \pm 0.05$, $\tan\delta = 2.7 \times 10^{-3}$@10 GHz) with 17 μm/17 μm Cu clad.

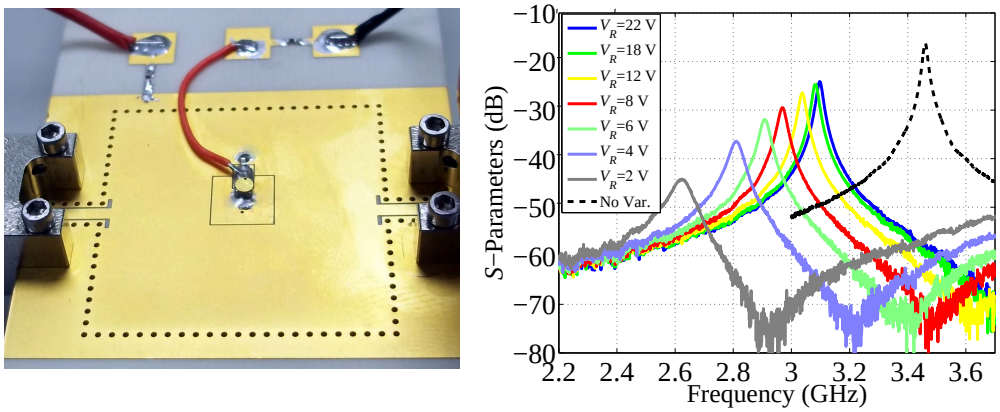

(a) (b)

Figure 4.8: (a) Photography of the varactor-tuned cavity resonator in coaxial SIW topology. (b) Measured frequency responses for the varactor-tuned resonator changing the varactor bias voltage V_R.

The prototype has made use of a standard single-layer PCB processing technology and ENIG finishing that is wirebondable, and guarantees easy assembly of SMD components. The final size of the resonator is 27.5×27.5 mm^2 (i.e. $0.55 \times 0.55\ \lambda_g^2$ and $0.29 \times 0.29\ \lambda_0^2$ at 3.1 GHz), showing an important size reduction compared to its equivalent conventional SIW counterpart due to the capacitive loading of the metal patch.

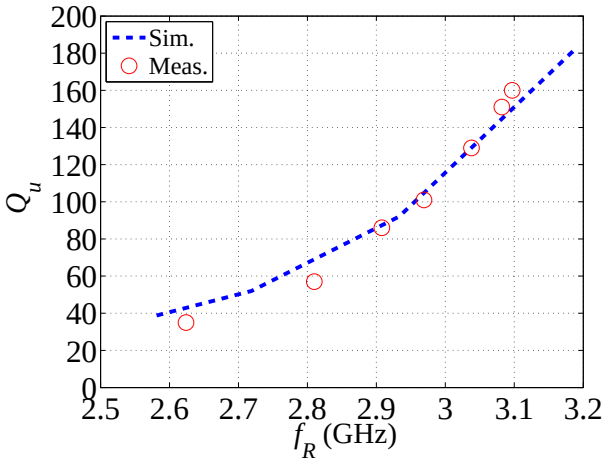

Figure 4.9: Q_u versus resonance frequency of the tunable resonator as a function of the reverse voltage applied to the varactor.

Fig. 4.8-(b) shows the measured S_{21} response for the tunable coaxial SIW resonator. The black dotted line in Fig. 4.8-(b) is the S_{21} response of the SIW resonator before the

assembly of the tuning element, which shows a measured resonant frequency of 3.46 GHz. Thus, we have estimated for the fixed coaxial SIW resonator a Q_u around 220, as expected from simulations. A tuning range of almost 20% is observed when changing the reverse bias voltage of the varactor from 2 to 22 V, between 2.64 GHz and 3.1 GHz, respectively. From these results, we can suppose that C_V should have changed between 0.225 pF for $V_R = 22$ V and 1.29 pF for $V_R = 2$ V.

The extracted $Q_u$of the resonator as a function of f_R is shown in Fig. 4.9. These values have been compared to the simulated results previously shown in Fig. 4.5. Note that the resonator Q_u ranges from ≈ 40 to 160, being above 100 for the first 150 MHz of frequency shift. Note that the slight increase of losses between experimental and simulated results is attributed to the mounting and soldering of the components, and especially for using the bias wire to provide the varactors with DC voltage. In addition, the slightly frequency shift towards lower frequencies of the resonator responses is mainly due to fabrication and substrate laminate tolerances.

4.2.5.2 Tunable 2-pole Filter

To fully validate our reconfigurable solution, the 2-pole bandpass Chebyshev filter was designed, fabricated and measured following the same procedure and materials [113]. The layout of the proposed filter with its main dimensions is shown in Fig. 4.10-(a). The SIW filter size is 27.5×55.6 mm^2 (i.e. $0.55 \times 1.08\ \lambda_g^2$ and $0.29 \times 0.58\ \lambda_0^2$ at 3.1 GHz), while including the input/output ports the filter length would be 69.5 mm. An equivalent SIW filter based on the TE_{101} fundamental mode would be centered at 4.2 GHz, thus the coaxial topology makes for a 15% of frequency reduction. The CPW feeding lines present a trace width of 1.3 mm and a ground plane spacing of 0.15 mm, so the characteristic impedance is closed to 50 Ω. The diameter of the vias for the SIW cavities and irises is 0.6 mm, and the via pitch in the walls is 1.25 mm.

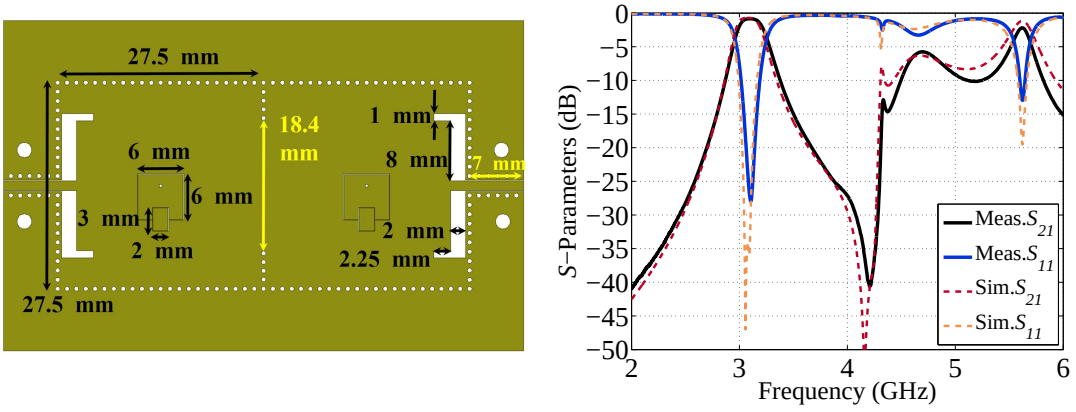

(a) (b)

Figure 4.10: (a) Layout and dimensions of the varactor-tuned 2-pole filter in coaxial SIW topology. (b) Measured (*solid*) and simulated (*dashed*) wide-band frequency response for the fabricated 2-pole filter before the assembly of the varactor diode.

The measured S-parameter responses of the fixed 2-pole filter (i.e. before the assembly of the diode) can be seen in Fig. 4.10-(b). The filter response shows a 3-dB bandwidth of 200 MHz around 3.11 GHz, which means that the 1-dB fractional bandwidth is 6.45%. Thus, there has been a frequency shift of about 24 MHz (i.e. 0.8% of shift) to higher

frequencies due to the tolerance on the through-hole electro-plating process that affects the final metal layer thickness, and especially to the wider isolating gaps of the capacitive patches. Nevertheless, the measured response shows insertion losses around 0.8 dB at mid-band, just 0.2 dB more than expected. The estimated filter Q-factor has been calculated to be close to 170, instead of being 195 as extracted from full-wave simulations. The return losses are better than 20 dB between 3.06 GHz and 3.14 GHz.

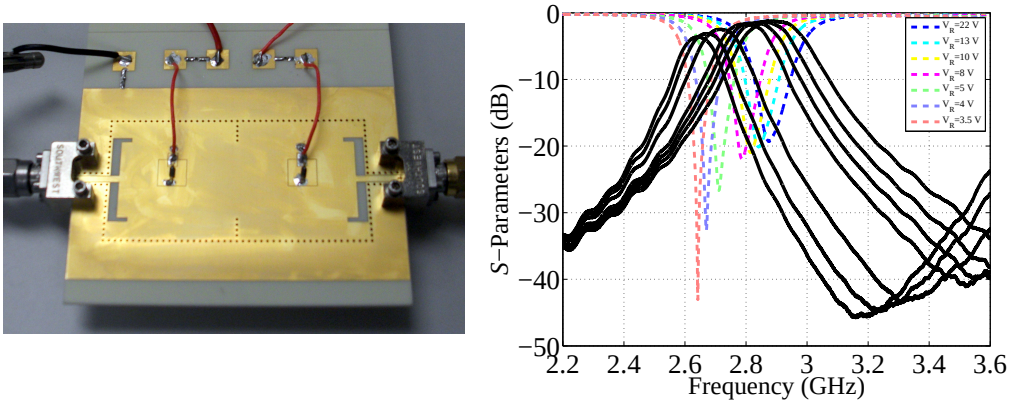

(a) (b)

Figure 4.11: (a) Photo of the varactor-tuned 2-pole filter in coaxial SIW topology. (b) Measured wide-band frequency response for the varactor-tuned 2-pole filter changing the varactor bias V_R.

Moving to the tunable prototype, Fig. 4.11-(a) includes its picture, and the measured S-parameter responses are shown in Fig. 4.11-(b). As it can be seen, the measured results agree quite well with the simulations. The filter centre frequency can be tuned between 2.64 and 2.88 GHz (i.e. 8.7% of tuning range) for a bias voltage ranging from 3.5 V to 22 V. The insertion losses vary from 1.25 dB to 3.62 dB across the whole tuning range. It is worth mentioning that the 2-pole filter suffers a strong variation of the fractional bandwidth. The 1-dB FBW varies between 2.61% for 3.5 V and 4.6% for 22 V along the tuning range, from 3.5 V to 22 V, which is due to the short length of the coaxial resonators.

Taking into account these values, the extracted filter Q-factor would range between 150 at 2.88 GHz and 80 at 2.64 GHz. Decreasing V_R below 3 V would further reduce the filter centre frequency, although the filter Q would be drastically degraded by the poor performance of the varactor diode. In fact, if $V_R = 2$ V, the tunable filter is centered at 2.52 GHz showing a 1-dB FBW of 2.33% and a measured insertion loss of 6.5 dB that corresponds to a filter $Q = 55$. In this case, the tuning range increases up to $\simeq 14\%$.

4.2.5.3 Power Handling Measurements

The presence of the tuning elements introduces non linear effects that will limit the maximum input power level of the tunable filters. In order to evaluate the power handling of the proposed tunable topology, different tests have been performed.

Results of intermodulation distortion and linearity of the fabricated filter can be seen in Fig. 4.13. These effects have been measured for the worst-case scenario, which means in the case of a high varactor capacitance. Thus, a two-tone Third-order Intermodulation Intercept Point (IIP3) of +24 dBm has been measured for a bias voltage $V_R = 5$ V (i.e.

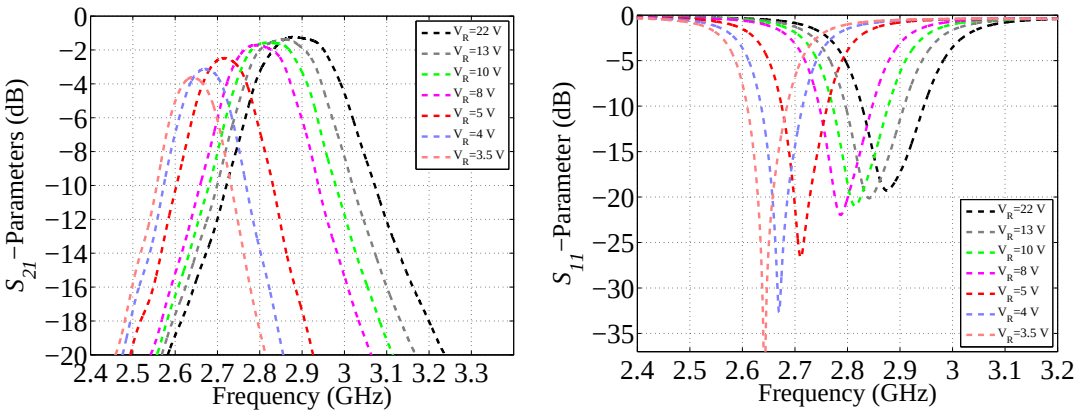

(a) (b)

Figure 4.12: (a) Measured S_{21} frequency responses.(b) Measured S_{11} frequency responses.

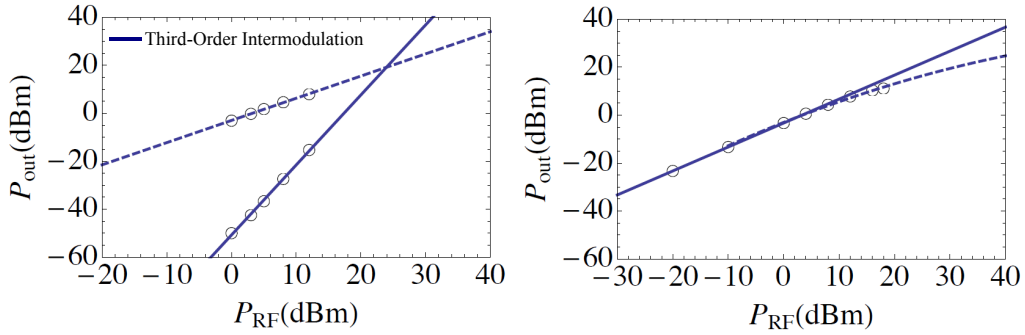

Figure 4.13: Results of (*left-thick*) two-tone IIP3 point and (*right*) measured filter output power as a function of the input carrier level.

that should correspond to $C_V \simeq 0.6$ pF) and a two-tone separation $\triangle f = 50$ kHz. Finally, the 1-dB compression point of the filter has been also measured for the same bias voltage and it results to be only +10 dBm, which is a typical value of semiconductor-based tuning elements.

4.3 SMD Packaged Varactor-Loaded Tunable Filter

The results shown in the previous section have demonstrated that the proposed topology can be used for the design of wide tunable microwave devices with unloaded quality factors easily better than 50-70. Nevertheless, it is clear that in the design of this structure, greater focus should be dedicate on improving the performance of the coupling structure. As the previous results have shown, the coupling coefficients suffer wide variations in the case of short coaxial resonator, resulting in strong reduction of the filter bandwidth over frequency.

As it has been demonstrated in [31], if a tunable combline filter is designed to be as close as possible to 52.885° long in the middle of the tuning range, octave tuning could be obtained with just 20% deviation in passband bandwidth.

It is thus evident that following this approach and obtaining the recommended value is

hard-pressed to achieve precisely with coaxial SIW topology and PCB fabrication process. As a matter of fact, θ_0 only depends on the laminate thickness in such structure, thus only preassigned values are made available by suppliers of dielectric substrates in the market. By the way, the high design flexibility of the coaxial SIW topology allows us to play with different key parameters at once when setting up a cavity resonator. So, the designers will be able to satisfy diverse specifications at a time by controlling properly the fundamental parameters of the coaxial topology, which are C_l, Z_0 and θ_0.

Additionally, even if combline SIW filters are intrinsically smaller when compared to conventional approaches for the design of SIW filters that use the fundamental TE_{101}-mode [68–70], further size reduction is usually prevented due to the limited thickness of the substrate or the room required for integration of the tuning elements.

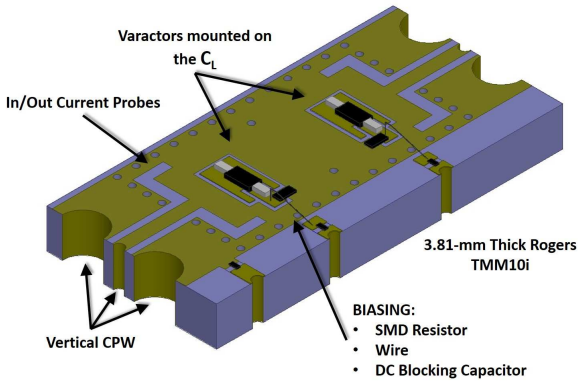

Figure 4.14: Scheme of the miniaturized tunable filter comprising the coaxial resonator SIW filter with the tuning element and passive components mounted on top.

In this context, the SMD packaging of the coaxial SIW filters, which was presented in Section 3.3.1, permits us to solve both problems: increasing the resonator θ_0 without losing planar integration. To do that, a 3.81 mm-thick laminate of Rogers Thermoset Microwave Material TMM10i substrate ($\epsilon_r = 9.8 \pm 0.245$ and $\tan\,\delta = 0.002$) [79] with 17 μm/17 μm Cu clad has been selected for the design of a 2-pole tunable filter using varactor diodes. This material belongs to the Rogers TMM$^{\text{TM}}$family that are ceramic, hydrocarbon, thermoset polymer composites designed for high plated-thru-hole reliability applications. TMM laminates are available in a wide range of thickness, dielectric constants and claddings. The selected laminate presents a very high permittivity that will help us reduce the filter size.

It is worth mentioning that it is not recommended by PCB manufacturers to select ceramic laminates like the Rogers TMM10i that are thicker than 4 mm. That recommendation concerns mainly fabrication problems related to the aspect ratio relative to the manufacture of the PCB. Aspect ratio is the ratio between the thickness of the board and the size of the drilled hole before plating and is used as a guide to ensure that a manufacturer does not exceed the mechanical capability of the drilling equipment. Additionally, manufacturing problems can be related to plated-through holes as the case of SIW structures. In fact, after the drilling phase in the PCB process, via holes must be made conductive and then electroplated with copper. For ceramic substrate boards, drilling typically produces impurities due to the high temperature decomposition products of the laminate system. So, before the holes can be plated through, these impurities must be removed by chemical processes, or by plasma-etching. Therefore, if the laminate thickness is increased, such processes can not remove properly these impurities, so that

the holes are not plated suitably and they do not become integral with the deposited copper.

4.3.1 Tuning Element

In this design, we are going to employ the tuning mechanism that has been used in the previous tunable resonator and filter. In addition, the reconfigurable filter should cover the same frequency band, which is the S-band below 3 GHz. Thus, GaAs varactors have been inserted in the capacitive loading patch in order to provide the filter with continuous frequency tuning. Concretely, abrupt GaAs varactor diode MGV050 − 18 from Aeroflex-Metelics™ [114] has been used as tuning element due to its higher Q-factor than the one used previously. It exhibits a typical capacitance ratio of 3.4 for a reverse voltage between 22 and 0 V, being the junction capacitance $C_J = 0.38$ pF for 4 V of biasing. The nominal Q-factor at 50 MHz is 4000 giving an estimated series resistance of about 2 Ω. The diode presents a capacitance from 0.26 and 0.77 pF for $V_R = 20 - 1$ V, respectively, with a Q-factor ranging from 100 to 67 at the frequencies of interest.

4.3.2 Filter Design

The proposed filter structure is depicted in Fig. 4.14. It consists on two coaxial resonators coupled through an iris window, and a standard CPW-to-SIW transition is used for the external coupling. The filter size is only 16.5×33 mm^2 including the bias network and the vertical transition. That corresponds to $0.5 \times 1\ \lambda_g^2$ and to $0.16 \times 0.32\ \lambda_0^2$ at 3 GHz, the latter highlighting the excellent compactness of the structure.

The use of thicker material with high permittivity aids in extending the resonator electrical length, which is now close to 42° (i.e. $0.11\lambda_g$ at 3 GHz). That value means tripling the electrical length of the previous resonator, being comparable to the optimal value proposed in [31].

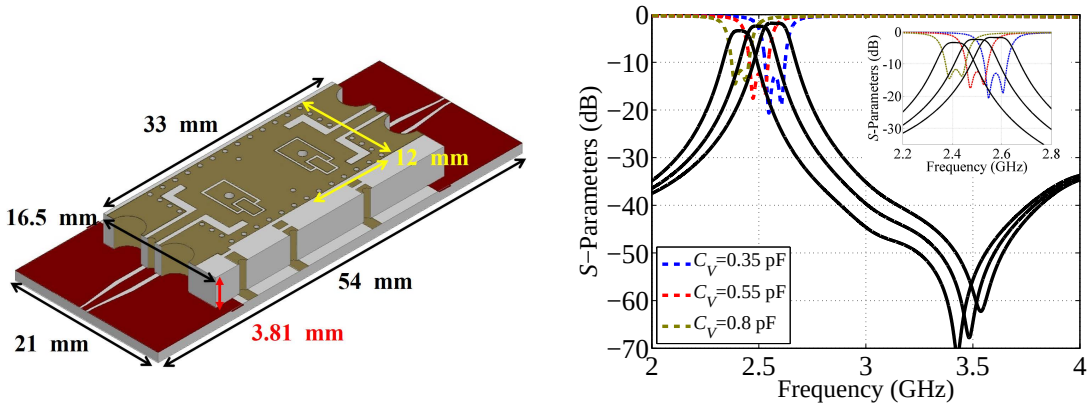

(a) (b)

Figure 4.15: (a) Scheme of the fixed filter mounted on top of a carrier substrate showing the SMD assembly approach and the footprint of the input/output and bias signals.(b) Simulated results of the continuously tunable filter changing the varactor capacitance.

The use of longer resonators means moving to lower frequencies the filter passband. In order to compensate such effect and center the filter again at the S-band, the characteristic

coaxial impedance has been reduced with respect to previous design. As it is shown in (2.1), the lower Z_0, the higher the resonant frequency of the structure. To do that we have increased the diameter of the inner via hole (i.e. D_V=1.1 mm), and we have also reduced the SIW cavity size up to l_{siw}=12 mm. This permits achieving that the characteristic coaxial impedance is just $Z_0 = 47.2\,\Omega$.

Finally, by setting the slope parameter to $b = 30$ mS, a loading capacitance of $C_l = 1.25$ pF has been obtained that is good compromise between wider tuning range and acceptable Q degradation over frequency. To implement that, the capacitive patches are now rectangular with $r_{p,x} = 4.9$ mm and $r_{p,y} = 2.9$ mm, while the air-gap spacing has been set to $s_c = 0.3$ mm. A scheme of the filter mounted onto a carrier substrate is shown in Fig. 4.15-(a), where its main dimensions are also displayed.

In addition to the GaAs varactor diode MGV050 − 18, fixed SMD capacitances of 1.5 pF have been mounted between the floating islands and the top metal layer. The simulated response of the proposed continuously tunable filter for the whole varactor capacitance range can be seen in Fig. 4.15-(b).

The varactor-tuned filter can be tuned by approximately 200 MHz around 2.5 GHz, showing IL between 1.9 dB and 3.2 dB. The return loss should maintain the level of 10 dB over the whole tuning range, while the filter 1-dB FBW should slightly decrease from 4% at the upper edge to 3.4% at the lower edge of the tuning range.

4.3.3 Experimental Results

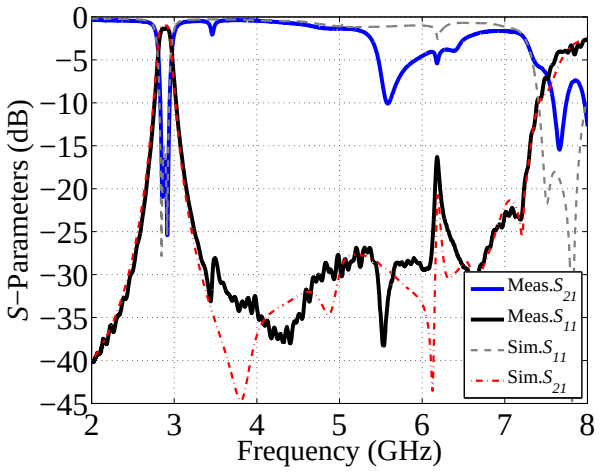

Figure 4.16: Comparisons of simulation (*dashed*) and measurement results (*solid*) for the 2-pole fixed SIW filter with input/output lines on the Rogers R4003 carrier substrate. The EM simulation was done using ANSYS HFSS 2014.

First, the frequency responses of the fixed 2-pole SIW filter before the assembly of the lumped components have been measured, and Fig. 4.16 depicts the comparison between the simulated and measured results. The measured response has been shifted down by about 17 MHz at 2.88 GHz, corresponding to 0.5% of shift, and the measured in-band IL has increased from 1 dB to 1.4 dB. This is due to the additional loss of the ENIG finishing that has been used in the PCB fabrication process of this filter. However, the measured frequency response of the fixed filter shows a good Q_u factor of 201.

Finally, the SMD assembly of the tuning elements has been performed using a semi-automatic pick-and-place machine, and Fig. 4.17-(a) displays the complete prototype.

The measured results of the varactor-tuned filter are shown in Fig. 4.17-(b), where it is possible to observe a continuous tuning of the filter response from 2.4 to 2.6 GHz for biasing voltages between 0 and 22 V, respectively. Insertion loss ranges from 1.9 to 3.4 dB, while fractional bandwidth and return losses are kept almost constant along the tuning range. In fact, the 1-dB FBW ranges from 3.9% for $V_R = 22$ V to 3.3% for $V_R = 0$ V. The tuning range of the GaAs varactor tuned filter is 170 MHz that corresponds to 6.8% with respect to 2.5 GHz. Filter rejection higher than 35 dB is achieved up to 6 GHz. From measurements, the unloaded Q factor is estimated to be 145 for highest bias voltage and 110 for the lowest value, being more than 100 in the whole tuning range.

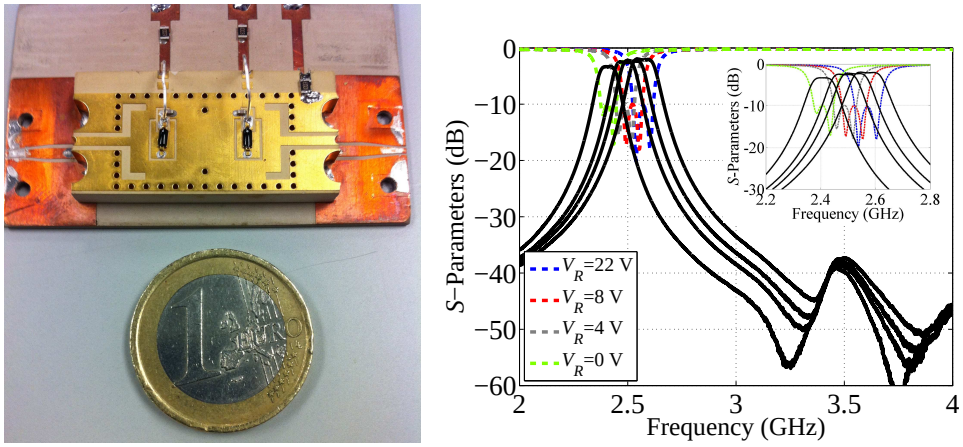

(a) (b)

Figure 4.17: (a) Photo of the fabricated and assembled filter with GaAs varactors.(b) Measured results of the tunable filter using GaAs varactors and mounted on top of the carrier substrate.

The results of the varactor-tuned filter are very promising, showing reduced variation of the filter FBW, especially if compared to the results of the tunable filter of Section 4.2. Fig. 4.18 gives that comparison between both filters, where it is possible to see how the filter IL behaviour is similar in both cases. The higher the loading effect of the varactor is, the lower the filter centre frequency is, the higher the filter losses are. In addition to this, the FBW behaviour has been clearly corrected by increasing the coaxial resonator length. Since the results are in very good agreement with the simulated results obtained using 3D EM simulations with circuital simulations (see red lines in Fig. 4.18), it is possible to claim that a proper modeling for these reconfigurable structures has been determined and used.

4.3.4 Power Handling Measurements

An Agilent Technologies E8257D analog signal generator, a vector spectrum analyzer and a power meter have been used in the test setup to measure power handling capabilities of the device, and results of inter-modulation distortion and linearity can be seen in Fig. 4.19. Since GaAs varactors are used as tuning elements, a two-tone IIP3 point of +25 dBm has been measured for a two-tone separation $\Delta f = 100$ kHz and for $V_R = 20$ V, as shown in Fig. 4.19-(a). The varactor capacitance would be close to 0.35 pF at this bias level.

However, increasing the varactor capacitance from 0.35 pF to 0.5 pF applying $V_R =$ 10 V, the IIP3 is only +18 dBm. Fig. 4.19-(b) presents the measured 1-dB compression

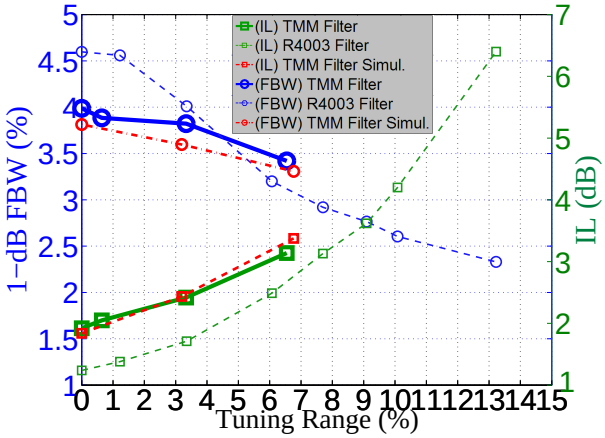

Figure 4.18: Results of filter 1-dB FBW (*blue lines*) and filter IL (*green lines*) versus tuning range for the varactor-tuned 2-pole filter in Rogers TMM10i (*solid lines*), compared to the results of the varactor-tuned 2-pole filter in Rogers R4003 (*dashed lines*). Red lines show the simulated results of the varactor-tuned filter in Rogers TMM10i of Fig. 4.15-(*b*).

point for the GaAs varactor tunable filter. The filter can handle up to +16.5 dBm at 2.6 GHz (V_R = 20 V) before power compression occurs. Decreasing the bias voltage to 5 V that corresponds to f_c = 2.5 GHz, the 1-dB compression point slightly decreases to +16 dBm.

4.4 Discretely Tunable Filters Using Switched Capacitors in RF MEMS Technology

Looking at the analog tuning mechanism that has been successfully implemented for the coaxial SIW structures up to now, it is evident that a simple digital tuning can be obtained by replacing the varactor diode by means of switched capacitors. These elements are usually composed by switches that would give different capacitance values when these are opened and closed. If we use such components as tuning elements in the proposed topology, the modulation of the loading capacitance should be performed discretely, depending only on the ratios between the available capacitance values provided by the switched capacitor. For obtaining a coarser tuning range with low-loss and high linearity, RF MEMS switched capacitors would represent an optimal solution.

Thus, a first attempt of digital-like tuning has been addressed by using RF MEMS switched capacitors, which will be assembled on the 2-pole filters of Section 4.2 (named FR-1) and Section 4.3 (named FT-2), respectively. The centre frequency of the filter is controlled by switching the RF MEMS switched capacitors. Note that the filter layouts have not been modified, showing the same characteristics already shown in the previous sections, since there is enough room for assembling the RF MEMS on the capacitive patches of both filters.

The idea is to compare the EM performance of these filters when different tuning elements and opposite reconfiguration mechanism are used, especially in terms of the unloaded quality factor, insertion loss, power handling and tuning range. In such a way, these differences can directly related to the properties of the tuning elements used.

In this context, tuning elements have a crucial impact on the filter performance as

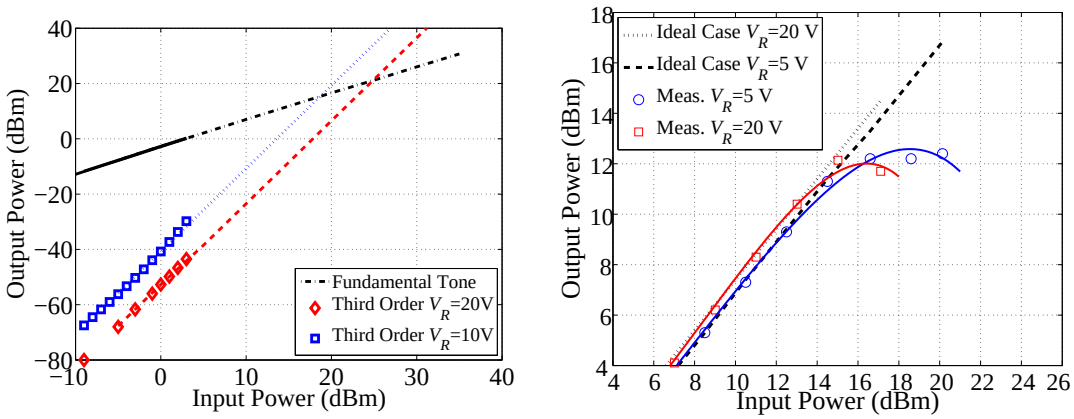

(a) (b)

Figure 4.19: (a) Measured IIP3 of the GaAs varactor tunable filter for a two-tone input signal with a frequency separation of $\Delta f = 100$ kHz.(b) Measured S_{11} frequency responses.

it has already been demonstrated. Even with high-Q Gallium Arsenide (GaAs) tuning varactors, the result is a degradation of Q_u joined to the introduction of non-linearities that limit the power handling of the device. Thus, RF MEMS are good candidates for implementing digitally switched capacitors with high-Q, very low power consumption and superior linearity.

4.4.1 Tuning Element

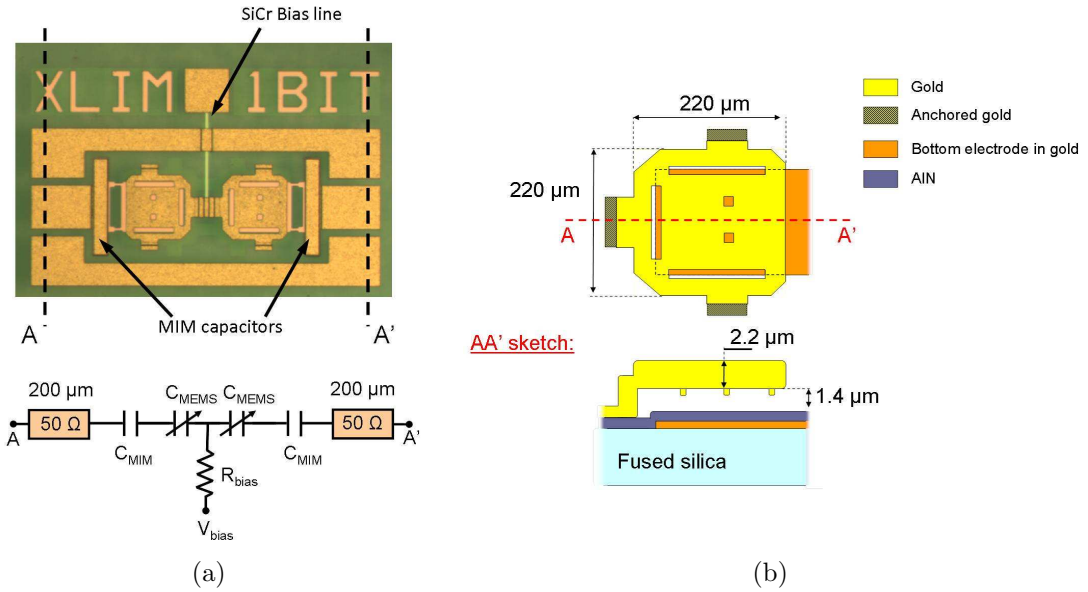

(a) (b)

Figure 4.20: (a) Picture of the 1-bit back-to-back RF MEMS switched capacitor and its equivalent circuit. (b) The MEMS structure is displayed, providing information about materials and dimensions.

In the proposed tests, 1-bit back-to-back RF MEMS switched capacitors have been chosen due to the high Q-factor and power handling performance. The digital tuning

has been obtained inserting an RF MEMS switched capacitor on the metal patch of each resonator. These tuning elements are connected to those patches by means of Au bondwires, which afford electrical connections. On the one hand, the bondwires connect the MEMS input RF pad and the loading patch. On the other, the MEMS output pad is connected to the SIW top metal layer that is the RF ground. Glue paste has been used to mount the MEMS on the filter surface providing excellent mechanical properties. It is worth mentioning that the MEMS capacitors will be biased by means of DC probes in these preliminary tests.

Concerning the RF MEMS components that have been employed, these are 1-bit back-to-back switched capacitors designed and fabricated at the XLIM laboratory of the Université de Limoges and the Centre National de la Recherche Scientifique (CNRS), in France. These are based on a 220 × 220 × 2.2 μm cantilever structure, maintained on both sides by tethers and separated from the bottom metal layer by a 1.8 μm gap [115]. A 0.4 μm Aluminum Nitride (AlN) layer has been deposited to isolate the cantilever from the bottom electrode when actuated. Fig. 4.20 shows a photo and the layout of the component, showing its main dimensions.

This tuning element has been fabricated on fused silica and placed in back-to-back configuration for improving power handling capabilities. Finally, two 1-pF Metal-Insulator-Metal (MIM) capacitors are placed in series with the movable structures in order to achieve good matching of the down-state. As provided by XLIM, the extracted values of capacitance are $C_{up} = 92$ fF and $C_{down} = 260$ fF, with an estimated Q-factor higher than 200 measured at 1 GHz.

4.4.2 Experimental Results

Detailed views of the assembled RF MEMS on both filters are shown in Fig. 4.21 for FR-1, and in Fig. 4.22 for FT-2. The measured results can be seen in Fig. 4.23, where (a) shows S-parameter responses of FR-1, and (b) of FT-2, respectively. It is worth mentioning that the RF MEMS position is different in the filter FT-2 with respect to filter FR-1, since the loading patch of FT-2 is smaller than the one of FR-1. Nevertheless, the bondwires have been done respecting the same interconnection between RF MEMS and coaxial SIW filter.

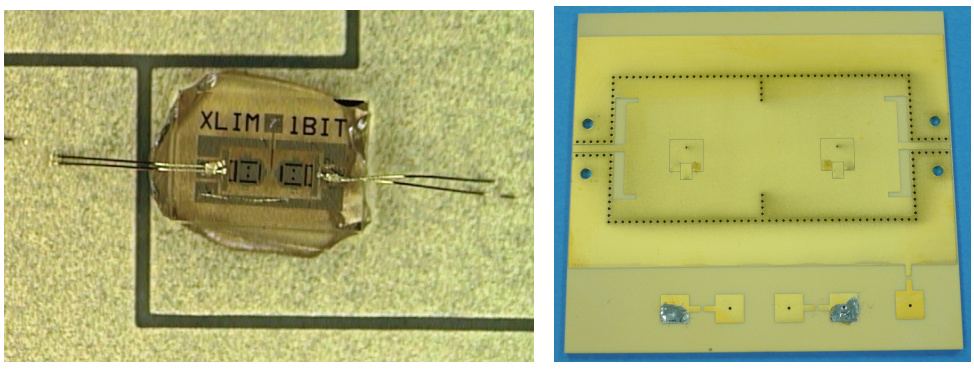

(a) (b)

Figure 4.21: (a) Photo of the 1-bit MEMS switchable capacitance mounted on the FR-1 filter using adhesive epoxy and bond-wires. (b) RF MEMS-tuned 2-pole filter in 1.524 mm-thick Rogers R4003.

In the case of the filter FR-1, the pass-band that can be switched from 2.98 GHz in the up-state to 2.61 GHz in the down-state. The corresponding insertion loss are about 1.45 and 4 dB, respectively. Therefore, the obtained tuning range is ≈ 400 MHz that corresponds to ≈ 13%. The 1-dB FBW ranges from 4.65% in the up-state to 2.75% in the down-state position. These values are comparable to the ones measured in the case of the varactor-tuned filter. The extracted unloaded Q-factors have been calculated from the measured S-parameter responses: the lowest measured value is 70 at 2.6 GHz, whereas the highest is 125 at 3 GHz, when the RF MEMS is in the up-state.

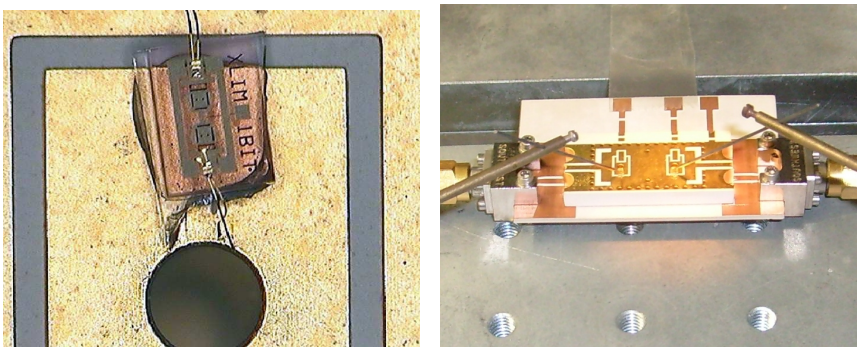

(a) (b)

Figure 4.22: (a) Photography of the 1-bit MEMS switchable capacitance mounted on the FT-2 filter using adhesive epoxy and bond-wires.(b) RF MEMS-tuned 2-pole filter in 3.81 mm-thick Rogers TMM10i during measurements. Probes have been used for biasing the MEMS.

The RF MEMS-tuned filter FT-2 shows a pass-band can be switched from 2.8 GHz in the up-state to 2.4 GHz in the down-sate, with insertion loss about 1.5 and 4.3 dB, respectively. The measured tuning range is 400 MHz that corresponds to 15.5% with respect to 2.6 GHz. The filter 1-dB FBW ranges from 3.2% to 2.8%, respectively for the up-state and the down-state position. This represents a slightly reduction across the whole tuning range, and it is comparable to the results of the analog tunable filters. The extracted unloaded Q-factors have been calculated from the measured S-parameter responses. In fact, the lowest measured value is 70 at 2.4 GHz, whereas the highest is 175 when the RF MEMS is in the up-state. The extracted filter Q_u are similar in both filters as expected from simulations.

The measured tuning range of filter FT-2 is slightly wider than filter FR-1, since the loading capacitance of its coaxial SIW resonator is smaller than the one of filter FR-1 (i.e. $C_{l,FT-2} \approx 1.25$ pF versus $C_{l,FR-1} \approx 1.95$ pF, respectively). Moreover, these results proof that if the MEMS assembly is realized on the loading patch, there is no different between positions in terms of performance.

It is worth mentioning that, in both filters, the measured tuning range is wider than the simulated one when taking into account the capacitance values given by XLIM research group. Thus, using post-tuning circuital simulations, the values of the MEMS switched capacitors have been extracted to be 95 fF in up-state and 691 fF in down-state. These wide gaps could depend on the MEMS assembly on the loading patches.

The presence of the MEMS fused silica substrate in close proximity of the isolating gaps would create parasitic capacitances that virtually increase the MEMS capacitance. Indeed, preliminary results have been obtained in a circuital simulator just including the

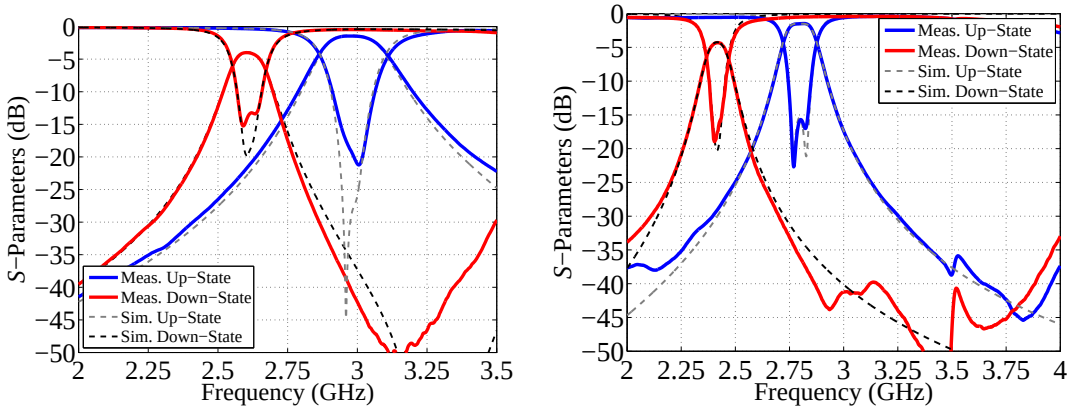

Figure 4.23: (a) Measured results of the tunable filter FR-1. (b) Measured results of the tunable filter FT-2, being mounted on top of the carrier substrate.

equivalent circuit of the MEMS devices attached to the 3D EM simulation box of the SIW filter. The latter does not contemplate the presence of the MEMS structure mounted on the top of the loading capacitances.

4.4.3 Power Handling Measurements

An Agilent Technologies E8257D analog signal generator, a vector spectrum analyzer and a power meter have been used in the test setup to measure power handling capabilities of the discretely tunable filters FR-1 and FT-2. It is well known that RF MEMS present better linearity than semiconductor devices. The measurements of the 1-dB compression point of both filters shown in Fig. 4.24 clearly demonstrate this superior performance. Note that power handling capabilities have been tested in the up-state position of the RF MEMS switched capacitors. This is the worst case in terms of self-actuation because as the RF power is increased the potential between the moveable and the fixed part of the MEMS is also increased, thus pulling the moveable part (i.e. the cantilever) downwards until commuting the MEMS state.

As can be seen in Fig. 4.24-(a), in the filter FR-1 the RF MEMS can handle up to 35 dBm before self-actuation occurs, resulting in the commutation of the filter response. Additionally, a 1-dB compression point of 33 dBm has been measured, which corresponds to 2 W, showing that such tuning elements provide the filter with high linearity over a wide dynamic range. Moving to the results of filter FT-2 that are shown in Fig. 4.24-(b), the self-actuation of the RF MEMS occurs when input power is 35.5 dBm, and a 1-dB compression point of 35 dBm has been measured.

4.5 Discretely Tunable Filters Using PIN Diodes

A novel concept for the design of discretely tunable filters based on the proposed combline topology in SIW is presented in this section. As Fig. 4.25 displays, a digital frequency tuning can be simply applied in coaxial SIW topology for the reconfiguration of resonators and filters. Let us consider the same coaxial SIW square cavity of the analog tuning case. The proposed approach makes use of switchable planar capacitances in order to modify

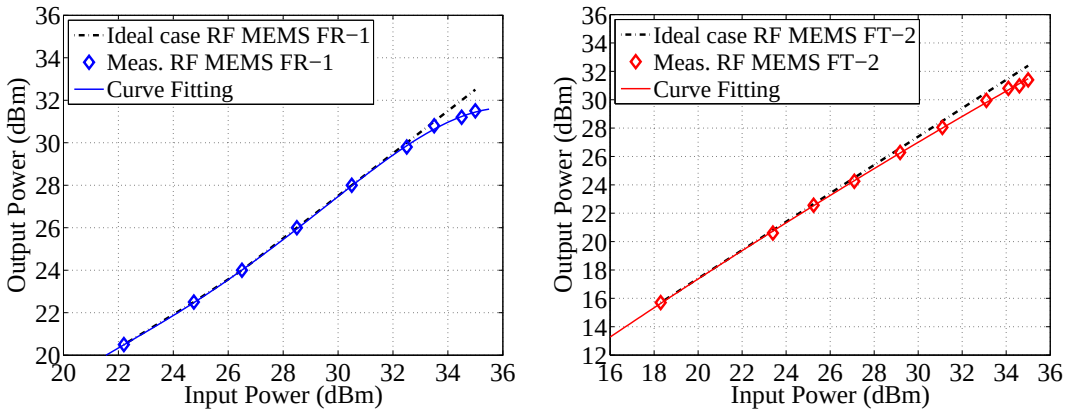

(a) (b)

Figure 4.24: Measured output power of the (a) tunable filter FR-1 and (b) tunable filter FT-2 using RF MEMS switched capacitors, which have been tested in up-state position.

the total capacitive loading of the combline resonator. The bit capacitances have been electrically isolated from the main part of the loading patch by closing a gap around them. These bits are called $C_{bit,n}$ in the following, and in the case of the structure of Fig. 4.25-(a), these would be ($C_{bit,0}$, $C_{bit,1}$ and $C_{bit,2}$).

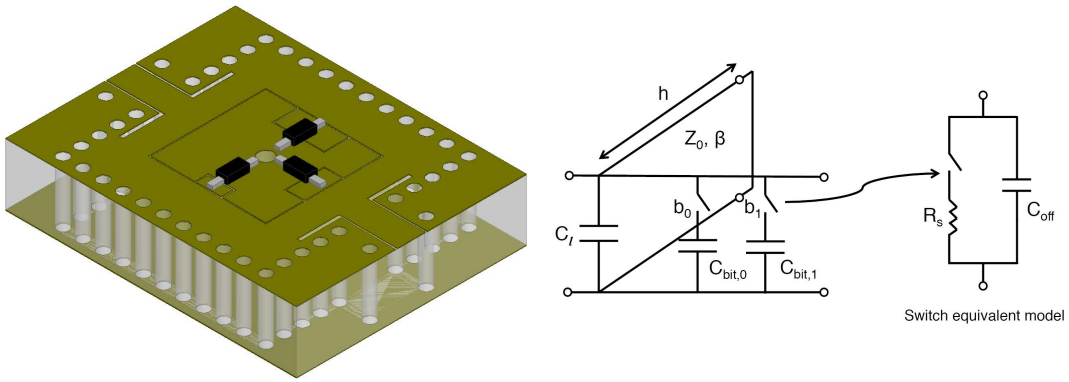

(a) (b)

Figure 4.25: (a) First attempt of digital-like reconfigurable coaxial SIW resonator and (b) its equivalent circuit.

Looking at the scheme of the proposed structure shown in Fig. 4.25-(a), it is clear that the proposed idea is to use switching elements to connect or disconnect these bit capacitances from the capacitive patch. In a specific way, the total C_l of the coaxial SIW resonator can be increased adding the capacitance of a bit when the relating switching element will be activated, thus performing the frequency tuning.

During the 3D EM simulation stages of this kind of reconfigurable SIW resonators, some important conditions must be taken into account. On the one hand, when the bit capacitance is connected, a small series resistance R_S has to be taken under consideration in series with the bit capacitance element, as shown in Fig. 4.25-(b).

On the other hand, when the bit capacitance is unconnected, it is necessary to consider the off-state capacitance C_{OFF} of the switching elements. As it will be proved later in

this section, C_{OFF} turns out to be in a series connection with the bit capacitance $C_{bit,i}$, while these are connected together in parallel with the main loading capacitance of the resonators. As a result, this configuration leads to a rise of C_l when tuning elements are in the off-state. In the following, let us use binary numbers to represent the state of the tuning elements, thus the symbol 1 means that the tuning element is switched on, otherwise the symbol 0 that is switched off.

Note that both the loading capacitance C_l and the bit capacitances $C_{bit,n}$ are integrated into the same top metal layer of the structure, as it can be seen in Fig. 4.25. Therefore, this approach would reduce the effect of the ohmic losses of the tuning elements on the cavity Q_u when compared to a varactor-loaded tunable filter, since the EM field distribution would be confined into the substrate instead of being concentrated into the diode when performing the tuning.

4.5.1 Tuning Element

To implement the digital tuning in such reconfigurable structure, PIN diodes can be employed as switching elements. As a matter of fact, a PIN diode is a diode with a wide, undoped intrinsic semiconductor region sandwiched between a p-type and an n-type regions. The $p-$type and n-type regions are typically heavily doped because they are used for ohmic contacts, as the case in this structure. These tuning elements will be assembled between the bit capacitances and the remaining metallization of the capacitive disk, which is connected to the inner conductor of the coaxial resonator. The latter makes for the bias of the diodes. The position and size of the bit capacitive patches inside the main loading one have been adjusted taking into account the size of the PIN diode, so that a simple assembly can be performed.

A glass PIN diode surmount chip MADP-042308-13060 from MACOM$^{\text{TM}}$ [116] has been used as tuning element. This device is a rugged silicon-glass PIN diode surmount chip$^{\text{TM}}$, which does not require wirebonds and shows low parasitic capacitance and inductance. This device features two silicon pedestals embedded in a low loss, low dispersion glass. The diode is formed on the top of one pedestal and connections to the backside of the device are facilitated by making the pedestal sidewalls electrically conductive. Selective backside metallization is applied producing a surface mount device. The top side is fully encapsulated with silicon nitride (silicon nitride passivation) and has an additional polymer layer for scratch and impact protection.

Fig. 4.26 shows the performance of the selected PIN diode from MACOM$^{\text{TM}}$. The diode off-state capacitance is 100 fF for a reverse bias voltage of $V_R = 10$ V, while the series resistance R_S is 1.38 Ω for a bias current of 20 mA.

Nevertheless, incorporating PIN diodes as switching elements implies some variations on the formerly described combline structure in order to isolate the PIN diode biasing network from the SIW filter. Since it is necessary to provide a DC current flow for switching a PIN diode, a novel integrated bias line has been created at both top and bottom metal layer of the SIW, as Fig. 4.27 shows. These lines enter the SIW cavity resonator through the via hole walls, connecting to each capacitance bit.

Each bias line consists on a high-impedance CPW line with two SMD inductors (i.e. $L_{1,T}$ and $L_{2,T}$) placed in series connection in order to avoid RF leakage towards the bias circuitry. To ensure that, a SMD capacitor $C_{1,T}$ is then assembled between the line and RF ground. The width c_b of the conductor and the air spacing s_b from the ground have been both set to 0.15 mm.

Electrical Specifications @ T_{AMB} = + 25 °C

Parameter	Symbol	Conditions	Units	MADP-042308-13060		MADP-042508-13060	
				Typ.	Max.	Typ.	Max.
Capacitance	C_T [1,3]	- 10V, 1 MHz [1]	pF	0.10	0.20	0.18	0.30
Capacitance	C_T [1,3]	- 10 V, 1 GHz [1,3]	pF	0.10		0.19	
Capacitance	C_T [1,3]	- 40 V, 1 MHz [1]	pF	0.09	0.20	0.18	0.30
Capacitance	C_T [1,3]	- 40 V, 1 GHz [1,3]	pF	0.10		0.18	
Resistance	R_S [2,3]	+ 20 mA, 1 GHz [2,3]	Ω	1.38		0.97	
Resistance	R_S [2,3]	+ 50 mA, 1 GHz [2,3]	Ω	1.18		0.87	
Forward Voltage	V_F	+ 10 mA	V	0.85	1.00	0.82	1.00
Reverse Leakage Current	I_R	-100V	µA		10		10
Input Third Order Intercept Point	IIP[3]	F 1= 1000 MHz F2 = 1010 MHz Input Power = +20 dBm I bias = + 20 mA	dBm	73		77	

(a)

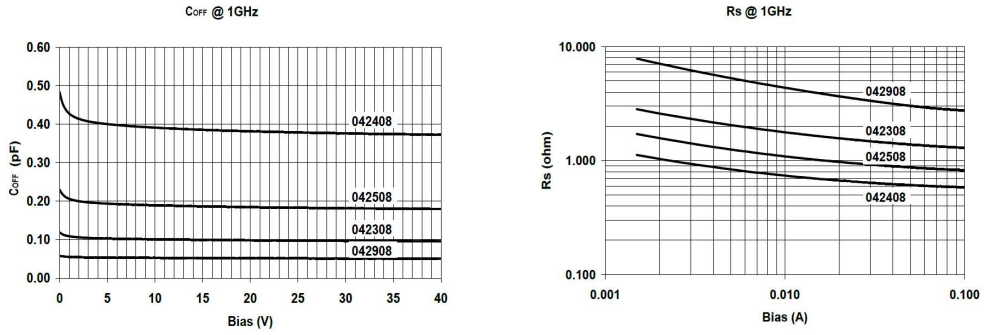

(b)

Figure 4.26: (a) Performance table of MADP-042308-13060 from MACOM^{TM}. (b) Typical performance curves of C_{OFF} and R_S versus bias voltage and current.

Note that a DC path for the PIN diode biasing current must be also inserted at the bottom layer of the structure. To do that, an additional isolating gap has been created around the inner via hole, and then three SMD capacitors have been mounted on it. Thus, by inserting these capacitors (i.e. C_{RF} in the following), it is possible to obtain a short-circuit at the filter centre frequency, while the integrated bias line guarantees an adequate DC current return path, as is depicted in Fig. 4.27-(b).

Finally, 3D EM simulations of the reconfigurable filter have been performed in order to select the proper lumped components by maximizing the filter EM performance, thus reducing their parasitic effects on the responses. Table 4.2 shows the final values for these components that form the PIN diode biasing circuitry.

4.5.2 Filter Design

As a proof-of-concept, a 2-pole narrow-band filter has been designed to show almost equi-spaced responses at the C-band, with a tuning range bigger than 10% [117]. Thus, three different capacitance bits have been created at the capacitive disk of each resonator, providing eight different frequency responses. These digital states are achieved by changing the dimensions of each capacitance bit (in terms of side lengths and isolating gap widths, following the same procedure that has already been applied for the capacitive disk) in order to properly weight their contribution to the effective loading capacitance. The filter consists again on two square coaxial SIW cavity resonators coupled by means of post-wall iris, and CPW-to-SIW transition with 90° bend slots that control the external coupling.

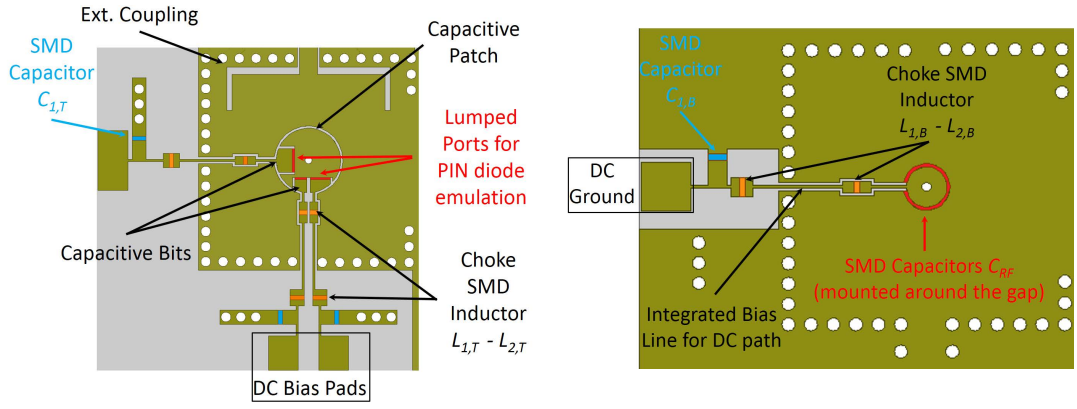

(a) (b)

Figure 4.27: (*a*) Layout top view of the proposed discretely tunable resonator: bit capacitances have been created into the loading capacitive disk. (*b*) Layout bottom view: integrated bias line affords a DC path for the PIN diode biasing current, while SMD capacitors around the bottom isolating gap make that the RF signal sees a short-circuit to ground.

Table 4.2: Elements of the Bias Circuitry - PIN Diode Tunable Filter

Component	Unit	Value	Case Size
$C_{1,B}$	pF	2.7	0402
$C_{1,T}$	pF	2.7	0402
C_{RF}	pF	1.5	0402
$L_{1,B}$	nH	38.1	0603
$L_{1,T}$	nH	38.1	0603
$L_{2,B}$	nH	24.1	0603
$L_{2,T}$	nH	24.1	0603

In its fixed state, which includes the assembly of the whole biasing circuitry excepting the switching elements, the 2-pole filter shows an equi-ripple fractional bandwidth of 2.5% (i.e. $BW = 120$ MHz), centre frequency of 4.9 GHz, while the requested in-band return losses are 15 dB. In this design, the slope parameter is $b = 0.015$ mS, thus the coaxial SIW resonator would have $Z_0 = 141\ \Omega$ and $C_l = 0.49$ pF. Taking into account that the dielectric substrate has $\epsilon_r = 2.2$ and a thickness of $h = 3.175$ mm, the SIW cavity resonator will measure 13.6×13.6 mm^2 by setting the inner hole diameter to 0.45 mm.

Concerning the loading and the bit capacitances, all isolating gaps have been fixed to 0.15 mm, and these will not be modified during the filter optimization. As previously demonstrated in Section 2.1.2, while using a low-permittivity dielectric substrate, it is important to maintain narrower isolating gaps in order to reduce radiation loss and maintaining higher Q-factor.

The capacitive disk radius has been adjusted to be 2.15 mm, resulting in a disk area of 14.52 mm. After the 3D EM optimization of the capacitive bit dimensions that enables the filter to have equi-spaced frequency responses, the bit capacitance $C_{bit,2}$, $C_{bit,1}$ and $C_{bit,0}$ will take up approximately 10%, 6.4% and 4.7% of the disk area, respectively. The filter has been designed to cover 500 MHz around 4.4 GHz with eight frequency states.

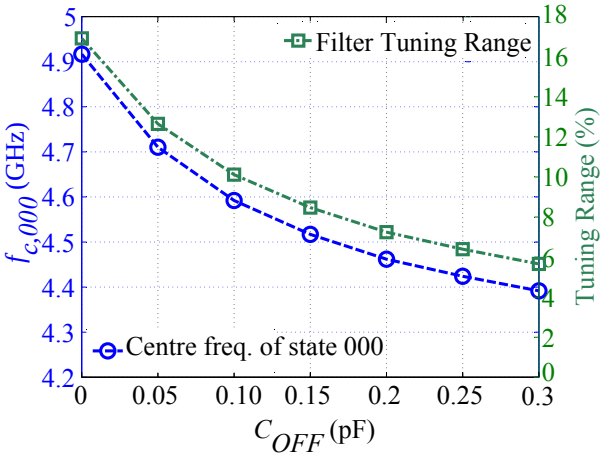

Figure 4.28: Tuning range of the tunable filter and centre frequency of the filter state 000 for several PIN diode C_{OFF}.

Once the bit capacitance configuration has been fixed, preliminary full-wave 3D EM simulations of the proposed tunable filter concept have been performed in order to study its dependence on the tuning element performance. Firstly, some parametric analysis were done by changing the value of C_{OFF} and R_S of the PIN diodes, so that the variations of filter centre frequency, tuning range and overall insertion loss can be estimated.

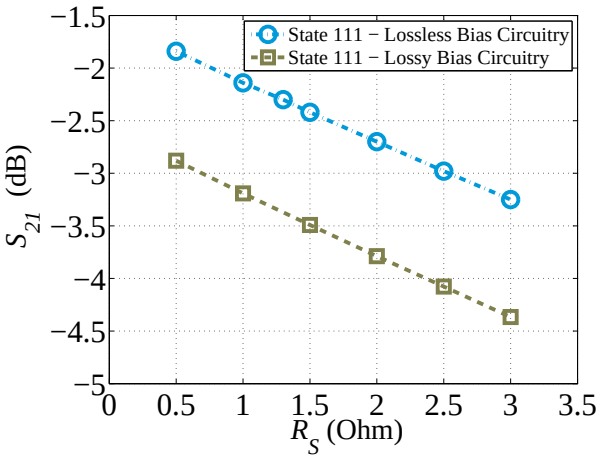

Figure 4.29: Insertion loss of the reconfigurable filter for several on-state series resistance of the PIN diodes, considering the frequency state 111.

Fig. 4.28 depicts the effect of off-state capacitance on the filter tuning range, and especially on the centre frequency of the filter state 000 (i.e. $f_{c,000}$), which is shown in the figure. For instance, C_{OFF} affects the capacitive contribution of the each bit in the off-state, thus its relative state frequency. The dependence of the tuning range upon C_{OFF} values can be estimated just looking at the variation of $f_{c,000}$.

Looking at the equivalent circuit of the reconfigurable resonator of Fig. 4.25-(b), the series of C_{OFF} and $C_{bit,n}$ is in a shunt connection with the loading capacitance C_l. At this frequency range, C_{OFF} is usually smaller than $C_{bit,n}$, or at least comparable, thus its value dominates the series connection. As a consequence $f_{c,000}$ does depend on the parallel connection between C_{OFF} and C_l. The higher the C_{OFF} value is, the lower the centre frequency $f_{c,000}$ is. Therefore, the total tuning range of the reconfigurable resonator

does reduce for increasing C_{OFF} values. As it can be observed in Fig. 4.28, for a C_{OFF} value above 150 fF, the tuning range would be importantly reduced (i.e. less than 8%).

In addition to this, the frequency state $f_{c,111}$ does not depend on C_{OFF}, since it is only the ratio between the bit capacitances and the loading capacitance that determines its centre frequency. For the proposed configuration, $f_{c,111}$ is centered at 4.15 GHz, therefore increasing values of C_{OFF} would directly lower the tuning range.

Concerning the filter insertion loss, Fig. 4.29 shows the effect of the on-state series resistance of PIN diodes for the filter worst case, which now corresponds to the lowest frequency state 111. As a matter of fact, when all tuning elements are activated the loading capacitance and the bit capacitances are acting together. Thus, the switch intrinsic R_S are connected to each resonator worsening its Q_u. As it can be observed, the Q_u degradation would imply higher filter insertion losses, which would be around 2.5 dB (for the lossless bias circuitry) if the R_S is greater than $2\,\Omega$.

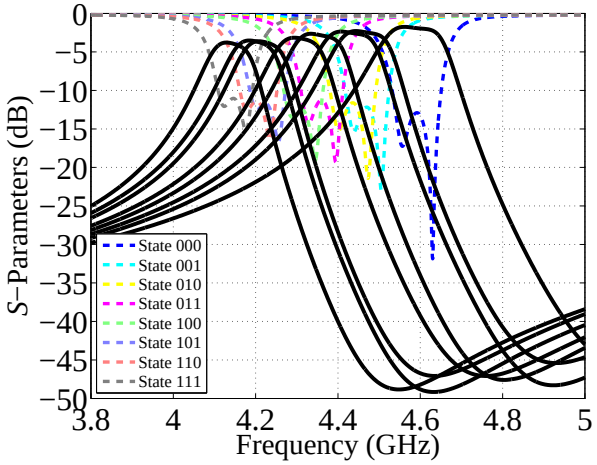

Figure 4.30: Simulated results of the discretely tunable filter changing the state from 000 ($f_{c,000} = 4.6$ GHz) to 111 ($f_{c,111} = 4.15$ GHz).

Note that these preliminary results have been obtained considering a lossless bias circuitry, thus SMD lumped components have been considered ideal. As Fig. 4.29 shows, if losses are included in the equivalent circuits of these lumped components, there would be an increase of 1 dB in the filter insertion loss at the state 111. Taking into account that IL would range from 2.9 dB to 4.4 dB for a lossy bias circuitry, it is possible to estimate the resonator Q_u, which would be 175 is $R_S = 0.5\,\Omega$ and 110 is $R_S = 3\,\Omega$.

It is worth mentioning that the digital tuning approach seems to be more robust against the resonator Q degradation, due to the employed tuning elements, than the analog tuning method. Let us consider a tuning element showing $R_S = 3\,\Omega$. As Fig. 4.5 displays, the analog tuning method allows a Q_u better than 100 just over a $4 - 5\%$ of tuning around 3 GHz. Using a discrete tuning approach, the resonator Q_u would be always better than 100 over a 10% of tuning around 4.4 GHz, which are better Q-factors at higher frequency bands. Thus, losses are not so strongly dominated by the tuning element series resistance, and the expected degradation of the resonator Q_u when the loading capacitance is increased (and the resonant frequency is reduced) would be much lower. Additionally, these results demonstrate that integrated bit capacitances present higher Q-factor than GaAs varactor diodes, especially at frequencies higher than 3 GHz.

Finally, the simulated response of the 8-state discretely tunable filter can be seen in Fig. 4.30. Taking into account $C_{\mathrm{OFF}} = 100fF$ and $R_S = 2\,\Omega$ for the PIN diodes, the filter

response would range between 4.6 GHz for the state 000 and 4.15 GHz for the state 111 (i.e. 10.5% of tuning with respect to 4.4 GHz).

The minimum IL would increase from 1.75 dB for the upper frequency state to 3.8 dB for the lower one, so that Q_u would change between 220 and 125, respectively. Along the whole tuning range, the filter BW should vary between 106 MHz at 4.6 GHz and 75 MHz at 4.15 GHz. It is worth mentioning that the proposed filter would show a reduced FBW variation (i.e. from 2.3% to 1.8%) thanks to the use of longer coaxial resonator for the filter implementation.

4.5.3 Experimental Results

4.5.3.1 Fixed 2-pole Filter Demonstrator Using SMD Resistances

A 2-pole filter demonstrator has been designed on a 3.175 mm-thick Rogers RT/Duroid 5880 substrate ($\epsilon_r = 2.2 \pm 0.02$, $\tan\delta = 9 \times 10^{-4}$@10 GHz) with 17 μm/17 μm Cu clad [118]. This design shows a resonator electrical length of 26.26° at 4.65 GHz, which corresponds to $0.07\lambda_g$. As previously mentioned, the use of thicker dielectric laminate helps us increase the resonator θ_0, which allows the filter to show better performance in terms of bandwidth variations over frequency.

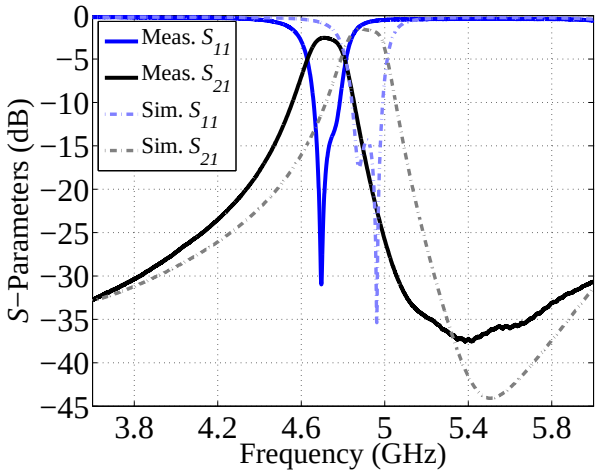

Figure 4.31: Measured wide-band frequency responses of the 2-pole filter (*solid lines*), compared to its simulated results (*dashed lines*).

The filter size is 14.25×28 mm^2 that grows up to 28.2×42.3 mm^2 including the bias circuitry and its specific pads. The structure shows a higher compactness degree, especially at the lower frequency band around 4 GHz, where its full size matches $0.37 \times 0.56\ \lambda_0^2$ and $0.56 \times 0.84\ \lambda_g^2$.

After the assembly of the bias circuitry and before mounting the PIN diodes, the prototype of the fixed 2-pole filter has been measured. Fig. 4.31 shows these measurements compared to the 3D EM simulations for the same filter configuration. As it can be observed, the filter undergoes an important frequency shift towards lower frequencies, from 4.9 GHz to 4.7 GHz (i.e. 4% of shift). This deviation affects also the 1-dB FBW that decreases from 3.15% to 2.75%, and the filter IL that increases up to 2.6 dB, instead of being 1.6 dB at the passband. The increase of the filter IL is due to the ENIG finishing, and especially, to the thickness of the nickel layer that has been deposited on the copper foil.

A dimensional measurement of the filter layout under an optical microscopy shows that the gap widths of the loading capacitive patches are narrower than expected, creating bigger loading capacitances. That problem justifies the shift to lower frequencies.

As it is well known, there are many techniques that can be used for etching/removing the unwanted copper from the substrate laminates in the PCB process, following the desired top and bottom patterns. Since high-resolution was required for obtaining isolating gap in the order of 0.15 mm in this design, it is possible that, during the etching process, the photoengraving technique has not been done properly, resulting in narrower gaps.

In order to firstly evaluate the discrete tuning capabilities of the proposed topology and for demonstration purposes, 1 Ω SMD resistors have been soldered using standard solder paste between the capacitance bits and the loading capacitance in order to emulate the presence of a lossy PIN diode at the on-state. Clearly, this test emulates the use of tuning elements having an ideal $C_{\mathrm{OFF}} = 0$ pF, so that we expected to obtain the maximum filter tuning range. Previously to the SMD resistors assembly, the complete bias circuitry has been mounted in order to take into account its losses on the filter performance. A photo of the device in the 111 configuration is shown in Fig. 4.32 that also shows the measured S_{21} and S_{11} parameters for the eight frequency states.

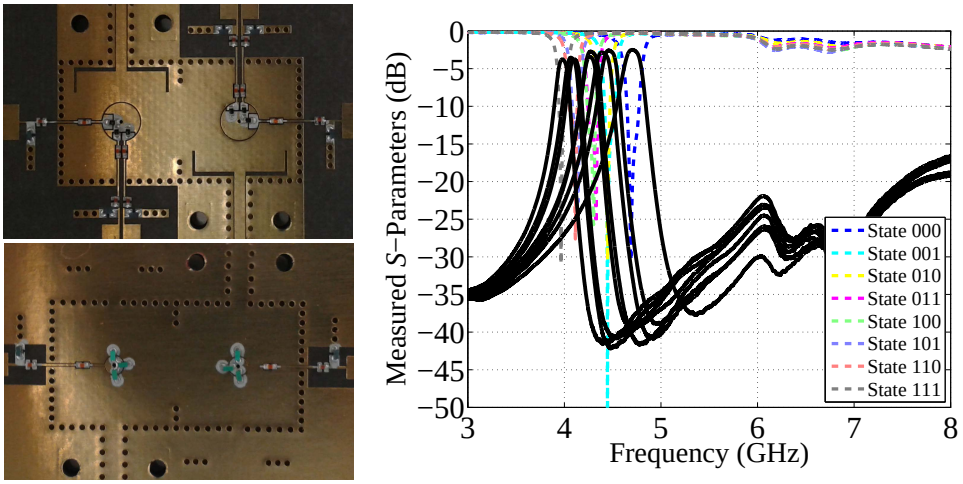

(a) (b)

Figure 4.32: (*a*) Photo of the reconfigurable 2-pole filter emulating the frequency state 111. (*b*) Measured wide-band frequency responses of the eight frequency state assembling/removing SMD resistances.

The filter centre frequency can be controlled between 4.7 and 4 GHz (i.e. 16.5% of tuning range with respect to 4.35 GHz) changing the filter state from 000 to 111. The equi-ripple measurement of the filter bandwidth is not easy to perform due to the return loss responses that have been modified by the copper patterning tolerances. As we have usually done up to now, the BW is measured at -1 dB level of the passband to estimate its variation over frequency.

So, the filter BW changes slightly over the whole tuning range, from 128 MHz for the state 000 to 77 MHz for state 111. That means the corresponding 1-dB FBW decreases between 2.7% and 1.95% along the filter tuning. In addition to the advantages of using longer coaxial resonators, integrating monolithically the tuning capacitances into the SIW metal layer enables less degradation of the coupling mechanisms over frequency.

To sum up these preliminary tests, Fig. 4.33 shows the centre frequency and insertion

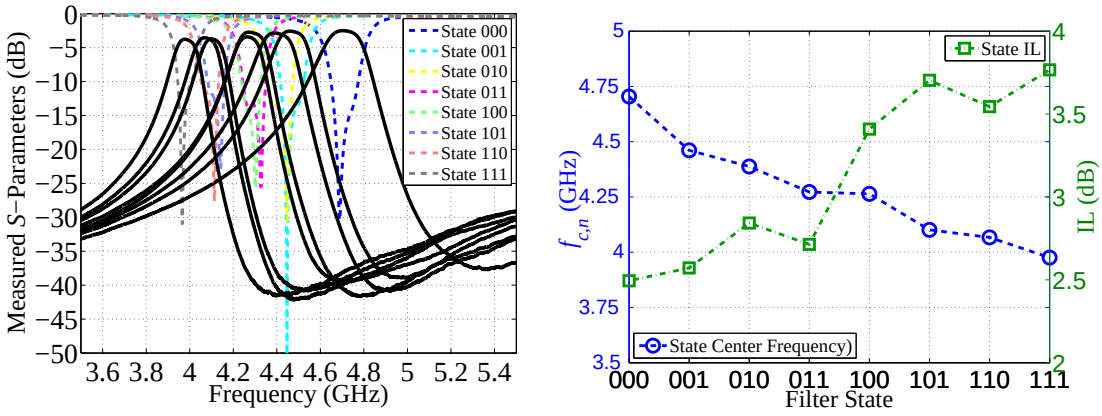

(a) (b)

Figure 4.33: (*a*) Measured S_{21} (*solid lines*) and S_{11} (*dashed lines*) for the discretely tunable filter using SMD resistances. (*b*) Centre frequency $f_{c,n}$ (*blue line*) and filter IL (*green line*) versus filter state.

loss for each frequency state of the discretely tunable filter. It is worth mentioning that the measured IL is in good agreement with the simulated results of Fig. 4.30, showing values that ranges from 2.5 dB to 3.8 dB. Taking into account these values, the extracted filter Q-factor would range between 130 at 4.7 GHz and 110 at 4 GHz.

4.5.3.2 Experimental Results of the Discretely Tunable 2-pole Filter Using PIN diodes

Due to limited stock of the PIN diode from MACOM [116] it was not possible to test the complete 3-bit discretely tunable filter. As a result, just two PIN diode surmount chip MADP-042308-13060 have been assembled on the 2-pole filter, one at the most significant capacitive bit of each resonator that is $C_{bit,2}$. In this context, only the states 000 and 100 could be tested and studied.

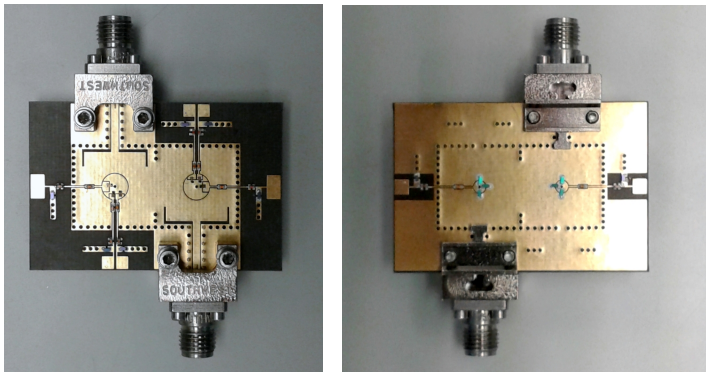

(a) (b)

Figure 4.34: (*a*) Top view and (*b*) bottom view of the PIN diode-tuned 2-pole filter in coaxial SIW topology.

Fig. 4.34 displays pictures, and Fig. 4.35 shows the measured S-parameter responses of the PIN diode 1-bit reconfigurable filter based on the coaxial SIW topology. The centre frequency can be centered at 4.59 GHz for the state 000 and 4.25 GHz for the state

Table 4.3: Measured centre frequency (GHz), IL (dB), filter Q, and 1-dB FBW (%) for the PIN diode tuned filter.

State	f_c (GHz)	IL (dB)	1-dB FBW (%)	Extr. Q_u
000	4.59	2.85	2.2	≈ 125
100	4.25	4	1.75	≈ 105

100. Thus, the measured tuning range is around 7.5%, as it has been extracted from simulations considering the specific case, although they are centered at other frequency band (see Fig. 4.35).

Table 4.3 highlights the filter main performance that are in good agreement with previous results. Note that the Q-factor is better than 100 for both states. As a result, the proposed implementation provides the filter with increased compactness and low-cost fabrication procedure using single-layer PCB fabrication process. Additionally, the integration of the bias network onto the SIW metal layers has been shown to be a key factor for easing the tuning element assembly while avoiding additional degradation of the filter performance.

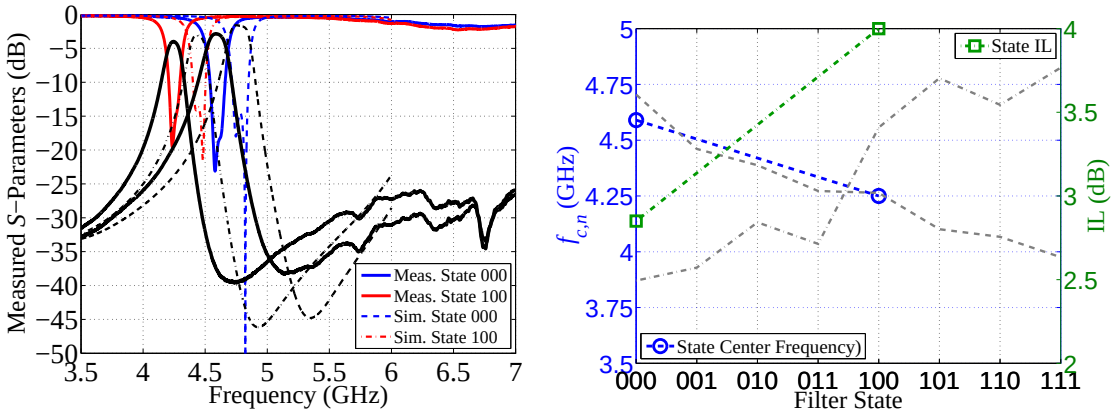

(a) (b)

Figure 4.35: (*a*) Measured S_{21} (*solid lines*) and S_{11} (*dashed lines*) for the PIN diode discretely tunable filter. (*b*) Centre frequency $f_{c,n}$ (*blue line*) and filter IL (*green line*) versus filter state. Grey lines display measured results of the filter demonstrator with SMD resistors.

4.6 Discretely Tunable Filters Using RF MEMS Resistive Switches

Following the approach for the digital tuning of coaxial SIW resonators presented in Section 4.5, an RF MEMS 2-pole tunable filter in coaxial SIW topology is designed, fabricated and measured in C-band [119]. The frequency band between 4.7 GHz and 5.2 GHz is then covered by 16 frequency responses with uniform frequency resolution. This tuning concept is now demonstrated by employing RF MEMS resistive switches from the XLIM research group of the University of Limoges (France). The use of RF

MEMS devices should enable us to improve the EM performance of the reconfigurable filters due to its superior performance.

4.6.1 RF MEMS Resistive Switch

The key advantages of RF MEMS switches over conventional switches include low power consumption, high isolation and low insertion loss. They are attractive because of their high throughput, cost efficiency, small size, and high integration capability with electric circuits. RF MEMS devices have also extremely high linearity, which means that they create no harmonics or intermodu s for broadband communications sy

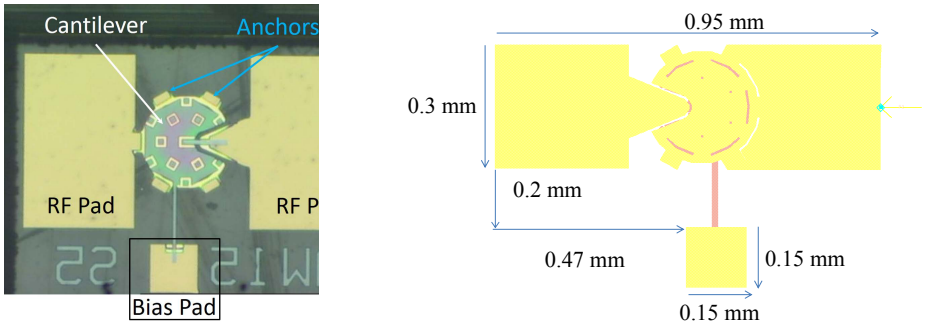

(a) (b)

Figure 4.36: (a) Picture of a single RF MEMS resistive switch from XLIM laboratory. (b) MEMS layout showing its main dimensions.

An RF MEMS resistive switch is used in this work as switching elements. These have been fabricated on a fused silica substrate. Actuation is made by applying a voltage on the SiCr bias line ($R_{bias} > 10$ kΩ) connected to the beams. The extracted RF MEMS C_{OFF} is 30 fF, while the estimated parasitic series inductance is 0.35 nH. The estimated Q is very high ($\gg 200$ @1 GHz). Therefore, the MEMS R_S has been extracted to be close to 1 Ω for biasing voltage of $V_B = 35\ V$.

A photograph of the MEMS switch is shown in Fig. 4.36, together with a 2D sketch of the layout including its main dimensions. Actuation is made by applying a voltage on the Silicon Chrome (SiCr) bias line ($R_{bias} > 10$ kΩ) connected to the beams in back-to-back configuration and by maintaining a DC ground on the input/output lines.

The SMD components that compose the bias circuit have been assembled directly on the integrated bias lines created into the SIW top metal layer. Bias lines have been fitted to assembly 1 MΩ SMD 0402 resistors on it to isolate DC bias and ground from the RF path. Those lines present a conductor wide of 0.15 mm with a spacing of 0.15 mm, ending on 3×3 mm^2 pads where DC voltages can be simply applied.

Moreover, in this design a flip-chip assembly of RF MEMS switches will be applied in order to avoid the necessity of wire bonding. Due to the SMD assembly procedure, the filter layout has been modified to present MEMS mounting pads. Thus, a specific square air-gap space has been etched on the top metal layer in correspondence to the RF MEMS cantilever, as it can been at Fig. 4.37-(b).

As the MEMS is equipped with a specific bias pad, the integrated bias lines etched at the top metal layer do not contact loading capacitive patches in this structure. Thus,

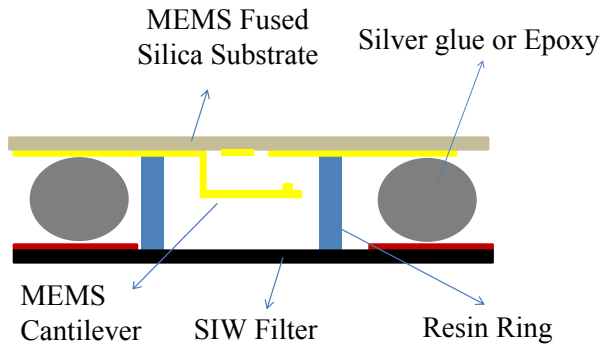

(a)

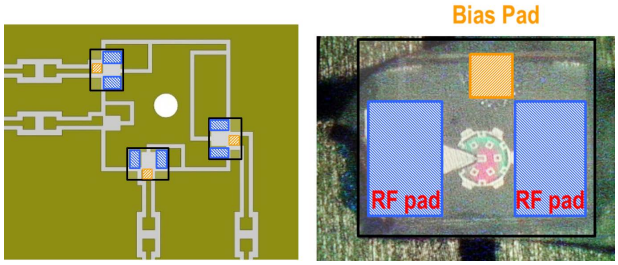

(b)

Figure 4.37: (*a*) Slice view of the flip-chip assembly of the MEMS on the SIW filter. (*b*) SMD assembly of the RF MEMS switches on the filter.

epoxy paste has been used for providing electrical and mechanical connections to RF MEMS switches as follows:

- Between the input RF pad and the loading capacitive patch;
- Between the output RF pad and the capacitive bit;
- For connecting MEMS bias pads and integrated bias lines, where DC bias can be directly applied.

Optionally, a resin ring could be inserted at the square pad level in order to protect RF MEMS from atmospheric agents. This ring has to be created at the substrate laminate level, after removing the copper clad. That element has been highlighted in blue in Fig. 4.37-(*a*). By the way, in this first attempt, we did not use this solution to protect the RF MEMS switches.

4.6.2 Filter Design

The basic idea of this work is to demonstrate that it is possible to design discretely reconfigurable filter with more states and low losses at higher frequencies by using RF MEMS as tuning elements. The filter structure is very similar to the one described in the previous section. Now, four capacitance bits have been created in order to show sixteen different frequency responses around 5 GHz.

So, the design of the tunable resonator have started setting all isolating gaps to 0.15 mm. To easy the assembly of the MEMS and the creation of the air-gap spaces

Table 4.4: Dimensions of the Capacitive Bits.

Element	x-size (mm)	y-size(mm)	Perimeter (mm)	Estimated C (fF)
bit 0	0.5	0.8	2.6	≈ 50
bit 1	0.6	1	3.2	≈ 65
bit 2	0.8	1.4	4.4	≈ 80
bit 3	2.65	1.05	7.4	≈ 110
Load. Patch	4	4	16	≈ 440

for the cantilevers (whose size is 0.5×0.6 mm^2), we changed the shape of the loading capacitive patch that now is squared, as well as the capacitive bits. The size of these elements are shown in Table 4.4.

Since this design is an evolution of the previous filter concept, it shares some characteristics with that, as the same dielectric material and its main dimensions. In fact, we have kept approximately the same cavity resonator size in order to guarantee an easy MEMS assembly. Nevertheless, we wanted to move the filter to higher frequency in order to prove that RF MEMS and SIW technology can be used for the design of tunable structures above 4 GHz. For this reason, the inner via diameter has been enlarged without reducing the SIW resonator size. It implies that the coaxial characteristic impedance has been reduced, and the resonator f_R can be increased.

As a result, the coaxial SIW topology now presents $b = 16.6$ mS, $Z_0 = 113\,\Omega$ and $C_l = 0.44$ pF. It is worth mentioning that the previous tests have demonstrated the advantage of using longer resonator in tunable structures. Therefore, this frequency shift has resulted in a rise of the resonator θ_0 that is now 30.5° at 5.4 GHz, which corresponds to $0.085\lambda_g$.

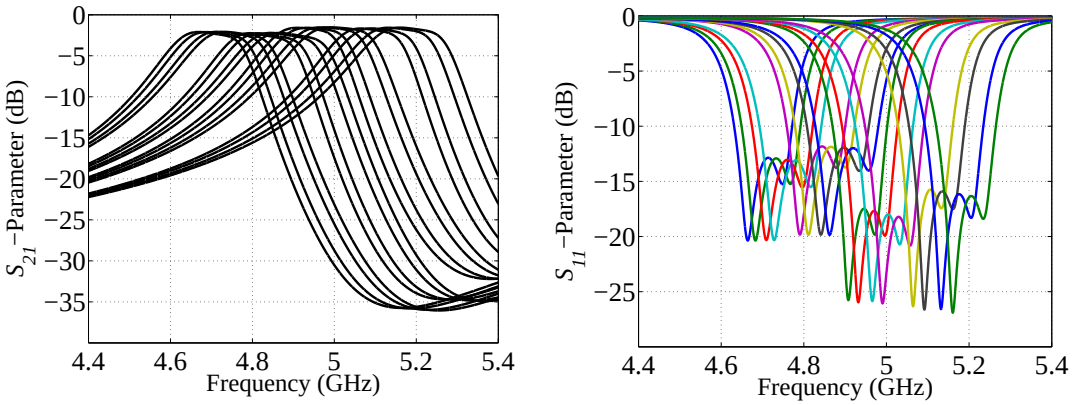

(a) (b)

Figure 4.38: (*a*) Simulated S_{21}- and (*b*) S_{11}-parameter responses changing the state from $f_{c,0000} = 5.2$ GHz) to $f_{c,1111} = 4.71$ GHz, taking into account $C_{\text{OFF}} = 30$ fF and $R_S = 3\ \Omega$.

Finally, using the same substrate laminate and keeping an SIW resonator size of 12.2×12.2 mm^2, by setting the inner hole diameter to 0.8 mm, the fixed 2-pole passband filter has been centered at 5.4 GHz with an equi-ripple FBW of 1.7% (i.e. equi-ripple BW= 92 MHz while 1-dB BW= 170 MHz, which is 3.2%). The requested in-band return losses are 20 dB.

Table 4.5: Simulated results of the 4-bit RF MEMS tunable SIW filter with $R_S = 3\Omega$ and $C_{\mathrm{OFF}} = 30$ fF.

State	f_c(GHz)	IL(dB)	Extr. Q_u	State	f_c(GHz)	IL(dB)	Extr. Q_u
0000	5.20	1.56	≈ 200	1000	4.92	2.21	≈ 145
0001	5.18	1.58	≈ 200	1001	4.90	2.21	≈ 145
0010	5.14	1.66	≈ 180	1010	4.87	2.25	≈ 145
0011	5.11	1.67	≈ 180	1011	4.84	2.25	≈ 145
0100	5.03	1.52	≈ 200	1100	4.78	2.08	≈ 160
0101	5.00	1.53	≈ 200	1101	4.76	2.07	≈ 160
0110	4.97	1.58	≈ 190	1110	4.73	2.11	≈ 160
0111	4.95	1.59	≈ 190	1111	4.71	2.1	≈ 160

Fig. 4.38 depicts the 3D EM simulations that have been performed with ANSYS HFSS 2014 using the following MEMS parameters: $C_{\mathrm{OFF}} = 30$ fF and $R_S = 3\Omega$ for studying worst case scenarios. The filter centre frequency would range from $f_{c,0000} = 5.2$ GHz to $f_{c,1111} = 4.7$ GHz, thus the simulated tuning range is 10%. The simulated filter FBW is expected to remain quasi-constant along the whole tuning range. For instance, the 1-dB FBW has been estimated to be 3% (155 MHz at 5.2 GHz) for the 0000 tuning state, while it would increase up to 3.15% (148 MHz at 4.7 GHz) for the 1111 state.

The variation of filter FBW with the frequency tuning has been minimized, and even an increasing trend has been obtained, when the resonator length verifies $\lambda/7 < h < \lambda/6$. This reduced impact on the slope parameter enables us to keep an almost constant fractional bandwidth by limiting the variation on the inverter values required for maintaining a particular filter response at different centre frequencies. Table 4.5 summarizes the simulated results for each tuning state.

4.6.3 Experimental Results

4.6.3.1 Fixed 2-pole Filter Demonstrator Using SMD Resistances

A 2-pole filter demonstrator has been designed on a 3.175 mm-thick Rogers RT/Duroid 5880 substrate ($\epsilon_r = 2.2 \pm 0.02$, $\tan\delta = 9 \times 10^{-4}$@10 GHz) with 17 μm/17 μm Cu clad. The filter size including the bias circuitry and pads is 15×27 mm^2. The compactness degree of filter is quite high through the use of longer coaxial resonators. Its full size matches $0.37 \times 0.67\,\lambda_g^2$ and $0.25 \times 0.45\,\lambda_0^2$ at 5 GHz that is the middle of the tuning range.

Fig. 4.39 displays the measured results of the fixed 2-pole coaxial SIW filter, compared with initial and post-tuning simulations. Again, the filter is shifted towards lower frequencies, from 5.4 GHz to 5.1 GHz (i.e. 6% of shift). In fact, this filter and the previous PIN diode-tuned filter have been fabricated by the same company in the 3.175-thick laminate of Rogers R5880, approximately at once. Both components present similar problems related to the etching of the isolating gaps, resulting in those frequency shifts towards lower frequencies. Moving to the measured results, the filter has a 1-dB FBW of 3.1% with IL that are increased up to 1.4 dB, instead of being 0.9 dB in the passband. That means the extracted resonator Q from filter measurements is now around 205.

Concerning reconfigurability, a preliminary test was performed with 1 Ω SMD resistors that have been soldered using standard solder paste between the capacitance bits and the fixed loading capacitance in order to emulate the presence of RF MEMS

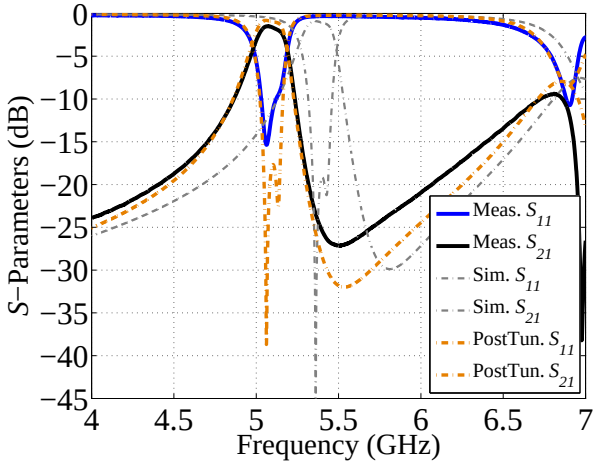

Figure 4.39: Measured wide-band frequency responses of the 2-pole filter (*solid lines*), compared to its simulated results (*dashed lines*). Grey lines are initial simulations, while orange lines are post-tuning simulations.

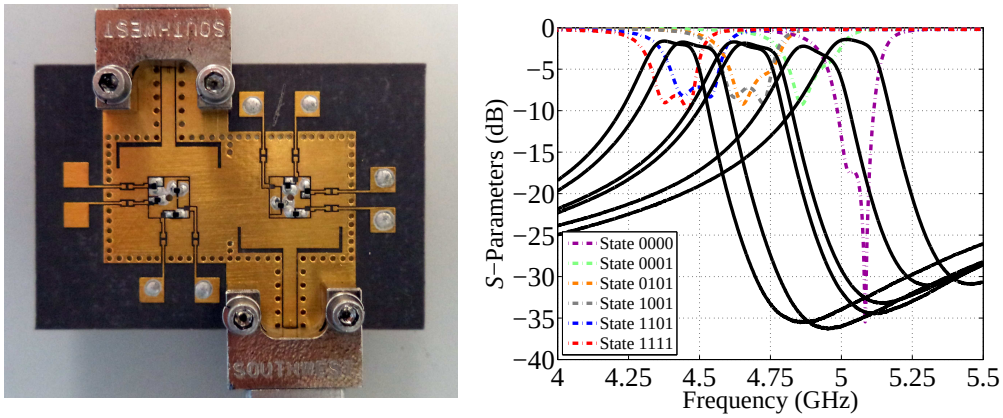

(a) (b)

Figure 4.40: (*a*) Photo of the reconfigurable 2-pole filter emulating the frequency state 1111. (*b*) Experimental results of the preliminary tunable filter at the different states 0000-0001-0101-1001-1101-1111 using SMD resistances.

switches. A photo of the device in the 1111 configuration is shown in Fig. 4.40, where are also depicted the measured S_{21} and S_{11} responses for the 8 frequency states that have been tested. Particularly, during this test the following states have been measured: $\{0000, 0001, 0101, 1001, 1101, 1111\}$.

The filter centre frequency can be controlled between ≈ 5 and ≈ 4.4 GHz corresponding to 0000 and 1111-state, respectively. The obtained tuning range is 13% with respect to 4.7 GHz for this ideal case of $C_{\text{OFF}} = 0$ fF, which confirms previous simulations of this kind of structure. The filter IL ranges between 1.4 and 2.2 dB (0000 and 0001-state, respectively). It is worth mentioning that the worst IL value has been obtained in the 0001-state because it was the last frequency state that was measured. Since the filter demonstrator suffered different re-work cycles for assembling/disassembling SMD resistors in order to test the different frequency states, the EM performance of the 0001-state has been partially deteriorated. Finally, the filter 1-dB FBW has increased up from 2.7% to 3.35% along the whole tuning range. Table 4.6 shows the measured results for the

Table 4.6: Measured Centre Frequency (GHz), IL (dB), Filter Q, and 1-dB FBW (%) for some Tuning State Using 1 Ω SMD Resistors.

State	f_c (GHz)	IL (dB)	1-dB FBW (%)	Extr. Q_u
0000	5.02	1.30	2.70	≈ 205
0001	4.87	2.23	2.80	≈ 180
0101	4.66	1.86	3.10	≈ 190
1001	4.62	1.71	3.15	≈ 180
1101	4.44	1.73	3.35	≈ 180
1111	4.37	1.61	3.25	≈ 190

implemented device.

4.6.3.2 Experimental Results of the Discretely Tunable 2-pole Filter Using RF MEMS Switches

Finally, RF MEMS switches from XLIM have been assembled on the SIW filter, and it was possible to measure the S-parameter frequency responses and also to perform a power handling test. Due to the irregular shape of the MEMS components after the device singulation from the main fused silica coupon, it was not possible to assembly four RF MEMS switches in each SIW resonator. Indeed, this phase consisted on two steps. First, a dicing machine partially removed the fused silica around each MEMS device. Then, the MEMS singulation was performed breaking the thin layer of silica that was left. As Fig. 4.41 shows, the RF MEMS are bigger than expected and there is not enough space for mounting all devices together on the capacitive bits $C_{bit,1}$ and $C_{bit,0}$ without affecting the RF connections.

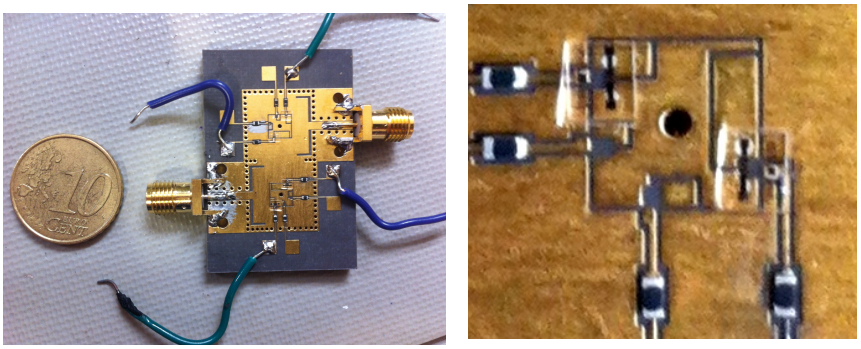

(a) (b)

Figure 4.41: (*a*) Top view of the RF MEMS-tuned 2-pole filter in coaxial SIW topology. (*b*) Particular of the RF MEMS assembly on the first resonator of the SIW filter.

As a result, just four RF MEMS switches have been assembled on the 2-pole filter, two for each resonator. Particularly, these have been assembled on the most significant bits that are $C_{bit,3}$ and $C_{bit,2}$ of each cavity. Thus, $C_{bit,1}$ and $C_{bit,0}$ are in ideal off-state with $C_{\mathrm{OFF}} = 0$ that loads them. In this context, the state $\{0000, 0100, 1000, 1100\}$ could be tested and studied.

Fig. 4.42 shows the measured S-parameter responses of the reconfigurable filter under test, and Table 4.7 highlights its main performance. Compared to the PIN diode tuned

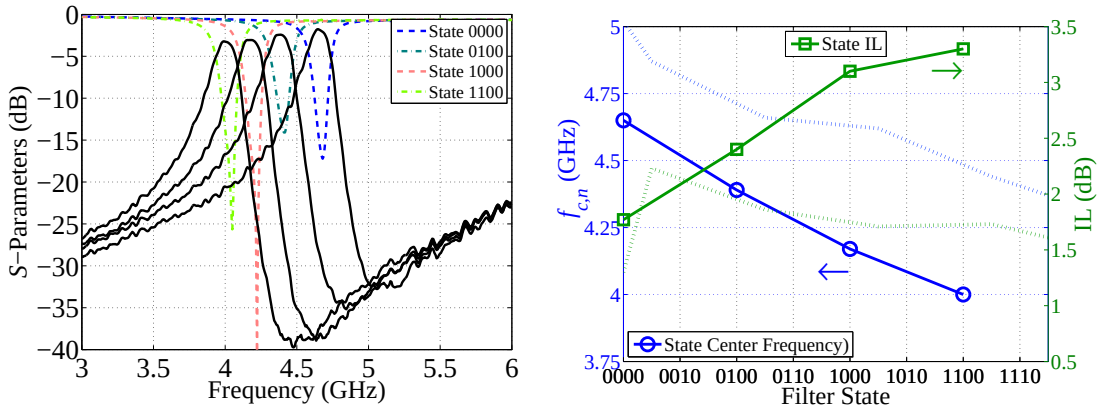

(a) (b)

Figure 4.42: (*a*) Measured S_{21} (*solid lines*) and S_{11} (*dashed lines*) for the RF MEMS discretely tunable filter. (*b*) Centre frequency $f_{c,n}$ (*blue line*) and filter IL (*green line*) versus tuning state. Dotted lines display measured results of the filter demonstrator using SMD resistors.

Table 4.7: Measured centre frequency (GHz), IL (dB), filter Q_u, and 1-dB FBW (%) for the RF MEMS tuned filter.

State	f_c (GHz)	IL (dB)	1-dB FBW (%)	Extr. Q_u
0000	4.65	1.8	2.4	≈ 205
0100	4.39	2.4	2.45	≈ 160
1000	4.17	3.1	2.4	≈ 120
1100	4	3.3	2.4	≈ 105

filter, the RF MEMS version shows higher Q-factor over a wider tuning range, which are reflected in better filter IL. It is worth mentioning that the proposed approach makes for almost constant filter fractional bandwidth (i.e. 1-dB FBW is around 2.5%) over the whole tuning range. The latter is measured to be around 15%, which is a very promising result.

The novel approach for discrete frequency tuning of SIW filters using combline SIW resonators and RF MEMS has demonstrated this solution keeps the higher Q-factor of the SIWs over frequency, due to the lower influence of the switching elements compared to varactor-loaded tunable designs. In this context, the flexibility in setting up the tuning range and its frequency resolution is one of the main advantages of the proposed solution. Employing capacitive bits to fine control the centre frequency of the filter, the tuning effect just depends on their sizes and it can be easily set or even enhanced by increasing the bit sizes.

4.6.3.3 Power Handling Measurements

The same test setup shown in the previous sections has been used to measure power handling capabilities of the device. In this context, the 1-dB compression point for the RF MEMS tunable filter has been measured. Power handling capabilities have been tested at 4.65 GHz, corresponding to off-state position, being the worst case in terms of

self-actuation. The RF MEMS can handle up to 33.5 dBm before self-actuation occurs, resulting in the commutation of the filter response.

4.7 Comparison of Reconfigurable Filter Performance

Among the three frequency-agility approaches (i.e. analog tuning, discrete tuning with lumped switched capacitances and discrete tuning with integrated bit capacitances) described in this chapter, the discrete tuning approach that employs integrated bit capacitances and RF MEMS resistive switches offers many advantages, and has the potential to be the best approach for implementing reconfigurable filters based on coaxial SIW resonators. Let us take a look at Fig. 4.43 and Fig. 4.44. In these figures, a comparison of the EM performance obtained from measurements of the three frequency tuning approaches are shown, especially in terms of filter Q_u and filter FBW variations over the obtained tuning range. Thus, the measured results of the six filters presented in the previous sections are collected in four different graphs.

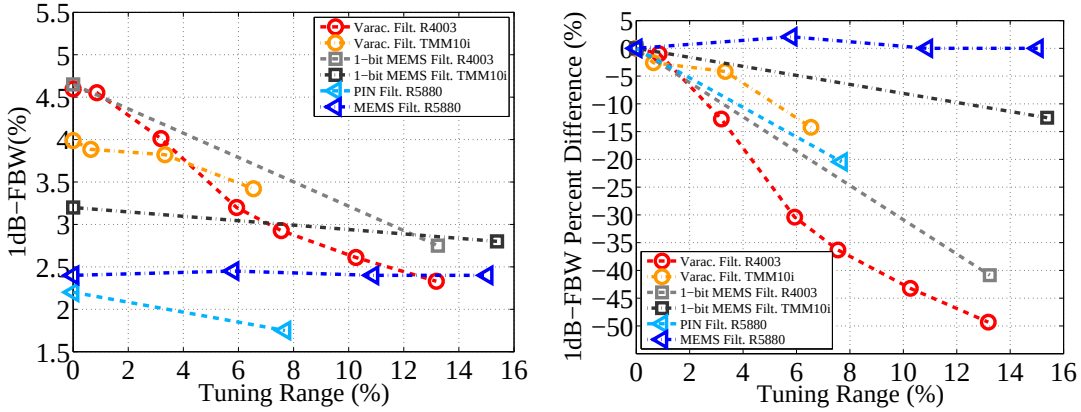

(a) (b)

Figure 4.43: (a) Reconfigurable filter FBW versus filter tuning range. (b) Percent difference of the filter FBW versus filter tuning range

As Fig. 4.43-(a) shows, the use of longer coaxial resonators joined to the integration of bit capacitances into the top metal layer allows filters to have a quasi-constant FBW over a wide tuning range. Since the EM field is confined into the substrate when performing the tuning, the internal and external magnetic couplings do not suffer wide variations in the different frequency states. This is clear looking at Fig. 4.43-(b) that displays the percentage difference of the filter FBW while performing the tuning. The first varactor-tuned filter implemented in Rogers R4003 presented the worst bandwidth variation, and the improvement of the last RF MEMS tunable filter are evident.

Nevertheless, looking at Fig. 4.43, it is clear that both discretely tunable filter using bit capacitances are narrow-band filters. As it has been demonstrated by now in Section 2.3.1, the magnetic coupling using post-wall irises between coaxial SIW resonators is strongly reduced when higher miniaturization is required. Thus, the latter can be applied to both PIN diode-tuned and the RF MEMS-tuned filter, which are very compact filter implementations. This means that the design of wide-band tunable filter should be accomplished by using the electric coupling mechanism, which will guarantee stronger couplings even in the case of miniaturized structures.

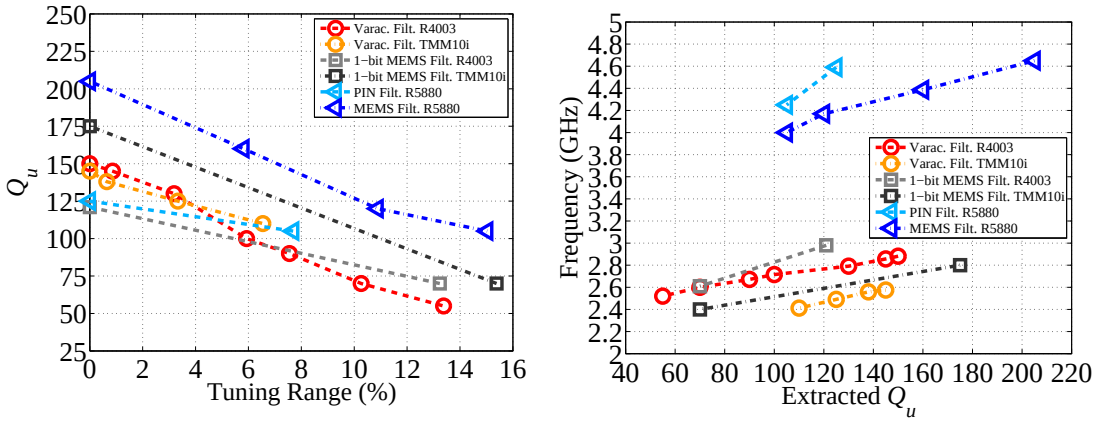

(a) (b)

Figure 4.44: (a) Extracted values of filter Q versus filter tuning range. (b) Extracted values of filter Q versus filter centre frequency.

Accordingly to Fig. 4.44-(a), the RF MEMS tunable filter with integrated bit capacitances shows the highest Q among the six prototypes, which is always better than 100. Additionally, this approach shows one of the wider tuning range. Besides, the integration of bit capacitances into the top metal layer can be considered to be a key factor that enables us to achieve higher Q-factor over the whole tuning range. As Fig. 4.44-(b) displays, it is remarkable that those improvements have been achieved at higher frequency band, more specifically at C-band.

On the one hand, the influence of the lossy varactor diode on the filter performance are clearly demonstrated when compared to performance of an RF MEMS-tuned solution. On the other hand, one of the main advantage of using varactor diodes is the continuous tuning of the filter centre frequency.

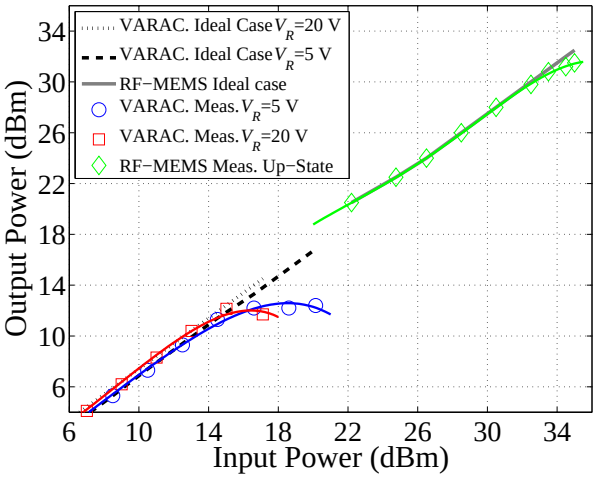

Figure 4.45: Comparison of power handling performance for the analog and discrete tunable filters in coaxial SIW topology using different kind of tuning elements.

It is worth mentioning that the discrete tuning approach makes for additional filter design flexibility, considering that the tuning range mainly depends on the bit capacitances configurations. Therefore, the design of tunable filters can be adapted to give more states (including additional bits), and/or more tuning range (changing the ratio between bit ca-

pacitances and loading capacitance) and/or a specific tuning state distribution (changing the ratio between the capacitance of different bits).

Finally, Fig. 4.45 displays the comparison of the filters performance in terms of power handling. As it is well known, this is one of the most important common deciding factors while designing reconfigurable filters. Taking into account that simultaneously achieving wide frequency tuning and high power handling is significantly more challenging for filters employing high-Q tunable elements rather than low-Q lumped elements, as it has been demonstrated in [41], the results show the superiority of the RF MEMS devices. Power handling capabilities of these components allows the filters to handle up to 35.5 dBm before self-actuation occurs.

Chapter 5

Conclusions and Future Work

As it was outlined at the beginning of this document, the main aim of this PhD Thesis is to study and further develop an innovative coaxial topology implemented in SIW technology that can be the basic building block for implementing advanced filtering responses, including reconfigurable microwave filters. Even if the obtained results are promising, there is still a lot of work that need to be done in order to allow such solution to be widely used in the microwave field. In the next sections, we go little more in detail through the main conclusions and the future research lines derived from this work.

5.1 Conclusions and Future Research Areas

There is a huge interest in developing modern communication systems operating at microwave frequencies, which are expected to improve performance of current systems used in radio and television broadcasting, mobile communication services or satellite payloads. On the other hand, the SIW technology is now fully considered a promising scheme for implementing such future microwave (and even millimeter-wave) devices with advantages of low-cost, small size, relatively high power, high Q, and high-density integration. Therefore, this PhD Thesis has been focused on a further study of SIW technology in order to propose and develop various innovative and original microwave filters, which enable the realization of advanced and reconfigurable filtering responses.

The first objective of this work was to develop and characterize a novel coaxial SIW topology, and these aims have been performed in Chapter 2. The application of the coaxial topology to the SIW provided for an important size reduction of the microwave resonator without worsening the EM performance. The latter has been demonstrated in Section 2.1.2, where the in-depth analysis of its performance helped us understand the resonant nature of the structure, providing us with a conclusive equivalent circuit composed by a substrate integrated coaxial line loaded by a capacitor. That topology showed a wide variety of configurations, which were represented by the variations of the resonator slope parameter, enabling designers to adapt easily the resonator properties for satisfying different requirements.

Additionally, in sections 2.4 and 2.3, it was demonstrated that this topology is excellent for the introduction of different coupling schemes in the SIW. For this aim, different coupling configurations involving magnetic and electric coupling mechanisms have been proposed and studied in detail. Therefore, it is clear that the coaxial SIW topology increased considerably the design flexibility of microwave filters, enabling the designer to implement a wide variety of filter topologies. Therefore, the second objective of this

Thesis was also fulfilled.

In Chapter 3, the design of coaxial SIW resonator filters with advanced performances has been deeply investigated. It has been proved that the proposed electric coupling configuration ensures high flexibility in filter design, which allows us to design very compact filters by keeping a reasonable level of losses, as well as to increase the maximum achievable passband bandwidth in coaxial SIW technology. To prove that, a variety of filters have been proposed where the magnetic and electric coupling schemes has been arranged in order to design a very compact bandpass filter with advanced and very selective responses.

The fourth objective was to introduce a self-packaged solution in the coaxial SIW topology. Since the planar integration of such coaxial filters must be as high as the one of standard SIW components, a vertical transition that provides the input/output ports with accesses through castellated plated via holes was proposed and studied. Thus, the results shown in Sections 3.3 and 3.4 proved that the low-cost, easy-to-manufacture procedure enables coaxial SIW filters to be assembled using standard SMD assembly processes, with negligible degradation of the EM performance. So that, the fourth objective was also fulfilled.

Finally, the last objectives of the Thesis were focused on the introduction of frequency-agility in the coaxial topology, and its demonstration by means of several proof-of-concept designs. The special characteristics of the coaxial SIW topology makes the implementation of reconfigurable resonator easy and effective. Taking into account that the work was focused on creating a frequency tuning mechanism that permits analog-like and digital-like reconfigurations, a step-by-step procedure was proposed in Chapter 4. It is based on the adjustments of the proposed topology, especially the main capacitive patch configuration, which permit the introduction of common tuning elements to make the coaxial loading capacitance controllable. Analog and digital tuning mechanisms were presented and studied separately in sections 4.2 and 4.5, respectively, demonstrating that miniaturized tunable filter can arrange up to 15% of tuning range using RF MEMS switched capacitors. Additionally, varactor diodes, PIN diodes and RF MEMS tuning elements can be easily accommodated showing low insertion losses and almost constant fractional bandwidth. To culminate this Thesis, reconfigurable coaxial SIW filters were successfully designed and results compared with measurement. Last but not least, the power handling capability has been also studied for such filtering structures for different tuning elements, demonstrating that this solution could be used to withstand up to 35 dBm, thus resulting in a significant improvement in terms of power handling.

The RF MEMS tunable filters presented in this Thesis have been developed in collaboration with the XLIM research group of the Universite of Limoges (France), so two different knowledge backgrounds were joined together: design of microwave devices in SIW technology and expertise in the MEMS field, in order to establish a fruitful technical collaboration. The results presented in Chapter 4 can be seen as a proof of this fruitful collaboration.

In conclusion, all the main goals initially proposed for this PhD Thesis have been accomplished successfully. As a result, this Thesis has generated multiple international publications in relevant journals and conferences dedicated to microwave engineering, as it is summarized in Appendix A. Additionally, a patent has also been issued in the framework of this work, which was published in April 2013. Furthermore, the C- and K-band 6-pole quasi-elliptic coaxial SIW filters for frequency conversion applications designed in Section 3.4 were developed under a project funded by the European Space Agency (ESA)

and are currently being manufactured at the Laboratory of High Frequency LTCC Circuits of the Universitat Politécnica de Valéncia, located in Valencia (Spain).

Nevertheless, this Thesis has generated new research areas that can be further explored and studied in the future. The following could be considered the main ones:

- **Development of bandpass filters with dynamically adjustable bandwidth**. As it has been shown in Chapter 4, the proposed coaxial SIW topology permits the design of reconfigurable filters having quasi-constant FBW. In this context, recently, there has been a growing interest on the design of bandpass filters with dynamically adjustable bandwidth. Clearly, bandwidth control is a more challenging objective to achieve in any technology, and this is particularly true in SIW. Since the coaxial SIW topology permits the simple implementation of different kind of coupling mechanisms using the same fabrication processes, much effort should be done on the design of tunable coupling systems between coaxial resonators. The proposed electric coupling seems to be a good candidate to implement such tunable control, since its coupling value strongly depends on the capacitive contribution of the CPW probes that compose it. Therefore, tuning elements could be easily introduced to modify this capacitive contribution, allowing us to control external and inter-resonator couplings. This would help us improve the EM performance of tunable filters, especially when wider tuning ranges are required.

- **Development of new topologies based on coaxial SIW resonators**. For instance, recent efforts have been done in collaboration with Dr. Ing. M. Á. Sánchez-Soriano on the development of dual-mode SIW coaxial resonators, resulting in two recent publications (i.e. [120] and [121]). This new compact filtering building block consists of two via holes embedded into an SIW cavity connected to specific capacitive metal patches at the top layer. Thus, the proposed topology provides two coaxial modes performing a doublet filtering configuration. By applying the frequency-agility mechanisms proposed in this Thesis, it is possible to enable the design of reconfigurable-bandwidth SIW filters. Furthermore, the flexibility of such dual-mode topology would permit the implementation of reconfigurable advanced filtering responses by controlling the direct coupling of the modes in the same cavity resonators.

- **Bias networks and control logic units for fully reconfigurable filters**. As it is well known, incorporating switching elements in reconfigurable filters does imply the design of a bias network and associated electronics to control the state of the tuning elements, so that we can tune the filter response. On the one hand, when RF MEMS switches are employed, it is usually necessary to apply high DC voltages, which can go up to an amplitude of 90-100 V, to change the RF MEMS state. On the other hand, the RF MEMS switch requires just few μA of supply current for commuting, thus the control unit will be able to drive different RF MEMS at the time with a small power consumption. A similar bias specifications, but with lower DC voltage amplitude, can be also applied to the control of varactor diodes. In the case of PIN diodes, the difference is substantial since a DC current flow of hundreds of mA should be applied in order to switch on the elements, thus performing the tuning. Taking into account the increasing number of tuning elements that are necessary for achieving full filter reconfigurability, bias networks and control logic will play an important role in the next generation of modern communication systems.

Initially, these elements may be designed separately from the microwave tunable filters that must control. However, the monolithic integration of tunable filters and its related control unit in the same substrate can be a great advantage in terms of EM performance, planar integration and cost reduction. So, further study could be performed in order to proposed integrated solutions that fit the proposed coaxial SIW topology.

- **Development of an automatic synthesis and design procedure for coaxial SIW filters**. Even though it has been demonstrated that the basic design procedure shown in Chapter 2 can be easily used, there is still a need for performing an extended 3D EM optimization in order to adjust some filter dimensions to achieve the desired response. To speed up the filter design and automatizing many of these adjustments, an elaborated synthesis technique can be of great interest.

- **Alternative materials and fabrication processes**. The performance of SIW filters is fundamentally governed by substrate properties as well as conductor properties and geometrical details. If we consider the unstoppable request for microwave resonators having higher Q-factor, the study of alternative materials and fabrication processes that allow the design of improved coaxial SIW resonators could be very useful. Theoretically, any kind of dielectric material could be used for implementing SIW devices. But, the material selection must be done compatible with the available fabrication processes. Indeed, the most difficult task when creating SIW devices is always related to the through-hole plating process. Thus, additional effort should be put on selecting dielectric materials with lower loss tangent, or fabrication processes that permit using better conductors and provide tighter tolerances. This should guarantee the ability of moving to higher frequency bands of theses coaxial SIW components while preserving reasonably high-Q values. For instance, a preliminary study was performed to understand the feasibility of implementing coaxial SIW resonators in fused silica for the design of cross-coupled filters filter at Ka-band, with a stringent requirements of resonator Q_u better than 500.

Appendix A

List of Publications

A.1 International Journal Publications

- J. D. Martínez, S. Sirci, M. Taroncher, and V. E. Boria, "Compact CPW-fed combline filter in substrate integrated waveguide technology," *IEEE Microwave and Wireless Components Letters*, vol. 22, no. 1, pp. 7–9, Jan. 2012

- S. Sirci, J. D. Martínez, J. Vague, and V. E. Boria, "Substrate integrated waveguide diplexer based on circular triplet combline filters," *IEEE Microwave and Wireless Components Letters*, vol. 25, no. 7, pp. 430–432, Jul. 2015

- S. Sirci, M. A. Sánchez-Soriano, J. D. Martínez, V. E. Boria, F. Gentili, W. Bösch, and R. Sorrentino, "Design and multiphysics analysis of direct and cross-coupled SIW combline filters using electric and magnetic couplings," *IEEE Trans. Microwave Theory Techn.*, vol. 63, no. 12, pp. 4341–4354, Dec. 2015

- M. A. Sánchez-Soriano, S. Sirci, J. D. Martínez, and V. E. Boria, "Compact dual-mode substrate integrated waveguide coaxial cavity for bandpass filter design," *IEEE Microwave and Wireless Components Letters*, vol. 26, no. 6, pp. 386–388, Jun. 2016

A.2 International Conference Publications

- S. Sirci, J. D. Martínez, M. Taroncher, and V. E. Boria, "Varactor-loaded continuously tunable SIW resonator for reconfigurable filter design," in *Proc. of* 41*st Eur. Microwave Conf.*, Manchester, UK, Oct. 2011, pp. 436–439

- S. Sirci, J. D. Martínez, M. Taroncher, and V. E. Boria, "Analog tuning of compact varactor-loaded combline filters in substrate integrated waveguide," in *Proc. of* 42*st Eur. Microwave Conf.*, Amsterdam, NL, Oct. 2012, pp. 257–260

- S. Sirci, J. D. Martínez, R. Stefanini, M. Taroncher, P. Blondy, and V. E. Boria, "High linearity 2.6-3 GHz switchable combline filter in MEMS-loaded substrate integrated waveguide," in *Proc. of MEMSWAVE Inter. Workshop*, Antalya, Turkey, Jul. 2012, pp. 1–4

- J. D. Martínez, S. Sirci, and V. E. Boria, "Compact SIW filter with asymmetric frequency response for C-band wireless applications," in *Proc. of IEEE International Wireless Symposium (IWS)*, Beijing, China, Apr. 2013, pp. 1–4

- S. Sirci, J. D. Martínez, and V. E. Boria, "Low-loss 3-bit tunable SIW filter with PIN diodes and integrated bias network," in *Proc. of 43st Eur. Microwave Conf.*, Nuremberg, Germany, Oct. 2013, pp. 1211–1214

- S. Sirci, J. D. Martínez, R. Stefanini, P. Blondy, and V. E. Boria, "Compact SMD packaged tunable filter based on substrate integrated coaxial resonators," in *Proc. of IEEE MTT-S Int. Microw. Symp. Dig.*, Tampa Bay, USA, Jun. 2014, pp. 1–4

- S. Sirci, E. Lemoine, A. Harck, J. D. Martínez, V. E. Boria, and P. Blondy, "RF MEMS tunable SIW filter with 16-state digital responses," in *Proc. of MEMSWAVE Inter. Workshop*, La Rochelle, France, Jun. 2014, pp. 1–4

- S. Sirci, J. D. Martínez, and V. E. Boria, "LTCC packaging of substrate integrated coaxial filters," in *Proc. of 6th. CNES/ESA Inter. Workshop on Microw. Filt.*, Toulouse, France, Mar. 2015, pp. 1–4

- S. Sirci, F. Gentili, J. D. Martínez, V. E. Boria, and R. Sorrentino, "Quasi-elliptic filter based on SIW combline resonators using a coplanar line cross-coupling," in *Proc. of IEEE MTT-S Int. Microw. Symp. Dig.*, Phoenix, Arizona (USA), May 2015, pp. 1–4

- M. A. Sánchez-Soriano, S. Sirci, J. D. Martínez, and V. E. Boria, "Compact bandpass filters based on a new substrate integrated waveguide coaxial cavity," in *Proc. of IEEE MTT-S Int. Microw. Symp. Dig.*, San Francisco, California (USA), May 2016, pp. 1–4

A.3 International Workshops

- S. Sirci, J. D. Martínez, and V. E. Boria, "Analog and digital tunable filters based on substrate integrated coaxial resonators," in *Short Course of 6th. CNES/ESA Inter. Workshop on Microw. Filt.*, Toulouse, France, Mar. 2015

- S. Sirci, "Compact tunable filters based on substrate integrated coaxial resonators," in *Workshop WS06 of 45st Eur. Microwave Conf.*, Paris, France, Oct. 2015, WS06 Title: *Recent Advances on High Performance Reconfigurable Filters*

A.4 National Conference Publications

- S. Sirci, J. D. Martínez, M. Taroncher, and V. E. Boria, "Cavidad resonante en tecnología SIW sintonizable entre 2.6-3.1 GHz mediante varactores de GaAs," in *Proc. of 26st Spanish URSI*, Madrid, Spain, Sep. 2011, pp. 1–4

- J. J. Vague-Cardona, S. Sirci, J. D. Martínez, and V. E. Boria, "An X-band surface mounted cavity oscillator with low phase noise," in *Proc. of 28st Spanish URSI*, Valencia, Spain, Sep. 2014, pp. 1–4

- S. Sirci, J. J. Vague-Cardona, J. D. Martínez, and V. E. Boria, "Filtros combline SIW embebidos en tecnología LTCC," in *Proc. of 28st Spanish URSI*, Valencia, Spain, Sep. 2014, pp. 1–4

A.5 Patents

- V. E. Boria, J. D. Martínez, S. Sirci, and M. Taroncher, "Tunable microwave filter in surface-mounting technology on the basis of coaxial resonant cavities built into the substrate," Patent Number: WO2013050636A1, Priority date: 2011-10-07, Filing date: 2012-09-12, Publication date: 2013-04-11, Original Assignee: Universitat Politècnica de València

Acronyms

APHC	Average Power Handling Capability
BST	Barium Strontium Titanate
BW	Bandwidth
CNRS	Centre National de la Recherche Scientifique
CPW	Coplanar Waveguide
CSRRs	square Complementary Split-Ring Resonators
CTE	Coefficient of Thermal Expansion
CW	Continuous Wave
DC	Direct Current
EM	Electromagnetic
ENIG	Electroless Nickel Immersion Gold
FBW	Fractional Bandwidth
GSG	Ground-Signal-Ground
HMSIW	Half-Mode Substrate Integrated Waveguide
IDC	Inter-Digital Capacitor
IIP3	Third-order Intermodulation Intercept Point
IL	Insertion Loss
IP1	1-dB Compression Point
LTCC	Low Temperature Co-fired Ceramics
LTE	Long Term Evolution
MIM	Metal-Insulator-Metal
PCB	Printed Circuit Board
PHC	Power Handling Capability
PIN	Positive-Intrinsic-Negative
PPHC	Peak Power Handling Capability
Q_e	External Quality Factor

Q_u	Unloaded Quality Factor
QMSIW	Quarter-Mode Substrate Integrated Waveguide
RF	Radio Frequency
RF MEMS	Radio-Frequency Micro Electro-Mechanical Systems
SIW	Substrate Integrated Waveguide
SMD	Surface Mounting Device
TMM10i	Thermoset Microwave Material 10i
TMM4	Thermoset Microwave Material 4
TZ	Transmission Zero
UHF	Ultra High Frequency
U-NII	Unlicensed National Information Infrastructure
USA	United State of America
WiMAX	Worldwide Interoperability for Microwave Access
WLAN	Wireless Local Area Network

Bibliography

[1] D. Deslandes and K. Wu, "Integrated microstrip and rectangular waveguide in planar form," *IEEE Microw. Wireless Compon. Lett.*, vol. 11, no. 2, pp. 68–70, Feb. 2001.

[2] K. Wu, "Integration and interconnect techniques of planar and non-planar structures for microwave and millimeter-wave circuits-current status and future trend," in *Proc. of 2001 Asia Pacific Microwave Conference*, Tapei, Taiwan, Dec. 2001, pp. 411–416.

[3] X.-P. Chen and K. Wu, "Substrate integrated waveguide filter: Basic design rules and fundamental structure features," *IEEE Microw. Mag.*, vol. 15, no. 5, pp. 108–116, Jul. 2014.

[4] X.-P. Chen and K. Wu, "Substrate integrated waveguide filters: Design techniques and structure innovations," *IEEE Microw. Mag.*, vol. 15, no. 6, pp. 75–83, Sep.-Oct. 2014.

[5] K. Entesari, A. P. Saghati, V. Sekar, and M. Armendariz, "Tunable SIW structures: Antennas, VCOs, and filters," *IEEE Microw. Mag.*, vol. 16, no. 5, pp. 34–54, Jun. 2015.

[6] R. M. Kurzrok, "General three-resonator filters in waveguide," *IEEE Trans. Microwave Theory Techn.*, vol. MTT-14, no. 1, pp. 46–47, 1966.

[7] J. S. Hong and M. J. Lancaster, "Microstrip cross-coupled trisection bandpass filters with asymmetric frequency characteristics," *IEE Proc. Microw. Antennas Propag.*, vol. 146, no. 1, pp. 84–90, Feb. 1999.

[8] J. S. Hong and M. Lancaster, *Microstrip filter for RF/Microwave Applications*, 1st ed. New Jersey: John Wiley and Sons, inc., 2001.

[9] R. Levy, "Filter with single transmission zeros at real or imaginary frequencies," *IEEE Trans. Microw. Theory Tech.*, vol. 24, no. 4, pp. 172–181, 1976.

[10] J. B. Thomas, "Cross-coupling in coaxial cavity filters - A tutorial overview," *IEEE Trans. Microw. Theory Techn.*, vol. 51, no. 4, pp. 1368–1376, 2003.

[11] X. P. Chen and K. Wu, "Self-equalized pseudo-elliptical filter made of substrate integrated waveguide," *Electron. Lett.*, vol. 45, no. 2, pp. 112–113, Jan. 2009.

[12] X. Chen, W. Hong, T. Cui, J. Chen, and K. Wu, "Substrate integrated waveguide linear phase filter," *IEEE Microw. Wireless Compon. Lett.*, vol. 15, no. 11, pp. 787–789, 2005.

[13] X. P. Chen, W. Hong, J. X. Chen, and K. Wu, "Substrate integrated waveguide elliptic filter with high mode," in *Proc. of 2005 Asia Pacific Microwave Conference*, Suzhou, China, Dec. 2005, pp. 2056–2059.

[14] X. P. Chen and K. Wu, "Self-packaged millimeter-wave substrate integrated waveguide filter with asymmetric frequency response," *IEEE Trans. Compon., Packag., Manuf. Technol.*, vol. 2, no. 5, pp. 775–782, May 2012.

[15] X. P. Chen, K. Wu, and D. Drolet, "Substrate integrated waveguide filter with improved stopband performance for satellite ground terminal," *IEEE Trans. Microwave Theory Techn.*, vol. 57, no. 3, pp. 674–683, Mar. 2009.

[16] X. P. Chen, K. Wu, and Z. L. Li, "Dual-band and triple-band substrate integrated waveguide filters with chebyshev and quasi-elliptic responses," *IEEE Trans. Microwave Theory Techn.*, vol. 55, no. 12, pp. 2569–2578, Dec. 2007.

[17] X. P. Chen and K. Wu, "Substrate integrated waveguide cross-coupled filter with negative coupling structure," *IEEE Trans. Microw. Theory Techn.*, vol. 56, no. 1, pp. 142–149, Jan. 2008.

[18] G. H. Lee, C. S. Yoo, J. G. Yook, and J. C. Kim, "SIW quasi-elliptic filter based on LTCC for 60-GHz application," in *Pr. 4th Eur. Microw. Integ. Circ. EuMiC*, Sep. 2009, pp. 204–207.

[19] K. Gong, W. Hong, Y. Zhang, P. Chen, and C. J. You, "Substrate integrated waveguide quasi-elliptic filters with controllable electric and magnetic mixed coupling," *IEEE Trans. Microw. Theory Techn.*, vol. 60, no. 10, pp. 3071–3078, Oct. 2012.

[20] B. Potelon, J. Favennec, C. Quendo, E. Rius, C. Person, and J. Bohorquez, "Design of a substrate integrated waveguide (SIW) filter using a novel topology of coupling," *IEEE Microw. Wireless Compon. Lett.*, vol. 18, no. 9, pp. 596–598, 2008.

[21] N. Grigoropoulos, B. Sanz-Izquiredo, and P. R. Young, "Substrate integrated folded waveguides SIFW and filters," *IEEE Microw. Wireless Compon. Lett.*, vol. 15, no. 12, pp. 829–831, 2005.

[22] W. Hong, Y. Wang, Q. H. Lai, and B. Liu, "Half mode substrate integrated waveguide: a new guided wave structure for microwave and millimeter wave application," in *Proc. Joint 31st Int. Conf. Infr. Millim. Waves 14th Int. Conf. Terahertz Electron.*, Shangai, China, Sep. 2006, pp. 1–4.

[23] Y. Wang, W. Hong, Y. Dong, B. Lui, H. J. Tang, J. Chen, X. Yin, and K. Wu, "Half mode substrate integrated waveguide HMSIW bandpass filter," *IEEE Microw. Wireless Compon. Lett.*, vol. 17, no. 4, pp. 265–267, 2007.

[24] C. Jin and Z. Shen, "Compact triple-mode filter based on quarter-mode substrate integrated waveguide," *IEEE Trans. Microw. Theory Techn.*, vol. 62, no. 1, pp. 37–45, Jan. 2014.

[25] A. P. Saghati, A. P. Saghati, and K. Entesari, "Ultra-miniature SIW cavity resonators and filters," *IEEE Trans. Microwave Theory Techn.*, vol. 63, no. 12, pp. 4329–4340, Dec. 2015.

[26] Y. D. Dong, T. Yang, and T. Itoh, "Substrate integrated waveguide loaded by complementary split-ring resonators and its applications to miniaturized waveguide filters," *IEEE Trans. Microw. Theory Techn.*, vol. 57, no. 9, pp. 2211–2223, Sep. 2009.

[27] L. S. Wu, L. Zhou, X. L. Zhou, and W. Y. Yin, "Bandpass filter using substrate integrated waveguide cavity loaded with dielectric rod," *IEEE Microw. Wireless Compon. Lett.*, vol. 19, no. 8, pp. 491–493, 2009.

[28] T. C. Lee and J. Y. Park, "Compact PCB embedded tunable filter for UHF TV broadcasting," in *IEEE MTT-S Int. Microw. Symp. Dig.*, Jun. 2009, pp. 505–508.

[29] N. Tanzi, "Varactor-tuned coupled resonator front-end bandpass filters for cognitive radio applications," in *Pr. IEEE Radio and Wireless Symposium*, Jan. 2006, pp. 155–158.

[30] Y. Shim, J. Ruan, Z. Wu, and M. Rais-Zadeh, "Varactor-tuned coupled resonator front-end bandpass filters for cognitive radio applications," in *Pr. IEEE 25th International Conference on Micro Electro Mechanical Systems (MEMS)*, Jan. 2012, pp. 15–18.

[31] I. C. Hunter and J. D. Rhodes, "Electronically tunable microwave bandpass filters," *IEEE Trans. Microw. Theory Techn.*, vol. 30, no. 9, pp. 1354–1360, Sep. 1982.

[32] A. R. Brown and G. M. Rebeiz, "A varactor-tuned RF filter," *IEEE Trans. Microw. Theory Techn.*, vol. 48, no. 7, pp. 1157–1160, Jul. 2000.

[33] M. Sánchez-Renedo, R. Gómez-García, J. I. Alonso, and C. B. Rodríguez, "Tunable combline filter with continuous control of center frequency and bandwidth," *IEEE Trans. Microw. Theory Techn.*, vol. 53, no. 1, pp. 191–199, Jan. 2005.

[34] Y. H. Cho and G. M. Rebeiz, "0.73-1.03 GHz tunable bandpass filter with a reconfigurable 2/3/4-pole response," *IEEE Trans. Microw. Theory Techn.*, vol. 62, no. 2, pp. 290–296, Feb. 2014.

[35] J. Nath, D. Gosh, J. P. Maria, A. Kingon, W. Fathelbab, P.Franzon, and M. Steer, "An electronically tunable microstrip bandpass filter using thin-film Barium-Strontium-Titanate (BST) varactors," *IEEE Trans. Microw. Theory Techn.*, vol. 53, no. 9, pp. 2707–2712, Sep. 2005.

[36] C. Lugo and J. Papapolymerou, "Electronic switchable bandpass filter using PIN diodes for wireless low cost system-on-a-package applications," *IEE Proc. Microw. Antennas Propag.*, vol. 151, no. 6, pp. 497–502, Dec. 2004.

[37] P. W. Wong and I. C. Hunter, "A new class of low-loss high-linearity electronically reconfigurable microwave filter," *IEEE Trans. Microw. Theory Techn.*, vol. 56, no. 8, pp. 1945–1953, Aug. 2008.

[38] E. Fourn, A. Pothier, C. Champeaux, P. Tristant, A. Catherinot, P. Blondy, G. Tanne, E. Rius, C. Person, and F. Huret, "MEMS switchable interdigital coplanar filter," *IEEE Trans. Microw. Theory Techn.*, vol. 51, no. 1, pp. 320–324, Jan. 2003.

[39] A. Abbaspour-Tamijani, L. Dussopt, and G. M. Rebeiz, "Miniature and tunable filters using MEMS capacitors," *IEEE Trans. Microw. Theory Techn.*, vol. 51, no. 7, pp. 1878–1885, Jul. 2003.

[40] A. Ocera, P. Farinelli, P. Mezzanotte, R. Sorrentino, B. Margesin, and F. Giacomozzi, "A novel MEMS-tunable hairpin line filter on silicon substrate," in *Proc. of* 36*th. European Microwave Conferences*, Manchester, UK, Sep. 2006, pp. 803–806.

[41] P. Blondy and D. Peroulis, "Handling RF power: the latest advances in RF MEMS tunable filters," *IEEE Microw. Mag.*, vol. 14, no. 1, pp. 24–38, Sep. 2013.

[42] C. C. Cheng and G. M. Rebeiz, "High 4-6 GHz suspended stripline RF MEMS tunable filter with bandwidth control," *IEEE Trans. Microw. Theory Techn.*, vol. 59, no. 10, pp. 2469–2476, Oct. 2011.

[43] A. C. Guyette, "Intrinsically switched varactor-tuned filters and filter banks," *IEEE Trans. Microw. Theory Techn.*, vol. 60, no. 4, pp. 1044–1056, Apr. 2012.

[44] A. C. Guyette, "Alternative architectures for narrowband varactor-tuned bandpass filters," in *Proc. of* 39*th. European Microwave Conferences*, Roma, Italy, Oct. 2009, pp. 1828–1831.

[45] A. C. Guyette, "Theory and design of intrinsically switched multiplexers with optimum phase linearity," *IEEE Trans. Microw. Theory Techn.*, vol. 61, no. 9, pp. 3254–3264, Sep. 2013.

[46] R. Gómez-García, M. A. Sánchez-Soriano, M. Sánchez-Renedo, G. Torregrosa-Penalva, , and E. Bronchalo, "Lowpass and bandpass filters with ultra-broad stopband bandwidth based on directional couplers," *IEEE Trans. Microw. Theory Techn.*, vol. 61, no. 12, pp. 4365–4375, Dec. 2013.

[47] R. Gómez-García, M. A. Sánchez-Soriano, K.-W. Tam, and Q. Xue, "Flexible filters: Reconfigurable-bandwidth bandpass planar filters with ultralarge tuning ratio," *IEEE Microw. Mag.*, vol. 15, no. 5, pp. 43–54, Jul.-Aug. 2014.

[48] J. Uher and W. J. R. Hoefer, "Tunable microwave and millimeter-wave band pass filters," *IEEE Trans. Microw. Theory Techn.*, vol. 39, no. 4, pp. 643–653, Apr. 1991.

[49] B. Yassini, M. Yu, and B. Keats, "A Ka-band fully tunable cavity filter," *IEEE Trans. Microw. Theory Techn.*, vol. 60, no. 12, pp. 4002–4012, Dec. 2012.

[50] S. Fouladi, F. Huang, W. D. Yan, and R. R. Mansour, "High-Q narrowband tunable combline bandpass filters using MEMS capacitor banks and piezomotors," *IEEE Trans. Microw. Theory Techn.*, vol. 61, no. 1, pp. 393–402, Jan. 2013.

[51] D. W. Winter and R. R. Mansour, "Tunable dielectric resonator bandpass filter with embedded MEMS tuning elements," *IEEE Trans. Microw. Theory Techn.*, vol. 55, no. 1, pp. 154–159, Jan. 2007.

[52] R. R. Mansour, "High-Q tunable dielectric resonator filters: challenges and potential," *IEEE Microw. Mag.*, vol. 10, no. 6, pp. 84–98, Oct. 2009.

[53] W. D. Yan and R. R. Mansour, "Micromachined millimeter-wave ridge waveguide filter with embedded MEMS tuning elements," in *IEEE MTT-S Int. Microw. Symp. Dig.*, San Francisco, USA, Jun. 2006, pp. 1290–1293.

[54] D. Scarbrough, C. Goldsmith, J. Papapolymerou, and Y. Li, "Miniature microwave RF MEMS tunable waveguide filter," in *Proc. of* 39*th. European Microwave Conferences*, Roma, Italy, Oct. 2009, pp. 1860–1863.

[55] L. Pelliccia, F. Cacciamani, P. Farinelli, P. Ligander, O. Persson, and R. Sorrentino, "High-Q MEMS-tunable waveguide filters in K-band," in *Proc. of* 42*th. European Microwave Conferences*, Amsterdam, NL, Oct. 2012, pp. 273–276.

[56] L. Pelliccia, F. Cacciamani, P. Farinelli, and R. Sorrentino, "High-Q tunable waveguide filters using ohmic RF MEMS switches," *IEEE Trans. Microwave Theory Techn.*, vol. 63, no. 10, pp. 3381–3390, Oct. 2015.

[57] R. Stefanini, M. Chatras, A. Pothier, J. C. Orlianges, and P. Blondy, "High Q tunable cavity using dielectric less RF MEMS varactors," in *Proc. of* 39*th. European Microwave Conferences*, Roma, Italy, Oct. 2009, pp. 1744–1747.

[58] R. Stefanini, J. D. Martínez, M. Chatras, A. Pothier, V. E. Boria, and P. Blondy, "Ku-band high-Q tunable surface-mounted cavity resonator using RF MEMS varactors," *IEEE Microw. Wireless Compon. Lett.*, vol. 21, no. 5, pp. 237–239, May. 2011.

[59] S. J. Park, I. Reines, C. Patel, and G. M. Rebeiz, "High-Q RF MEMS 4-6 GHz tunable evanescent-mode cavity filter," *IEEE Trans. Microwave Theory Techn.*, vol. 58, no. 2, pp. 381–389, Feb. 2010.

[60] X. Liu, L. Katehi, W. Chappell, and D. Peroulis, "High-Q tunable microwave cavity resonators and filters using SOI-based RF MEMS tuners," *IEEE J. Microelectromech. Syst.*, vol. 19, no. 4, pp. 774–784, Aug. 2010.

[61] M. S. Arif and D. Peroulis, "All-silicon technology for high-Q evanescent mode cavity tunable resonators and filters," *IEEE J. Microelectromech. Syst.*, vol. 23, no. 3, pp. 727–739, Jun. 2014.

[62] H. Joshi, H. H. Sigmarsson, M. Sungwook, D. Peroulis, and W. J. Chappell, "High-Q fully reconfigurable tunable bandpass filters," *IEEE Trans. Microwave Theory Techn.*, vol. 57, no. 12, pp. 3525–3533, Dec. 2009.

[63] F. Mira, J. Mateu, and C. Collado, "Mechanical tuning of substrate integrated waveguide resonators," *IEEE Microw. Wireless Compon. Lett.*, vol. 22, no. 9, pp. 447–449, Sep. 2012.

[64] F. Mira, J. Mateu, and C. Collado, "Mechanical tuning of substrate integrated waveguide filters," *IEEE Trans. Microwave Theory Techn.*, vol. 63, no. 12, pp. 3939–3946, Dec. 2015.

[65] H. Fanfan, X. P. Chen, K. Wu, and W. Hong, "Electrically tunable Substrate Integrated Waveguide reflective cavity resonator," in *Proc. of 2009 Asia Pacific Microwave Conference*, Singapore City, Singapore, Dec. 2009, pp. 119–122.

[66] H. Fanfan, K. Wu, and W. Hong, "Electrically tunable half mode Substrate Integrated Waveguide resonator," in *Proc. of 2011 Asia Pacific Microwave Conference*, Melbourne, Australia, Dec. 2011, pp. 1166–1169.

[67] T. Yang, K. Ho, and G. M. Rebeiz, "Compact self-shielded 2-3 GHz high-Q coaxial fixed and tunable filters," *IEEE Trans. Microwave Theory Techn.*, vol. 62, no. 12, pp. 3370–3379, Dec. 2014.

[68] M. Armendariz, V. Sekar, and K. Entesari, "Tunable SIW bandpass filters with PIN diodes," in *Proc. of 40th. European Microwave Conferences*, Paris, France, Sep. 2010, pp. 830–833.

[69] V. Sekar, M. Armendariz, and K. Entesari, "A $1.2 - 1.6$ GHz substrate integrated waveguide RF MEMS tunable filter," *IEEE Trans. Microw. Theory Techn.*, vol. 59, no. 4, pp. 866–876, Apr. 2011.

[70] S. Adhikari, A. Ghiotto, and K. Wu, "Simultaneous electric and magnetic two-dimensionally tuned parameter agile SIW devices," *IEEE Trans. Microwave Theory Techn.*, vol. 61, no. 1, pp. 423–435, Jan. 2013.

[71] S. Adhikari, S. Hemour, A. Ghiotto, and K. Wu, "Magnetically tunable ferrite-loaded half-mode Substrate Integrated Waveguide," *IEEE Microw. Wireless Compon. Lett.*, vol. 25, no. 3, pp. 172–174, Mar. 2015.

[72] G. L. Matthaei, "Combline band-pass filters of narrow or moderate bandwidth," *Microwave Journal*, vol. 6, pp. 82–91, Aug. 1963.

[73] E. G. Cristal, "Coupled circular-cylindrical rods between parallel ground planes," *IEEE Trans. Microw. Theory Techn.*, vol. MTT-12, pp. 428–439, Jul. 1964.

[74] J. D. Rhodes, "The stepped digital elliptic filter," *IEEE Trans. Microw. Theory Techn.*, vol. MTT-17, pp. 178–184, Apr. 1969.

[75] J. D. Martínez, M. Taroncher, and V. E. Boria, "Capacitively loaded resonator for compact substrate integrated waveguide filters," in *Proc. of 40th. European Microwave Conferences*, Paris, France, Sep. 2010, pp. 192–195.

[76] J. D. Martínez, S. Sirci, M. Taroncher, and V. E. Boria, "Compact CPW-fed combline filter in substrate integrated waveguide technology," *IEEE Microwave and Wireless Components Letters*, vol. 22, no. 1, pp. 7–9, Jan. 2012.

[77] H. J. Riblet, "An accurate approximation of the impedance of a circular cylinder concentric with an external square tube," *IEEE Trans. Microw. Theory Techn.*, vol. 31, no. 10, pp. 841–844, Oct. 1983.

[78] H. S. Lee and H. J. Eom, "Potential distribution through an annular aperture with a floating inner conductor," *IEEE Trans. Microw. Theory Techn.*, vol. 47, no. 3, pp. 372–374, Mar. 1999.

[79] TMM Laminates. Rogers Corporation, Connecticut, USA, 2016, [Online]. Available: https://www.rogerscorp.com/acs/producttypes/8/TMM-Laminates.aspx.

[80] ANSYS HFSS, Version: 2014.0.7, ANSYS Inc., Canonsburg (PA), USA, 2016, Web site: http://www.ansys.com/Products/Electronics/ANSYS-HFSS.

[81] X. P. Chen and K. Wu, "Substrate integrated waveguide filter: basic design rules and fundamental structure features," *IEEE Microw. Mag.*, vol. 15, no. 5, pp. 108–116, Jul.-Aug. 2014.

[82] Bilayer General Tolerances. LAB CIRCUITS SA, Barcelona, Spain, 2016, [Online]. Available: http://www.lab-circuits.com/en/para_fabricaci_bicapa.php.

[83] X.-P. Chen and K. Wu, "Substrate integrated waveguide filters: practical aspects and design considerations," *IEEE Microw. Mag.*, vol. 15, no. 7, pp. 75–83, Nov. 2014.

[84] RO4000 Laminates. Rogers Corporation, Connecticut, USA, 2016, [Online]. Available: https://www.rogerscorp.com/acs/producttypes/9/RO4000-Laminates.aspx.

[85] D. Deslandes and K. Wu, "Integrated transition of coplanar to rectangular waveguides," in *Proc. of IEEE MTT-S International Microwave Symposium 2001*, vol. 2, 2001, pp. 619–622.

[86] S. Sirci, F. Gentili, J. D. Martínez, V. E. Boria, and R. Sorrentino, "Quasi-elliptic filter based on SIW combline resonators using a coplanar line cross-coupling," in *Proc. of IEEE MTT-S Int. Microw. Symp. Dig.*, Phoenix, Arizona (USA), May 2015, pp. 1–4.

[87] S. Sirci, J. D. Martínez, and V. E. Boria, "LTCC packaging of substrate integrated coaxial filters," in *Proc. of 6th. CNES/ESA Inter. Workshop on Microw. Filt.*, Toulouse, France, Mar. 2015, pp. 1–4.

[88] Heralock HL2000. Heraeus Holding GmbH, Hanau, D, 2016, [Online]. Available: http://www.seaceramics.com/Download/Design%20Guides/HL2KDG.pdf.

[89] J. D. Martínez, S. Sirci, and V. E. Boria, "Compact SIW filter with asymmetric frequency response for C-band wireless applications," in *Proc. of IEEE International Wireless Symposium (IWS)*, Beijing, China, Apr. 2013, pp. 1–4.

[90] J. B. Ness, "A unified approach to the design, measurement and tuning of coupled-resonator filters," *IEEE Trans. Microw. Theory Techn.*, vol. 46, no. 4, pp. 343–351, Apr. 1998.

[91] S. Sirci, J. D. Martínez, J. Vague, and V. E. Boria, "Substrate integrated waveguide diplexer based on circular triplet combline filters," *IEEE Microwave and Wireless Components Letters*, vol. 25, no. 7, pp. 430–432, Jul. 2015.

[92] Z. C. Hao, W. Hong, J. X. Chen, X. P. Chen, and K. Wu, "Planar diplexer for microwave integrated circuits," *IEE Proc. Microw. Antennas Propag.*, vol. 152, no. 6, pp. 455–459, Dec. 2005.

[93] Y. Dong and T. Itoh, "Substrate integrated waveguide loaded by complementary split-ring resonators for miniaturized diplexer design," *IEEE Microw. Wireless Compon. Lett.*, vol. 21, no. 1, pp. 10–12, Jan. 2011.

[94] A. García-Lampérez, M. Salazar-Palma, and S. H. Yeung, "SIW compact diplexer," in *IEEE MTT-S Int. Microw. Symp. Dig.*, Tampa Bay, USA, Jun. 2014, pp. 1–4.

[95] S. Sirci, M. A. Sánchez-Soriano, J. D. Martínez, V. E. Boria, F. Gentili, W. Bösch, and R. Sorrentino, "Design and multiphysics analysis of direct and cross-coupled SIW combline filters using electric and magnetic couplings," *IEEE Trans. Microwave Theory Techn.*, vol. 63, no. 12, pp. 4341–4354, Dec. 2015.

[96] J. Lee, E. J. Naglich, H. H. Sigmarsson, D. Peroulis, and W. J. Chappell, "Tunable inter-resonator coupling structure with positive and negative values and its application to the field-programmable filter array," *IEEE Trans. Microw. Theory Techn.*, vol. 59, no. 12, pp. 3389–3400, Dec. 2011.

[97] W. Shen, W. Y. Yin, X. W. Sun, and L. S. Wu, "Substrate integrated waveguide bandpass filters with planar resonators for system-on-package," *IEEE Trans. Compon., Packag., Manuf. Technol.*, vol. 3, no. 2, pp. 253–261, Feb. 2013.

[98] F. Zhu, W. Hong, J. X. Chen, and K. Wu, "Cross-coupled substrate integrated waveguide filters with improved stopband performance," *IEEE Microw. Wireless Compon. Lett.*, vol. 22, no. 12, pp. 633–635, Dec. 2012.

[99] K. C. Gupta, R. Garg, I. J. Bahl, and P. Bhartia, *Microstrip lines and slotlines*, 2nd ed. Artech house Boston, 1996.

[100] M. A. Sánchez-Soriano, Y. Quere, V. Le Saux, C. Quendo, and S. Cadiou, "Average power handling capability of microstrip passive circuits considering metal housing and environment conditions," *IEEE Transactions on Components, Packaging and Manufacturing Technology*, vol. 4, no. 10, pp. 1624–1633, Oct. 2014.

[101] M. A. Sánchez-Soriano, M. Edwards, Y. Quere, D. Andersson, S. Cadiou, and C. Quendo, "Mutiphysics study of RF/Microwave planar devices: effect of the input signal power," in *2014 15th EuroSime*, Apr. 2014, pp. 1–7.

[102] ANSYS Multiphysics, Version: 17.1, ANSYS Inc., Canonsburg (PA), USA, 2016, Web site: http://www.ansys.com/Products/Multiphysics.

[103] J. S. Hong, *Microstrip Filter for RF/Microwave Applications*, 2nd ed. New Jersey: John Wiley and Sons, inc., 2011.

[104] C. Ernst and V. Postoyalko, "Prediction of peak internal fields in direct-coupled-cavity filters," *IEEE Trans. Microw. Theory Techn.*, vol. 51, no. 1, pp. 64–73, Jan. 2003.

[105] M. Yu, "Power-handling capability for RF filters," *IEEE Microw. Mag.*, vol. 8, no. 5, pp. 88–97, Oct. 2007.

[106] R. E. Collin, *Foundations for microwave engineering.* John Wiley & Sons, 2007.

[107] M. A. Sánchez-Soriano, E. Bronchalo, and G. Torregrosa-Penalva, "Parallel-coupled line filter design from an energetic coupling approach," *IET Microw., Antennas and Prop.*, vol. 5, no. 5, pp. 568–575, Apr. 2011.

[108] R. J. Cameron, C. M. Kudsia, and R. R. Mansour, *Microwave filters for communication systems*. Wiley-Interscience, 2007.

[109] W. Woo and J. DeGroot, "Microwave absorption and plasma heating due to microwave breakdown in the atmosphere," *IEEE Physical Fluids*, vol. 27, no. 2, pp. 475–487, 1984.

[110] Ferro A6M LTCC Green Tape. Ferro Electronic Packaging Materials, Mayfield Heights (Ohio), USA, 2016, [Online]. Available: http://www.ferro.com/noncms/ems/EPM/content/docs/A6M%20LTCC%20System.pdf.

[111] MA46H200 through MA46H204 GaAs Hyperabrupt Series. MACOM, Lowell (MA), USA, 2015, [Online]. Available: https://www.macom.com/products/productdetail/MA46H200-1056.

[112] S. Sirci, J. D. Martínez, M. Taroncher, and V. E. Boria, "Varactor-loaded continuously tunable SIW resonator for reconfigurable filter design," in *Proc. of 41st Eur. Microwave Conf.*, Manchester, UK, Oct. 2011, pp. 436–439.

[113] S. Sirci, J. D. Martínez, M. Taroncher, and V. E. Boria, "Analog tuning of compact varactor-loaded combline filters in substrate integrated waveguide," in *Proc. of 42st Eur. Microwave Conf.*, Amsterdam, NL, Oct. 2012, pp. 257–260.

[114] MGV050-18 Abrupt Varactor Diodes. Cobham AvComm and Formerly Aeroflex Test Solutions, New York, USA, 2015, [Online]. Available: http://www.ckassoc.com/pdf/aeroflexmetelics.pdf.

[115] R. Stefanini, C. Guines, F. Barriere, E. Lemoine, and P. Blondy, "High power handling low-voltage RF MEMS switched capacitors," in *Proc. 7th. Eur. Microw. Integ. Circ. Conf.(EuMiC)*, Amsterdam, NL, Oct. 2012, pp. 449–452.

[116] MADP-042XX8-13060 SURMOUNT PIN Diode Series. MACOM, Lowell (MA), USA, 2015, [Online]. Available: http://cdn.macom.com/datasheets/MADP-042XX8-13060%20Series.pdf.

[117] S. Sirci, J. D. Martínez, and V. E. Boria, "Low-loss 3-bit tunable SIW filter with PIN diodes and integrated bias network," in *Proc. of 43st Eur. Microwave Conf.*, Nuremberg, Germany, Oct. 2013, pp. 1211–1214.

[118] RT/duroid Laminates. Rogers Corporation, Connecticut, USA, 2016, [Online]. Available: https://www.rogerscorp.com/acs/producttypes/6/RT-duroid-Laminates.aspx.

[119] S. Sirci, E. Lemoine, A. Harck, J. D. Martínez, V. E. Boria, and P. Blondy, "RF MEMS tunable SIW filter with 16-state digital responses," in *Proc. of MEMSWAVE Inter. Workshop*, La Rochelle, France, Jun. 2014, pp. 1–4.

[120] M. A. Sánchez-Soriano, S. Sirci, J. D. Martínez, and V. E. Boria, "Compact bandpass filters based on a new substrate integrated waveguide coaxial cavity," in *Proc. of IEEE MTT-S Int. Microw. Symp. Dig.*, San Francisco, California (USA), May 2016, pp. 1–4.

[121] M. A. Sánchez-Soriano, S. Sirci, J. D. Martínez, and V. E. Boria, "Compact dual-mode substrate integrated waveguide coaxial cavity for bandpass filter design," *IEEE Microwave and Wireless Components Letters*, vol. 26, no. 6, pp. 386–388, Jun. 2016.